Glass production from desert sand

Proof of concept and characterisation

J. A. Minkels

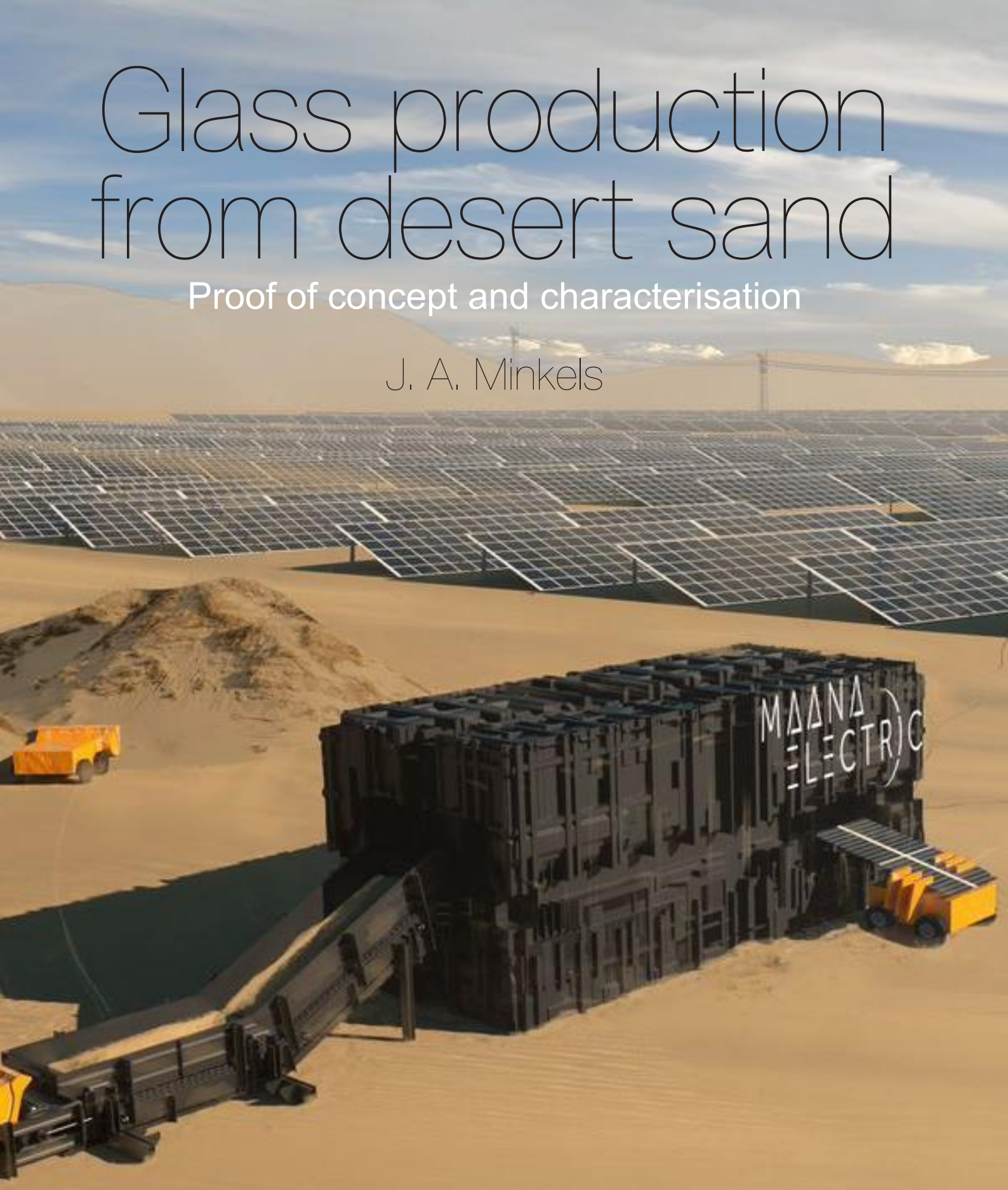

TU Delft

Glass production from desert sand

Proof of concept and characterisation

by

J. A. Minkels

to obtain the degree of Master of Science
at the Delft University of Technology,
to be defended publicly on October 30, 2020

Student number:	1365401	
Project duration:	May 1, 2019 – October 30, 2020	
Thesis committee:	Dr. ir. M.J.M. Hermans	TU Delft, committee chair
	Prof. dr. I.M. Richardson,	TU Delft, supervisor
	Dr. ir. F.A. Veer,	TU Delft, supervisor
	Dr. V. Popovich,	TU Delft
	D. Beijer Msc,	Former Maana Electric, supervisor
	J. Schleppi PhD,	Maana Electric

This thesis is confidential and cannot be made public until October 30, 2022.

TU Delft

Abstract

For *in-situ* resource utilisation start-up Maana Electric, an investigation was undertaken to determine whether a cover glass for solar panels can be produced using only desert sand as the raw material. During this investigation, the composition of desert sand, melt formation, processing temperatures, and mechanical and optical properties were considered.

The composition of 18 desert sands was analysed by means of X-ray fluorescence and estimations of mineralogical composition were made, after which an attempt was made to melt the unmodified sand samples in a microwave furnace built for the purpose. Melt formation was further observed by melting binary combinations of store bought minerals that were found in the desert sands. The composition data and modelling of temperature-viscosity curves were employed to explore lowering the practical melting of the sand point by modification of the composition through benificiation. 'Synthetic benificiated desert sand' was produced and melted based on the results. Glass samples produced were characterized using X-ray fluorescence, visual inspection, optical spectrometry, and fracture mirror analysis.

It was found that about half of the desert sand samples assessed contain over 90 wt% silica, making it less feasible for use as raw material for glass due to high melting temperatures and/or large waste streams from benificiation, while sands containing larger fractions of carbonates and/or feldspars will form a melt at less than 1650 °C if the SiO_2 content is less than 55 wt%.

Transmission of 85 % of ~550 nm wavelength light was shown to be possible for desert sand glass of 3 mm thickness if Fe_2O_3 content is lower than 0.1 wt%, while for the same transmission in the complete effective spectrum of silicon based solar cells the iron content needs to be lowered further. Known absorbing species such as Cr_2O_3, NiO and CuO were detected in desert sand in trace amounts, but were not present in the synthetic mixtures, the influence of these contaminants on transmission requires further research.

Mechanical analysis was inconclusive due to a limited number and low quality of the samples produced, but a review of the literature implies that a Young's modulus of >70 GPa and flexural strength of >45 MPa are attainable in a glass produced from desert sand components.

Preface

After a delay typical for my ‘academic career’, the (provisional) conclusion of it finally lies before you. It was an interesting time, including two supervisors changing jobs, building a high temperature microwave furnace, and seeing multiple colleagues joining and leaving MaanaNL. Part of it all from home due to corona.

When my interest in material science developed during my Bsc project about steel, I would never have expected to end up making glass. For this project I’ve ventured in to a variety of fields that were completely new to me, and developed a number of new skills leading to new and renewed interests.

I would like to thank my daily supervisors, David Beijer and Ian Richchardson. David specifically for providing the opportunity to join Maana. Both for keeping involved after moving on to different employment and the valuable feedback on this thesis. Fred Veer’s guidance in exploring the field of glass science and help in taking micrographs was invaluable as well.

This thesis would not have been possible without the desert sand samples provided by Nadine Sterk and Lonny van Ryswyck of Atelier NL, the XRF analysis executed by Ruud Hendrikx, and help in optical and mechanical testing by Martijn Tijssen and Ton Riemslag respectively. While I haven’t met them, Daniele Giordano, James Russell and Donald Dingwell provided their viscosity model to the public, which was of great use during this project.

Furthermore I would like to thank Jürgen Schleppi for great discussion on melting of oxides, and Marcel Hermans and Vera Popovich for joining the committee.

Mental support of my sister Meike, and my friends, enabled me to carry on through difficult times throughout my studies, and last, but certainly not least; I would not have made it to this point without the unwavering support of my parents. Joop en Mirjam, bedankt voor alles!

Watching a start-up with ambitious goals move toward them at speed, while being able to contribute in the process, was a great experience. Hence I would like to finally acknowledge all my (former) colleagues. I had a great time and look forward to continue working at Maana, and see where it, or we, will go!

J. A. Minkels
Delft, October 21, 2020

Contents

Glossary

List of symbols

Some symbols on this list are repeated, if this is the case, they do not occur in the same section.

Symbol	Unit	Description
δ	[m]	Deflection
ϵ	[-]	Strain
ε	[-]	Emissivity
ζ	[J m^{-2}]	Surface energy
η	[Pa s]	Viscosity
λ	[m]	Wavelength
σ	[Pa]	Stress
A	[m^2]	Area
a	[cm^{-1}]	Absorption coefficient
a^*	[m]	Critical crack length
E	Pa	Elastic modulus
F	[N]	Force
G	[J]	Gibbs free energy
H	[J]	(Activation) Enthalpy
I_A	[m^4]	Second moment of area
I	[W m^{-2}] or [%]	Intensity of light, absolute or % of incident
IFS	[Å^{-2}]	Ionic field strength
K	[MPa$\sqrt{\text{m}}$]	Stress intensity factor
L	[m]	Length
m	[-]	Weibull modulus
M	[MPa$\sqrt{\text{m}}$]	Mirror constant
M	[g]	Molar weight
n	[-]	Refractive index
n	[-]	Moles of component per mole of mixture of compounds
r	[m] or [Å]	Radius
R	[%]	Reflection, % of incident.
S	[J K^{-1}]	Entropy
T	[°C] or [K]	Temperature
t	[s] or [min]	Time
T	[%]	Transmission
V	[m^3]	Volume
v	[m s^{-1}]	Velocity
w	[-]	Weight fraction
x	[-]	Mole fraction
Z	[e]	Ionic charge
z	[cm]	Distance travelled by light in medium

List of acronyms

BO bridging oxygen
CN coordination number
DSC differential scanning calorimetry
DTA differential thermal analysis
ICP inductively coupled plasma
IFS ionic field strength
IR infra-red
ISRU *in-situ* resource utilisation
LOI loss on ignition
NBO non bridging oxygen
PV photo voltaic
SLS soda lime silica
UV ultraviolet
VFT Vogel-Fulcher-Tammann
XRD X-ray diffraction
XRF X-ray fluorescence

List of minerals

Mineral	Chemical formula	Description
Albite	$NaAl_3Si_3O_8$	Sodium rich end member of the feldspar series.
Alkali feldspar	$(K,Na)AlSi_3O_8$	Solid solution series between Albite and K-feldspar.
Anhydrite	$CaSO_4$	Dehydrated gypsum.
Ankerite	$Ca(Mg,Fe,Mn)(CO_3)_2$	Dual carbonate of Ca and Mg, Fe, and/or Mn.
Anorthite	$CaAl_2SI_2O_8$	Calcium rich end member of the feldspar series.
Aragonite	$CaCO_3$	Unstable under atmospheric conditions.
Calcite	$CaCO_3$	Limestone, also referred to as lime.
Dolomite	$CaMg(CO_3)_2$	Dual carbonate of Ca and Mg.
Feldspar	$(M)Al_xSi_xO_8$	Where M is Na, K or Ca.
Gypsum	$CaSO_4{\cdot}2H_2O$	Calcium sulphate dihydrate
Plagioclase	$(Ca,Na)Al_xSi_xO_8$	Solid solution series between Anorthite and Albite.
Quartz	SiO_2	Stable form of silica at atmospheric conditions.

1 Introduction

Maana Electric is a start-up company with its main focus on *in-situ* resource utilisation (ISRU). The goal of the company is to produce solar panels using only electricity and resources locally available from sand or regolith. Ultimately the resulting mini-factory could be utilized in space colonisation.

For practical reasons the first versions will be run on earth. In the process of developing this system, valuable information for development of the system for space is gained. The system(s) deployed on earth will also contribute to the fight against climate change by increasing solar power supply capacity, for a fraction of the cost of conventional solar panels.

On Earth, the entire solar panel will be produced from constituents of sand. As a high fraction of sand consists of SiO_2, a form of silica glass could be manufactured to protect the photo voltaic (PV) cells from the environment, and provide structural support.

The challenge will be to develop a process that yields glass panes suitable for covering solar panels, using only available constituents, while optimizing optical, mechanical and processing properties.

Most industrial flat glass production today is done using the float process [1, 2], with established recipes and supply of pure raw materials. Research regarding glass panes conducted today focuses mainly on soda-lime glass and the aforementioned process. With expected growth in the PV-industry, interest has developed in producing rolled glass optimized for solar applications [2], but it seems unlikely that such glass can be replicated using desert sand. As such, widely researched and applied combinations of process and composition are not applicable in the envisioned situation, and a new system has to be developed.

Before system design for the needed glass production subsystem can fully commence, it has to be proven that it is possible to use only (beneficiated[1]) sand, and elements extracted from the sand, to produce glass suitable for covering solar panels. Furthermore critical processing temperatures should be known, and minimized by altering the composition where possible.

Glass production has been an empirical process for millennia, and still is to a certain extent. Formulation of new recipes still involves a fair share of trial and error, as will be reflected in this research. Variations in composition and processing path can have severe influence on the final product. While relations between composition, processing and properties are better known today, making accurate predictions of results will be difficult without experimentation.

The focus will be on melting glass from desert sand, while considering possible effects on optical properties and mechanical properties. When the melting succeeds, the relevant properties will be analysed. The composition will also influence properties that might be of importance in this application, for example, thermal shock resistance, chemical properties and electrical properties. As these are not included in the current design criteria, they will be left for further investigation.

[1] Beneficiation: *'crushing and separating ore into valuable substances or waste by any of a variety of techniques'*

The objective of this research is to answer the following questions:

1. Is it possible to manufacture a cover glass from benificiated desert sand, complying to the specifications provided by Maana Electric?
   - > 85% transmission of the 350 nm to 1100 nm range of light.
   - Youngs modulus > 70 GPa.
   - Flexural strength > 45 MPa.
2. What are the critical process temperatures for such a glass?

To address these objectives, first a literature review was conducted. Chapter 2 covers some of the principles of glass formation and the structure of silicate glasses first, followed by an investigation of the chemical and mineralogical composition of desert sand. After that the steps of melting a glass batch are discussed, together with the the steps required to melt a batch of desert sand. The last three sections cover the properties of interest, being viscosity, mechanical and optical properties, in relation to the feedstock.

Chapter 3 contains a description of the sand and mineral samples acquired, followed by a description of methods applied and experimental equipment used to answer the questions left at the end of the literature review.

The results and discussion, presented in chapters 4 and 5, follow the same main structure. First a selection of desert sand samples is analysed in terms of chemical and mineralogical composition, followed by a similar analysis of store bought components that were found to be present in desert sand according to the literature reviewed. The desert sand samples are then melted and inspected. The steps that take place in melt formation and the effect on melting temperatures of various hypothetical benificiation operations are explored next. The experimental chapters are concluded with the melting and analysis of synthetic batches created from store bought components.

As is customary, the conclusions drawn are summarized in chapter 6, followed by recommendations for further research.

Supporting material regarding the microwave furnace built for purpose and emissivity measurements conducted for calibration can be found in appendices A and B respectively. Furthermore all results gathered during the analysis and melting of unmodified desert sand are collected in appendix C. Finally, an overview of less successful casting attempts is presented in appendix D.

2

Literature review

The purpose of this literature review is to familiarize the reader with relevant topics and concepts applied in the following chapters. The first section contains a general introduction to glass, including the definition of glass and how it is formed, as a basic understanding will be needed to proceed.

After discussion of relevant fundamentals in the first section, the focus will shift to silicate glasses specifically in section 2.2. As most properties are based in the structure of the glass, a general understanding of the interaction between components will provide better understanding of the behaviour discussed in later sections.

Section 2.3 covers desert sand and how it could be used as feedstock for glass production. After the definition of sand, the chemical composition and mineralogy of desert sand is reviewed, as are the melting temperatures of the minerals found in significant amounts.

To convert sand to glass, the input material has to be melted. This process can be problematic when the feedstock is limited. For reference, the process for possible desert sand batches is compared to the well known soda lime silica (SLS) process in section 2.4. The behaviour of the resulting melt is controlled by the viscosity, which is in turn controlled by the composition and temperature. These relationships are discussed in section 2.5.

The mechanical properties specified in the requirements, and their relationship to composition and processing, are discussed in section 2.6. The same is done for optical properties in section 2.7.

When applicable, sections are concluded with a short summary of the main points of importance for reaching the objectives outlined in the previous chapter.

2.1. Introduction to glass

A general understanding of how and why glass forms is of importance for understanding of the influence of composition and processing on properties discussed in later sections.

After defining glass, a short overview of relevant theories of glass formation is given. The fundamentals of glass formation are discussed in terms of thermodynamics and kinetics, followed by a discussion of the glass transition.

2.1.1. Definition of glass

In his paper from 1932, Zachariasen [3] contemplated the structure of glasses and described the difference between a crystal and a glass as follows:

> 'The presence or absence of periodicity and symmetry in the network distinguishes a crystal from a glass.'

He captured the first essential property of a glass, being an non-crystalline solid. As there are amorphous solids in existence that are not considered glasses, another criterion is needed.

The second criterion to be classified as a glass, is that a material displays glass transformation behaviour [4–8]. This behaviour can be described as a material being able to be cooled below the supercooling range without forming crystalline phases, and continuously transform into a liquid upon reheating [6]. The phenomenon is discussed in section 2.1.5.

While the most common way to form a glass is via cooling and glass transition from a melt, it is not the only option. Various trajectories of pressure and temperature, from a material in the solid, liquid or gas phase, can be taken to reach the glassy state. To include glass formed via one of these paths in the definition, it can be said that [8]:

> 'Glasses are dense, isotropic and homogeneous non-crystalline solids characterized by the absence of any internal phase boundaries.'

A glass is not defined by its composition. Most materials can form a glass if cooled sufficiently quick so that crystallisation is prevented. Why some materials form glasses and others do not will be discussed in the following sections.

Usually a substance is considered a glass when the volume fraction of crystalline phases V_x/V is under 10^{-6}, the detection limit for X-ray diffraction (XRD) [4], as well as the resolution limit of the optical microscope [7]. With current design criteria this isn't a hard limit. As long as the crystallized fraction does not hinder transmission, the criteria can be met.

2.1.2. Theories of glass formability

In most introductory material about the structure of glass that was reviewed, theories regarding whether a composition is prone to form a glass are presented in historical order. In this section, some useful concepts are presented, summarizing the interpretations of [4–6]. A number of the concepts introduced are used in further explanation of glass behaviour, others are included for context.

Further historical review of the science of (silicate) melts is interesting, but beyond the scope of this review. The first chapter by Mysen and Richet [7] is recommended for a extended overview of the development of knowledge on silicate melts an glasses.

Note that none of the theories presented here are suitable to completely describe all glass behaviour, but are useful tools in understanding aspects of it [5].

Goldschmidt (1926) observed that in known oxide glasses the cation to anion-ratio fell in the range from 0.2 to 0.4. This corresponds to tetrahedral coordination according to Pauling's rules, from which Goldschmidt believed that only tetrahedrally coordinated oxides could form glasses. While silica glass consists of silicon surrounded by an oxygen tetrahedron, it was not explained why this is favourable [9].

Zachariasen (1932) built on this notion, and presented 'simple rules' for the ability of a metal oxide to form a glass:

1. An oxygen atom is linked to not more than two atoms A;
2. The number of oxygen atoms surrounding atoms A must be small;
3. The oxygen polyhedra share corners with each other, not edges or faces;
4. At least three corners in each oxygen polyhedron must be shared.

He theorized that these conditions were necessary to form a continuous network without long range order, while keeping the internal energy of the system close to that of the crystalline form. This was illustrated with figure 2.1.1 [3].

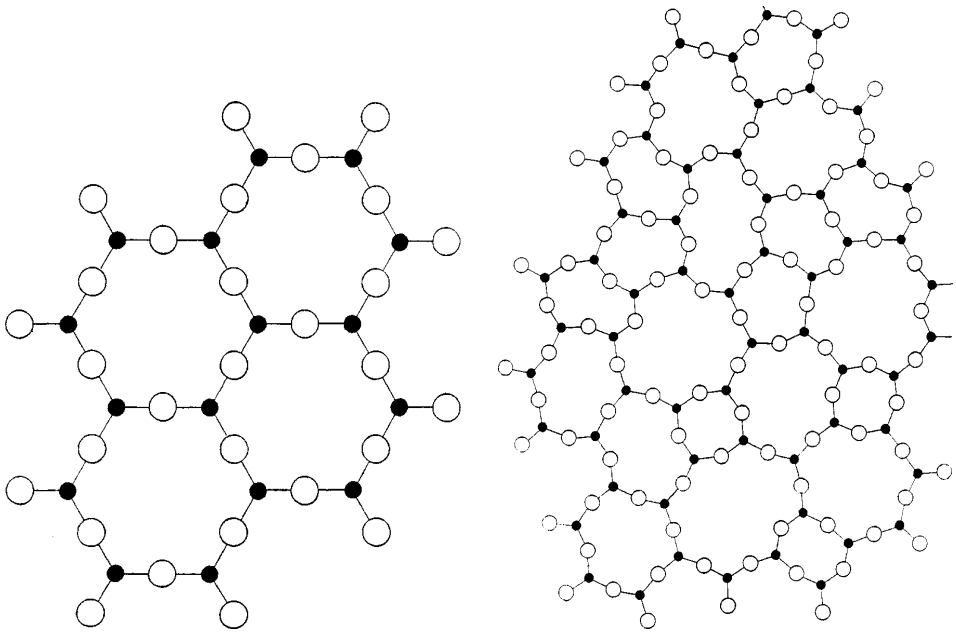

(a) Crystalline SiO_2. **(b)** Vitreous SiO_2.

Figure 2.1.1: Two-dimensional representation of different structures of silica by Zachariasen [3].

Dietzel (1942) related glass formability to the field intensity of the cation, by dividing the cation charge by the square of the distance from the oxygen anion. A higher field intensity implies a better glass former, low intensity anions behave as modifiers of an existing glassy network [10].

Sun (1947) classified glass forming ability by the bond energy of a single bond, defined by the dissociation energy of the ion divided by the coordination number (CN) of the cation, suggesting that stronger bonds prevent crystallisation from the melt [11].

Stanworth (1948) tried to quantify oxides by electronegativity of the cation, and as such the mixed bond concept. Good glass formers have about half-ionic bonds and are classed in group I. Slightly less electronegative ions are in group II. They do not form glasses on their own, but can replace ions from group I. Group III consist of the modifier anions, meaning the bond they form is highly ionic and as such does not form a glass, but modify the structure by filling spaces in the network [12].

Smekal (1949) proposed the mixed bond theory, stating that to form a mostly random network a combination of bond types is preferable. By combining for example covalent, highly directional bonds and ionic, completely non directional bonds as in silica, the resulting melt has "some" directionality. This favours polymerisation and formation of molecules in the melt, promoting glass formation [13].

Rawson (1956) added the influence of the melting temperature to the theory of Sun, stating that the ratio of single bond energy to melting temperature indicates glass forming ability, so oxides with high bond energy and low melting temperatures are good glass formers [14].

2.1.3. Thermodynamics of glass formation

Formation of a crystalline phase is driven by the lower Gibbs free energy compared to the liquid. Hence, the possibility of under cooling a melt, and therefore formation of a glass, is higher for materials with a low difference in free energy between the two phases.

This can be understood by the definition of the Gibbs free energy, and taking the difference between the liquid and the crystalline phase,

$$\Delta G = \Delta H - T\Delta S, \tag{2.1.1}$$

where G is the Gibbs free energy and H is the enthalpy, both in [J]. T is the temperature in [K] and S is the entropy in [J K^{-1}] [4]. At the melting temperature, the free energy of the liquid and the crystal are the same, so $\Delta G = 0$. Rewriting equation 2.1.1 for the melting temperature yields

$$\Delta S_m = \frac{\Delta H_m}{T_m}. \tag{2.1.2}$$

Intuitively it 'makes sense' that a bigger difference in the structural ordering, represented in part by the difference in entropy between the melt and crystal makes it more difficult to make the transition. From equation 2.1.2 it can be seen that this is the case for a higher enthalpy of melting ΔH_m or a lower melting temperature. As the heat of melting is proportional to the bond energy, this is what Rawson [14] implied.

This thermodynamic criterion influences the tendency to nucleate, the rate at which this happens is discussed in the next section.

2.1.4. Kinetics of glass formation

As established in section 2.1.1, to acquire a glassy state, crystallisation has to be prevented. Crystallisation occurs when enough nuclei are available, that can grow sufficiently quickly [6]. The difference in free energy discussed in the previous section is the driving force for nucleation. In this section, the rate of nucleation, as well as the speed of growth of nuclei after formation, is discussed.

In the literature, qualitative discussion of nucleation theory is available, for example in [5, 6], as well as virtually any material science introductory text. Due to difficulty in estimation of constants and measuring of nucleation, relevant predictions of results are rarely achieved. Therefore the discussion here is mostly qualitative, to provide conceptual understanding of the process.

The rate of nucleation is determined by a trade-off between the drop in free energy by forming a crystalline phase, against the energy cost of forming a new solid-liquid interface. In a small nucleus the surface energy is large compared to the energy gain from crystallisation, and the chance of redissolving is significant. Past a certain size, usually know as the critical radius, the nucleus is free to grow as any gain in radius will lead to a decrease of free energy. This is illustrated in figure 2.1.2, where r^* is the critical radius.

The energy barrier is lowered significantly if a pre-existing surface is available in the liquid. This is known as heterogeneous nucleation, as opposed to homogeneous nucleation in the bulk of the melt, and takes place at contact with crucible walls or inclusions and impurities within the melt. It can be influenced or reduced by better dissolution of batch components, homogenisation of the melt and composition control [5, 15].

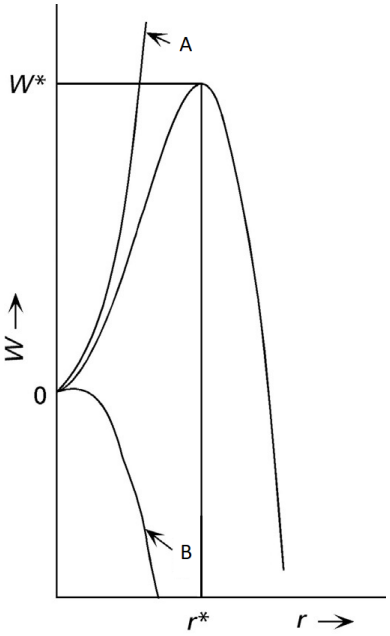

Figure 2.1.2: Total change in energy for nucleation (W) for radius (r), A: gain in surface energy by creation of new surface, B: reduction in free energy from crystallized volume. Adapted from [6].

When a nucleus is formed, under the right conditions it can grow. Similar to nucleation, an energy barrier has to be overcome. In this case the crossing of the solid-liquid interface by the atoms or molecules and the diffusion of building blocks to the interface (see figure 2.1.3). The diffusion coefficient D is related to the viscosity η by the Stokes-Einstein relation,

$$D = \frac{RT}{3N\pi d\eta}, \tag{2.1.3}$$

where R is the gas constant, T is the absolute temperature, N is Avogadro's number and d is the average jump distance assumed to be a molecular diameter [6]. As this relationship is presented for conceptual purposes, units are omitted. Equation 2.1.3 implies that a higher viscosity around the melting temperature yields a better glass former, by increasing the energy barrier for crystal growth.

In reality nucleation and growth are not separated processes, but happen simultaneously. Both are regulated by an activation energy and as such are highly temperature dependent. In turn the temperature dependence is influenced by the composition. Crystallisation will occur in melts where both nucleation and growth rates are high at the same time. This is illustrated in figure 2.1.4: the smaller the overlap between peaks, the better the ability to form a glass.

Crystallisation, should be prevented to form a glass. This can be achieved by cooling through the region of overlap in figure 2.1.4 at an appropriate rate and/or making the range of overlap smaller by modifying the composition. In a multi component mixture this is not as straight forward as it seems, as various different phases could nucleate.

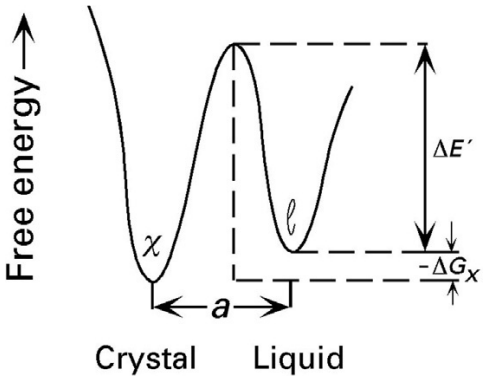

Figure 2.1.3: Activation energy and change in Gibbs free energy for atoms or molecules crossing the solid-liquid interface [6].

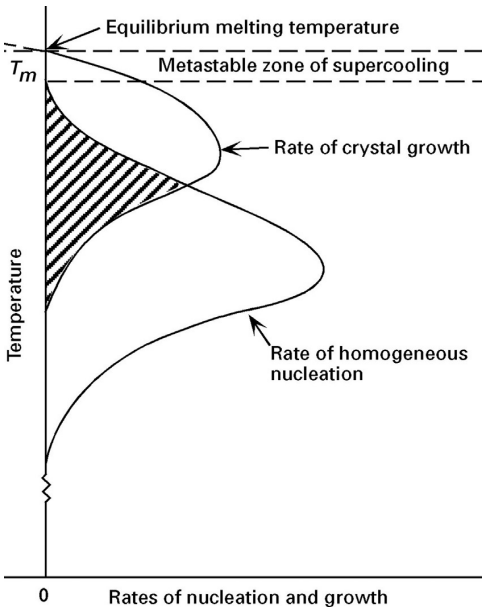

Figure 2.1.4: Nucleation and growth rate versus temperature [6].

2.1.5. The glass transition

When the comparably predictable process of nucleation and growth does not take place in a glass forming melt, properties of the supercooled liquid can at first be extrapolated from the temperature dependence of the liquid. Upon further cooling, the glass transition occurs [6].

The glass transition can be described as the gradual transition between first order thermodynamic properties, for example enthalpy as displayed in figure 2.1.5, of the supercooled liquid and the glass. This transition is not a sharp discontinuity, but takes place in a temperature interval, where properties are depending on time as well as thermal history. This process takes place from the start of deviation of properties from the supercooled liquid state, and ends at the temperature where viscosity is so high no observable rearrangement of structure takes place over practical time scales; a glass has formed [6, 7, 16].

While in a (supercooled) liquid state, a change in temperature or pressure will lead to almost instantaneous adaptation of the equilibrium structure for the new situation. In the fully solid state, no restructuring will take place at observable timescales. During the transition between the two, the change in structure and thus properties takes place during timescales in the order of hours. This will lead to relaxation behaviour, where properties change under constant circumstances, illustrated by means of figure 2.1.6: for a change of temperature within the glass transition range, the equilibrium viscosity is reached after multiple hours [5, 6].

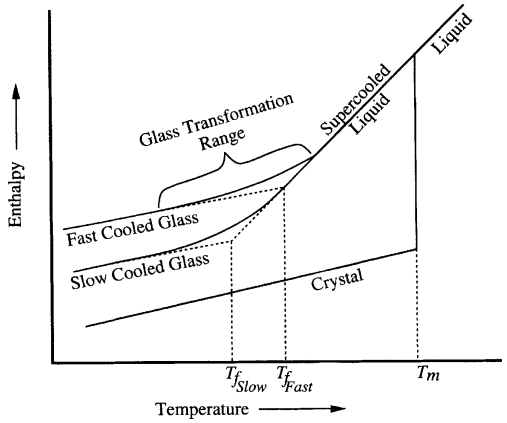

Figure 2.1.5: Illustration of glass transformation behaviour and the fictive temperature concept by enthalpy vs. temperature [5]

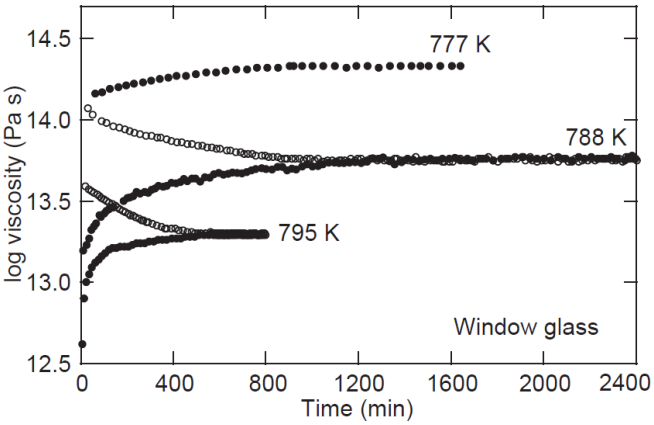

Figure 2.1.6: Relaxation behaviour of a window glass for different initial and target temperatures within the glass transition range [7].

As the focus of this work is on behaviour at room temperature and in the melt, in depth discussion of relaxation effects during the transition is of limited interest. The interested reader is referred to Mysen and Richet [7, ch.2] and Varshneya and Mauro [6, ch.13] for a more comprehensive description and further references.

The kinetic nature of the glass transition means that the transition cannot be classified or described easily as a phase transition. Describing glass behaviour in thermodynamic terms has been, and still is, a very actively researched subject. An elaborate review of these efforts, as well as an overview of the fundamentals of the thermodynamics of phase transitions, is given by Schmelzer et al. [16]. In depth discussion of this subject is beyond the scope of this work, and therefore omitted.

In practice the properties of a silicate glass can be described well by the empirical concept of the fictive temperature, T_f, introduced by Tool [17], as the heat capacity and thermal expansion of these glasses are are relatively independent of thermal history [7]. The fictive temperature is defined as the temperature were the glass would be in the equilibrium structure of the under cooled liquid [5].

Effectively this means that the fictive temperature of a quickly cooled glass will be higher, since the melt had less time to reorganise before being ‘frozen in’. This can be illustrated by reheating a glass in a dilatometer. Figure 2.1.7 shows a quenched glass will relax to a state of lower temperature (more compact) than when it was frozen in. Upon further heating the glass will revert to the supercooled liquid state and recrystallize, as an annealed glass would. The dip in the end of the graph in this figure is the deformation under the weight of the sample.

Relaxation during reheating is an endothermic process, making it detectable by differential scanning calorimetry (DSC) (figure 2.1.8) or differential thermal analysis (DTA). Figure 2.1.8 also clearly displays the exothermic recrystallisation, also known as devitrification when it happens on reheating of a previously vitreous substance. A more complex composition may exhibit a less clear drop for the glass transition and multiple crystallisation peaks as multiple stable phases might exist at different temperatures.

While in practice the effects can be less defined, both techniques mentioned can be used to determine the glass transition temperature of a glass. This temperature is close to the annealing temperature discussed in section 2.5, which is an important point in glass processing.

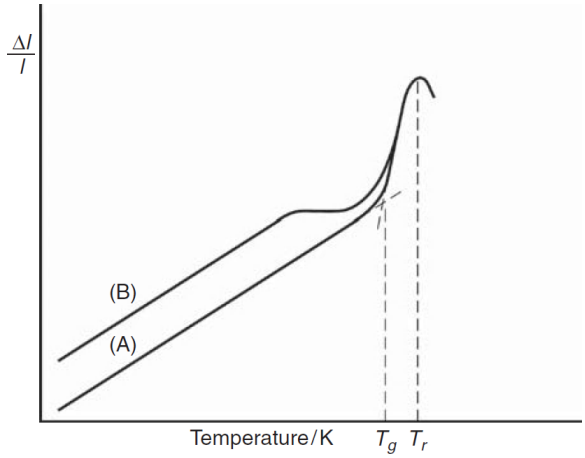

Figure 2.1.7: Thermal expansion upon reheating for (A) a well annealed glass, (B) quickly cooled glass [4].

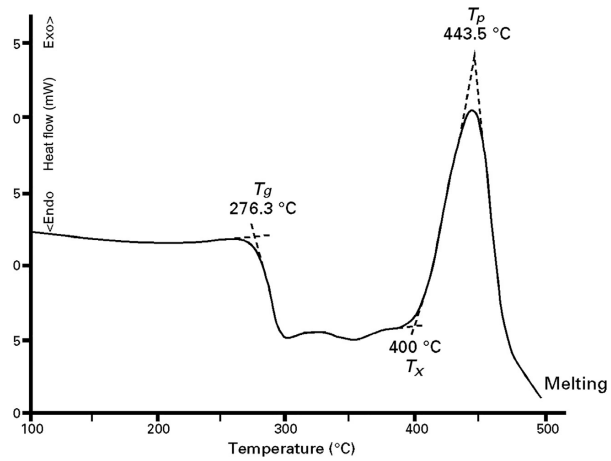

Figure 2.1.8: DSC analysis of an unknown homogeneous glass [6].

2.1.6. Summary

To create a glass from desert sand, the following conditions need to be considered:

- Sufficient network forming elements in the composition.
- High enthalpy of melting and/or low melting temperature of the mixture.
- High viscosity at the melting temperature.
- Cooling through the crystallisation range at sufficient rate.

In addition, the thermodynamic and physical effects caused by the glass transition upon reheating, can possibly be used to determine the glass transition temperature by DTA or DSC.

2.2. Silicate glasses

With the basics discussed, the focus can close in on the subject at hand; silicate glasses. This section starts with a discussion of the structure of vitreous silica, as this will be the main building block of the desert sand glass to be created. Some principles regarding the effect of addition of other oxides are introduced in section 2.2.2, relevant in further discussion of properties in later sections.

A more in depth discussion of silicate glasses in general, as well as the concepts discussed here, is provided by Mysen and Richet [7, ch4], the Springer Handbook of Glass [8, ch13], and Varshneya and Mauro [6, ch3.1.1, 5.2].

2.2.1. Structure of vitreous silica

The basic building block of a silicate glass is the same as that of crystalline silica (quartz): a silicon ion (Si^{4+}) surrounded by 4 oxygen ions (O^{2-}) in tetrahedral coordination. While the bonds are not fully ionic, and thus this reasoning must not be taken literally, one might notice that in the case of a single unit local charge neutrality is not maintained. In pure silica glass, each O^{2-}-ion is part of two tetrahedra acting like a bridging oxygen (BO), to counter this. The connected units form a continuous network of rings and cages by stringing units, as displayed in figure 2.2.1, together with varying bond angles [7, 8, 18].

This follows Zachariasen's rules [3], and interestingly his idea of amorphous silica closely resembles 2-dimensional amorphous silica displayed in figure 2.2.2. This image was produced by Huang et al. [19] in 2012, by growing 2-d amorphous silica on a graphene substrate and imaging the result using scanning transmission electron microscopy. Despite an increasingly clear picture of the structure of silica glass with progressing insight, no full consensus on the (dis)order on medium and long range, and description thereof, has been reached [8]. For all intents and purposes of this project, this fundamental discussion has no direct influence, as the current understanding is sufficient for most practical application.

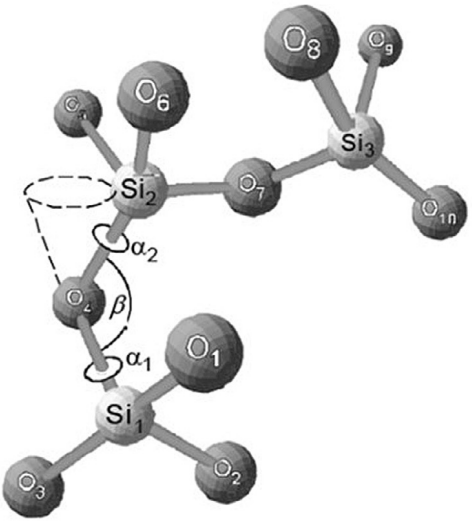

Figure 2.2.1: Three SiO_4-tetrahedra as found in vitreous silica. Adapted from [6].

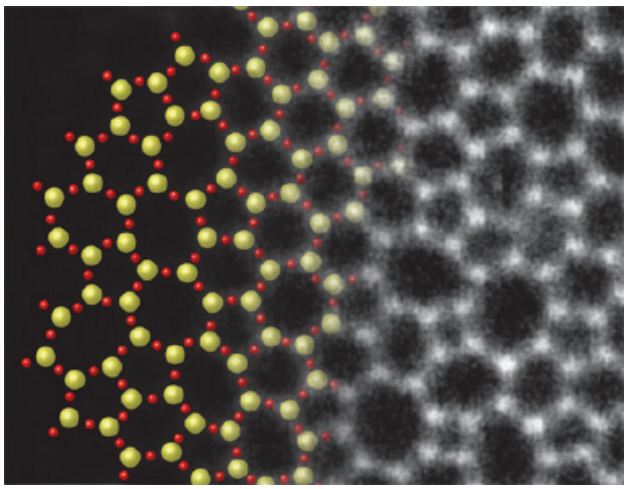

Figure 2.2.2: Cartoon (left) and scanning transmission electron microscopy image of 2-dimensional amorphous silica formed on a graphene substrate [19].

2.2.2. Additional oxides in silicate glass

Silica is contained in the group of network formers, as it forms a network. Additions of other elements can enter the melt as modifier, charge compensator, additional network former, or intermediate. Additional network formers are included in the network formed by silica tetrahedra, but can be any polyhedron adhering to Zachariasen's rules itself. Modifiers break up the existing network, creating an non bridging oxygen (NBO) in the network. When conditional network formers are present, modifiers can act as charge compensation to maintain local charge neutrality. Intermediates are the group of oxides that behave as a network former or modifier depending on the availability of charge compensation.

This distinction can be better understood using the concept of the ionic field strength (IFS). Similar to Dietzel's concept [10] mentioned in section 2.1.2. The IFS is defined as

$$IFS = \frac{Z}{r^2}, \tag{2.2.1}$$

where Z is the ionic charge of the element in [e], and r the ionic radius of the cation in [Å]. Cations with an IFS of under 8 $Å^{-2}$ are typically found in silicate glasses as either network modifier or charge compensator. For comparison; the IFS of Si^{4+} is 59.1 $Å^{-2}$ [8].

Oxides other than silica that are considered network formers are GeO_2, TiO_2 P_2O_5 and V_2O_5 and will fulfil Zachariasen's rules by forming a rigid polyhedron of oxygen around the cation. They will typically become part of the network when added to a silica-based glass. B_2O_3 and Al_2O_3 have some interesting properties in silicate glass that will be discussed shortly. In pure form alumina will not form a glass, but will with the correct additions of stabilisers [6].

Modifier anions are accompanied by an appropriate number of oxygen cations, which replace BOs by NBOs, decreasing the degree of connectivity. In figure 2.2.3 this is illustrated for Ca^{2+} and Na^{+} ions. The most well know modifiers are the alkali and alkaline earth oxides: Li_2O, Na_2O, and K_2O (alkali) and MgO, CaO, SrO, and BaO (alkaline earth). The latter are bivalent and therefore will create 2 NBOs. While the bonds are weaker than the original network, the M^{2+} ion will maintain some connectivity, as seen in figure 2.2.3 [6, 8].

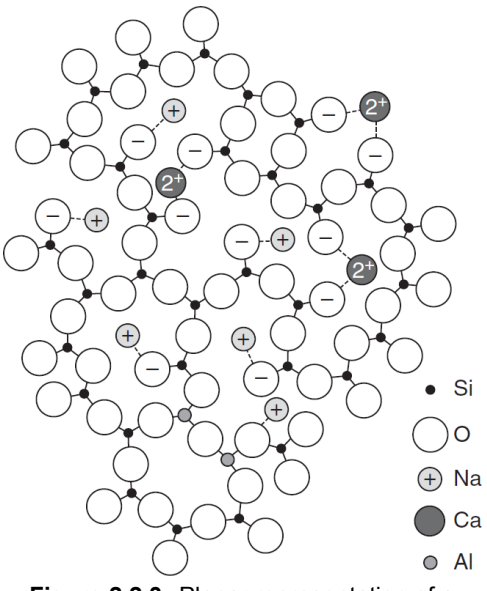

Figure 2.2.3: Planar representation of a silicate glass with typical additions [4].

The molar fraction of modifiers M^{i+} largely determines the amount of NBOs (when no other elements are present), hence the degree of polymerisation of the network. The average amount of NBOs per (silicon) tetrahedron T can be calculated [8]:

$$\frac{NBO}{T} = \frac{2O - 4T}{T} = \sum_{j=1}^{j} \frac{iM_j^{i+}}{T}. \qquad (2.2.2)$$

The distribution of these over the available Si is thoroughly researched and modelled and depends, among other factors, on CN and IFS of the anions as well as temperature. A unit with a number of BOs is denoted Q^n. On increasing the amounts of modifiers the distribution will shift, until non of the tetrahedra is connected and glass formation will be unlikely. Figure 2.2.4 displays the progression of Q^n units using two different bonding models, in both cases 100 % of tetrahedra occurs as Q^0 when ~65 mol % of modifiers is exceeded, preventing glass formation at acceptable cooling rates completely. The resulting range of glass formation for different combinations of alkali and alkaline earth oxides in silica is shown in figure 2.2.5. As such the typical modifiers can be added to SiO_2 upto about 50 mol % [5, 6, 8].

This is not a hard cut-off, as the loss of network connectivity with increased modifier content is gradual, glass forming ability will decrease gradually depending on composition. CaO, while acting as a stabilizer in fractions of ~10 wt%, is known to increase tendency to crystallize if added in larger amounts, due to lowering of viscosity of the mixture, while the overall melting temperature is increased [15].

Some elements act either as a network former or modifier, depending on circumstances, including other elements present and the oxidation state of the melt. Iron, for example, acts as a modifier when present as FeO, while Fe_2O_3 resembles a network former. Boron and aluminium are trivalent, but may enter the silica structure in tetrahedral coordination. In that case all oxygen will be BO, the remaining charge being compensated by a modifier ion. This converts a NBO to a BO, increasing network connectivity.

If no charge compensation is available, Al increasingly converts to a modifier in either 4, 5 or 6 fold coordination. figure 2.2.6 illustrates how a 6-fold coordinated modifying Al_3^+ ion would break up the silica network, where figure 2.2.7 shows the increase of 5-fold coordinated Al for decreasing relative aluminium content. The dependence of behaviour of the aluminium ion on the ratio of Al to modifiers, causes a shift in properties around the point were they are equal. As this ratio plays a large role in both natural and technical melts, the terms *peralkaline*, *metaaluminous* and *peraluminous* are used for aluminosilicate systems were the $M^{n+}O_{n/2}/Al_2O_3$ ratio is < 1, 1 and > 1 respectively, as visualized in figure 2.2.8 [6–8].

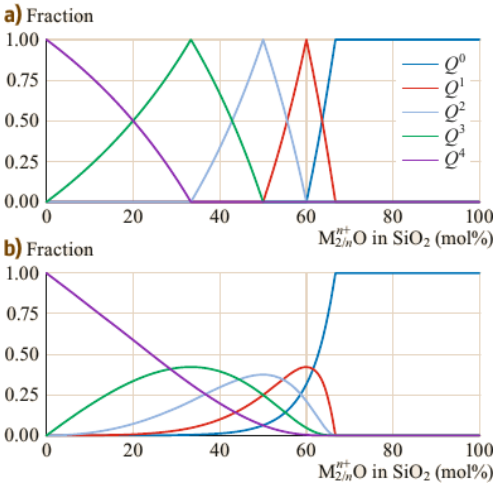

Figure 2.2.4: (a) Binary, and (b) random bonding models to estimate the distribution of BO's over available network formers [8].

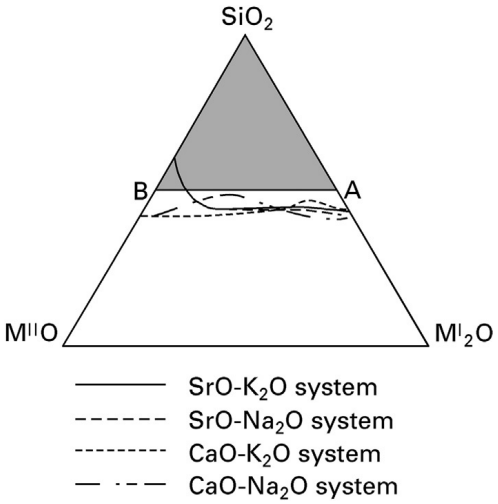

Figure 2.2.5: Glass forming region in alkali (M^I_2)-alkaline earth (M^{II})- silicate systems, in mol % [6].

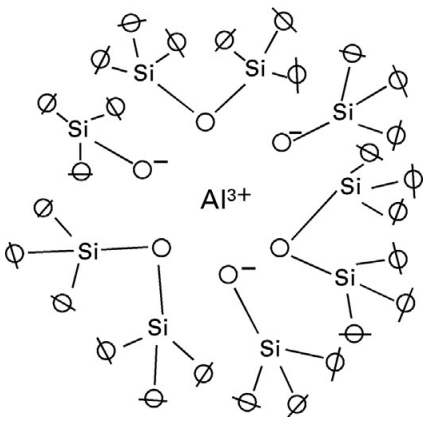

Figure 2.2.6: Schematic view of Al^{3+} as a modifier ion in octahedral coordination [6].

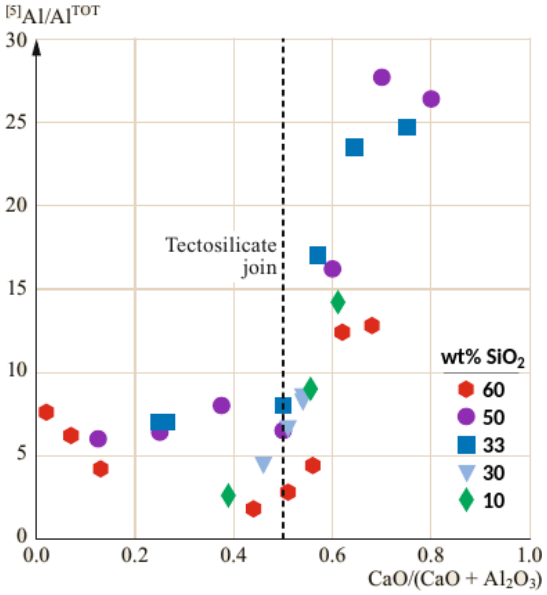

Figure 2.2.7: Fraction of 5-fold coordinated aluminium ions in CaO-Al_2O_3-SiO_2 glasses for different fractions of SiO_2 [8].

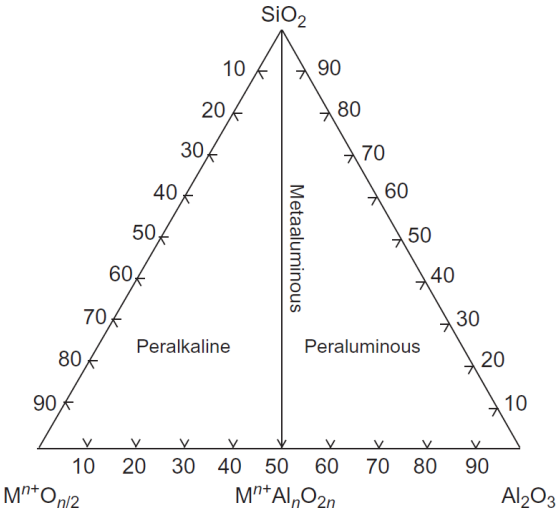

Figure 2.2.8: Different regions in aluminosilicate systems, in mol % [7].

2.2.3. Structure property relationships

The influence of composition on the structure of a glass is non-trivial, as is the resulting effect on properties. While in some cases additive models are accurate on small ranges, interactions between different elements can cause very non-linear variations [5, 6, 8].

Relating glass properties to composition is a complicated subject. The non-equilibrium state of often complex mixtures makes the processing path a factor in the eventual properties. It would be virtually impossible to try an cover this immense volume of information here. Instead Schmelzer et al. [16, ch7] may be referred to for an overview of efforts. The Springer Handbook of Glass [8] and Varshneya and Mauro [6] are examples of reference works covering the current state of affairs.

For this work, practical methods of predicting properties of interest are discussed in the relevant section. Processing temperatures depend mostly on the breaking down of raw material, discussed in section 2.4, and viscosity, discussed in section 2.5. Mechanical and optical properties are discussed in sections 2.6 and 2.7 respectively.

2.2.4. Summary

(Semi)metal ions other than silica are found in silicate glass as either network former, modifier, or intermediate. A silicate melt can contain up to ~40 mol % modifiers, and still be able to form a glass. Conditional network formers such as Al_2O_3 can possibly increase this threshold, as they consume modifiers for charge compensation and thus increases connectivity.

2.3. Desert sand as raw material

To use desert sand as a raw material, knowing what it consist of is of importance. The (overall) chemical composition will determine the composition of the resulting glass, while the mineralogy will determine how the process of melting occurs.

First a definition of sand is discussed, after wich an overview of some examples of chemical composition of desert sand found in the literature is presented. The structures in which the various oxides occur are discussed next, as this influences the behaviour of the batch in the melting process, as well as opportunities for benificiation.

2.3.1. Introduction to sand

While at first glance sand might seem a simple product, there are a lot of complexities to be accounted for. The International Sand Collectors Society [20] defines sand as follows:

> 'To a sedimentologist sand is an unconsolidated (loose), rounded to angular rock fragment or mineral grain having a diameter in the range of 1/16 mm to 2 mm. An engineer on the other hand may restrict the meaning of sand to include only rounded fragments having a diameter of 0.074 mm (retained on U.S. standard sieve no.200) to 4.76 mm (passing U.S. standard sieve no.4). Practically, sand may be considered to consist of small detrital fragments (rock or mineral particles liberated by mechanical disintegration of parent rock material), biogenic particles (shells or shell fragments) or chemical precipitates (evaporates or oolites) occurring in nature and distinguishable by the naked eye.'

From this description it is clear that there is not one form, let alone composition, to work with. Sand found in deserts has gone trough various geological processes underway from source to desert, and structure and composition are affected by chemical and mechanical weathering. During the process of transportation, material from different sources, either geological or biological, can end up mixed and weathered. Each mineral is affected differently by each processes, yielding a variety of results in different locations [21].

2.3.2. Chemical composition of sand

Reports of sand composition were sourced from different fields of research. An overview of collected compositions is presented in table 2.3.1. Depending on the interest and method of the research (other) trace elements were reported, but omitted in the table for clarity. It has to be noted that most measurements reported here were performed using X-ray fluorescence (XRF), and thus some lighter elements might have gone undetected due to the nature of the method. Furthermore XRF does not differentiate between oxidation states, hence the presented compositions are a measure of the amount of each (semi)metallic element more than a literal representation of the oxides listed.

Table 2.3.1: Selection of sand compositions in wt% from various deserts, some trace elements not listed. a) Western desert of Iraq, averaged over 20 dunes, b) 'a Middle East country', c) Hobq desert, inner Mongolia, China, d) Great Indian Thar desert, e) Taklimaken desert, Tibet, f,g) Kuwait; Ashegaya, Qurtabo respectively, h,i) Ordos deserts, northern China, maximum and minimum SiO_2 content from large dataset.

	SiO_2	Fe_2O_3	Al_2O_3	MnO	TiO_2	Na_2O	K_2O	MgO	CaO	Reference
a)	73.30	1.60	11.00	-	-	2.10	3.10	1.10	3.60	[22]
b)	59.80	0.60	8.20	-	<0.50	<0.50	1.50	2.60	25.20	[23]
c)	78.75	2.49	5.32	0.51	0.45	3.21	3.67	1.37	3.91	[24]
d)	80.37	2.10	5.53	0.03	0.14	1.20	1.61	0.97	4.60	[25]
e)	69.70	3.29	12.10	0.07	0.54	2.64	2.62	2.13	6.77	[26]
f)	83.42	0.64	5.12	-	-	-	-	2.40	4.06	
g)	67.36	0.72	9.86	-	-	-	-	2.22	11.42	[27]
h)	73.02	3.36	12.80	0.06	0.73	3.43	2.57	0.66	1.68	
i)	83.48	1.99	7.81	0.03	0.29	1.71	1.65	0.73	1.00	[28]

While most of the references presented were published in a field out of the scope of this research, Bansal and Choi [23] investigated undesired glass formation in jet-engines when used in the desert. Interestingly this seems one of the few occurrences of creation of glass from only desert sand in the context of research. The location is not specified beyond 'a Middle East country'.

From table 2.3.1, it appears that this selection of examples could theoretically form a glass, as sufficient SiO_2 is available. Modifiers are less widely present, with the exception of CaO, which is abundant in some cases. Furthermore the conditional network former Al_2O_3 is present in all sands displayed. It can also be observed that the composition varies significantly, even in the same region or desert.

2.3.3. Mineralogy of sand & melting temperatures

Creating a homogeneous melt from the original material requires breaking up the source minerals. To do this, familiarity with minerals found in desert sand is required. Furthermore the benificiation process could be influenced by the oxides listed in table 2.3.1 being contained in complex minerals.

Desert sand, especially in dunes, is usually of aeolian origin. This means that it was transported by wind and has undergone a fair amount of chemical and mechanical weathering. As a result only the most stable minerals are left. As confirmed in previous section, the bulk of the material will be silica. This will be contained in quartz in various fractions, while most of the remainder of the silica listed will be contained in a group of minerals knows as feldspars [21].

Pettijohn et al. [21] and various others also list micas, chlorites, clay minerals, heavy minerals and rock fragments as possible constituents of sand(stone), but these will be minor portions and for now it is assumed they will not influence the melting behaviour significantly.

In addition there are 'chemical minerals' found in sand, split up in groups of carbonates, sulphates, sulphides, and others by [21]. According to the references from section 2.3.2, the most prevalent of these are calcium compounds. Significant amounts of calcite [22, 25–27] and gypsum [22, 23] are reported. The most likely mineral to contain Mg is the combined carbonate dolomite. Therefore a discussion of these also is appropriate.

The discussion here will be mostly thermodynamic. The liquid state being the most stable at a given temperature, does not imply that this state will be reached during acceptable time scales. Additionally, the temperature needed to reach practical viscosities might be higher, as will be discussed in section 2.5.

Quartz

(Low) quartz is the phase of silica stable under atmospheric conditions. Upon heating, multiple different phases may form as displayed in figure 2.3.1. The properties of the intermediate phases, while important for calculation of for example energy consumption, are out of the scope of this review. Of interest is the melting temperature of silica, effectively the melting temperature of high cristobalite, which is 1713 °C [29].

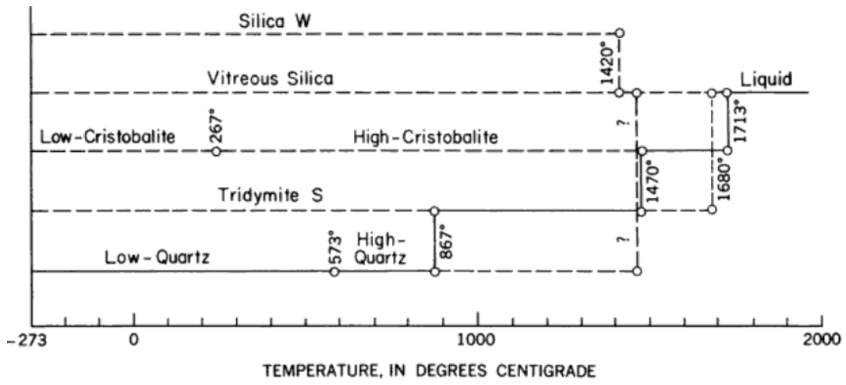

Figure 2.3.1: Multiple phases of silica at atmospheric pressure, and transition temperatures [29].

As will be discussed in section 2.4, it is not always needed to reach temperatures this high if lower melting substances are present to dissolve, or react with, the quartz. Small impurities of the common oxides, almost certainly present in quartz found in desert sand, will usually lower the melting temperature [29].

Feldspars

The general formula for the family of feldspars can be written as $(M)Al_xSi_xO_8$, where M can be calcium, potassium or sodium. Figure 2.3.2 illustrates the common forms and accompanying names. The balance of phases vary with temperature, but as the kinetics are sluggish high temperature phases can have formed and exist in a metastable state at ambient temperature. For this discussion the field of interest is the higher temperatures, where the feldspars form a solid solution series between Na-feldspar and the other two end members [21].

The Na-K series is known as the alkali feldspars, displayed in a phase diagram of the melting range on page 16, in figure 2.3.3a. The plagioclase feldspars consist of the series from Na-Ca, displayed in figure 2.3.3b. Note that both diagrams are sections of a complex multi-component system and as such can have regions with more than two phases.

Superficially inspecting the diagrams in figure 2.3.3, it can be estimated that the first melting effects for an alkali feldspar will be expected around 1100 °C. The plagioclase fraction has a more composition dependant starting temperature between 1118 °C and 1553 °C. All fractions will be stable in liquid form at around 1550 °C, while alkali feldspars with a high sodium content will prefer the liquid state close to the starting temperature around 1100 °C. This of course not accounting for interactions with other minerals present.

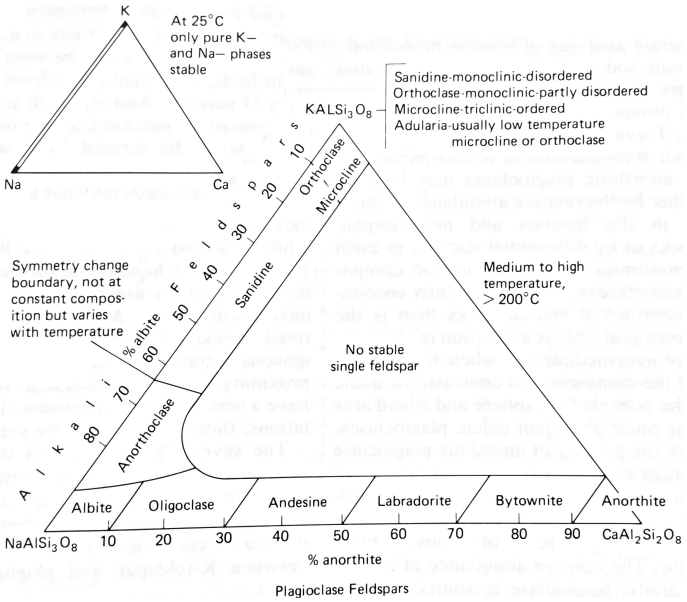

Figure 2.3.2: Overview of the K-Na-Ca feldspar system with common names of minerals and solid solutions [21].

Calcite and dolomite

Calcite, or limestone, is the stable phase of calcium carbonate, $CaCO_3$, at ambient conditions. It might be recrystallized over time from another known, but less stable, form of calcium carbonate: aragonite [21].

The melting temperature of calcite is listed at 1330 °C [31], but might decompose into CO_2 and CaO around 990 °C while the decomposition might start at lower temperatures [15].
The melting temperature of CaO is 2899 °C [31]. This order of temperature is unlikely to be needed, as discussed under quartz.

Dolomite is very similar to calcite in structure and behaviour as it is a dual carbonate, $CaMg(CO_3)_2$. Decomposition occurs in two steps where the first is the formation of MgO, $CaCO_3$ and CO_2 taking place just under 700 °C [15], after which the formed calcite decomposes upon further heating.

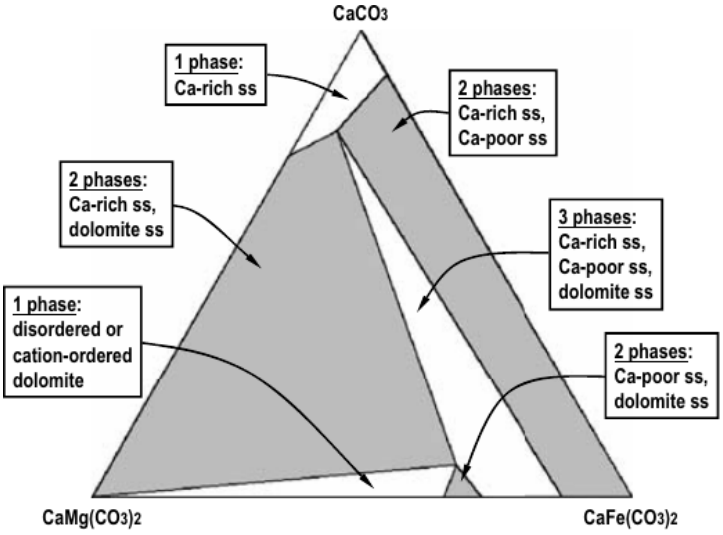

Figure 2.3.4: The $CaCO_3-CaMg(CO_3)_2-CaFe(CO_3)_2$ system [15].

Natural dolomite typically does not occur in the pure form, but as some combination of phases as displayed in figure 2.3.4, where the Fe containing phases are undesirable for optical reasons [15].

Gypsum

Gypsum is the common name for calcium sulphate dihydrate, $CaSO_4 \cdot 2H_2O$, is typically deposited from water. As such gypsum mostly found in area's of desert where a body of water used to be [21].

Gypsum will be dehydrated at 150 °C to form anhydrite, which will melt at 1460 °C [31]. Again, the release of water during the decomposition might influence the process and resulting glass, to be discussed in other sections.

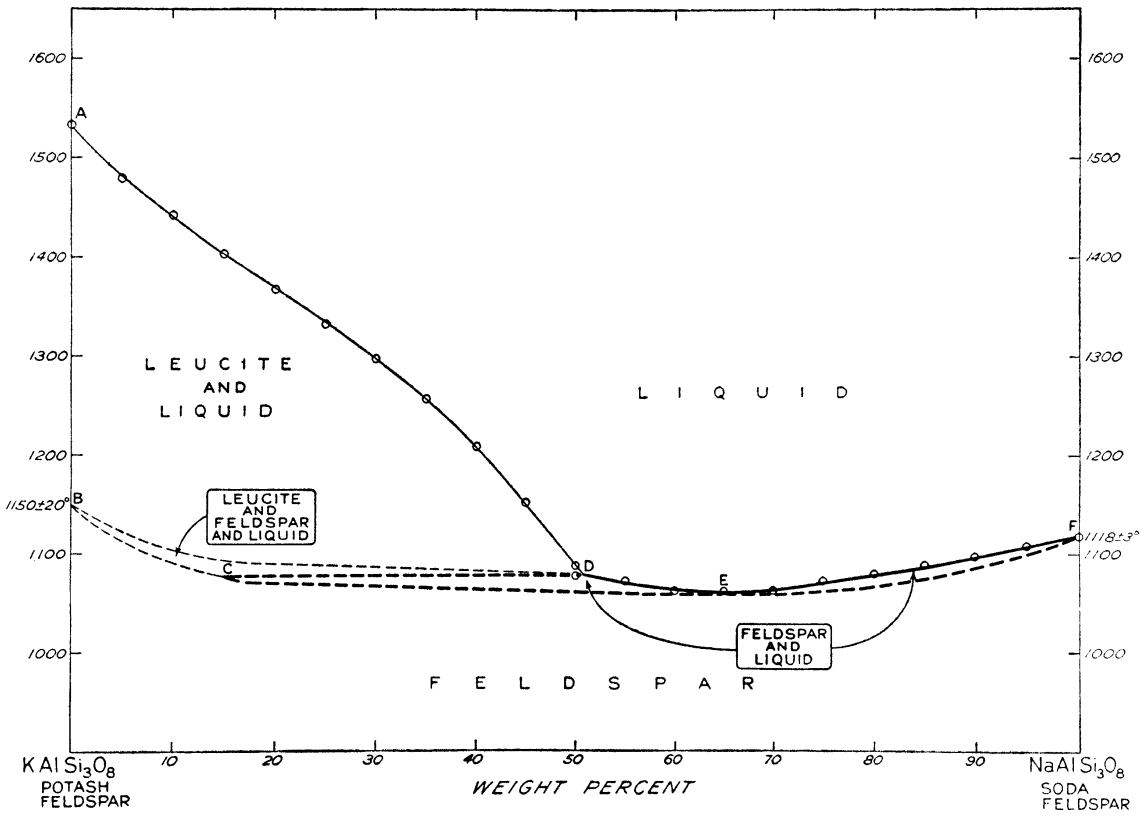

(a) Alkali-feldspars. Heavy lines refer to binary, light to ternary equilibrium [30].

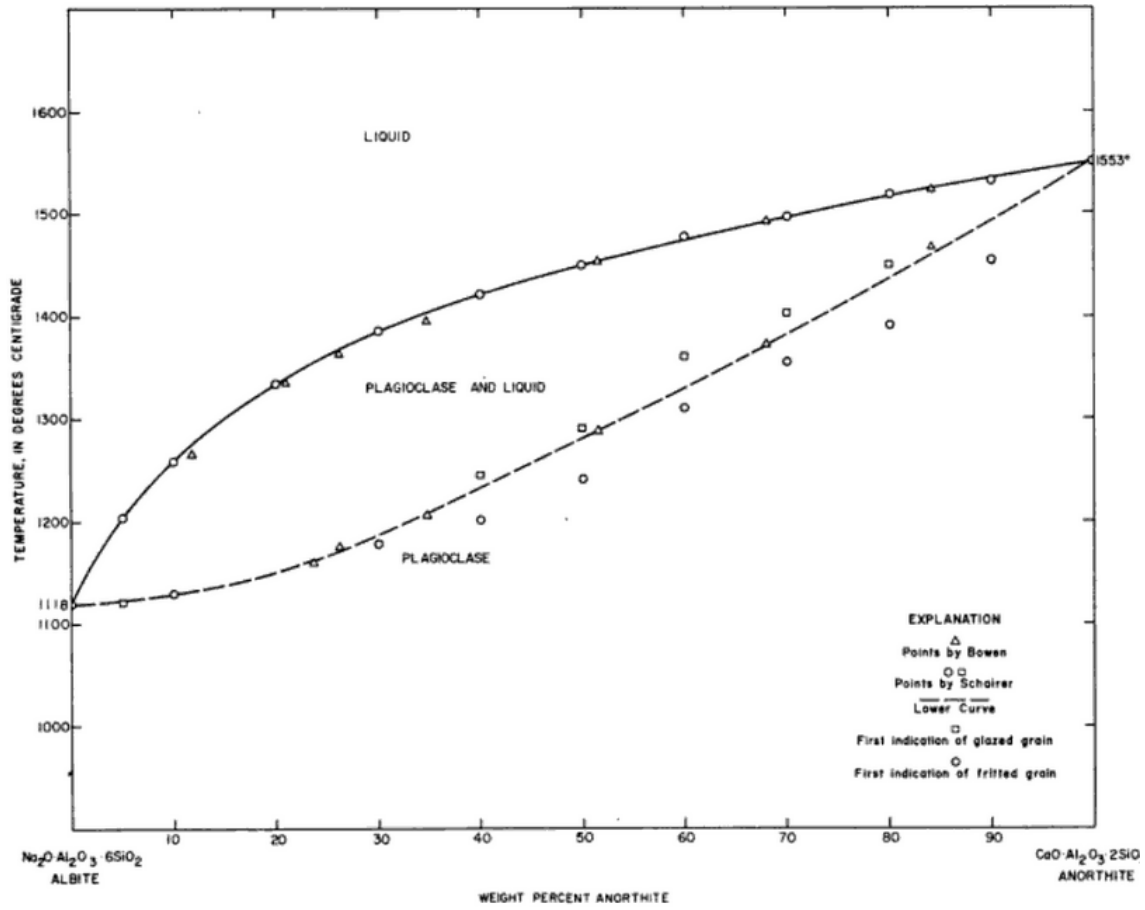

(b) Plagioclase feldspars [29].

Figure 2.3.3: (Sections of) phase diagrams of the melting range of the two feldspar series displayed in figure 2.3.2.

2.4. Batch melting

Control of the melting of a batch is very important in industry, as it is the most important factor in both time and energy consumption. For laboratory scale glass melting these factors are less important, but a grasp of the processes involved will be of use. In this section, some of the reactions occurring in a typical soda lime batch are discussed, and an attempt is made to extrapolate the expected processing temperatures for a desert sand batch.

Figure 2.4.1 gives an overview of the batch reaction taking place during melting of a soda lime batch. While the temperatures might vary when using only desert sand constituents, a similar succession of reactions can be expected.

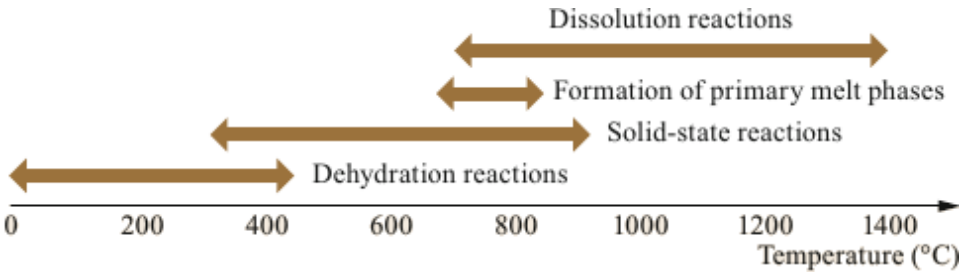

Figure 2.4.1: Schematic overview of batch reaction in a soda lime glass [8].

Assuming restricted availability of water, the only dehydration reaction to be expected is that of gypsum, if present. In industry 1 % to 4 % of water by weight might be added to improve batch cohesion and initial heat transfer, which in part will be released to the atmosphere when heated [8, 15].

The phase of solid-state reactions is more complex and harder to predict for the desert sand case. In a soda lime batch most of the solid state reactions are based around Na_2CO_3 reacting with other batch components such as the formation of $Na_2Ca(CO_3)_2$ between 550 °C and 850 °C. Between 700 °C and 850 °C a variety of sodium silicates are formed [8].

As from section 2.3.2 it seems unlikely to find sodium carbonate in the desert, this stage is expected to be mainly the decarbonation of dolomite and calcite around 600 °C and 990 °C respectively, where CO_2 is released and MgO and CaO are left behind [8, 15]. The weight loss resulting from the release of volatiles is referred to as the loss on ignition (LOI), were 'ignition' is considered heating to high temperatures rather than actually igniting the material [15].

The early decomposition of carbonates might present problematic, given the significantly higher melting point of CaO. In a soda lime batch, calcium oxide reacts with quarts to form $CaSiO_3$ at 1010 °C [15], but it could be that this reaction will be limited for the lack of liquid phases at this temperature.

The formation of primary melt phases increases contact between components, possibly accelerating ongoing solid state reactions and starting the dissolution of remaining components. In the soda lime case the bulk of these primary phases consist of eutectic liquid from the SiO_2-Na_2O-system, and in some cases additional lower melting point fluxes [8, 15], hence an alternative route is to be expected for a desert sand based batch.

The possibly available relatively low melting point minerals are the feldspars, gypsum, and if not decarbonated the carbonates. These might function in a similar fashion, but as their melting point is considerably higher, as found in the previous section, it is to be expected higher temperatures are needed. This would not be altered by the hypothetical calcium silicates, as the eutectics in the SiO_2-CaO-system are found at 1436 °C and 1455 °C [29], similar to the melting points of other components. As such it seems that a temperature of at least 1110 °C is needed when sufficient albite is available, if not temperatures close to 1500 °C will be required to initiate the formation of primary melt phases.

During the final stage the remainder of the batch, the remaining quartz, is dissolved. During this process the viscosity will increase as the silica content of the molten fraction is increased. To ensure the dissolution continues at an acceptable rate, and formed bubbles are able to escape the melt, a further temperature increase might be necessary [5]. This will be discussed in more detail in section 2.5.

The time it will take to complete the process is known as the batch free time. This duration is hard to predict due to the amount of variables involved, and hard to determine exactly, as detecting undissolved particles in a high temperature melt is far from trivial [5]. For the small scale expected for the batches for this project, this can be solved by trial and error.

In conclusion of this section, estimates of reaction temperatures are presented in figure 2.4.2.

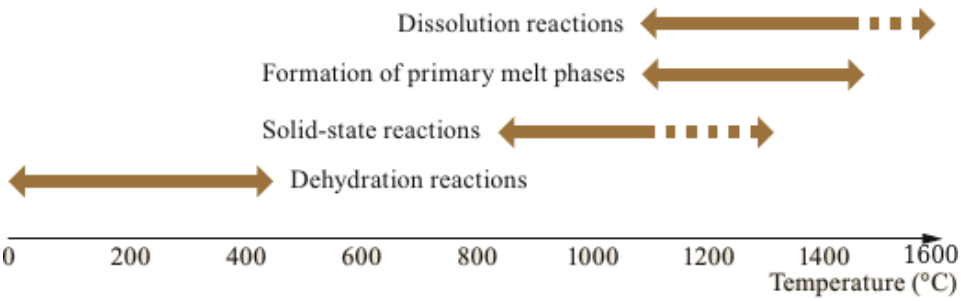

Figure 2.4.2: Overview of the estimated reaction ranges from this section, adapted from [8].

2.5. Viscosity of silicate melts

Once molten, the property of interest of the glass to be is the viscosity. The concept is introduced in this section, followed by a discussion of the reference points of interest for glass production. The relationship between viscosity, and temperature and composition is explored in the final two subsections.

2.5.1. Introduction to viscosity

Viscosity (η) is the quantity that relates the shear force on a liquid to the rate of displacement in a way similar to the shear modulus relating elastic deformation of a solid to a shear force,

$$\sigma_{xy} = \eta \frac{d\epsilon_{xy}}{dt}, \tag{2.5.1}$$

where σ_{xy} is the shear stress [Pa], and ϵ_{xy} is the shear strain [6]. In more practical quantities the viscosity can be defined by the force F in N needed to move two plates of area A in m^2 separated by a distance d [m] covered in fluid, with a relative velocity v [m s^{-1}] [5, 32]:

$$\eta = \frac{Fd}{Av}. \tag{2.5.2}$$

From equation 2.5.2 it can be derived that the SI unit of the viscosity is N s m^{-2} or Pa s, which will be used throughout this thesis. In literature and industry the Poise (P), the unit used in the cgs-system, is still regularly used. This can be easily converted as 1 Pa s = 10 P [5]. In other cases the dPa is used, which is equivalent to 1 Poise [8].

The viscosity can be regarded the inverse of fluidity, and is used in practice as a measure for the ease of flow during processing. When a glass melt is cooled, the viscosity changes over multiple orders of magnitude. This behaviour is one of the main reasons glass forms, as mentioned in section 2.1.

Determining viscosity of usual fluids can be a fairly straight forward process and a plethora of techniques is available. An overview of possible measuring methods is given in [5, ch6.4] and [8, ch3.2]. No one device can measure the full 14 orders of magnitude of viscosity for a glass, so for a full view of the melt properties multiple techniques have to be applied.

The elevated temperatures needed, complicate a full measurement even more. Few suitable facilities are available, so alternative methods have to be used. One option is an estimation be made by determining multiple points of known viscosity and fitting the results to (semi) empirical equations [4], discussed in section 2.5.3.

2.5.2. Viscosity reference points

Historically glass processing was done empirically and/or by gut feeling, mostly based on the colour of the glowing melt, changing with temperature. With advances in technology, reference points were defined by the viscosity of the glass. The temperature for each point will depend heavily on the composition of the glass.

The definition of each reference point will be discussed in order of increasing temperature. The definitions found in different references vary in some cases, when this is the case the one to be used for this research is specified.

The first milestone to be reached upon heating a glass is the **strain point** at $10^{13.5}$ Pa s [4–8]. This is the highest viscosity at which relaxation takes place over observable time scales, displayed by relaxation of internal stresses in about 6 hours. Effectively the response to applied stress or strain is elastic.

At the **annealing point** internal stresses formed during the glass transition will be released in 15 minutes or less by viscous flow. This has become generally accepted as the industry standard and takes place at a viscosity of 10^{12} Pa s to $10^{12.4}$ Pa s listed by [5], while other references state 10^{12} Pa s [4, 6–8], which will be used here due to the majority of sources giving this value. This is the first point that can be considered a critical processing temperature.

The **transition point** is technically a misnomer. As discussed in section 2.1.5, the transition temperature, and thus the viscosity during the transition, depends on the cooling rate. It seems agreed on that the viscosity must be a certain value during the transition, but different references disagree upon the value: $10^{11.3}$ Pa s [5], $10^{12.3}$ Pa s [4], $10^{10.9}$ Pa s [7]. The latter will be taken as the value for this section, but depending on the case, other suitable conventions might be used.

Above the glass transition temperature, the melt will display visco-elastic behaviour to applied stress or deformation: an instantaneous elastic response, followed by relaxation by viscous flow. More information on this response and mathematical description of the effect can be found in most glass science texts, e.g. [6, ch13.2] and [8, ch3.3.1], but will have no application during this project. As the glass now enters the supercooled liquid region, depending on composition recrystallisation could occur.

When the **(Littleton) softening point** is reached, the mechanical response will be predominantly viscous in nature, the elastic response effectively non-existent. The glass will deform under it's own weight as the shear modulus becomes essentially zero. The reported viscosity value is $10^{6.6}$ Pa s by [4, 5, 7, 8], and $10^{6.65}$ Pa s by [6].

The **working point**, 10^{3} Pa s [4–6, 8], is the viscosity around which most shaping operations take place. This is the temperature at which moulding and blowing operations begin. These processes typically are finished around the softening point. Operations requiring a more fluid melt, like casting and drawing, take place at slightly higher temperatures. Often a working range rather than a point is mentioned for that reason. A glass with a large range of temperatures in this course of viscosity, is known as a *'long glass'*, while a *'short glass'* has a small working range [8]. As the glass will have to shaped, the working point would be the second point of interest.

Finally the temperature where the glass is considered 'fully fluid' is reached, known as the **practical melting point**. Past the melting temperature grains dissolve, stirring is possible, and bubbles are released. The viscosity is anonymously reported as 10^{1} Pa s [4–8]. Note that fluid is a relative term. For comparison, the viscosity of water at room temperature is 10^{-3} Pa s [6]. Since the first step of creating a cover glass is the formation of a homogeneous melt, this point is of great interest.

An overview of the reference values, also referred to as *isokoms*, used in the remainder of this thesis is presented in table 2.5.1. To illustrate, a typical soda-lime-curve is shown in figure 2.5.1.

Table 2.5.1: Overview of reference points as referred to in the remainder of this thesis.

Reference point	$\log(\eta[\mathrm{Pa\,s}])$
Strain point	13.5
Annealing point	12
Transition point	10.9
Softening point	6.6
Working point	3
Practical melting point	1

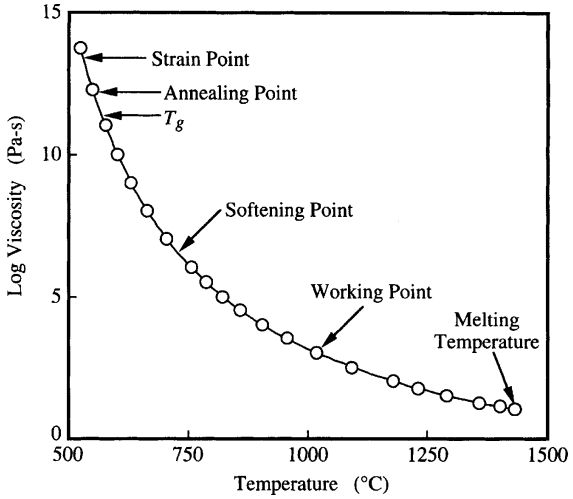

Figure 2.5.1: Typical viscosity reference points versus temperature for a soda-lime-silicate glass [5].

2.5.3. Temperature & viscosity

As viscosity plays an important role in research as well as technology, many attempts have been made to capture the variation of viscosity with respect to temperature mathematically. In this case the most important function of such a relation is to relate the viscosity at a certain temperature to the composition, which will be discussed in the next section.

As seen in figure 2.5.1, the viscosity is typically plotted on a $\log_{10}$-scale to be able to cover the extensive range of values.

The most basic way of relating the viscosity of a fluid to the temperature is an Arrhenius relation,

$$\eta(T) = \eta_\infty \exp(\frac{-\Delta H}{RT}), \tag{2.5.3}$$

where η is the viscosity, η_∞ is a constant representing the viscosity in case of infinitely high temperature, ΔH is the activation energy for viscous flow in J, R is the gas constant [$\mathrm{J\,K^{-1}}$] and T is the temperature [K].

For simple fluids, this basic relation can give accurate predictions over large temperature variations, and in glass forming melts for small ranges of temperature it can provide an acceptable fit. For larger ranges the deviation becomes unacceptable due to the assumption that the activation energy is a constant. As discussed in section 2.2, not only the mobility but also the degree of polymerisation in a silica based melt changes upon changing temperature, as connections made by various modifiers break at different temperatures. This constantly varies the activation energy for viscous flow making equation 2.5.3 lose its applicability [5, 6, 8].

In the 1920's Vogel [33] posed the mathematical form for an empirical solution, later studied by Fulcher [34] and, Tammann and Hesse [35]. The wide spread application of the equation in glass science and other fields lead to it being known as the Vogel-Fulcher-Tammann (VFT) equation:

$$\log\eta(T) = A + \frac{B}{T - T_0}. \tag{2.5.4}$$

The temperature dependence of the (logarithm of) the viscosity η is plotted by fitting 3 parameters. A can be regarded as the high temperature limit of $\log(\eta)$, B can be related to the activation energy. For $T_0 = 0$, the equation can be rewritten to equation 2.5.3, implying this constant accounts for the variation of the activation energy. For $T \to T_0$ the viscosity will diverge, leading to an overestimation of the viscosity for low temperatures. Despite this inaccuracy, the VFT equation has been applied often for almost a century, most notably on oxide melts [5, 6, 8].

For organic and some inorganic liquids the VFT provides less satisfying fits, and the search for a more fundamental description is still very much ongoing. Notable are the Avramov-Milchev, Adam-Gibs, and relatively recently the Mauro-Yue-Ellison-Gupta-Allen equations, based on atomic hopping, entropy, and topological degrees of freedom respectively. Since the melts to be created will be oxide based, and interest lies in the high temperature range initially, equation 2.5.4 will suffice. For further reading on other models [6, ch9.5] and [8, ch3.3.3-4] can be consulted.

2.5.4. Composition & viscosity

The non-Arhenian behaviour of silica based melts finds it's origin in the very interconnected structure discussed in section 2.2. In vitreous silica, the connectivity stays mostly intact to very high temperatures, causing the activation energy for viscous flow to be controlled by the breaking of bonds. This leads to near Arhenian behaviour [18]. Addition of modifier elements and consequent NBOs leads to significant changes in this activation energy, overall and in relation to temperature. Small additions can lead to significant drops in viscosity, as illustrated by the lowering of the glass transition temperature by impurities in figure 2.5.2.

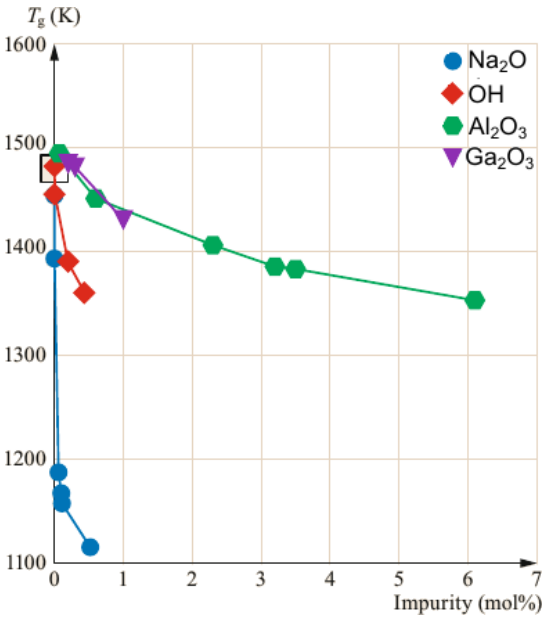

Figure 2.5.2: Decrease of the glass transition temperature of SiO_2 due to various impurities [8].

The lower the IFS of the modifier (equation 2.2.1), the stronger the modifying effect, hence bigger ions of similar valence, or similarly sized ions with lower valence, lead to a slightly larger decrease in viscosity [5].

The Al^{3+} ion, of which significant quantities seem to be present in desert sand, plays an interesting role due to the intermediate properties described in section 2.2. In peralkaline melts, where there are enough modifiers available for charge compensation, addition of Al will lead to an increase of viscosity as it will enter as a network former while consuming modifiers. For peraluminous composition, an incremental fraction will act as a modifier, lowering viscosity [8].

Volatiles influence the viscosity of silicate melts as well, especially H_2O. Water reacts in part with BOs to form OH^-, leaving NBOs in the process. The equilibrium between dissolved H_2O and OH^- depends on multiple factors including temperature, composition and atmosphere. The creation of NBOs leads to a significant reduction of the viscosity, as seen before in figure 2.5.2. A typical silicate glass synthesized under ambient conditions contains 0.02 wt% water [8]. In industrial glass production, more water might be added for various reasons, usually by wetting the batch [15].

For practical application, quantifying these general principles is needed. As there is no universal physical model (yet), this is usually accomplished by interpolating from known compositions. Software containing immense databases of compositions are available, but for the probably unusual compositions that this endeavour will yield, there is a risk of being to far out of range, leading to unjust extrapolations. Financial and practical arguments are reason for looking for an alternative as well.

Instead the empirical model by Giordano et al. [36] should prove useful, as it was developed for natural magmas, and thus the composition range approaches the range of natural sands. The model predicts the constants B and T_0 in equation 2.5.4 from the molar composition, based on a calibration set of 1774 data points from 58 different compositions. The high temperature viscosity limit A is taken as a constant (-4.55). The derivation of the parameters to calculate the constants, and references for the determination of A, as well as a comparison to other models can be found in the original paper.

The authors write that in developing the model it was determined that accounting for the oxidation state of Fe, and volatiles other than H_2O and F did not yield better results, implying they are of less influence on the viscosity than the oxides in table 2.5.2. In the same table the ranges of composition for which the model is valid are displayed [36]. Note that all the oxides found in significant amounts in sand (table 2.3.1) are included, and the range is appropriate.

Table 2.5.2: The composition range of validity of the model by Giordano et al. [36].

Oxide	SiO_2	TiO_2	Al_2O_3	FeO_T	MnO	MgO	CaO	Na_2O	K_2O	P_2O_5	H_2O	F_2O_{-1}
Min wt%	24	0	0	0	0	0	0	0	0	0	0	0
Max wt%	90	8	40	20	3	45	40	15	15	3	15	10

For anhydrous melts, which are to be expected for lack of water in deserts, and drying of the sand during the beneficiation process, the authors report an average misfit of ± 0.5 log-units and '*the accuracy of the model at conditions relevant to volcanic processes is usually within* 5 % *relative error.*', which is demonstrated in figure 2.5.3a. Comparison to a data set not used for calibration is presented in figure 2.5.3b, where the apparent deviation of the data labelled rhyolite is ascribed to limited measurements being available, in which a measuring error might have occurred [36]. The lack of data points in the range of roughly 10^5 Pa s to 10^{10} Pa s is due to crystallisation of the melt when kept there long enough for measurements.

All in all the model seems a useful tool to estimate the expected temperatures needed and viscosity behaviour of the melts to be produced. For illustrative purposes, plots for the compositions found in table 2.3.1 are presented in figure 2.5.4, the method of plotting is described in section 3.2.3. It can be observed that all but one composition do not reach the practical melting point below 1800 °C, and thus will not be able to be appropriately refined at acceptable temperatures. This implies that for most desert sands alteration of composition is needed to create a workable glass.

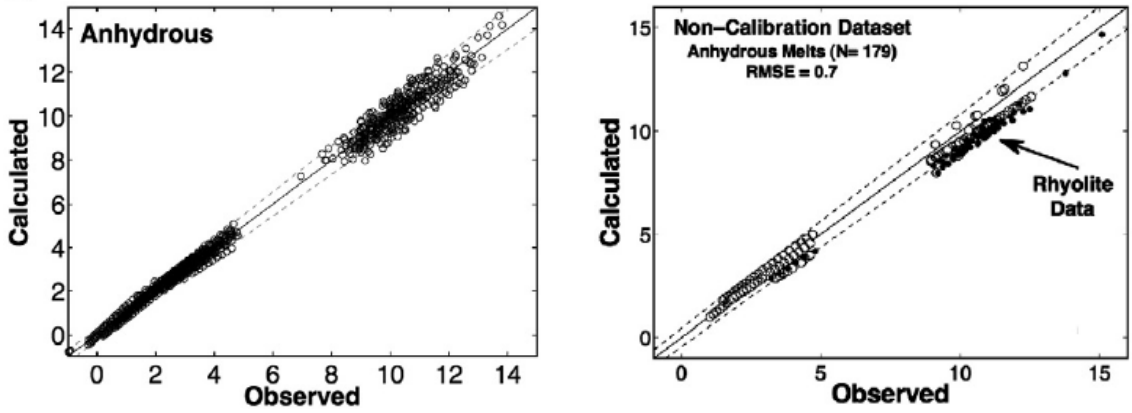

(a) Calibration data set.

(b) Non-calibration data set.

Figure 2.5.3: Values of $\log(\eta)$ predicted by the model of Giordano et al. [36] versus observed values of anhydrous parts of datasets. Dashed lines indicate 5% relative uncertainty. Adapted from [36].

2.5.5. Summary

The viscosity reference point of interest for determination of the processing temperatures needed are the annealing point, working point, and practical melting point. While measurements are difficult, modelling options are available. Based on compositions found in the literature and the predicted viscosity curves for those compositions, creating of a glass by melting unmodified desert sand is unlikely at acceptable temperature.

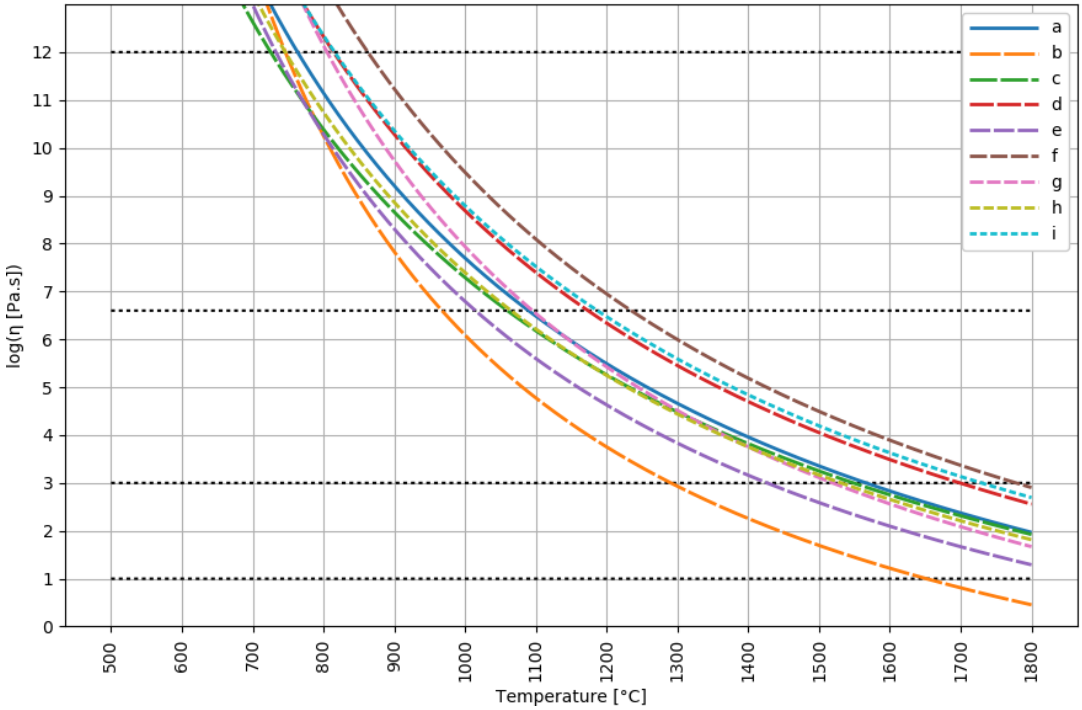

Figure 2.5.4: Plot of viscosity curves produced from examples of desert sand composition in table 2.3.1, using the model from [36] and assuming 0.02 wt% H_2O. Dashed isokoms are from top to bottom: annealing point, softening point, working point and practical melting point. As this graph is for illustrative purposes, uncertainty is omitted.

2.6. Mechanical properties of glass

Glass is thought to be a fragile material, as most household and window glass seems to break quite easily. Conversely, glass fibre reinforced materials and 'bullet proof glass' are not unheard of. How glass is given it's strength or lack thereof, and methods of controlling it are explored in this section.

The amorphous and interconnected structure of glass leads to atypical behaviour compared to crystalline solids. As there is no defined long range structure, dislocations are not defined, and while under particular circumstances local plastic deformation by viscous flow can occur [6, 8, 37], plastic deformation in the classic sense is not possible.

The mechanical properties specified in chapter 1 are the flexural strength (45 MPa), and the elastic modulus (70 GPa). The latter is relatively straight forward and will be briefly discussed first. Other elastic constants, such as the bulk and shear modulus, and Poison's ratio, that are not of direct interest at this point will be omitted here, but are well described by Varshneya and Mauro [6, ch8.2].

The 'strength' of glass proves to be a more complicated matter due to the brittle nature of glass failure, and will be discussed after. This section will conclude with a brief overview of possible characterisation methods that could be useful when producing a glass succeeds.

2.6.1. Elastic modulus of glass

The elastic modulus, or Young's modulus, E [Pa], is the material constant that relates the linear stress, σ [Pa], to the reversible linear strain ϵ [6, 37];

$$\sigma = E\epsilon, \tag{2.6.1}$$

and so is a measure for the deformation under a given stress. This relationship is valid for small strains ($\epsilon < 0.1$ for silicate glasses [37]), which seems applicable in the case of solar panels. Appropriate stiffness of the construction is important to limit the deformation of the cells, hence the deformations can be assumed to be relatively small.

The effect of addition of components other than silica, on the elastic behaviour of a silicate glass, is a balance of the filling of 'empty' space between the tetrahedra, and the breaking up of the network. Therefore the ionic field strength (IFS) (equation 2.2.1) of modifier ions is of influence on the Young's modulus. Intermediate elements, such as boron and aluminium that become part of the network have a tendency to either keep the modulus constant or even increase it, depending on other elements present [37].

Pure silica glass has a Young's modulus of 70 GPa [6]. A general idea of the influence of common components can be obtained by inspecting a collection of tabulated values such as [32, ch10]. With the exception of Li_2O, the alkali oxides lead to a decrease of the Young's modulus, illustrated in figure 2.6.1, where addition of alkaline earth oxides with their higher IFS typically lead to an increase [6], as shown in figure 2.6.2.

The addition of alumina appears to increase elastic modulus as well, as Bansal and Doremus [32] report an increasing velocity of sound for higher molar fractions, and Le Bourhis [37] shows a value of 83 GPa to 91 GPa for aluminosilicate glasses.

Glass density, which is dependant on both composition and cooling trajectory, also influences the elasticity. A glass that is cooled slower through the glass transition, will be denser and thus have a higher elastic modulus [8].

Circling back to the requirements, a Young's modulus of >70 GPa seems obtainable, as this is the reported modulus of vitreous silica, while the additional oxides that are available from desert sand appear to increase this value.

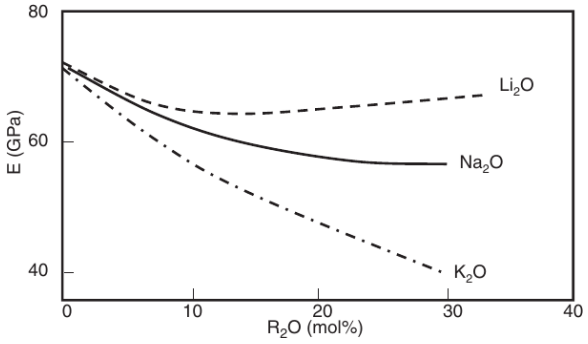

Figure 2.6.1: Young's modulus of silicates for different concentrations of alkali oxides [37].

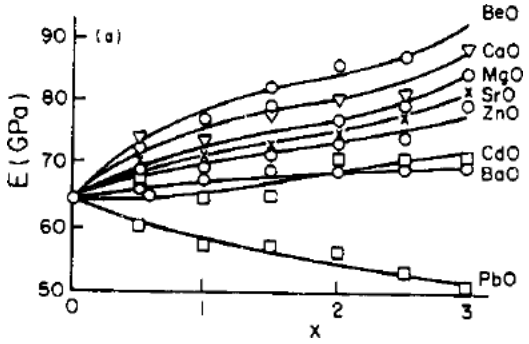

Figure 2.6.2: Young's modulus of Na_2O-xMO-$5SiO_2$ glasses [32].

2.6.2. Strength of glass

Strength is the term used for the stress at failure [6], hence the flexural strength is the stress a material will fail at when under a bending load. Why the bending strength is specified instead of the tensile strength will become apparent in section 2.6.3, but first some concepts useful in discussion of glass strength are introduced.

Intrinsic strength & fracture mechanics

The field of fracture mechanics came into existence when it was realized that the calculated theoretical strength of brittle materials, did not line up with reality. This calculation was based on separating two layers of atoms by more that a typical interatomic distance, leading to an energy balance of creating of new surface energy, against the release of elastic energy when strain is released on fracture [6, 37].

Observations such as the increasing strength of glass fibres with decreasing cross section, as displayed in figure 2.6.3, led to the conclusion the observed discrepancy must be caused by 'critical defects' in the material acting as stress concentrator. This was formalized in the stress intensity factor, which for a stress at fracture σ_f is defined as

$$\sigma_f \sqrt{\pi a^*} = \sqrt{2\zeta E} = K_{Ic}. \tag{2.6.2}$$

K_{Ic} [MPa$\sqrt{\text{m}}$] is known as the critical stress intensity factor. The subscript I refers to the mode of loading of a critical crack of length a^* in m, in this case crack opening. ζ [J m^{-2}] is the energy needed to create the new fracture surface. K is considered a material constant and, as can be seen in equation 2.6.2, depends on the elastic modulus and the surface energy, which in turn is influenced by the environment [6].

For different crack geometries and types of loading, a slightly different K is defined, but as glass is most prone to failure under a tensile stress, K_I is most common, and used as a measure for the fracture toughness [37].

From equation 2.6.2, it can be seen that the strength does not only depend on material properties, but also on the size of defects. In a typical glass, a defect length of 50 µm could lead to a maximum load before fracture in the order of 35 MPa, while the theoretical strength is in the order of GPa [6].

From this very brief discussion, the key point is that (undetectable) defects can lead to significant reduction in strength. A more extensive discussion of fracture mechanics of glasses, and derivation of equation 2.6.2, is provided by Varshneya and Mauro [6, ch.18], and Le Bourhis [37, ch.7]. An even more detailed review of fracture mechanics in general can be found in the book by Janssen et al. [38].

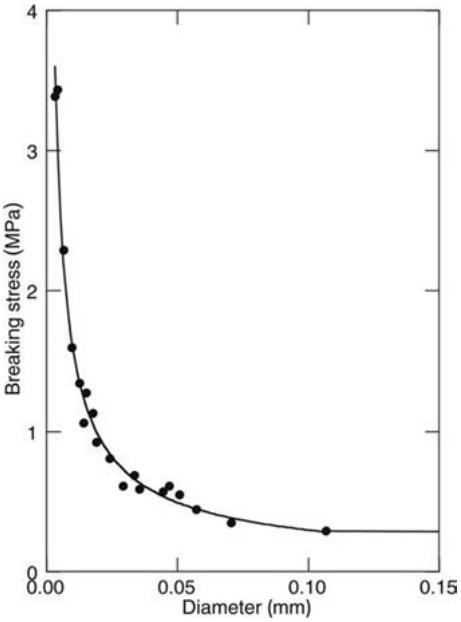

Figure 2.6.3: Tensile strength versus wire diameter for a glass of unknown composition [7].

Statistics of glass strength

Since failure of glass originates from practically undetectable flaws, the strength is not a certainty. It heavily depends on the (surface) quality of the glass item, influenced by production and handling. To be able to determine the maximum load a glass can bare, statistical analysis of a multitude of experiments is required.

While the suitability is questioned, e.g. [39–41], the most common way of performing such an analysis in industry, is by fitting experimental results to a Weibull distribution. This is based on a the assumption of the presence of a 'weakest link' causing fracture, in the form of the most serious flaw [6, 37].

The Weibull distribution is defined by:

$$P = 1 - \exp(-R), \tag{2.6.3}$$

where P is the probability of failure. R is the risk function, given by

$$R = \int_V \left(\frac{\sigma - \sigma_u}{\sigma_0} \right)^m dV. \tag{2.6.4}$$

In the risk function, V is the volume under (tensile) load, σ_u is the minimum stress level for failure, hence $R = 0$ for $\sigma < \sigma_u$. σ_0 is a normalizing parameter with the unit of stress, and m is the Weibull modulus [6, 37]. As σ_u and the volume are constants depending on load and material, equations 2.6.3 and 2.6.4 are usually simplified to the two-parameter Weibull distribution;

$$P = 1 - \exp\left[-\left(\frac{\sigma}{\sigma_0} \right)^m \right], \tag{2.6.5}$$

where the constants are lumped into a new σ_0 [6, 37]. Plotting this relationship yields figure 2.6.4a. As illustrated, a higher Weibull modulus leads to a smaller 'low strength tail', and thus is preferable. Typical glass products have a modulus between 5 and 15 [6].

When the natural logarithm of the survival probability, $(1 - P)$, is taken twice, the distribution can be rewritten to

$$\ln\left[\ln\left(\frac{1}{1-P} \right) \right] = m \ln \sigma + \ln\left(\frac{1}{\sigma_0^m} \right). \tag{2.6.6}$$

In this notation, plotting $\ln\left[\ln\left(\frac{1}{1-P}\right)\right]$ versus $\ln\sigma$, leads to a straight line with slope m. This can be used to find the variables in equation 2.6.5 by linear regression of experimental results, as illustrated in figure 2.6.4b [6, 37].

It is important to realise that the size of loaded volume has an effect on the results; with the same distribution of flaws, encountering a critical one is more likely if a larger volume is subjected to stress. The two parameter Weibull distribution also skips over the effect of integration over volume, which becomes more complicated when loading conditions are not uniform. These considerations are discussed well by Le Bourhis [37, ch7.8].

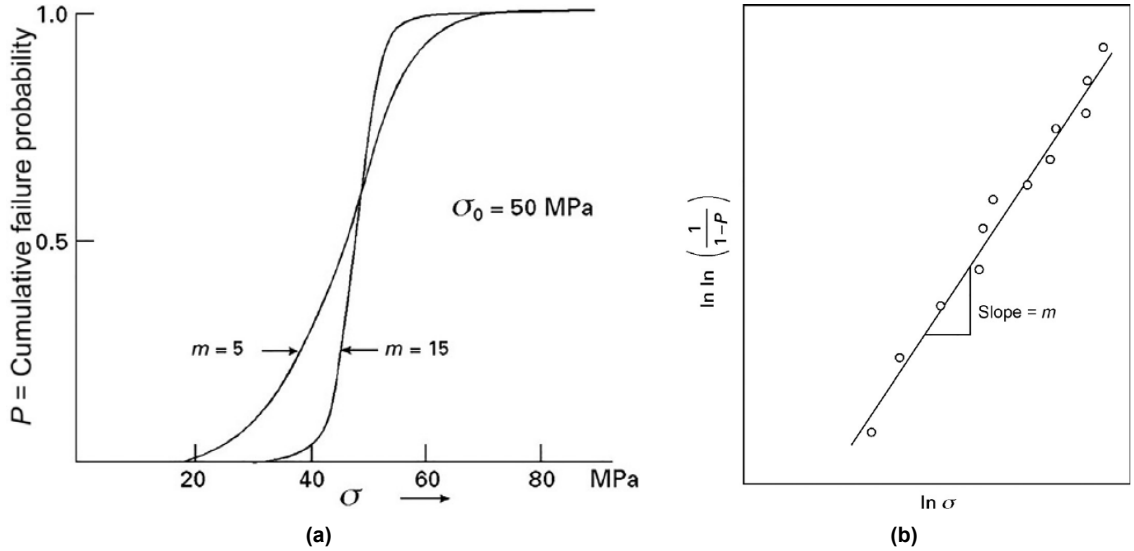

Figure 2.6.4: Examples of typical Weibull plots [6].

Composition & glass strength

With the statistical nature of flaw size and distribution, composition is far from the only determining factor when it comes to the strength of silicate glass. An indication of the influence that the composition has, can be acquired based on equation 2.6.2; the stress at failure for a given defect size depends on the fracture toughness, which depends on the surface energy and the Young's modulus. The latter was discussed in section 2.6.1.

From table 2.6.1, it appears that the surface energy is lowered by low IFS modifiers such as Pb, while it is relatively constant when conditional network formers are added. Since bonds have to be broken to create a new surface, it is in the line of expectation that introducing NBOs would lead to a decrease. As this energy is dependant on interaction with the surroundings of the glass, the atmosphere is of influence as well.

Again it is implied that the alumina from feldspars might have a positive influence on mechanical properties, while the effect of alkali and alkaline earth oxides varies with the IFS.

Table 2.6.1: Overview of properties influencing strength for some common silicate glasses [37].

Glass	K_c (MPa m$^{1/2}$)	E (GPa)	ζ (J m^{-2})
Silica	0.74–0.81	73	0.65
Soda–lime–silica	0.72–0.82	70–74	0.4–1
Borosilicate	0.75–0.82	64–89	0.63
Aluminosilicate	0.85–0.96	83–91	0.63
Lead–silicate	0.62–0.73	58–65	0.44

2.6.3. Characterisation of mechanical glass properties

Due to the brittle nature and lack of plastic deformation, a standard tensile test is not suited for glass. Shaping of the sample is complicated and might introduce flaws that influence the result. Furthermore, the clamping of the specimen needs to be executed with perfect alignment, to prevent undesired concentrations of stress that would be corrected by plastic deformation in a ductile sample [37].

Instead the common practice is to use various flexural tests, e.g 3 or 4-point beam bending, and ball or ring on ring tests. The latter have the advantage of not loading the edges of the glass, but require a sufficiently large sample which will be unlikely to be produced during this project. The 4-point bending test (figure 2.6.5) is preferred over the 3-point test because a larger volume is exposed to the maximum stress, leading to more statistically significant results. In both cases it is important for the sample to be long compared to the other dimensions [6].

From the measured force and deflection during a 4-point bending experiment, information on both elasticity and strength can acquired using the following equations for the deflection δ [m], and maximum stress σ_m[Pa] respectively [6].

$$\delta = \frac{F(L_1 - L_2)(2L_1^2 + 2L_1L_2 - L_2^2)}{96EI_A} \tag{2.6.7}$$

$$\sigma_m = \frac{(F/2)[(L_1 - L_2)/2]y}{I_A} \tag{2.6.8}$$

L_1 and L_2 are specified in figure 2.6.5, y is half the height of the beam; all dimensions are in m. In both cases F [N] is the applied load, I_A [m^4] is the second moment of area ($\pi d^4/64$ for a cylindrical or $bh^3/12$ for a rectangular beam) [6]. For $L_2 = 0$ equations 2.6.7 and 2.6.8 simplify to the 3-point test.

As these calculations stem from linear beam theory, care has to be taken that the deformations are small ($\delta < h$ for Young's modulus, $\delta < 3h$ for stress). For larger deflections corrections can be applied, or an alternative measurement can be chosen [6].

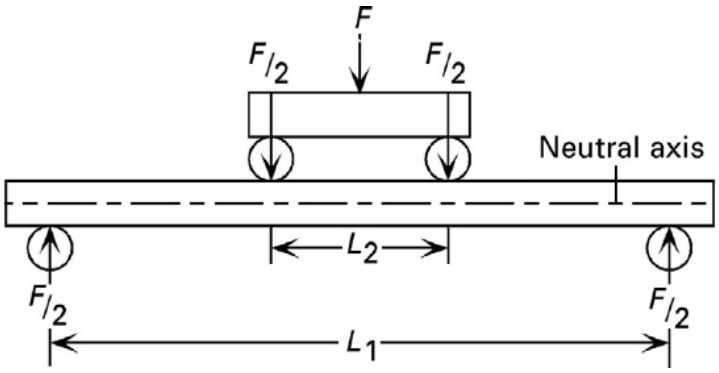

Figure 2.6.5: Diagram of a 4-point bending test [6].

For elastic modulus measurements, often acoustical measurements in the form of ultrasonic or resonance techniques are used. The natural frequency of, or the speed of sound in a sample of known geometry are measured. Both have a known relationship to the elastic properties of the material, which can be used to find E [8].

Finally, information can be gained from closely inspecting the fractures and scratches formed under specific loads. Fracture analysis is a field of research on it's own, and a complete discussion would be inappropriate here. One aspect of it, in the form of the fracture mirror, could be applicable during this project.

When moderate to high strength glass is broken, the succession of different stages of crack growth leads to a characteristic feature called the fracture mirror, displayed in figure 2.6.6. In a well annealed glass the mirror is (semi)circular, this shape deviates when residual stresses are present, providing the first piece of information [37, 42].

More important, it was found that a relationship exists between the radius of the mirror r [m], and the stress at fracture σ_f [Pa] [37, 42]

$$\sigma_f = \frac{M}{\sqrt{r}}, \tag{2.6.9}$$

where M is known as the mirror constant. M varies between 1.9 MPa$\sqrt{\text{m}}$ to 2.22 MPa$\sqrt{\text{m}}$ for common silicate glasses [37], and can be used to estimate the stress at fracture when no information on loading conditions is available.

The history of, and procedure for, mirror analysis is reviewed by Quinn [42].

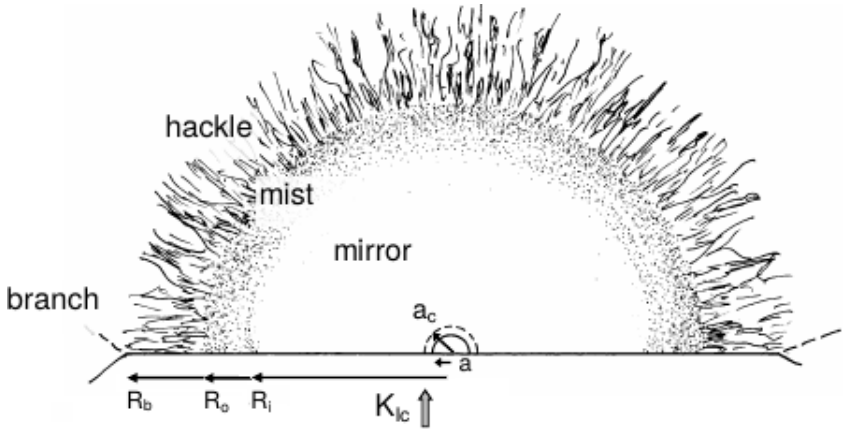

Figure 2.6.6: Schematic depiction of a fracture mirror of a fracture originated at the surface, adapted from [42].

2.6.4. Summary

The strength of glass is not strictly defined, but a statistic depending on the size and distribution of flaws, hence process control in the form of removal of seeds and stones (fining) and shaping is of great importance. The main fractions of chemical components, apart from silica, found in desert sand; CaO and Al_2O_3, listed in table 2.3.1, appear to have a positive influence on both Young's modulus and strength of silicate glasses. This indicates that achieving a Youngs modulus of >70 GPa and a bending strength of >45 MPa in desert sand glass is theoretically possible. Ideally characterisation of these properties is performed by a 4-point bending test, but size and shape requirements, and large amounts of samples required, could make this problematic. If no appropriate samples can be produced, fracture (mirror) analysis could give and indication of the strength of the produced glass.

2.7. Optical properties of glass

Transmission of 85 % of the effective spectrum for silicon based solar cells is the only optical property defined in the objectives in chapter 1. Transmissivity is not a direct property of the material, as it is defined as the fraction of incident light that passes trough the glass [5, 6]. As such it will be determined by the lack of losses from reflection and absorption, discussed in the remainder of this section.

When the intensity of incident light is defined as 100 %, the percentage of transmitted light T is given by

$$T = 100\,\% - R - A, \tag{2.7.1}$$

where R and A are the percentages reflected and absorbed.

Ideally the transmission in the effective spectrum of silica based photo voltaic (PV)-cells (350 nm to 1100 nm [8]) is as high as possible to increase efficiency, while the ultraviolet (UV) <380 nm and infrared (IR) >740 nm are reflected or absorbed outside of the effective range, to prevent heating and deterioration of the PV-cells. While this is desirable, it is not a requirement, and optimal transmission in the visible spectrum has priority.

As the goal is to have as much energy from the sun as possible reach the solar cells, this priority can be further specified. Figure 2.7.1 shows the two standard spectra for measuring solar panel efficiency, and it can be seen that the irradiance is highest around 550 nm. This means optimal transmission close to this wavelength is most important.

While the ideal cover glass would transmit close to 100 % in the complete visible spectrum, giving it a fully transparent appearance, this might not be possible given the limited feedstock. As some typical discolouration methods are based on 'levelling' the transmission spectrum by adding absorbing species [6], which would lower the overall transmission, it might be that the optimal option in the case of desert sand glass is slightly coloured.

Measurements of transmission can be fairly straight forward as off the shelf devices are quite commonplace. Devices can be roughly categorised into three groups, the most expensive option being full spectrum analysers. At lower cost, devices that give a reading for either 'optical transmission' or certain set wavelengths are available.

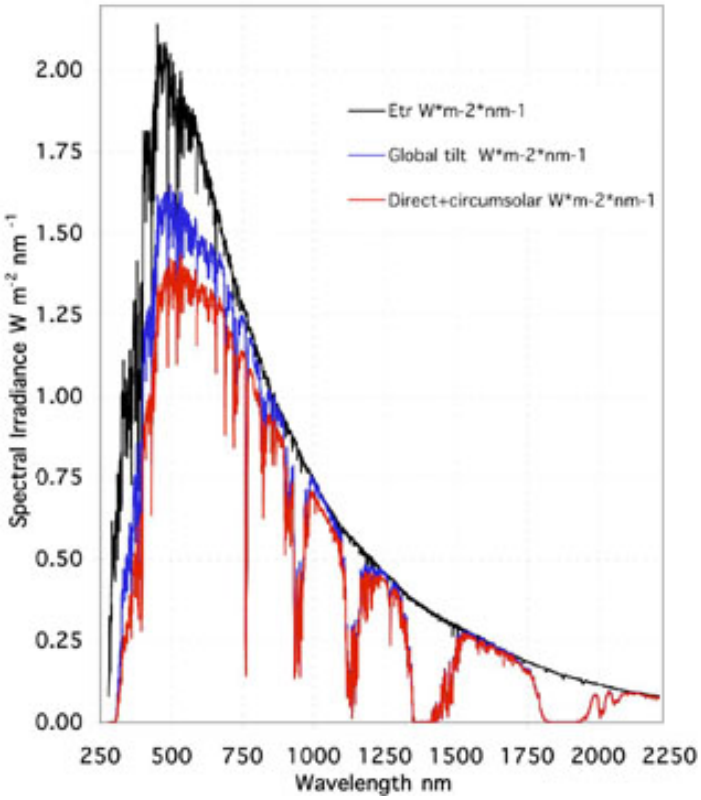

Figure 2.7.1: ASTM G173-03 Standard terrestrial solar spectral irradiance distributions. Black is the reference irradiance of the atmosphere, blue and red are the spectra transmitted by the atmosphere at different angles of incidence. Adapted from [43].

While unlikely to be applicable in this exploratory stage of research, it is useful to be aware that a method of measuring transmission of PV encapsulation materials has been proposed by Powell et al. [44], which accounts specifically for the solar spectrum and the specific effective spectrum of different types of solar cells.

2.7.1. Refraction, reflection & dispersion

When a ray of light crosses the interface between two transparent materials, it changes direction according to Snell's law,

$$\frac{n_2}{n_1} = \frac{\sin\Theta_i}{\sin\Theta_r}, \tag{2.7.2}$$

where n are the respective refractive indices, or the ratio of the velocity of light in vacuum to the velocity in the medium, of the two materials. Often the first medium is air, which has a refractive index of ~ 1, thus this index is omitted. Θ_i and Θ_r are the angles of incidence and refraction related to the normal. When $\Theta_i > \Theta_C$, the critical angle, total reflection takes place. This is the case when Θ_r >90° [5, 6].

For a 0° angle of incidence, the reflection can be calculated [5, 6, 45] in the form of a dimensionless fraction by

$$R = \left[\frac{(n_1 - n_2)}{(n_1 + n_2)}\right]^2, \tag{2.7.3}$$

from which it can be deduced that the fraction of reflected light is 0 when the two refractive indices are the same. Hence to reduce reflection, the refractive index should be as close to that of the media the glass will be in contact with as possible. This will be air on the first side and the solar cell or an intermediate layer on the other side. The details hereof are unclear, and thus not further reviewed.

Refraction finds it's origin in the interaction of light with the electrons of the atoms of the glass, which is controlled by the electron density and polarizability of the ions. The polarizability of a NBO is higher than of a BO, so additions of modifiers to silicate glasses typically lead to an increase of refractive index. For equal molar additions, this will lead to a higher increase in refractive index when moving down the periodic table due to the larger electron clouds of heavier atoms, as illustrated for alkali oxides in figure 2.7.2 [5].

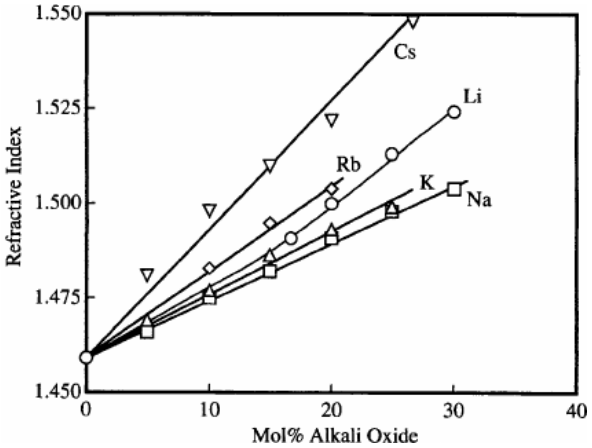

Figure 2.7.2: Refractive index of alkali silicate glasses [5].

Again, the density and as such the fictive temperature of the glass will be of influence [5], but as most silicate glasses have a refractive index roughly in the range of 1.4 to 1.8 [32], these slight variations are not of concern at this point.

Refractive indices for the same material are not constant for different wavelengths and polarisation of light, hence the behaviour can vary over the spectrum. The deviation for different wavelengths is known as dispersion [5, 6, 8]. These variation are minor in the visible region [8], and are mostly important for optical applications, hence further discussion is omitted.

Note that if light passes through different phases with different refractive indices, at every interface refraction and reflection will take place, reducing the overall transmission. As such it is beneficial to prevent any form of formation of separate phases by devitrification, phase separation, precipitation, bubble formation or otherwise.

2.7.2. Absorption

Reflection is relatively constant in the visible spectrum, meaning (dis)colouration is caused mostly by absorption. The overall absorption over a distance z [cm] in a medium can be described by Beer-Lambert's law,

$$I = I_0 \exp(-az), \tag{2.7.4}$$

where a is the absorption coefficient, in cm^{-1}, and $I_{(0)}$ is the (incident) intensity of light [6, 45]. Absorption is wavelength dependant as well.

Small amounts of undesired elements can lead to significant reduction of transmission, hence identifying and describing all possible contaminants given the unpredictable feed stock would be nearly impossible. Alternatively, the principles causing absorption are described in this section, while Bamford [45] can be consulted for more information on specific elements.

The most common cause for absorption in the visible spectrum is the transition of electrons within the unfilled orbits of transition metals and lanthanides, where split levels are formed in the empty band, by interaction of the element with the surrounding negative ions. This process is described by the ligand field theory [5, 6, 45], which is beyond the scope of this review, but is described in each of these references.

The key point is that this interaction is influenced by the oxidation state of the element in question, and thus by the interaction between constituents as well as the overall structure of the glass. Most notorious is iron, which causes the greenish tint visible from the edge of typical float glass, while <0.1 wt% Fe_2O_3 is present, but all transition elements on the same row of the periodic table can cause significant absorption, even in quantities of less than 1 % [6].

Fe was found in significant quantities in the desert sands presented in section 2.3. Iron occurs in silicate glasses in either ferric (Fe^{3+}) or ferrous (Fe^{2+}) state. Each type of ion has their own characteristic absorption spectrum, shown figure 2.7.3 for SLS glass. Interaction with other additional oxides can displace the spectrum, but the general shape will be similar [45]. It can be observed that both states have limited, but non zero, absorption around the peak of the solar spectrum. To achieve 85 % transmission in the complete effective spectrum, the iron content will have to be lowered considerably.

Absorption of IR light originates from bond bending and stretching oscillations in the (silicon) oxide tetrahedra, where the stretching mode determines the IR cut-off because of the higher characteristic frequencies. For most oxide glasses this cut-off lies in the range of 4500 nm to 6500 nm, thus out of the range of interest. The IR absorption can be influenced by varying the amount of NBOs, as well as replacing oxygen by anions of a different mass [6].

On the other end of the visible spectrum, caused by excitation of electrons and thus dependant on the band gap, the UV cut-off can be found. The band gap of SiO_2 is about 8.9 eV, meaning wavelengths under about 139 nm are typically absorbed in pure vitreous silica [6]. This edge is shifted to longer wavelengths when modifiers are added and more NBOs are formed. In practice this inherent edge is usually overshadowed by absorption bands from impurities such as iron, which causes very strong absorption around 200 nm for Fe^{2+}, and around 225 nm for Fe^{3+} [45]. Again, the exact location of the cut-off depends on interaction with other elements present.

Additionally intra-ionic transitions can occur upon absorbing UV radiation. In this case transfer of electrons between two ions takes place, changing the oxidation state of both. This can lead to changing absorption behaviour in the visible spectrum over time. As this typically occurs by exposure to sunlight, the process is known as ‘solarization’ of glass [5, 6].

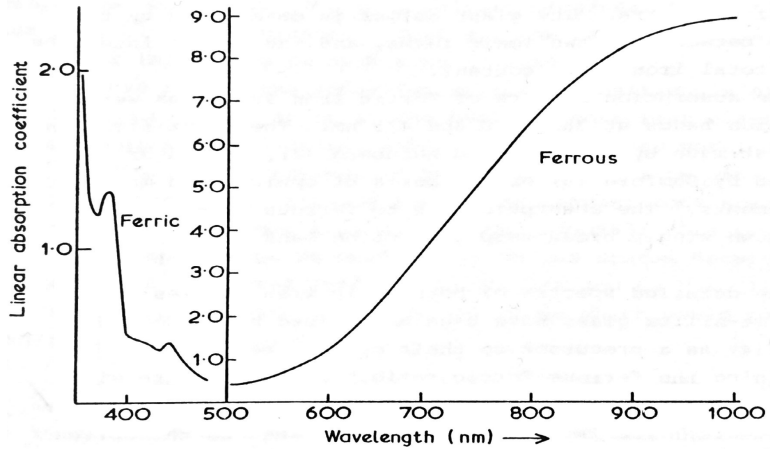

Figure 2.7.3: Linear absorption coefficients for different oxidation states of iron in SLS glass, per wt% Fe_2O_3 [45].

3

Materials, methods & equipment

From the review of literature, it is evident that the first objective (chapter 1), creating a glass from desert sand, is attainable under certain conditions. To confirm this, it needs to be shown that desert sand has, or can be benificiated to a composition that:

- Contains minerals that can be heated to form a melt at an attainable temperature.
- Has an attainable practical melting point to allow for sufficient fining.
- Forms a glass when cooled.

Furthermore it should be verified that the glasses formed have the following properties:

- >85 % transmission of the 350 nm to 1100 nm range of light.
- Youngs modulus >70 GPa.
- Flexural strength >45 MPa.

The second objective, determination of the critical temperatures for creation of such glass, first entails the temperature needed for the melting or dissolving of the original minerals. When a melt is formed, the viscosity reference points of interest are the annealing point, the working point (range), and the practical melting point, as described in section 2.5.

Investigation of desert sands was performed to validate and/or expand on the range of composition presented in section 2.3. The sands obtained to accomplish this are discussed in section 3.1, as are some desert sand components that were acquired for creation of 'synthetic desert sand'. The method of chemical and mineralogical analysis of the raw materials, and equipment used, are described in sections 3.2.1 and 3.2.2 respectively.

In sections 2.3 and 2.4, it was found that temperatures of at least ~1100 °C are needed to melt the first desert sand component, while quartz itself starts melting at 1713 °C. Depending on composition, the practical melting point of a mixture could lie upwards of 1800 °C as was found in section 2.5. No equipment capable of reaching temperatures over 1400 °C was available, hence a susceptor assisted microwave furnace was built to increase the attainable temperature range. The resulting furnace and method of operation is described in section 3.2.4.

During the process of building and testing the furnace, it was found that reactions leading to melt formation were observable by means of pyrometer measurements and controller response. This was used to corroborate the reactions discussed in sections 2.3 and 2.4 by observing melting reactions, and the resulting samples in unmodified desert sand (section 3.2.5) and combinations of components (section 3.2.6).

When a melt is formed, the viscosity of the melt, and thus the critical temperatures, depend on composition. As high temperature viscosity measurements were not possible, the viscosity behaviour of both unmodified desert sand and various mixtures was modelled using the model by Giordano et al. [36]. The steps required to produce the temperature-viscosity curves using the model are described in section 3.2.3.

To show desert sand can be benificiated to a meltable composition, 'hypothetical benificiation' was performed, as described in section 3.2.7. This includes the selection of suitable compositions, and the calculation to create synthetic mixtures to confirm the composition is indeed meltable. The method and equipment employed to create the imitation mixtures and transform them into a glass is found in section 3.2.8.

Where feasible, the resulting glass was characterized to asses if the property requirements were attained. Methodologies and instruments applied to determine optical and mechanical properties, and composition of the glass, are described in section 3.2.9.

3.1. Materials

Different sources were used to obtain a diverse range of desert sand. The origin of the samples as well as the amounts available are listed in table 3.1.1. Sand samples are referred to by code in the remainder of this thesis. The sources are summarized below.

- Small quantities from a plethora of desserts collected by Sterk and van Ryswyck [46] of AtelierNL, a collective of artist that make (glass) products based on natural sand and clay.
- Samples brought in by (friends and family of) employees of Maana Electric.
- Store bought:
  - Several 'natural desert sands', intended for use as a substrate for desert terraria.
  - Silver sand, high silica content.
  - Some of the components described in section 2.3

The sample codes for the samples of AtelierNL are the codes used in their collection, with trailing zeros removed. They can be found on their website `www.aworldofsand.com`. The other samples from desserts are referred to by the first 3 letters of the country of origin. The store bought sands are all sourced from South Africa, according to the packaging or the supplier. The chosen codes refer to the brand (Trixie and Exo-Terra) and when applicable colour (yellow and red). SS is silver sand.

The bottom six rows are slightly different in that these constituents, also found in desert sand, were ordered from a ceramics craft store and are provided finely ground. The codes are a reference to the name of the mineral in question.

Table 3.1.1: Overview of samples, their origin, and available mass.

	Code	Origin/description	Mass
AtelierNL	AE1	Nazwa, United Arabic Emirates	< 15 g
	AE2	Dubai, United Arabic Emirates	< 15 g
	OM1	Ash Sharqiyah, Oman	< 15 g
	KZ1	Altyn Emel, Kazakhstan	< 15 g
	NA1	Sossusvlei, Namibia	< 15 g
	MN2	Ikh Nart, Mogolia	< 15 g
	IR1	Chupanan, Iran	< 15 g
	DZ2	Djanet, Algeria	< 15 g
	IN1	Masooriya, India	< 15 g
	SD1	Al Fashir, Sudan	< 15 g
	SA2	Al Hufuf, Saudi Arabia	< 15 g
	TN2	Hazoua, Tunisia	< 15 g
	JO1	Wadi Rum Village, Jordan	< 15 g
	LY1	Murzuq, Lybia	< 15 g
Maana	MAR	Agadir, Marokko	250 g
	MEX	Baja Califorina Sur, Mexico	4 kg
Store	TRIX	South Africa	5 kg
	EXOY	South Africa	4.5 kg
	EXOR	South Africa	4.5 kg
	SS	Unknown/processed	20 kg
Components	CAL	Calcite	5 kg
	DOL	Dolomite	5 kg
	Q	Quartz	5 kg
	KSP	Potassium Feldspar	5 kg
	NaSP	Sodium Feldspar	5 kg
	GYP	Gypsum	5 kg

3.2. Methods & equiment

3.2.1. Chemical composition

The chemical composition of all samples listed in table 3.1.1 was analysed by means of X-ray fluorescence (XRF). The samples, except the components which were supplied in finely ground form, were ground in a laboratory ball mill for 10 min in portions of ∼5 g. 2.0 g of the (resulting) fine power was mixed with 1.0 g of Fluxana Boreox, an X-ray transparent binder, and pressed into a pellet fitting the holder of the machine.

The XRF measurements were performed by Ruud Hendrikx [47], using a Panalytical Axios Max WD-XRF spectrometer. Data evaluation was undertaken with SuperQ5.0i/Omnian software.

For the pressed powder pellets, the following settings were employed:

- Normalised to: 100 wt%
- Sample type: Pressed powder
- Initial sample weight (g): 2.000
- Weight after pressing (g): 3.000
- Oxygen validation factor: 0.00
- Correction applied for medium: No
- Correction applied for film: No
- Used Compound list: Oxides
- Results database: omnian 4 kW 27 mm

Here the increase in weight is the binding agent.

The results of the desert sand analysis are presented in section 4.1.1, in wt% and converted to mol %. The former provides grounds for comparison to the compositions found in the literature (section 2.3), while the latter provides information on glass formability, as discussed in section 2.2.

Section 4.1.1 contains additional results from a repeated analysis of the same batch of sand. These measurements were performed for Maana Electric and were included to gauge the precision of the method and variations within a batch. From one sample, two measurements were taken from the same milling, a second sampling was analysed twice in separate millings. Both were compared to an analysis of a third separate sampling of the same batch.

3.2.2. Mineralogical composition

The XRF-results for the sands were used to estimate the mineral composition. The chemical composition by weight was converted to molar percentages, by first calculating the average molar weight of the mixture [36], M_A, neglecting trace elements:

$$M_A = \left(\sum \frac{w_i}{M_i} \right)^{-1}, \tag{3.2.1}$$

where M_i[g] is the molar weight of each oxide, as listed in the XRF results, and w_i is the weight fraction of each component. Then the molar fraction x_i of each component was calculated [36];

$$x_i = M_A \frac{w_i}{M_i}. \tag{3.2.2}$$

The amounts of each (semi)metallic element contained in the oxides per 1 mol of mixture, was found from stoichiometry. The assumptions below were then used to assign the elements to the minerals discussed in section 2.3, and calculate the amounts of each mineral.

1. All Na and K is found in the end members of the alkali feldspar series ($KAlSi_3O_8$ and $NaAlSi_3O_8$).
2. The remaining Al is found in anorthite ($CaAl_2Si_2O_8$).
3. All Mg is contained in stoichiometric dolomite ($MgCa(CO_3)_2$).
4. The remaining Ca is in calcite ($CaCO_3$).
5. The Si left is in silica (SiO_2).

Weight fractions of each mineral w_j were then calculated by

$$w_j = \frac{n_j \cdot M_j}{M_A}. \tag{3.2.3}$$

Note that carbon, or CO_2, in the carbonates is not detected by XRF, and this calculation will thus lead to a sum of weight fractions greater than 1. Therefore the result was normalized before conversion to percentages and presentation in section 4.1.2.

Finally it was assumed that the only volatile released when heated, is the CO_2 from carbonates. The loss on ignition (LOI) was thus estimated by calculating the molar amount of CO_2 as follows,

$$n_{CO_2} = 2n_{MgCa(CO_3)_2} + n_{CaCO_3}, \tag{3.2.4}$$

followed by calculating the weight fraction using equation 3.2.3. The result was compared to the measured LOI to gauge accuracy of the estimates.

To further validate this method of estimation, the calculation was repeated for a desert sand sample from Abu Dhabi, of which the chemical and mineralogical composition are known, as Maana Luxembourg commissioned a combined inductively coupled plasma (ICP) and X-ray diffraction (XRD) analysis for this sample. This comparison can be found in section 5.1.

3.2.3. Modelling viscosity curves

When processing batches of either desert sand or synthetic mixtures, knowledge of the relationship between temperature and viscosity is of importance to determine the temperature that is needed to form a homogeneous melt. With the chemical composition analysed, it is possible to estimate this relationship using the model of Giordano et al. [36]. The authors provide a spreadsheet, Matlab program, and on-line implementation. As the composition data is stored in spreadsheets, this version of the program is most practical.

The composition is entered in wt%, after which the program normalizes the composition and converts it to molar percentages in a similar manner to equations 3.2.1 and 3.2.2. The constants for equation 2.5.4 are calculated by the program using the method described in [36].

Most oxides can be entered as they are presented in the results of XRF, except for Fe_2O_3 and H_2O;

As discussed in section 2.5, the model does not differentiate between different oxidation states of iron. The iron content is entered by means of FeO(T), while the results from the XRF are based on Fe_2O_3. This is accounted for by subtracting the relative atomic weight of oxygen from the mass fraction of Fe_2O_3. This will lead to the correct fraction of Fe in the calculation, but introduce a small error in normalisation in the program. This error is negligible compared to uncertainty in the results of the XRF.

Water content cannot be detected by means of XRF, hence it is assumed that 0.02 wt% is present in all glasses. This value is found in the literature for silicate glasses melted under atmospheric conditions [8].

An addition was made to the spreadsheet to automatically input combinations of fractions of available desert sand and components. For plotting, a simple python script was written, that can include isokoms (constant viscosity) and calculate the expected temperature for viscosity reference points if desired. The 0.5 log-units or 5% uncertainty margins, discussed in section 2.5.4, can also be plotted.

3.2.4. Microwave heating

A modified microwave oven was employed as a susceptor assisted microwave furnace, inspired by Leonel [48]. The furnace power is controlled by pulse width modulation of the magnetron, based on temperature readings from a pyrometer. The controller outputs the average power of the last duty cycle and the instantaneous heating rate for each pulse, both of which can be plotted against temperature.

The equipment used is described in the first subsection of this section, followed by specifications and calibration of the pyrometer in the second subsection. The method of operation of the furnace is found last. Additional information on the principles of microwave heating, description of the insulation package and control system, and results of the executed base line measurements are presented in appendix A.

Equipment

The basis of the furnace is a Primo PR200MG microwave oven, fitted with a control system, insulation package, and an Calex PyroUSB PUA2 CF HT pyrometer measuring through a 10 mm hole in the top of the microwave cavity and insulation. Alumina crucibles of approximately 2x2x5 cm, containing the sample, atop a block of SiC grinding disc, functioning as a susceptor, were placed in the centre of the insulation package.

An overview of the basic components of the microwave furnace is presented in figure 3.2.1, a schematic view of the positioning of the pyrometer can be found in figure 3.2.2.

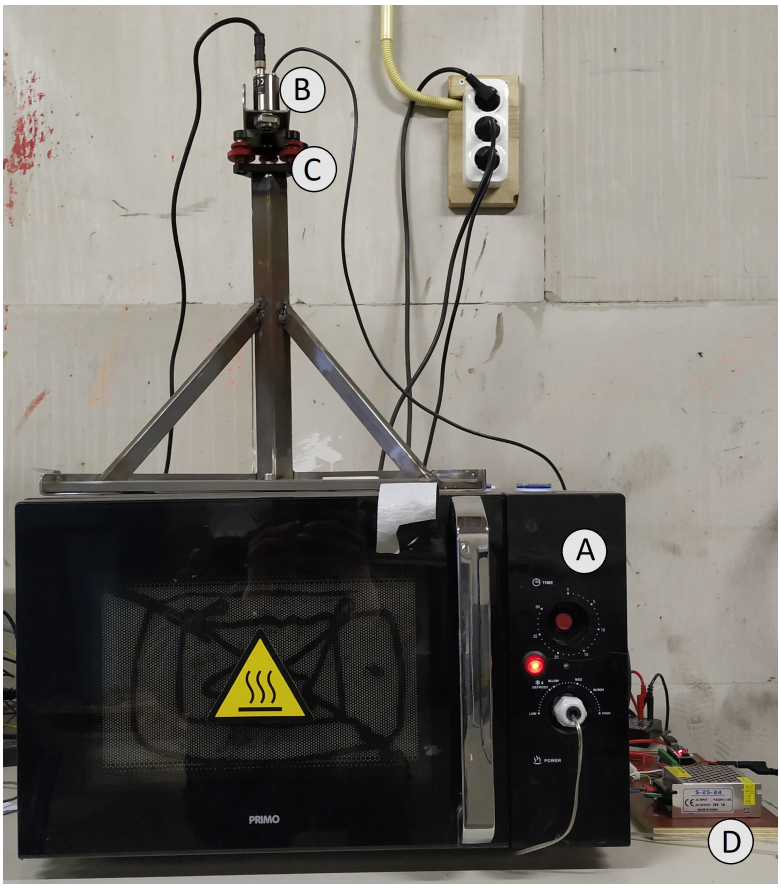

Figure 3.2.1: Overview of microwave set up: (A) Primo PR200MG microwave oven, cable connects relay and control system, (B) Calex PyroUSB PUA2 CF pyrometer, (C) Levelling stage on top of stand, (D) Control board.

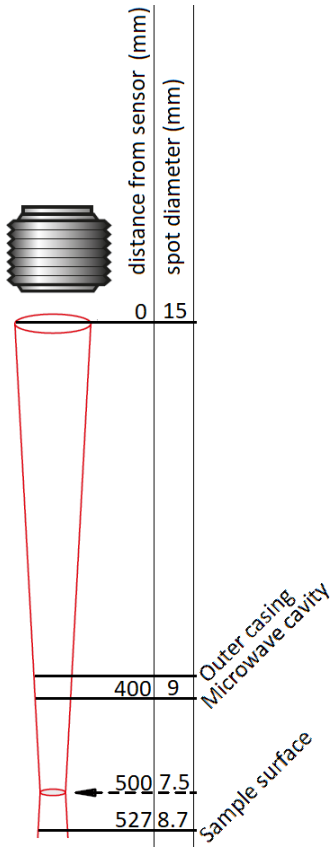

Figure 3.2.2: Optics and placement of the Calex PyroUSB PUA2 CF HT, adapted from [49].

Temperature measurements

The narrow band pyrometer used, measures at a wavelength of 2.2 µm, and can register temperatures from 450 °C to 2000 °C, but was set to a maximum of 1650 °C to increase resolution of the analogue output. The pyrometer and inner isolation box were aligned using a series of small bubble levels and a Calex Laser Sighting Tool.

The accuracy of the pyrometer is listed by the supplier as the greater one of either ± 2 °C or 1% of reading, while the resolution of the communication with the control system is 1.17 °C. The measurement is based on infra-red (IR) emissions, hence the emissivity ε of the sample has to be known measure temperature correctly.

The emissivity of a selection of samples was measured, as described in appendix B. The definition of emissivity and the determination of temperature using pyrometer measurements are also addressed.

All desert sands measured showed an emissivity in the range of 0.58 to 0.67, 0.62 measured most often, while composition and grain size varied widely. Therefore it was assumed that this holds true for the other desert sands as well, and the emissivity was set to 0.62 for the experiments described in section 3.2.5. If this assumption is correct, the maximum relative error in emissivity is 8 %. The maximum error in temperature reading this would lead to is plotted in figure 3.2.3, and is significantly larger than the accuracy of the pyrometer, and thus should be taken as guiding. This reasoning is based on assumption, hence the actual error might exceed the anticipated error, and temperature readings should be interpreted with care.

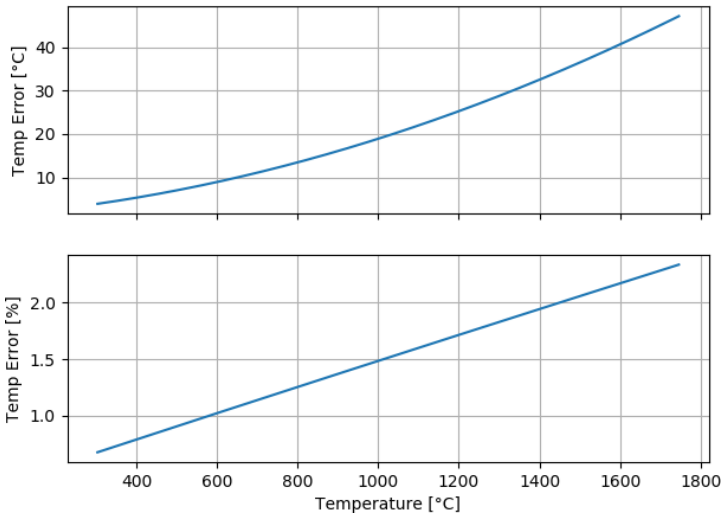

Figure 3.2.3: Deviation of temperature reading from actual temperature (positive or negative) for measurement at 2.2 µm and 8 % relative error in emissivity. Plotted using script by Pothoven [50].

Determination of emissivity of various mixtures of components proved problematic, as variations in the amount of compression of the fine powder, and type of minerals used, caused variations in the order of ∼0.25 in measured emissivity. An underestimation of emissivity would lead to a reading of temperature that is too high. Consequently there is a risk that the set temperature would not be reached in reality, therefore it was chosen to use a relatively high value of 0.67 for synthetic mixtures.

In addition to questionable certainty in the emissivity used, the quantity is also dependant on temperature, and likely to change when melting occurs. Hence extra care is merited in interpretation of temperature measurements.

Operation

During building and testing of the system, it was found that 1640 °C was an attainable temperature, which was chosen as the maximum temperature for all measurements using this system. At higher temperatures, heat loss through the insulation could no longer be compensated by the relatively low power magnetron and heating rates become impractically low.

Response of the system was assessed by recording multiple baseline measurements, presented in appendix A.4. For reference the recording of sample Q is shown in figure 3.2.4. As no melting effects or reactions are expected for quartz under 1640 °C, deviations in shape from this curve in other measurements are an indication that phase changes, reactions, and/or changes in emissivity caused by additional components have occurred. This makes the complete system function as a ‘qualitative DSC’.

In all cases the sample was pre-heated to a temperature within the range of the pyrometer (>450 °C) and appropriate for the measurement in question, before the controlled heating and measurement of heating rate and power commenced. This temperature, referred to as the starting temperature in the remainder of this thesis, was held for 30 min and then increased at a heating rate of 5 °C min^{-1} to the final temperature.

During the baseline measurements, it was found that in some cases the final temperature could not be reached at this rate, leading to a lack of data points at higher temperatures. Therefore a function was implemented to halve the heating rate if power exceeded 90 % or 95 %. This is mentioned where applicable.

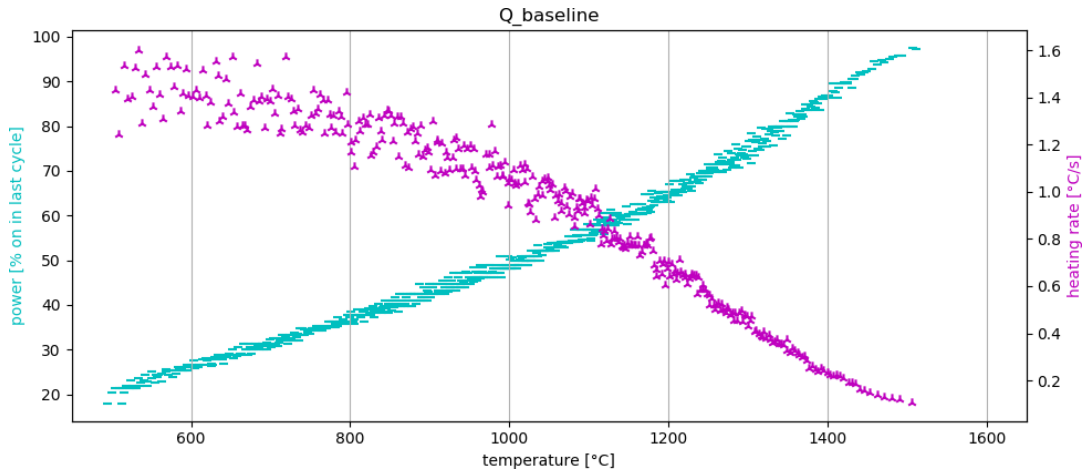

Figure 3.2.4: Power and instantaneous heating rate plot of sample Q heated at 5 °C min^{-1}, emissivity set at $\varepsilon = 0.64$.

3.2.5. Melting of desert sand

Following the method described in section 3.2.3, the viscosity curves for the samples of desert sand were plotted and the expected practical melting point, working point and annealing point were calculated.

The limited availability of most of the samples made it unfeasible to try and find suitable composition changes to all of them, as only one attempt at melting was possible for each. Therefore all desert sand samples were heated without modification. While it was unlikely this would lead to a glass fulfilling the requirements listed in chapter 1, it did yield valuable information on (melting) behaviour of sand from different deserts and a wide variety of compositions.

As solid state reactions, excluding the first decomposition step of dolomite, were only expected at temperatures around 900 °C and over, 800 °C was chosen as the starting temperature, while preheating to this temperature was done at 70 % of power to allow time for heat to transfer from the susceptor avoiding thermal shock to the crucible. The heating rate was halved when power exceeded 90 %.

After thermal soaking for 1 h, the result was briefly removed from the insulation and left to cool inside the inner insulation box to limit thermal cracking.

After the full series and observation of the results, the experiment was repeated for sample MEX after prior heating to 1100 °C and stopped at the moment of sudden expansion (see sections 4.3.3 and 5.3. Furthermore sample IR1 was reheated to 1640 °C and soaked for an additional 2 h.

The loss on ignition (LOI) was recorded to be compared to the calculated values and photographs were taken of the samples. Closer inspection by optical microscopy was performed using a Keyence VHX-7000 Digital Microscope.

3.2.6. Formation of primary melt phases

To further confirm the reactions between components found or theorized in sections 2.3 and 2.4, a series of binary mixtures of components was heated. The composition was chosen by varying the ratio and calculating the practical melting temperature following the method described in section 3.2.3, to find a composition with a practical melting point within range of the microwave furnace.

The mixtures were heated following a firing cycle similar to that for the desert sand: heated to 1000 °C at 70 % of power, held for 30 min, and heated at 5 °C min^{-1} to 1640 °C. The threshold value for halving the heating rate was raised to 95 % of full power.

3.2.7. Hypothetical beneficiation & synthetic recipes

To show a meltable mixture can be produced from desert sand by benificiation, and later produce characterizable samples of imitation glass, a series of possible benificiation operations was explored. Using the estimates of mineral composition, the 'beneficiated' composition was calculated by multiplying the weight fractions of the minerals in question by the intended increase;

$$w_j^\star = w_j^{(b)} \cdot B, \tag{3.2.5}$$

where $w_j^{(b)}$ is the original weight fraction of the benificiated compound(s), and $w_j^\star$ is the 'benificiated' weight fraction. B is the factor of beneficiation, e.g. 1.5 for a 50 % increase. After this, the total was brought back to 1 by decreasing the remaining fractions, while keeping the ratio constant between them as follows

$$w_j^\circ = \frac{w_j}{\sum w_j}(1 - \sum w_j^\star). \tag{3.2.6}$$

Here w_j° is the new fraction of each of the remaining elements, while w_j is the original.

From the new mineralogical composition the chemical composition was calculated by reversing the procedure described in section 3.2.2. The calculated chemical composition was in turn used to plot the predicted viscosity curve and calculate the practical melting point following the steps described in section 3.2.3.

The team working on benificiation suggested a 5 wt% increase of feldspars, which was calculated and plotted, but did not yield significant lowering of calculated melting temperatures. Therefore some more rigorous operations were selected:

- 50 % increase of feldspar content.
- 50 % increase of carbonate content.
- 50 % increase of both feldspar and carbonate content.
- Removal of all quartz.

The resulting compositions and predicted viscosity curves were assessed for acceptable practical melting temperature ($\lesssim$1650 °C). Furthermore the glass formability was considered based on the mole percentage of silica (figure 2.2.5). In the case of removal of all quartz, samples containing more than 50 wt% quartz were disregarded, as these would cause an enormous waste stream under this operation.

Suitable candidates were selected, as discussed in section 5.5. As no anorthite or other plagioclase feldspar was acquired, exact imitation by composition of minerals was not an available option. Instead an attempt was made to approach the chemical composition by varying the fractions of components in a mixture and using the measured composition of each component to calculate the average composition of the mixture.

Starting with only quartz, material Q, first the amounts of K_2O and Na_2O were approximated by increasing the fractions of the available feldspars, materials KSP and NaSP, respectively. In order, as material KSP contains significant amounts of Na as well (see sections 4.2 and 5.2). Then fractions of the carbonates acquired, materials DOL and CAL, were added to approximate the concentration of MgO and CaO.

The fraction of Al_2O_3 is more problematic, as the Al to modifier ratio of the plagioclase series is different from the available components. An attempt to negate this problem was made by keeping the sum of fractions of SiO_2 and Al_2O_3 similar. This is reasonable as the addition of feldspars will always lead to peralkaline composition, and the aluminium will act as a network former.

During this process, the calculated synthetic composition was continuously compared to the 'benificated' composition to be imitated, and tweaked to match. The resulting viscosity curves were plotted and compared to the samples they were meant to imitate.

3.2.8. Preparation, melting & shaping of synthetic batches

The expected loss on ignition (LOI) of the selected mixtures was estimated in a similar manner to section 3.2.2, to be able to add appropriate amounts of each component. The mixtures were prepared in batches of 100 g or 200 g, and thoroughly mixed in a purpose built tumbling mixer.

Portions of roughly 15 g to 20 g were given the same treatment as the unmodified sand to compare heating curves. The small volume and resulting temperature drop upon removal from the insulation package, resulted in problems casting the glass. Hence the samples produce in this manner where unsuitable for optical and mechanical measurements. As a solution, multiple ∼100 g portions were melted in a 8.5 kW thyristor controlled furnace built by Maana Electric. The furnace utilises six $MoSi_2$ heating elements and has a maximum operating temperature of at least 1750 °C. Temperature readings were provided by a B-type thermocouple.

A heating rate of 10 °C min^{-1} was approximated, but as there was no control system built for this furnace, power and temperature control was performed manually, causing exact rates to vary. Crucibles were removed from the furnace at a temperature ∼50 °C to 100 °C over the calculated practical melting point of each mixture, and cast onto graphite or steel.

Other casting methods were attempted, but proved unsuccessful. An overview of these efforts can be found in appendix D.

After casting the microwaved samples were placed back into the insulation box with the hot susceptor, to be gradually cooled. The bulk samples were placed in a 9 kW Westeneng industrial furnace. This furnace was preheated to 700 °C, close to the calculated annealing temperature of all imitation mixtures. As the annealing temperature was not determined precisely, samples were soaked for 1 h. After annealing the samples were cooled to room temperature over night.

3.2.9. Characterisation of imitation glass

To asses if the objectives regarding optical and mechanical properties had been reached, the resulting samples were characterized. In addition to transmission measurements and analysis of the fracture surfaces of broken samples, the chemical composition of the glass was determined to verify if the intended composition was obtained in the samples, providing grounds for discussion of the resulting properties.

Optical analysis

Transmission and reflection spectra of the as cast samples that were of appropriate size were analysed using a UV-VIS-IR spectrometer fitted with an integration sphere. As the surface quality differs from side to side, measurements were taken from both sides of each sample.

The measurements were performed using a Perkin Elmer Lambda 1050+ UV/VIS/NIR spectrometer equipped with a 150 mm InGaAs integration sphere. The spectra were recorded using UV WinLab software. Processing and plotting was done using a Python script.

The absorption was calculated from the measured reflection and transmission using equation 2.7.1. The calculated absorption is used to calculate the absorption coefficient for each data point by means of equation 2.7.4, where I_0 was taken as the fraction of incident light that was not reflected.

Using the absorption coefficient, the transmission spectrum for all samples for 3 mm thick glass was plotted for comparison. For calculation of the transmission, it was assumed that the reflection is the same as for the original samples.

Mechanical analysis

As no samples suitable for a correct 3- or 4-point bending tests were produced, it was decided to break all samples of sufficient size in a 3-point set-up, and preform a mirror analysis if possible. The samples were broken over a 20 mm span at cross head speed of 0.5 mm min^{-1}, if possible multiple times.

The machine used is a Zwick/Roell Z10 universal testing machine, equipped with testXpert III testing software. Fracture surfaces were examined using a Keyence VHX-7000 Digital Microscope.

Chemical analysis

The XRF analysis of the produced glass was again performed by Ruud Hendrikx [47], using a Panalytical Axios Max WD-XRF spectrometer. Data evaluation was undertaken with SuperQ5.0i/Omnian software.

The settings were identical to those reported in section 3.2.1, except the sample type is solid and weight is not reported:

- Normalised to: 100 wt%
- Sample type: Solid
- Oxygen validation factor: 0.00
- Correction applied for medium: No
- Correction applied for film: No
- Used Compound list: Oxides
- Results database: omnian 4 kW 27 mm

4

Results

For reference, the conditions for reaching the objectives found in chapter 1, listed at the start of chapter 3, are repeated here;
It needs to be shown that desert sand has, or can be benificiated to a composition that:

- Contains minerals that can be heated to form a melt at an attainable temperature.
- Has an attainable practical melting point to allow for sufficient fining.
- Forms a glass when cooled.

The results of the chemical analysis and mineral estimates presented in section 4.1 provide a starting point for assessment of all conditions listed, while the chemical analysis of the components in section 4.2 will be used to asses the suitability of the store bought material as a substitute for desert sand components, to be used for synthetic batches.

Formation of a melt from raw materials is discussed in chapter 5, based on the results of melting unmodified desert sand (section 4.3) and combinations of components (section 4.4).

The resulting melt properties, most importantly the practical melting point, are assessed for unmodified sands as well, both by modelling of the temperature-viscosity curve and melting experiments, found in section 4.3. The lowering of the practical melting temperature by benificiation will be explored using the results presented in section 4.5, and confirmed by the modelled viscosity curves and melting of synthetic ‘benificiated’ mixtures, presented in section 4.6.

Finally, the properties of the synthetic glass produced are surveyed based on the results of chemical analysis, visual inspection, and optical and mechanical analysis in section 4.7.

4.1. Analysis of desert sand

This section contains X-ray fluorescence (XRF) results and estimates of mineralogical composition of the sand samples before any processing.

A series of micrographs of the original sand was taken, this yielded no quantitative information, but might provide a way to relate appearance to (mineral) composition upon further investigation, hence the images are included in appendix C.1 for future reference.

4.1.1. Chemical composition

Table 4.1.1 is included to provide a frame of reference, and gauge consistency of XRF measurements on sand, an overview of the relevant deviations in this table is given in table 4.1.2.

Note the overall difference between samplings can be as high as 84 % of the mean value, while the differences for a second measurement on the same milling shows smaller deviations. The trace elements detected vary between all measurements. Discussion of this subject can be found in section 5.1.1, where the choice of presenting remaining composition data with one decimal is also explained.

The results of the XRF analysis of desert sand are presented in table 4.1.3, while table 4.1.4 contains the same data, converted to mol %, using the method described in section 3.2.1.

Table 4.1.1: Comparison of XRF results of different samplings from the same batch of sand. 1) Different sampling, 2) Two different millings of the same sampling, 3) Same milling of same sampling, different tablets.

Sampling	SiO_2	Fe_2O_3	Al_2O_3	TiO_2	Na_2O	K_2O	MgO	CaO	Trace-elements
1	92.90	0.99	3.89	0.06	0.54	1.24	0.15	0.12	Cr_2O_3, P_2O_5, Cl, BaO, SO_3, MnO, NiO, ZrO_2, CuO, Rb_2O, SrO, PbO.
2	94.33	0.98	3.01	0.06	0.28	0.97	0.12	0.09	Cr_2O_3, P_2O_5, SO_3, Cl, MnO, ZrO_2, NiO, Rb_2O, CuO, SrO, PbO.
2	94.71	0.94	2.78	0.06	0.25	0.92	0.14	0.06	Cr_2O_3, P_2O_5, Cl, SO_3, MnO, ZrO_2, Rb_2O, SrO.
3	93.84	0.87	3.42	0.07	0.36	1.05	0.15	0.09	Cr_2O_3, P_2O_5, SO_3, Cl, NiO, BaO, MnO, ZrO_2, Rb_2O, SrO.
3	93.84	0.91	3.38	0.06	0.36	1.06	0.17	0.08	Cr_2O_3, SO_3, P_2O_5, Cl, BaO, ZrO_2, Rb_2O, SrO, ZnO.

Table 4.1.2: Overview of absolute and relative deviations in table 4.1.1.

		SiO_2	Fe_2O_3	Al_2O_3	TiO_2	Na_2O	K_2O	MgO	CaO
Maximum	wt%	1.81	0.11	1.12	0.01	0.29	0.32	0.05	0.06
difference	% of mean	1.9	12.0	34.3	17.9	84.9	31.4	31.9	69.0
Average deviation	wt%	0.48	0.04	0.32	0.00	0.07	0.08	0.01	0.02
from mean	% of mean	0.5	3.9	9.9	6.0	21.5	8.0	8.2	17.6
Seperate	wt%	0.38	0.05	0.23	0.00	0.03	0.05	0.02	0.03
millings	% of mean	0.4	4.9	7.9	8.1	12.7	5.3	15.4	41.6
Same	wt%	0.00	0.04	0.05	0.01	0.00	0.01	0.02	0.01
milling	% of mean	0.0	4.6	1.4	18.2	1.1	0.8	11.5	13.3

Table 4.1.3: Overview of XRF-results of desert sand, composition in wt%. Sorted by decreasing silica content.

Sample	SiO_2	Fe_2O_3	Al_2O_3	TiO_2	Na_2O	K_2O	MgO	CaO	Trace-elements
SS	98.0	0.6	0.9	0.1	0.1	0.2	0.0	0.0	Cr_2O_3, Cl, SO_3, P_2O_5, NiO, CuO, ZrO_2, SrO.
DZ2	97.7	0.8	1.1	0.0	0.0	0.0	0.9	0.1	Cr_2O_3, P_2O_5, Cl, SO_3, ZrO_2, SrO.
EXOY	97.5	0.7	1.0	0.3	0.1	0.1	0.1	0.1	ZrO_2, Cr_2O_3, CuO, P_2O_5, Cl, SO_3, WO_3, SrO, Y_2O_3.
JO1	97.3	1.1	1.0	0.1	0.0	0.0	0.1	0.1	Cr_2O_3, P_2O_5, Cl, ZrO_2, SO_3, CuO, SrO, MnO.
LY1	95.9	1.5	1.7	0.1	0.0	0.1	0.1	0.3	SO_3, Cr_2O_3, Cl, ZrO_2, NiO, PbO, SrO.
EXOR	95.5	0.9	2.7	0.2	0.2	0.3	0.1	0.1	Cr_2O_3, P_2O_5, Cl, ZrO_2, SO_3, Rb_2O.
TN2	94.4	0.7	3.2	0.1	0.2	0.7	0.2	0.2	Cr_2O_3, ZrO_2, P_2O_5, Cl, BaO,SO_3, SrO, CuO, NiO, Rb_2O.
TRIX	94.1	1.1	3.5	0.3	0.3	0.4	0.2	0.1	Cr_2O_3, ZrO_2, Cl, Pr_2O_3, SO_3, SrO, Rb_2O, MnO.
SD1	93.0	1.3	3.5	0.2	0.4	0.3	0.3	0.8	Cr_2O_3, SO_3, P_2O_5, Cl, ZrO_2, SrO, ZnO, PbO, Rb_2O, MnO.
SA2	90.6	0.8	3.7	0.1	0.4	1.4	0.7	2.0	SO_3, Cr_2O_3, Cl, P_2O_5, BaO, SrO, Rb_2O, ZnO, MnO.
NA1	86.4	1.7	7.0	0.2	1.4	1.5	0.7	0.9	P_2O_5, Cr_2O_3, BaO, Cl, NiO, SrO, ZrO_2, SO_3, Rb_2O, ZnO, MnO.
MN2	79.2	0.9	12.2	0.1	2.8	3.8	0.3	0.6	P_2O_5, Cr_2O_3, BaO, Rb_2O, SrO, SO_3, ZrO_2, Cl, PbO, ZnO, MnO.
IN1	74.2	2.7	11.8	0.4	2.7	1.6	1.4	4.8	Cr_2O_3, SrO, ZrO_2, BaO, SO_3, CuO, Cl, Rb_2O, ZnO, PbO, Nb_2O_5, MnO.
KZ1	73.1	2.0	13.4	0.3	3.8	2.3	1.2	3.7	P_2O_5, Cr_2O_3, SrO, BaO, Cl, SO_3, ZrO_2, Rb_2O, CuO, ZnO, PbO, MnO.
MEX	68.5	4.3	15.9	0.9	3.1	1.6	1.3	3.8	P_2O_5 (0.47%), SrO, Cr_2O_3, ZrO_2, Cl, BaO, V_2O_5, SO_3, ZnO, NiO, MnO.
OM1	66.5	1.8	3.5	0.1	0.3	0.9	4.3	22.0	P_2O_5, Cr_2O_3,SO_3, Cl, SrO, NiO, BaO, ZnO, Rb_2O, MnO.
AE1	65.1	1.7	4.2	0.1	0.0	1.2	4.1	22.6	SO_3, Cr_2O_3, P_2O_5, SrO, NiO, Cl, ZnO, Rb_2O,MnO.
IR1	60.9	3.0	10.3	0.5	2.7	1.6	2.6	17.9	P_2O_5, SO_3, Cr_2O_3, SrO, BaO, Cl, NiO, PbO, ZnO, CuO, Rb_2O, MnO.
MAR	41.8	4.1	7.4	0.7	1.9	1.1	3.1	38.8	P_2O_5 (0,48%), SO_3, SrO, Cl, ZrO_2, BaO, Cr_2O_3, ZnO, PbO, Rb_2O, MnO.
AE2	2.1	0.2	0.4	0.1	0.6	0.1	1.7	92.6	SrO (1.7%),SO_3 (0.38%), P_2O_5, Cl, Cr_2O_3.

Table 4.1.4: Significant fractions of oxides from XRF results in table 4.1.3 converted to mol %. Sorted by decreasing silica content.

Sample	SiO_2	Fe_2O_3	Al_2O_3	TiO_2	Na_2O	K_2O	MgO	CaO
SS	98.9	0.2	0.5	0.0	0.1	0.1	0.0	0.0
EXOY	98.6	0.2	0.6	0.2	0.1	0.0	0.1	0.1
JO1	98.5	0.4	0.6	0.0	0.0	0.0	0.2	0.1
LY1	97.8	0.6	1.0	0.1	0.0	0.1	0.2	0.3
DZ2	97.6	0.3	0.6	0.0	0.0	0.0	1.3	0.1
EXOR	97.3	0.3	1.6	0.1	0.2	0.2	0.2	0.1
TN2	96.4	0.3	1.9	0.1	0.2	0.5	0.4	0.2
TRIX	96.4	0.4	2.1	0.2	0.3	0.2	0.2	0.1
SD1	95.4	0.5	2.1	0.2	0.4	0.2	0.4	0.8
SA2	92.7	0.3	2.2	0.1	0.4	0.9	1.1	2.2
NA1	90.3	0.6	4.3	0.1	1.4	1.0	1.1	1.1
MN2	85.2	0.4	7.7	0.1	2.9	2.6	0.4	0.6
IN1	79.4	1.1	7.4	0.3	2.8	1.1	2.2	5.5
KZ1	78.8	0.8	8.5	0.2	3.9	1.6	1.9	4.2
MEX	76.0	1.8	10.4	0.7	3.3	1.1	2.1	4.5
OM1	66.3	0.7	2.1	0.1	0.3	0.6	6.4	23.5
AE1	65.4	0.6	2.5	0.1	0.0	0.8	6.1	24.4
IR1	63.9	1.2	6.4	0.4	2.7	1.1	4.1	20.2
MAR	43.1	1.6	4.5	0.5	1.9	0.7	4.8	42.8
AE2	2.0	0.1	0.2	0.0	0.6	0.0	2.4	94.6

4.1.2. Estimates of mineralogical composition

Estimates of minerals mineral composition, following the assumptions described in section 3.2.2, are presented in table 4.1.5. The negative values for the calcite content and estimates of loss on ignition (LOI) are the result of inaccuracies in the method used, as is discussed in section 5.1.1.

For reference the measured LOI, determined during heating of the sand (section 3.2.5), is included. The missing values are caused by either breaking or overflowing of the crucible during the measurement.

It can be observed that LOI of the high silica sands is typically underestimated, while an overestimate is made for the sands containing large amounts of carbonates.

Table 4.1.5: Estimates of mineral composition and LOI (calculated and measured) of desert sand samples. In wt%, sorted by decreasing estimated quartz content.

Sample	$KAlSi_3O_8$	$NaAlSi_3O_8$	$CaAl_2Si_2O_8$	$MgCa(CO_3)_2$	$CaCO_3$	SiO_2	LOI (c)	LOI (m)
JO1	0.3	0.2	2.6	0.6	-1.1	97.4	-0.2	1.3
EXOY	0.4	0.8	2.1	0.3	-0.8	97.3	-0.2	-
DZ2	0.2	0.2	2.6	3.7	-3.0	96.2	0.6	0.0
LY1	0.6	0.3	4.3	0.5	-1.3	95.8	-0.3	0.9
EXOR	1.5	1.4	6.0	0.5	-2.4	92.9	-0.8	-
TRIX	2.2	2.7	7.1	0.7	-2.8	90.1	-0.9	-
TN2	4.4	2.0	5.5	1.0	-2.2	89.3	-0.4	0.0
SD1	2.1	3.2	6.9	1.2	-1.9	88.4	-0.2	2.2
SA2	8.2	3.6	4.1	3.1	0.2	80.7	1.7	1.6
NA1	9.3	12.0	8.5	2.9	-3.1	70.3	0.2	0.0
OM1	4.4	2.5	4.7	15.4	22.7	50.2	18.0	11.6
AE1	6.1	0.0	6.8	14.7	23.5	49.0	18.0	14.3
IN1	9.6	23.1	15.6	5.9	-0.4	46.3	2.9	-
MN2	22.9	24.0	9.7	1.1	-3.2	45.3	-0.8	0.8
KZ1	13.9	32.0	12.8	5.1	-1.0	37.1	2.2	1.8
MEX	9.8	27.8	26.4	5.6	-5.6	36.0	0.5	-
IR1	8.7	20.5	10.2	9.9	19.5	31.1	13.8	11.7
MAR	5.0	12.8	6.9	10.4	46.6	18.4	25.9	21.0

4.2. Analysis of components

Table 4.2.1 contains the results of the XRF analysis of the store bought components. The compositions shown in table 4.2.2 were calculated based on stoichiometry, to asses if the components match the specification by the supplier, and suitability for synthetic mixtures.

Table 4.2.1: Chemical composition of store bought components, determined by XRF, in wt%.

Sample	SiO_2	Fe_2O_3	Al_2O_3	TiO_2	Na_2O	K_2O	MgO	CaO	Trace-elements
CAL	4.4	0.3	0.7	0.0	0.1	0.1	0.4	93.5	SrO, SO_3, Cl, ZnO, MnO.
DOL	0.1	0.1	0.0	0.0	0.2	0.0	44.5	55.1	Cl, SO_3, SrO, P_2O_5.
Q	99.7	0.0	0.2	0.0	0.0	0.0	0.0	0.1	Cl, ZrO_2.
KSP	65.0	0.1	20.2	0.1	4.5	8.9	0.1	0.6	P_2O_5, SrO, BaO, Rb_2O, Cl, SO_3, PbO.
NaSP	66.7	0.1	19.5	0.2	12.5	0.3	0.2	0.4	P_2O_5, Cl, ZrO_2, PbO, SO_3, SrO.
GYP	0.1	0.0	0.1	0.0	0.0	0.0	0.9	47.4	SO_3 (50.5%), SrO, Cl.

Table 4.2.2: Calculated weight percentages of stochiometric components, as would be detected by XRF.

	SiO_2	Al_2O_3	Na_2O	K_2O	MgO	CaO
CaO	0.0	0.0	0.0	0.0	0.0	100.0
$MgCaO_2$	0.0	0.0	0.0	0.0	41.8	58.2
SiO_2	100.0	0.0	0.0	0.0	0.0	0.0
$KAlSi_3O_8$	64.8	18.3	0.0	16.9	0.0	0.0
$NaAlSi_3O_8$	68.7	19.4	11.8	0.0	0.0	0.0
$CaAl_2Si_2O_8$	43.2	36.6	0.0	0.0	0.0	20.2

4.3. Melting of desert sand

Modelling and melting of unmodified desert sand has yielded information on both melting and melt behaviour. In addition the accuracy of the model can be assessed by visual inspection of the samples after heating. Results of modelling, as described in section 3.2.3, of viscosity behaviour of desert sand, are presented in section 4.3.1.

Based on the composition results (section 4.1), the desert sands were grouped in three classes (see section 5.1):

- >90 wt% SiO_2 (including silica contained in feldspars)
- >25 wt% total feldspars
- >25 wt% carbonates

The results of the melting, both in heating rate and power curve and appearance of the sample, are quite similar per type of desert sand. Hence a selection is presented in sections 4.3.2 to 4.3.4, sorted by the three groups. A full overview of all recorded heating rate and power curves, photographs and low magnification micrographs can be found in appendix C.

For this series of measurements, the heating rate was halved at 90 % power, causing the sudden, but relatively small step that can be observed in most power and heating rate plots presented in sections 4.3.2 to 4.3.4. These sections, and the figures within them, generally follow the line of decreasing calculated practical melting point.

4.3.1. Modelling of viscosity

Figure 4.3.1 displays temperature viscosity relations as predicted by the model by Giordano et al. [36], for the compositions within range of the model. Dashed horizontal lines signify from top to bottom, the annealing point, softening point, working point and practical melting point. Uncertainty margins of ± 0.5 log-units or 5 %, are omitted for readability.

The expected temperatures at which the isokoms of interest are reached, are summarized in table 4.3.1. This table includes the samples out of the range of the model to illustrate the significantly higher processing temperatures for high silica sands.

Table 4.3.1: Predicted annealing, working and melting temperatures for desert sand samples sorted by practical melting temperature. Compositions above the dividing line have a SiO_2 concentration >90 wt%, hence are out of range of the model.

Sample	T_a[°C] ($\eta = 10^{12}$ Pa s)	T_w[°C] ($\eta = 10^{3}$ Pa s)	T_m[°C] ($\eta = 10^{1}$ Pa s)
EXOY	945	2063	2803
JO1	939	2046	2779
LY1	931	2020	2742
DZ2	926	2013	2734
EXOR	927	2011	2729
TN2	913	1979	2686
TRIX	915	1977	2681
SD1	905	1948	2639
SA2	875	1879	2544
NA1	832	1773	2397
MN2	771	1641	2218
IN1	760	1519	2022
KZ1	738	1496	1998
MEX	744	1439	1899
OM1	753	1369	1776
AE1	755	1359	1760
IR1	713	1268	1636
MAR	672	971	1169

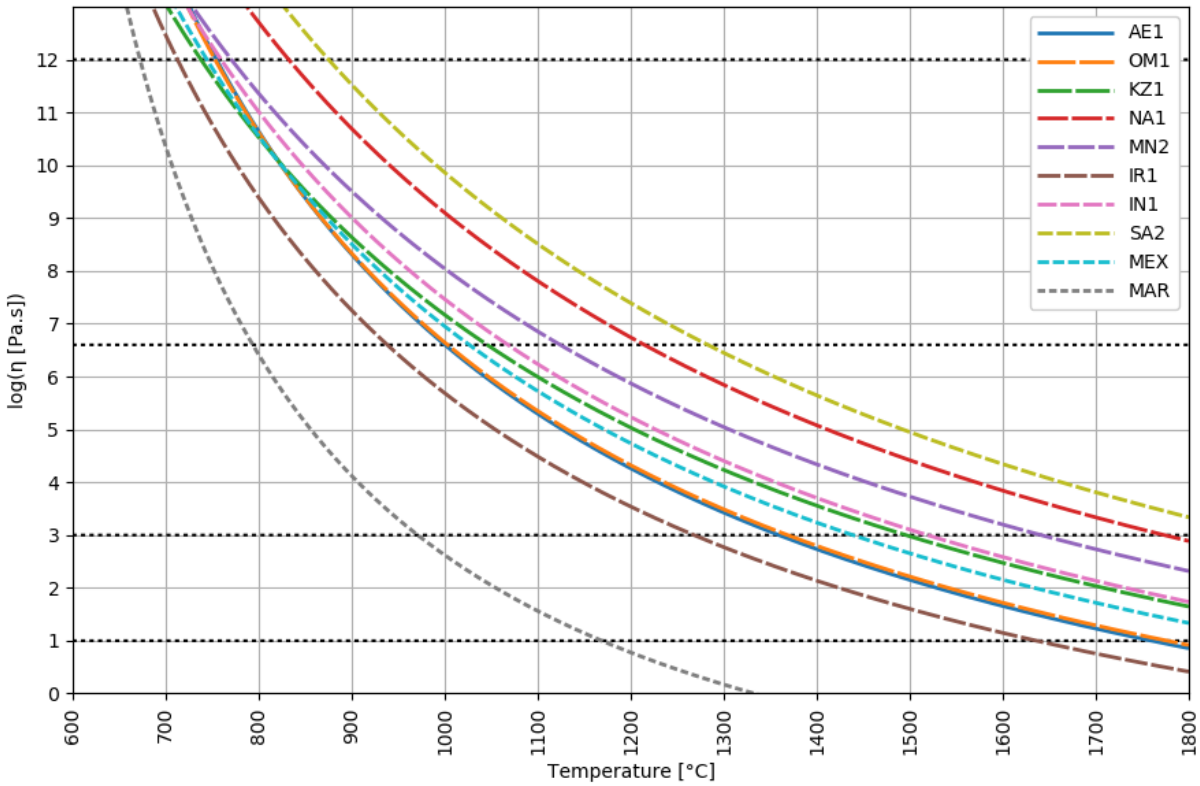

Figure 4.3.1: Viscosity curve predictions of samples within range of the model [36]. Uncertainty margins are omitted for readability, SA2 falls just out of range but is presented for reference.

4.3.2. High silica sand

From the predicted practical melting point and the melting point of quartz, it is unlikely heating of the high silica sands to 1640 °C will yield a glass, but observation of the process and result provides information on the interaction between quartz and the other smaller mineral fractions, and validity of the model used.

The sands containing mostly silica show a heating rate and power curve very similar to the baseline measurement of sample Q (figure 3.2.4), as illustrated by the curve from heating sample JO1 in figure 4.3.2. This results in slightly sintered sand as displayed in figures 4.3.4a and 4.3.5a, where part of the batch was ground.

Slightly higher (estimated) feldspar fractions can cause very locally molten features to occur, in addition to a glazed appearance of the remaining grains, as is the case for sample EXOR shown in figure 4.3.5b. The overall appearance remains sand-like, as seen in 4.3.4b.

Sample SA2 has a silica content of ∼91 wt%, but contains only 80.7 wt% quartz. The remaining silica is found in the estimated feldspar content of close to ∼15 wt%. This feldspar fraction leads to a slight effect during heating, seen in figure 4.3.3; a slight inflection in the power between 1200 °C and 1300 °C. The result appears a solid block to the naked eye (figure 4.3.4c), but on closer inspection the original grains are clearly visible (figure 4.3.5c).

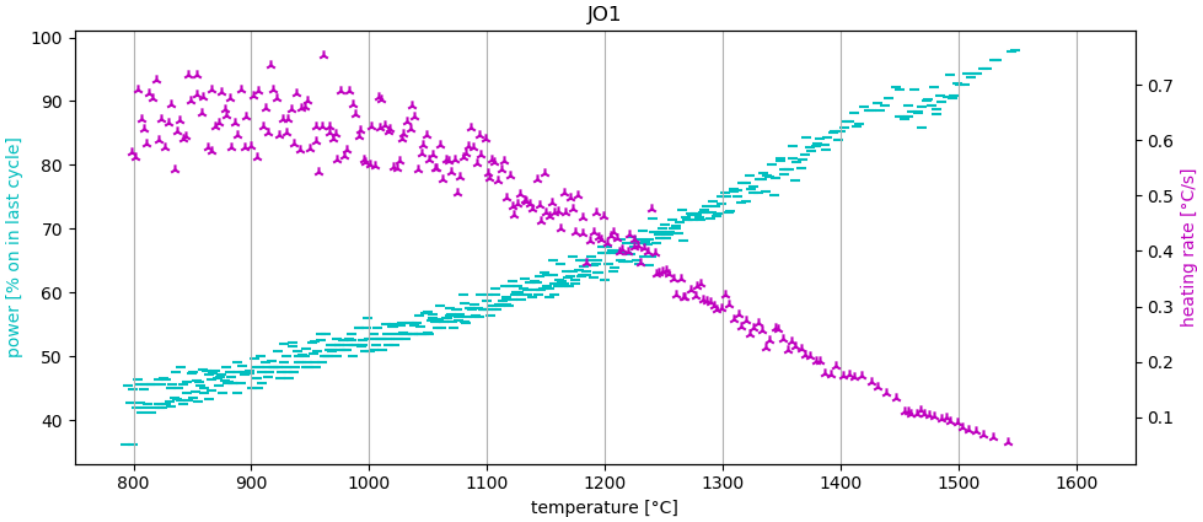

Figure 4.3.2: Power and heating rate plot of sample JO1.

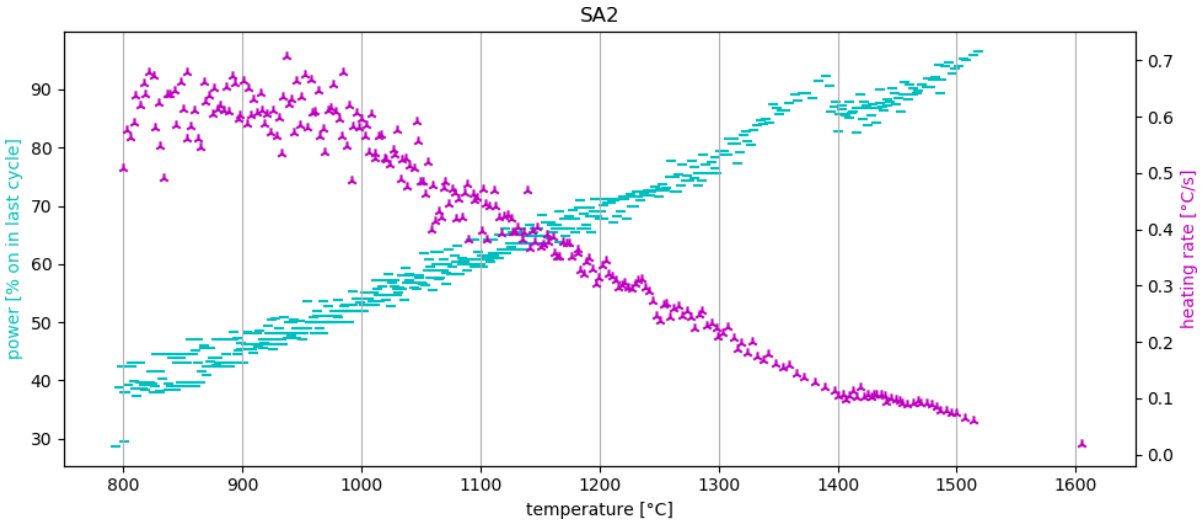

Figure 4.3.3: Power and heating rate plot of sample SA2.

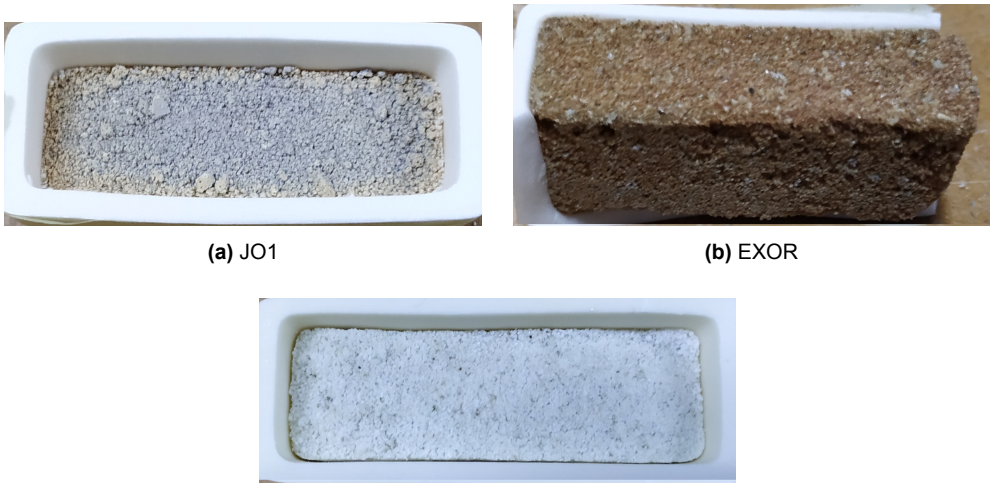

(a) JO1 **(b)** EXOR

(c) SA2

Figure 4.3.4: Selection of photographs of high silica sand after soaking at 1640 °C for 1 h. Crucibles are approximately 2x5 cm in size.

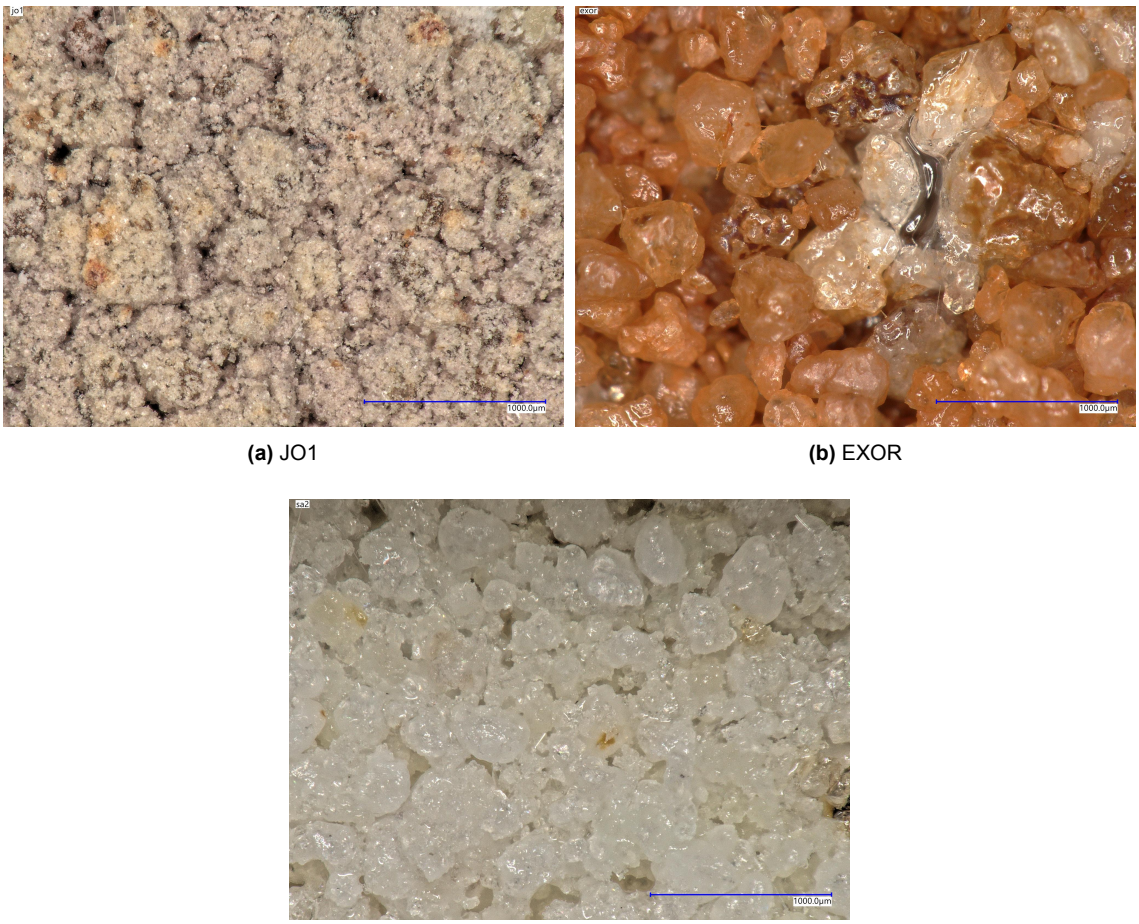

(a) JO1 **(b)** EXOR

(c) SA2

Figure 4.3.5: Selection of micrographs of high silica sand after soaking at 1640 °C for 1 h.

4.3.3. High feldspar sand

With increasing feldspar content, the recorded effects during melting become more obvious. Sample NA1 contains about 30 wt% feldspars, resulting in figure 4.3.6, which is not dissimilar to figure 4.3.3, except the deflection is displayed in the heating rate instead of the power. When the feldspar content exceeds 50 wt%, the onset of melting can be seen very clearly, as exemplified by sample KZ1 in figure 4.3.7.

The same progression can be seen when inspecting the samples after heating: with increasing feldspar content, an increasing amount of glassy mass compared to undissolved grains is observed, as shown in figures 4.3.8 and 4.3.9.

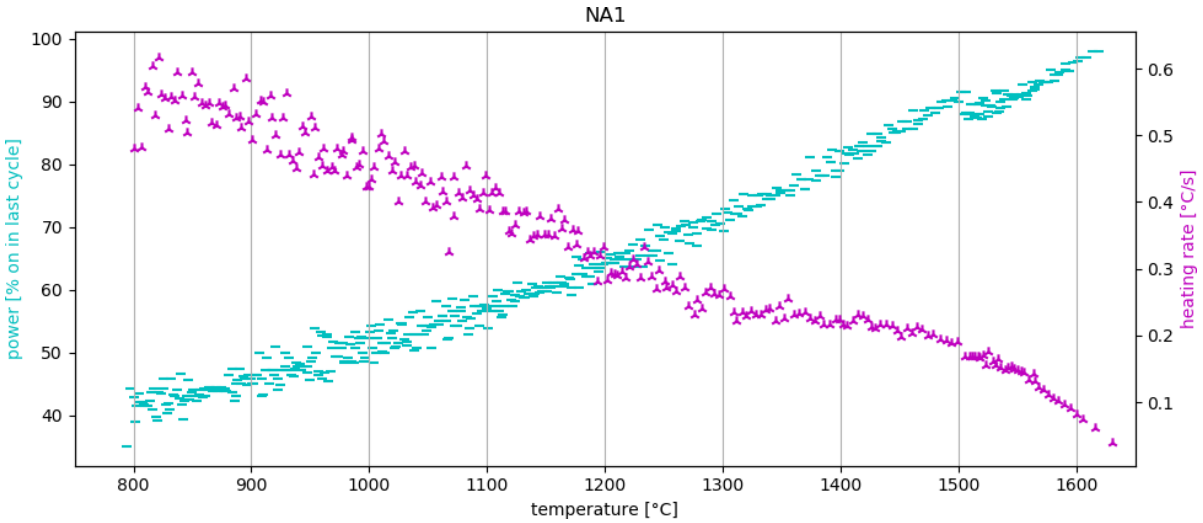

Figure 4.3.6: Power and heating rate plot of sample NA1.

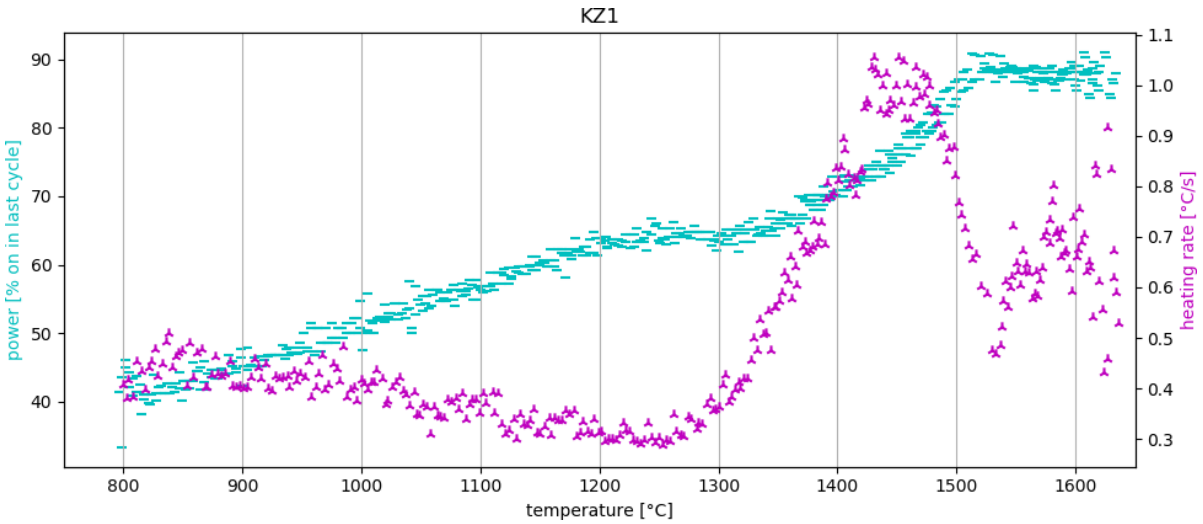

Figure 4.3.7: Power and heating rate plot of sample KZ1.

(a) NA1 **(b)** MN2 **(c)** IN1 **(d)** KZ1 **(e)** MEX

Figure 4.3.8: Selection of photographs of feldspar rich sand after soaking at 1640 °C for 1 h. Crucibles are approximately 2x5 cm in size.

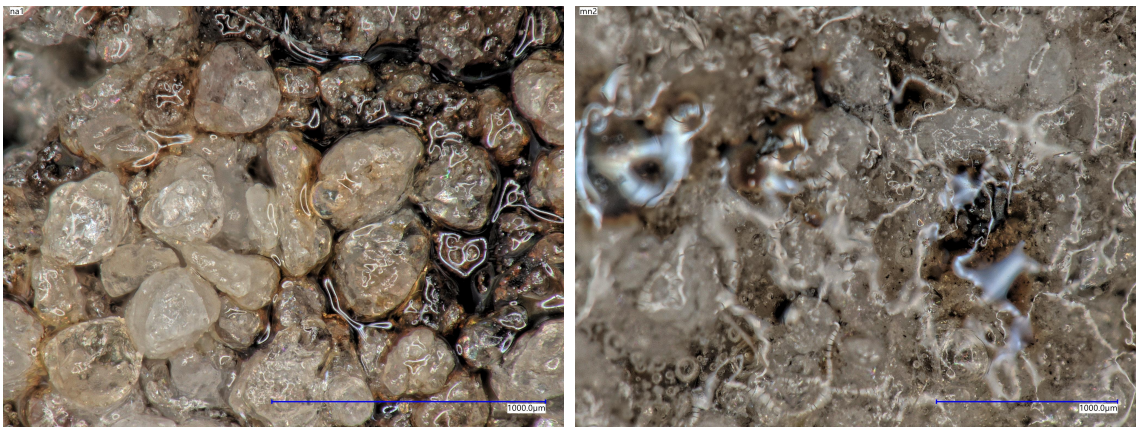

(a) NA1 **(b)** MN2

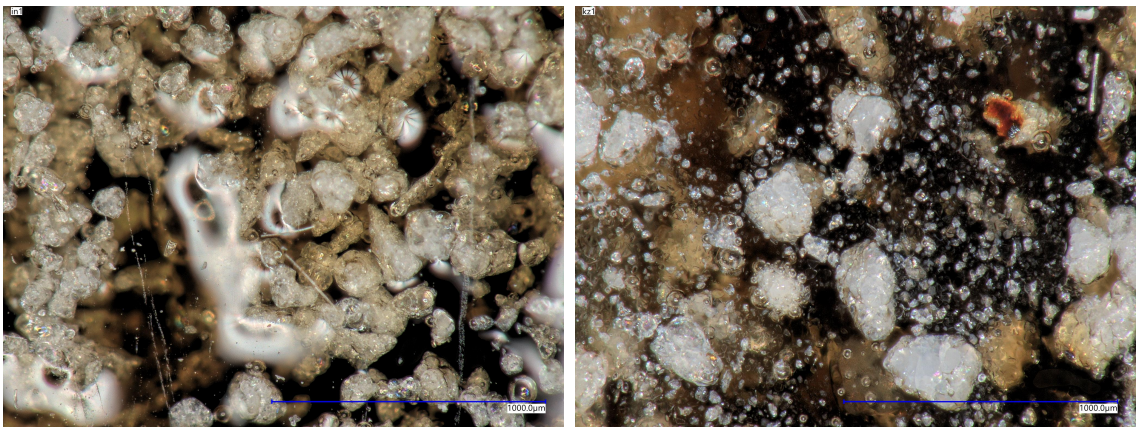

(c) IN1 **(d)** KZ1

Figure 4.3.9: Selection of micrographs of feldspar rich sand after soaking at 1640 °C for 1 h.

In figure 4.3.8, it can also be seen that samples IN1 and MEX have overflown the crucible during the experiment. In the process, a film formed covering the hole and blocking pyrometer measurements. This causes the temperature registered by the control system to be lower than the temperature of the sample, and the controller to switch to full power. As a result, the temperature at which this happened (~1500 °C) can be found in the heating curve, as seen in figure 4.3.10.

As sample MEX was abundant, the experiment was repeated, but stopped at the moment of expansion, the result of this repeat is displayed in figure 4.3.11. It can be seen here that, while it seems rough and porous to the eye, closer inspection reveals a glassy mass containing undissolved grains. The 3D mapping of the hole in the surface implies that instead of many small pores, one or more bigger pores have formed in the mass. The white spot in figure 4.3.11a is part of the insulation stuck to the sample.

Similarities between the plots of heating rate and power for samples IN1 (figure C.2.12) and MEX imply a similar mechanism is at work in both samples.

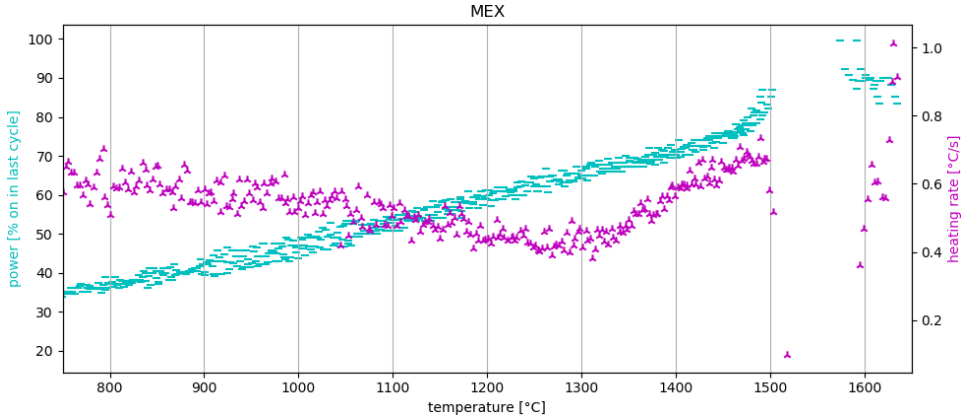

Figure 4.3.10: Power and heating rate plot of sample MEX, lack of data past 1500 °C is caused by the pyrometer measurements being blocked and consequently the controller switching to full power.

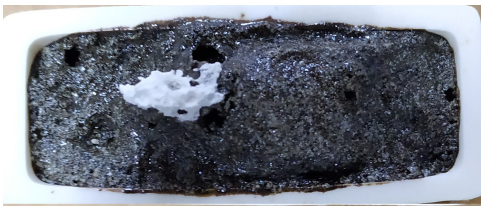

(a) Photograph.

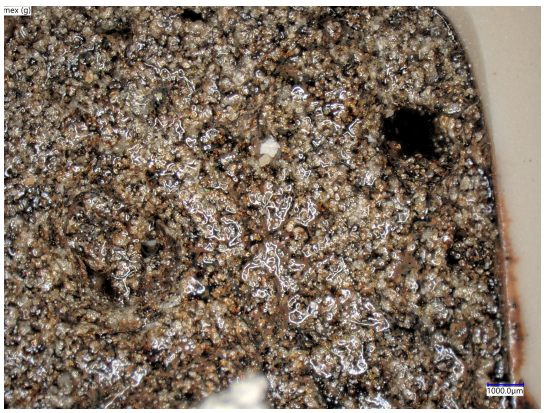

(b) Micrograph.

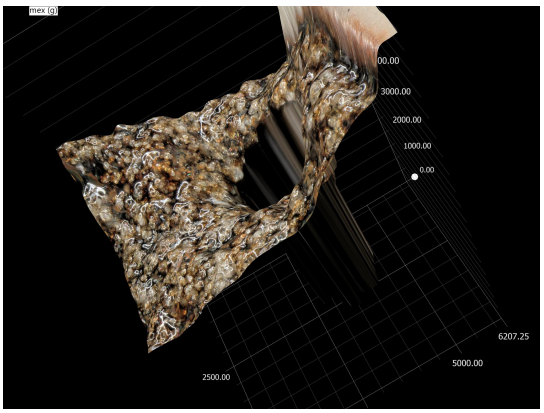

(c) 3D mapping.

Figure 4.3.11: Photograph, micrograph, and 3D mapping of sample MEX removed from furnace at time of expansion (~1500 °C).

This page is left blank for reading convenience in print.

4.3.4. High carbonate sand

In the group of high carbonate sands, there is a clear distinction between the samples that do (MAR and IR1), and do not (OM1 and AE1) reach the practical melting point predicted by the model.

Figure 4.3.12 displays little deviation from the baseline for sample Q, except for the slight deviation just under 1000 °C which is most likely caused by the release of CO_2 from the carbonates present. In figure 4.3.13, a more violent event occurs around the same temperature, followed by two inflections reminiscent of the effect that appears to be caused by the melting of feldspars. This is to be expected, as there is an estimated ~25 wt% of feldspars present in this sample. Around 1500 °C, very erratic measurements are displayed, most likely caused by melt formation.

In figure 4.3.14, the difference is clearly visible in the samples in crucibles, as is the progression of grain dissolution after reheating and additional soaking of sample IR1. Figure 4.3.15 provides more insight of what has happened. Samples OM1 and AE1 have formed a mass of partly dissolved grains surrounded by a glass like mass, while samples IR1 and MAR appear to have formed a glass. The former displays undissolved grains, while the latter has recrystallized on the surface.

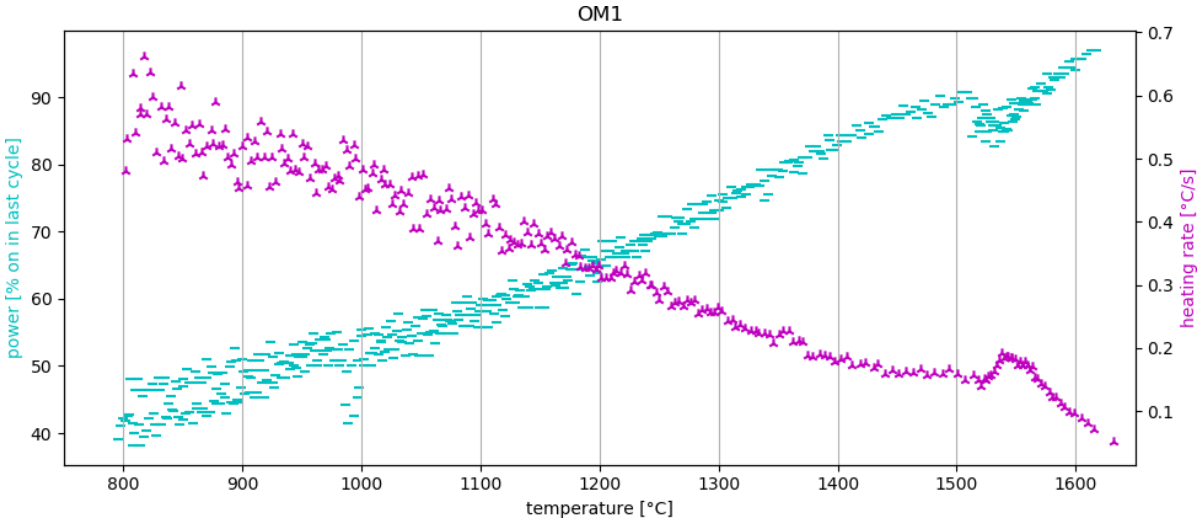

Figure 4.3.12: Power and heating rate plot of sample OM1.

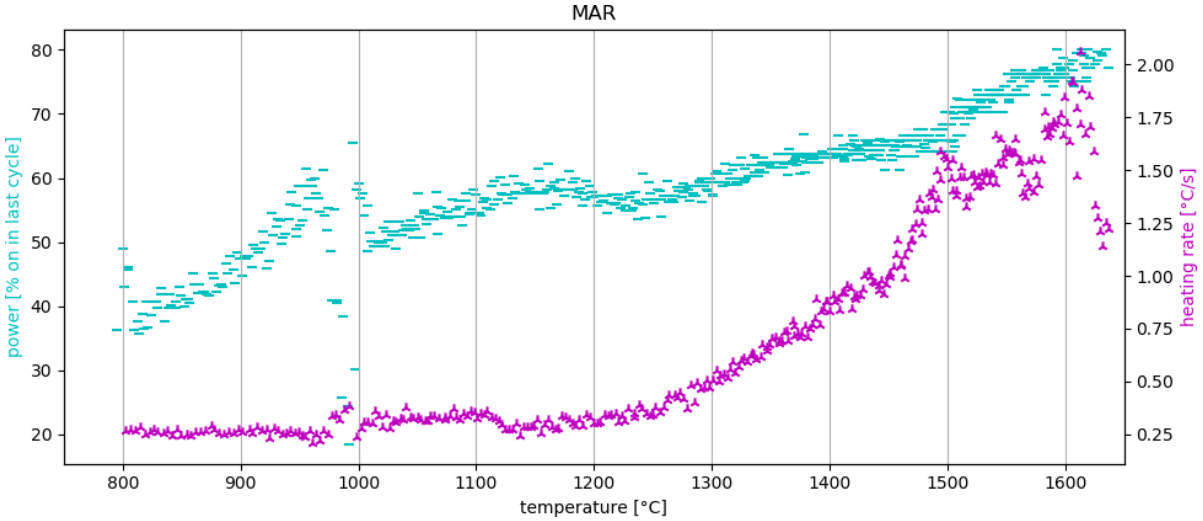

Figure 4.3.13: Power and heating rate plot of sample MAR.

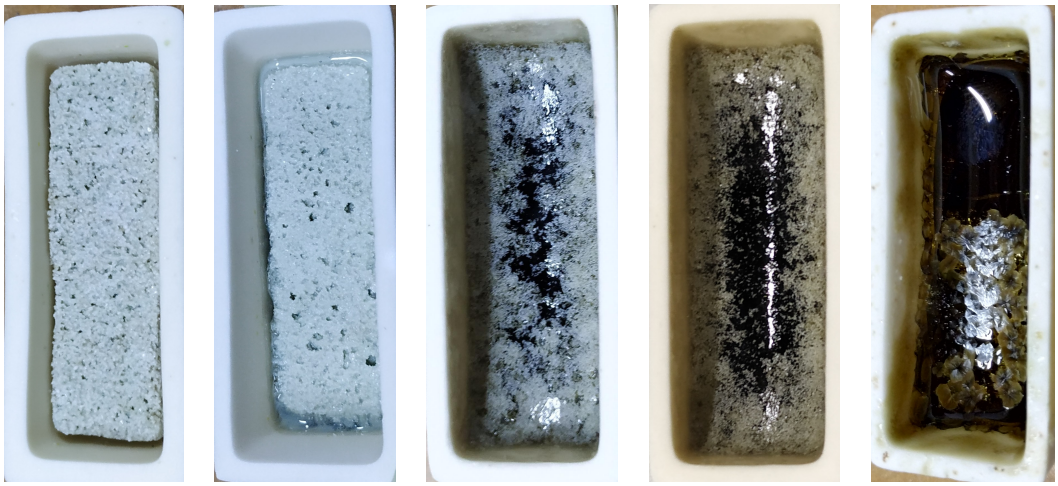

(a) OM1 **(b)** AE1 **(c)** IR1 **(d)** IR1, +2 h soaking **(e)** MAR

Figure 4.3.14: Selection of photographs of high carbonate sand after soaking at 1640 °C for 1 h. Crucibles are approximately 2x5 cm in size.

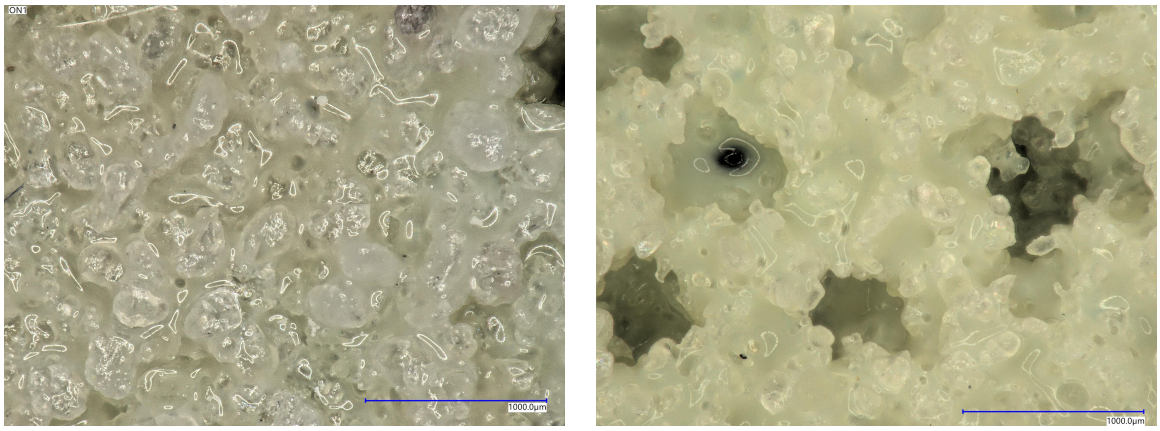

(a) OM1 **(b)** AE1

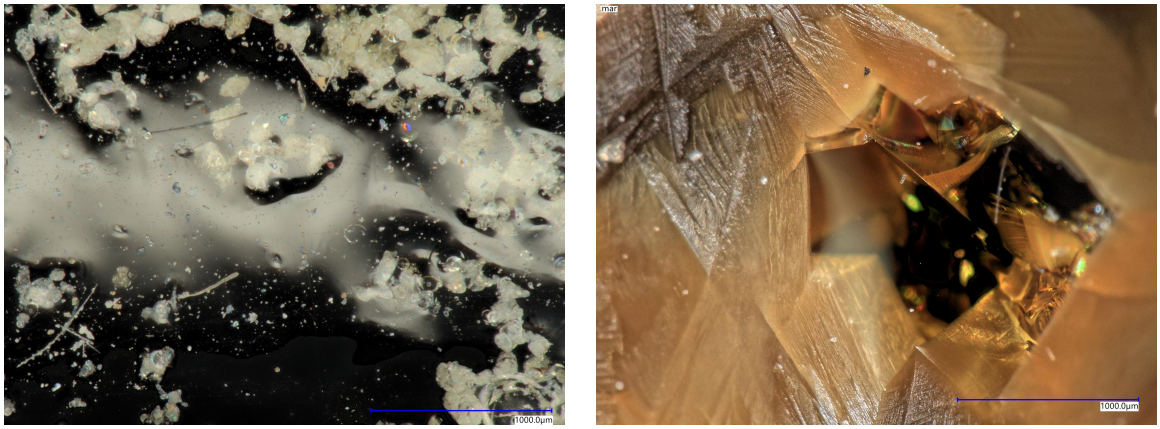

(c) IR1 **(d)** MAR

Figure 4.3.15: Selection of micrographs of high carbonate sand after soaking at 1640 °C for 1 h, 3 h in the case of sample IR1.

4.4. Formation of primary melt phases

The selected combinations of components chosen to observe the reactions leading to melt formation are presented in tables 4.4.1 and 4.4.2. The percentages of components were used to calculate the chemical composition of each mix based on the measured composition from table 4.2.1.

Figure 4.4.1 displays the heating rate and power curves from heating the mixtures.

The first notable observation to be made is the difference between the mixtures based on sample Q and feldspar based mixes: where the quartz mixes, QCAL and QDOL, display sudden and erratic effects, the feldspar mixes, SPCAL and SPDOL, show a more gradual change in heating rate and power.

Changes in heating rate and power of mixture QCAL, in figure 4.4.1a, occur just over 1000 °C and around 1600 °C. The scatter in both heating rate and power appears wider than both the other measurements in this series and the measurements of desert sand (sections 4.3.2 to 4.3.3, appendix C.2).

The onset of effects for mix QDOL in figure 4.4.1b occurs around 1300 °C, followed by a region containing multiple inflections, most extreme just over 1450 °C.

Both feldspar based mixtures, SPCAL and SPDOL, show a gradual change similar to the plots recorded during the heating of high feldspar desert sand samples (section 4.3.3). The onset is at slightly lower temperature for mixture SPCAL, which was expected due to the addition of NASP to the mixture. An additional small increase in scatter around 1400 °C takes place in both heating plots.

Table 4.4.1: Weight percentages of components and calculated LOI of binary mixtures.

Mix code	Q	KSP	NaSP	CAL	DOL	LOI
QCAL	51.3	0.0	0.0	48.7	0.0	17.1
QDOL	49.5	0.0	0.0	0.0	50.5	21.1
SPDOL	0.0	78.8	0.0	0.0	21.2	7.9
SPCAL	0.0	56.4	23.5	20.1	0.0	6.4

Table 4.4.2: Calculated chemical composition of binary mixes in wt%.

Mix code	SiO_2	Fe_2O_3	Al_2O_3	TiO_2	Na_2O	K_2O	MgO	CaO
QCAL	61.5	0.1	0.4	0.0	0.0	0.1	0.2	37.4
QDOL	59.8	0.0	0.1	0.0	0.1	0.0	17.8	22.1
SPDOL	55.3	0.1	17.1	0.0	3.9	7.6	6.8	8.8
SPCAL	56.3	0.1	17.1	0.1	5.9	5.4	0.2	14.5

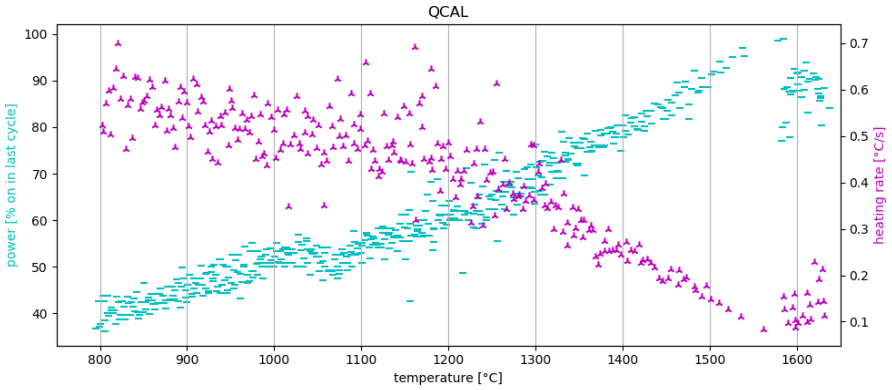

(a) QCAL

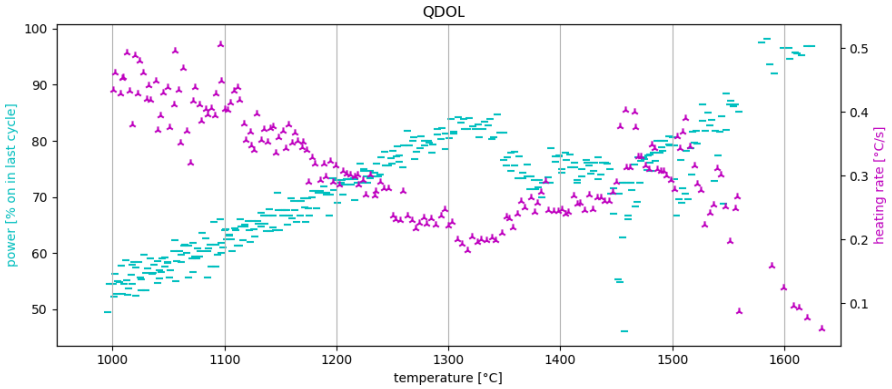

(b) QDOL

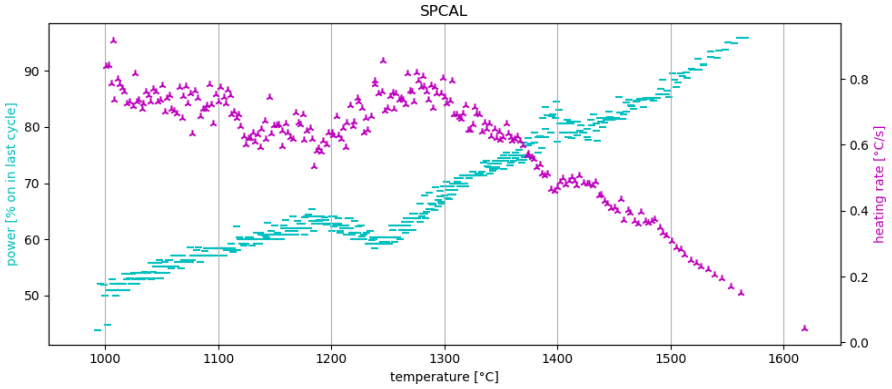

(c) SPCAL

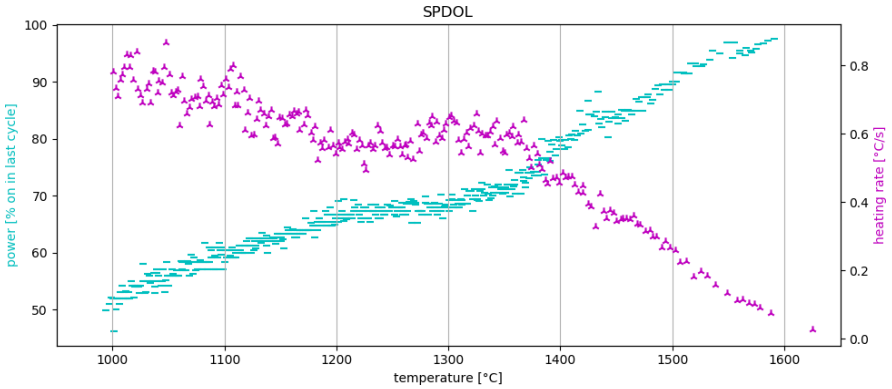

(d) SPDOL

Figure 4.4.1: Power and heating rate plots of mixtures of components.

4.5. Hypothetical beneficiation & 'synthetic sand' recipes

The main point of interest of benificiation is lowering the practical melting point of the sand. For the various hypothetical benificiation operations discussed in section 3.2.7, the resulting practical melting point prediction by the model is presented in table 4.5.1. Considerations regarding glassformability are given in footnotes, as are the compositions that were selected to be imitated. The practical melting points of the original sand found in table 4.3.1 are repeated for reference.

As was mentioned in section 3.2.7, increasing the feldspar content by 5 wt% has very little effect on the calculated melting point, and in some cases even increases it.

The more rigorous operations; increasing the carbonate and/or the feldspar content by 50 % and removal of all quartz, result in more considerable changes. It can be observed that the high silica sands in the lower half of the table show relatively small changes in melting temperature. Conversely, operations regarding carbonates have a hefty influence on the carbonate rich sands, and the feldspar rich sands are more heavily influenced by increase of feldspars. None of this is surprising, since the benificiation operations considered are relative to the original content of the mineral(s) 'benificiated', as described in section 3.2.7.

The selection of compositions to imitate is discussed in more detail in section 5.5. The calculated chemical compositions of the imitation mixtures, resulting from the procedure described in section 3.2.7, compared to the ('benificiated') composition(s) imitated (marked e in table 4.5.1) are presented in table 4.5.2. Note that the lack of plagioclase feldspars available (discussed in section 5.2) leads to less accurate approximations of feldspar rich samples.

The percentages of each component used to create the mixture are summarized in table 4.5.3, as is the calculated LOI.

Table 4.5.1: Calculated practical melting temperatures, in °C, of 'benificiated' desert sand. Sorted by calculated practical melting point of the original sand. (1) Original, (2) +5% feldspars, (3) +50% feldspars, (4) +50% carbonates, (5) +50% carbonates and feldspars, (6) all quartz removed.

Sample	(1)	(2)	(3)	(4)	(5)	(6)
MAR	1169[e]	1178	1267	816[b,c]	571[b,c]	-[b,c]
IR1	1636	1638	1659	1441[e]	1213[c]	1165
AE1	1760	1758	1734	1457[e]	1339[c]	-[d]
OM1	1776	1775	1755	1472[e]	1371	-[d]
MEX	1899	1873	1659	1881	1622	1593[e]
KZ1	1998	1980	1849	1955	1735	1640[e]
IN1	2022	2005	1856	1969	1740	1556[e]
MN2	2218	2192	1988	2223	2013	1930
NA1	2397	2381	2237	2384	2220	-[d]
SA2	2544[a]	2535[a]	2457	2503	2406	-[d]
SD1	2639[a]	2631[a]	2554[a]	2638[a]	2553[a]	-[d]
TRIX	2681[a]	2673[a]	2595[a]	2678[a]	2611[a]	-[d]
TN2	2686[a]	2678[a]	2606[a]	2683[a]	2611[a]	-[d]
EXOR	2729[a]	2722[a]	2662[a]	2726[a]	2675[a]	-[d]
DZ2	2734[a]	2731[a]	2711[a]	2703[a]	2684[a]	-[d]
LY1	2742[a]	2738[a]	2702[a]	2778[a]	2707[a]	-[d]
JO1	2779[a]	2777[a]	2755[a]	2778[a]	2756[a]	-[d]
EXOY	2803[a]	2801[a]	2779[a]	2803[a]	2783[a]	-[d]

[a] Out of range of model, >90wt% SiO_2.

[b] Out of range of model, >40wt% CaO.

[c] Unlikely to form glass, <50mol% SiO_2.

[d] >50wt% removed.

[e] Selected for imitation mix.

Table 4.5.2: Calculated chemical composition of imitation mixtures compared to ‘benificiated’ samples to approximate.

Operation	Code	SiO_2	Fe_2O_3	Al_2O_3	TiO_2	Na_2O	K_2O	MgO	CaO
None	**MAR**	41.8	4.1	7.4	0.7	1.8	1.1	3.1	38.8
	IM-MAR	48.6	0.1	5.5	0.0	2.3	1.2	3.3	38.6
+50% carbonates	**AE1**	54.5	1.7	3.5	0.1	0.0	1.0	6.2	33.0
	OM1	55.5	1.8	3.0	0.1	0.3	0.7	6.5	32.2
	IR1	54.1	3.0	9.1	0.5	2.4	1.4	3.9	25.5
	IM-MOREC	58.4	0.1	2.3	0.0	0.5	0.9	6.3	31.2
All quartz removed	**KZ1**	58.5	2.0	21.6	0.3	6.1	3.8	2.0	5.9
	IN1	54.3	2.7	22.5	0.4	5.1	3.1	2.7	9.2
	MEX	54.6	4.3	25.0	0.9	4.9	2.4	2.0	6.0
	IM-NOQ	61.0	0.1	15.9	0.1	6.8	3.7	2.4	9.7

Table 4.5.3: Percentage of components (by weight) and calculated LOI of imitation mixtures.

Mix code	Q	KSP	NaSP	CAL	DOL	LOI
IM-MAR	25.1	10.9	10.9	44.2	9.0	19.5
IM-NOQ	7.6	37.9	37.9	9.5	7.2	5.6
IM-MOREC	43.2	8.5	0.0	30.2	18.1	18.1

4.6. Melting of synthetic batches

To estimate the correct temperature to remove batches from the furnace for casting, the viscosity curves were modelled in the manner described in section 3.2.3, and compared to the curves of the 'benificiated' desert sand. These results are found in section 4.6.1.

The melting of the ~100 g batches in the resistive furnace provided no data, hence portions similar to the unmodified sand were given microwave treatment similar to the original sand (see section 3.2.4). The heating rate and power plots presented in section 4.6.2 provide grounds, in addition to the comparison of chemical composition, to asses (dis)similarities between the originals and imitations.

4.6.1. Modelling of viscosity

The modelled viscosity curves are presented in figures 4.6.1 to 4.6.3, and are based on the calculated compositions found in table 4.5.2. As in the table, the imitations are accompanied by the curves calculated for the compositions that were imitated.

In all cases the ±0.5 log-unit margins of imitation and goal overlap to some extent. The deviations were deemed acceptable, given the limited freedom caused by the lack of plagioclase feldspars.

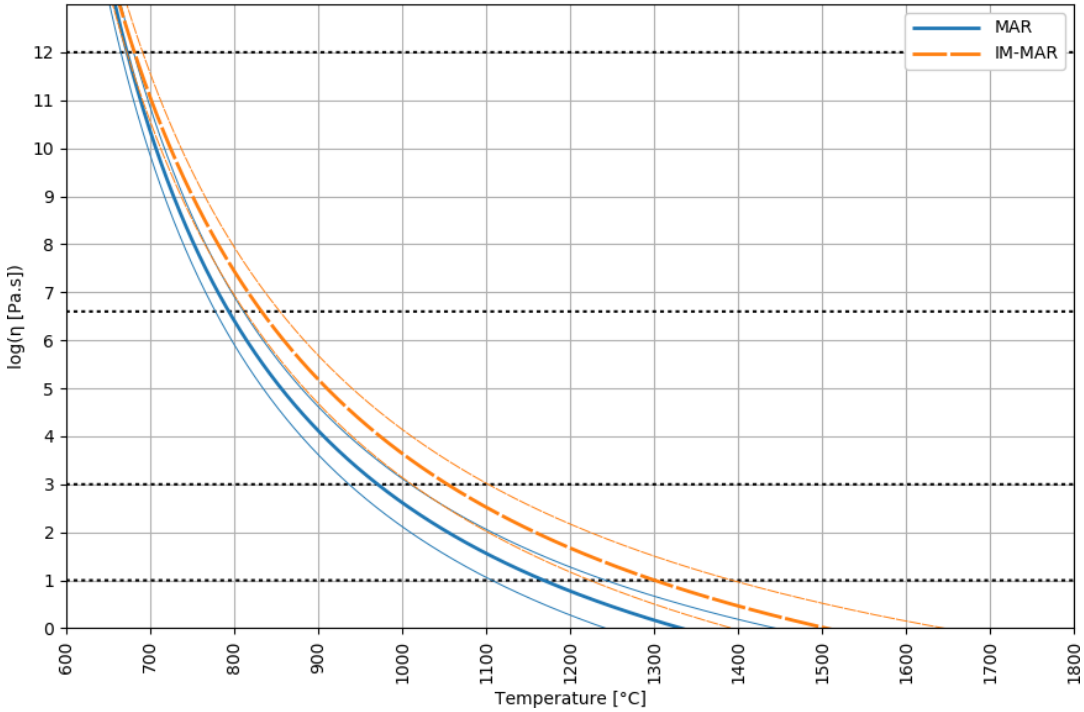

Figure 4.6.1: Comparison of viscosity curve of mixture IM-MAR and MAR, including ±0.5 log-unit margin.

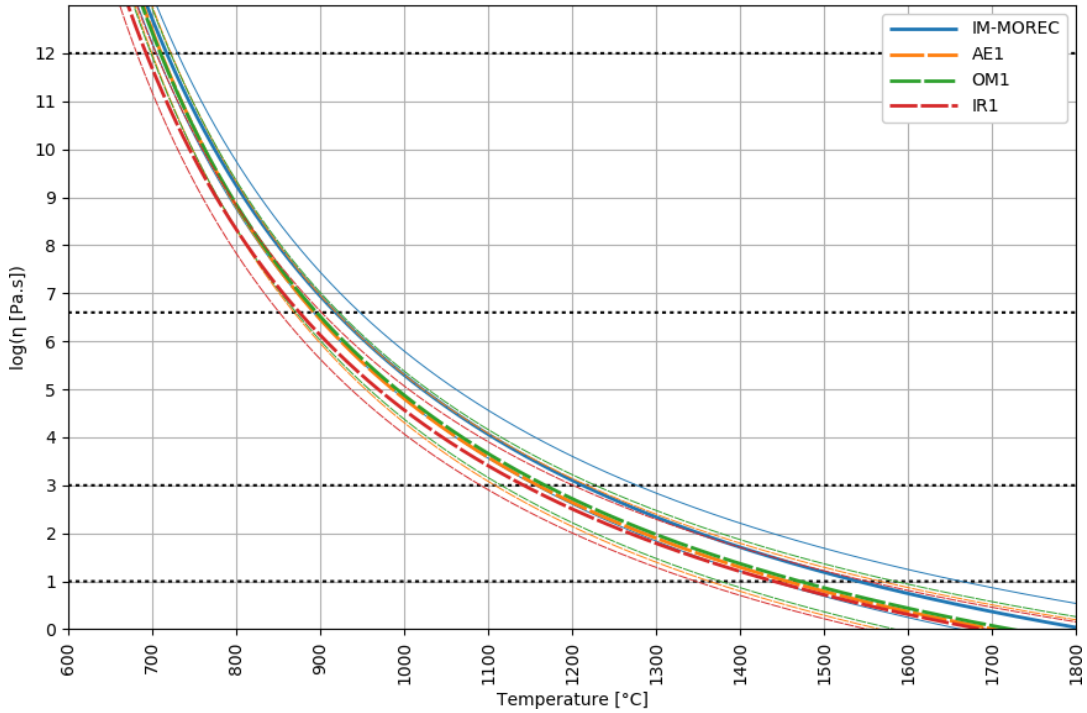

Figure 4.6.2: Comparison of viscosity curves of mixture IM-MOREC and samples with 50% increased carbonate content, including ±0.5 log-unit margin.

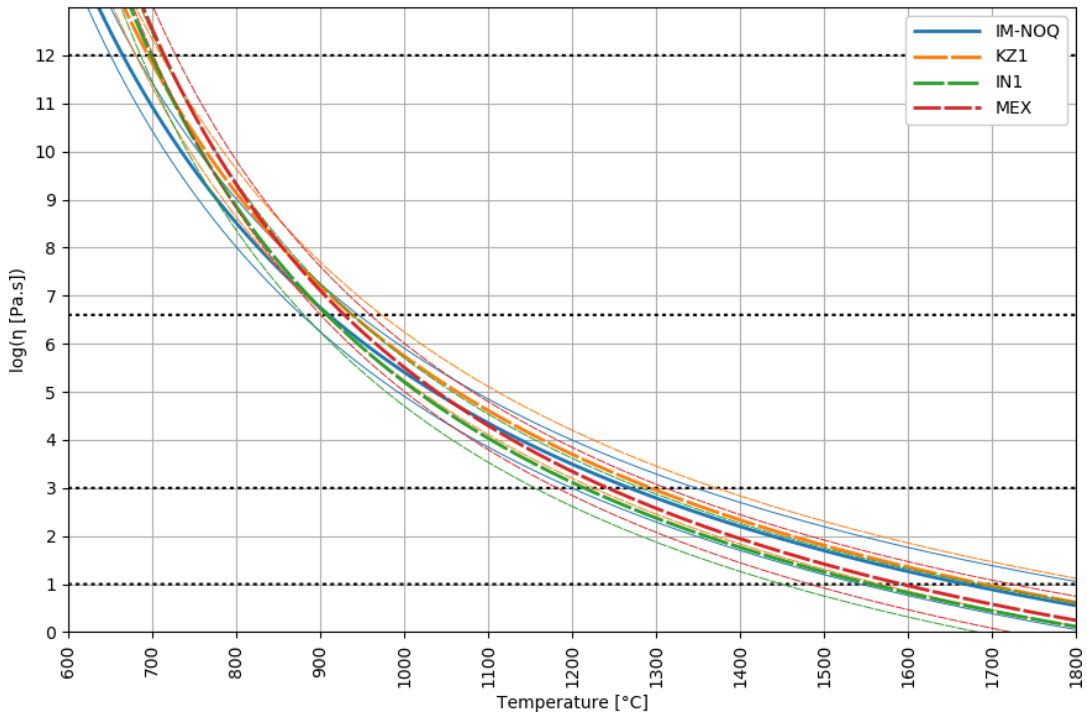

Figure 4.6.3: Comparison of viscosity curves of mixture IM-NOQ and samples with quartz removed, including ±0.5 log-unit margin.

4.6.2. Heating rate & power plots

The heating rate and power plots resulting from melting the synthetic batches in the microwave furnace are presented in figures 4.6.4 to 4.6.6. While not exactly alike, the patterns appear similar to the plots created by heating actual desert sand found in section 4.3.

The imitation of sample MAR stands out, as the small inflection caused by the melting of feldspars that is seen between 1100 °C and 1200 °C during melting of the original (figure 4.3.13) does not occur clearly in the imitation. This is unexpected as a similar fraction of feldspars is present in both.

Furthermore it is notable that all the observed features, generally seem to occur at lower temperatures than would be expected.

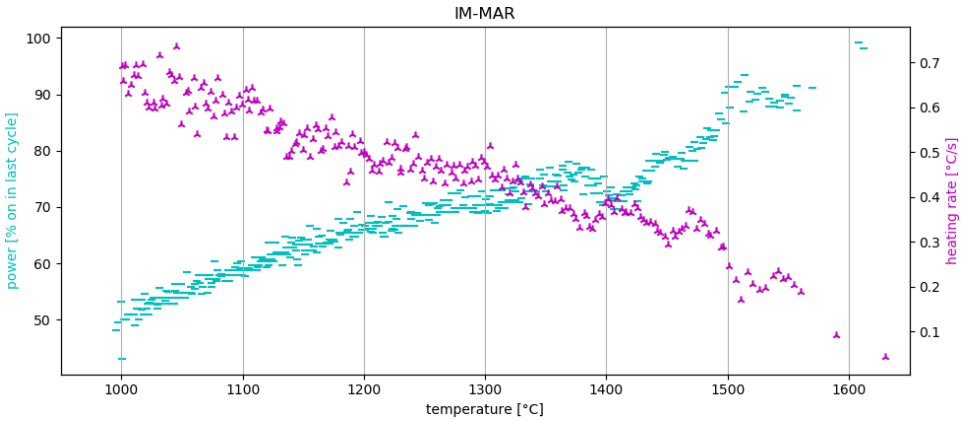

Figure 4.6.4: Power and heating rate plot of imitation mix IM-MAR.

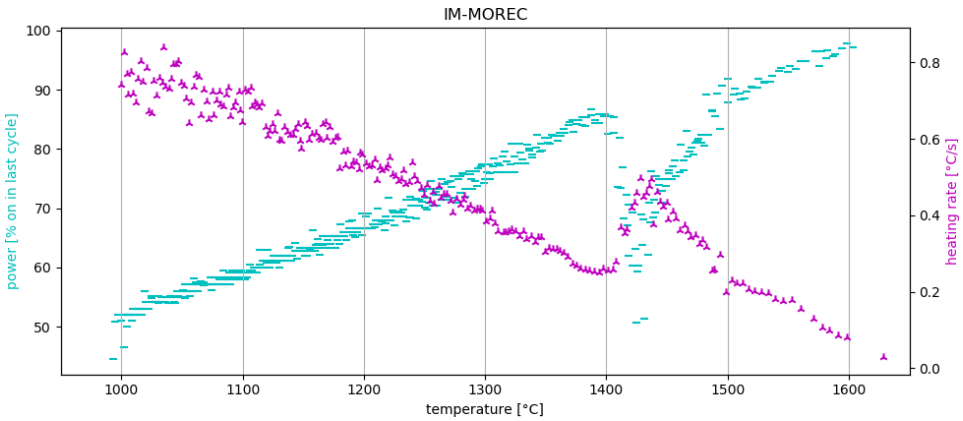

Figure 4.6.5: Power and heating rate plot of imitation mix IM-MOREC.

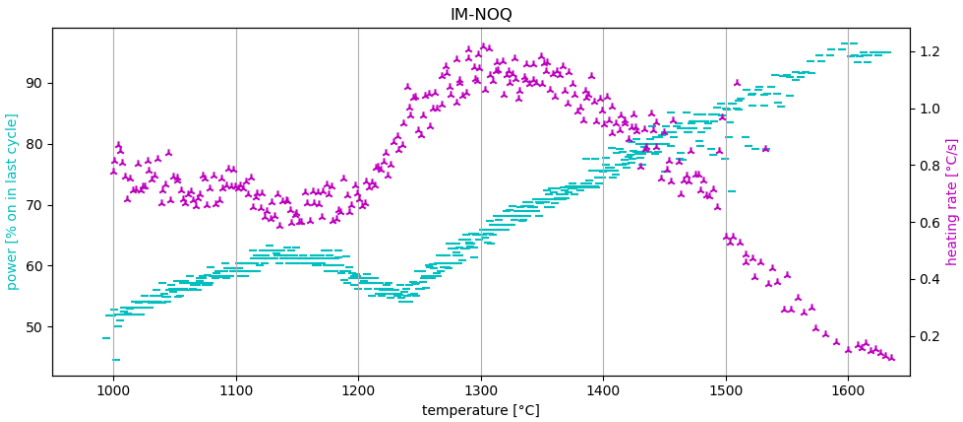

Figure 4.6.6: Power and heating rate plot of imitation mix IM-NOQ.

4.7. Characterisation of synthetic glass

This section contains results of the analysis of the samples formed by melting the three imitation mixtures. While not chronologically correct, the XRF results are presented first, as they provide context and explanation for the visual inspection and optical analysis. The section concludes with a selection of images of fracture surfaces of the glasses obtained.

As will become apparent, even the most successful techniques attempted, failed to produced suitable samples in some cases. Mixture IM-NOQ was too viscous to be cast from the microwave, and therefore could not be analysed by XRF. During heating of the batches to be cast on steel, a crucible broke, necessitating shutdown of the furnace and prevented casting of samples after IM-MAR, the lowest melting temperature mixture, was cast.

Images of samples that were suitable for further investigation and discussion are collected in figures 4.7.1 to 4.7.3.

4.7.1. XRF measurements of glass

Table 4.7.1 summarizes the XRF results of samples of a form suitable for analysis, in some cases after breaking them. The calculated compositions are included for comparison.

It can be observed that there is a significant discrepancy between calculated and resulting composition: all samples contain more SiO_2 and less CaO than intended, and some variations both ways occur in the other modifiers. The Al_2O_3 content of the microwaved IM-MAR and the resistively heated IM-MOREC samples is considerably higher than was calculated, and the IM-MAR sample cast on steel contains more Fe_2O_3 than would be expected based on the composition of the components.

Most trace elements detected can be traced back to the components in table 4.2.1. Exceptions are MoO_3, and sometimes WO_3 in the resistively heated samples. CuO in resistively heated IM-MOREC is unexpected as well.

Table 4.7.1: XRF results of the glass samples produced. (c): calculated, (r): resistive heating, (m): microwave heating, (g): cast on graphite, (s): cast on steel.

	SiO_2	Fe_2O_3	Al_2O_3	Na_2O	K_2O	MgO	CaO	Trace elements
IM-MAR (c)	48.6	0.1	5.5	2.3	1.2	3.3	38.6	-
IM-MAR (r, s)	51.8	0.3	6.2	1.8	1.2	3.3	35.1	P_2O_5, SrO, BaO, TiO_2, Cl, MnO, SO_3, Rb_2O, MoO_3.
IM-MAR (r, g)	51.6	0.1	5.0	1.5	1.2	3.5	36.7	P_2O_5, SrO, BaO, TiO_2, SO_3, MnO, Cl, Rb_2O, MoO_3.
IM-MAR (m, g)	53.1	0.1	10.0	1.7	1.1	2.6	31.0	P_2O_5, SrO, SO_3, TiO_2, Cl, BaO, MnO, ZrO_2, PbO , Rb_2O , MnO.
IM-MOREC (c)	58.4	0.1	2.3	0.5	0.9	6.3	31.2	-
IM-MOREC (r, g)	55.0	0.1	17.5	1.8	0.7	4.2	20.3	P_2O_5, MoO_3, TiO_2, SrO, BaO, WO_3, ZrO_2, SO_3, Cl, CuO, Rb_2O, MnO.
IM-MOREC (m, g)	66.5	0.1	2.2	0.4	0.9	4.9	24.9	SrO, P_2O_5, BaO, TiO_2, Cl, SO_3, ZnO, Rb_2O.
IM-NOQ (c)	61.0	0.1	15.9	6.8	3.7	2.4	9.7	-
IM-NOQ (r, g)	64.0	0.1	17.3	5.9	3.1	1.8	7.4	BaO, P_2O_5, SrO, TiO_2, MoO_3, SO_3, Cl, ZrO_2, Rb_2O, WO_3, PbO, ZnO, MnO.

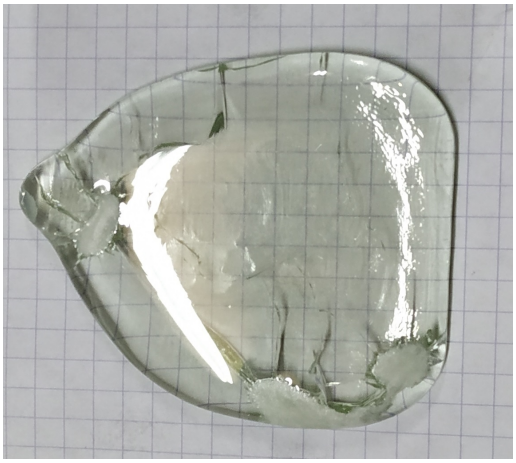

(a) Mixture IM-MAR

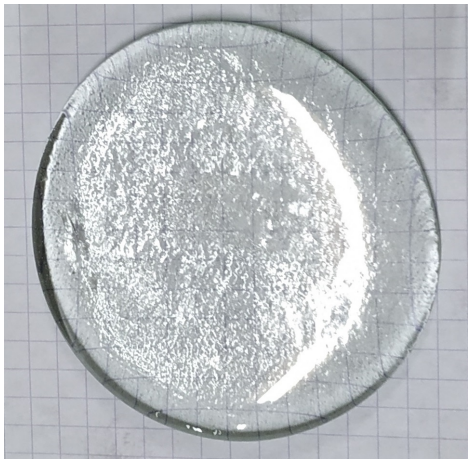

(b) Mixture IM-MOREC

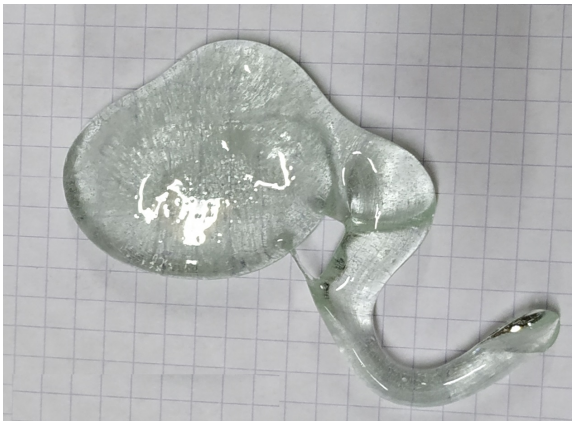

(c) Mixture IM-NOQ

Figure 4.7.1: Samples produced by resistive heating and casting onto graphite, on a 5 mm grid.

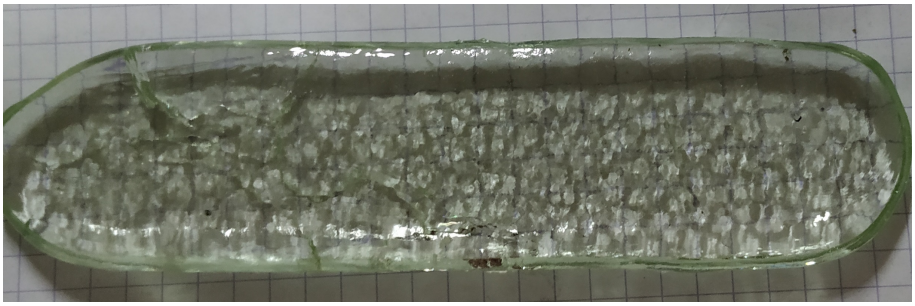

Figure 4.7.2: Mixture IM-MAR, cast on steel.

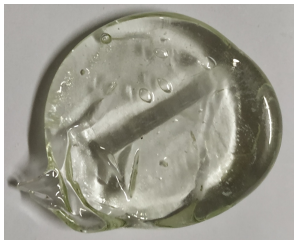

(a) Mixture IM-MAR

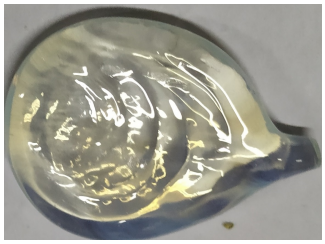

(b) Mixture IM-MOREC

(c) Mixture IM-NOQ

Figure 4.7.3: Samples produced using the microwave furnace. Cast tablets measure ~2.5 cm in diameter, the crucible is approximately 2x5 cm in size.

4.7.2. Visual inspection

Figures 4.7.1 and 4.7.2 show the resulting glass samples from resistive heating.

The cracks visible in both IM-MAR samples were caused by moving the sample to the annealing furnace using a cold tool. Upon closer inspection, in figure 4.7.4, it can be seen that the thermal shock has also caused local crystallisation. While the scale is different, the appearance is similar to the devitrification of the glass resulting from the sand that was imitated (figure 4.3.15d).

The glass sample resulting from mixture IM-MOREC appears rough in figure 4.7.1b, this is shown to be caused by a large amount of small bubbles by figure 4.7.5. The large amount of bubbles in sample IM-NOQ is visible to the naked eye in figure 4.7.1c, as is the less flat shape compared to the other samples.

Samples produced by microwave heating are found in figure 4.7.3. Note that the tablets have an irregular surface. A large amount of bubbles is visible in in mix IM-NOQ, that was too viscous to be removed from the crucible. In figure 4.7.6, it is shown that streaks in the microwaved sample IM-MOREC have crystallized.

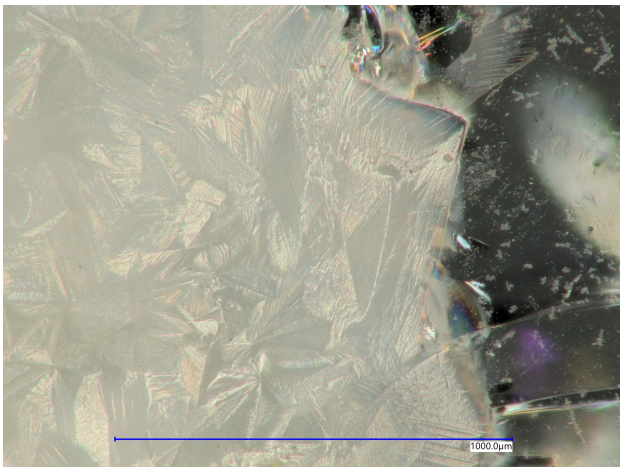

Figure 4.7.4: Crystallisation in thermal shocked IM-MAR.

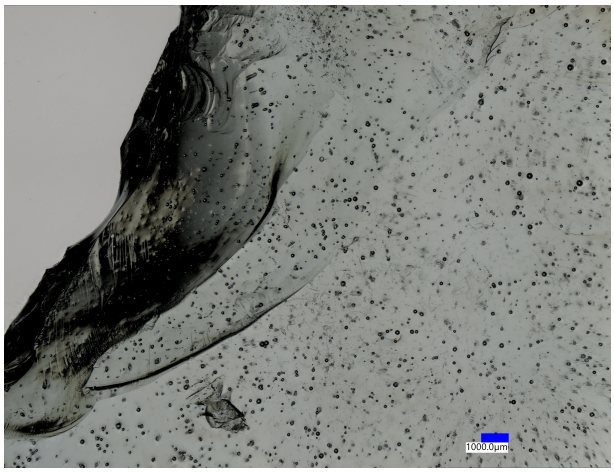

Figure 4.7.5: Stitched micrograph of sample IM-MOREC produced by resistive heating, displaying seeds.

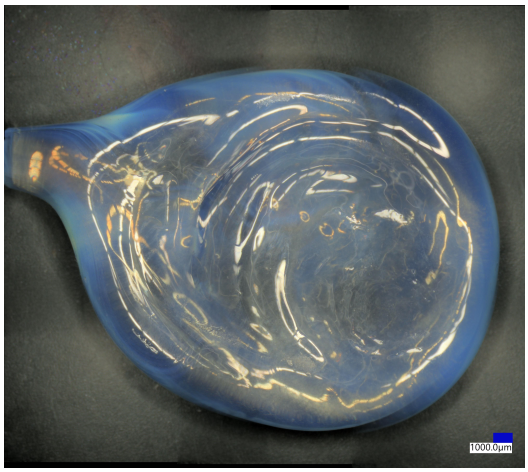

Figure 4.7.6: Stitched micrograph of IM-MOREC from microwave, polarized light reveals devitrified areas as a white haze.

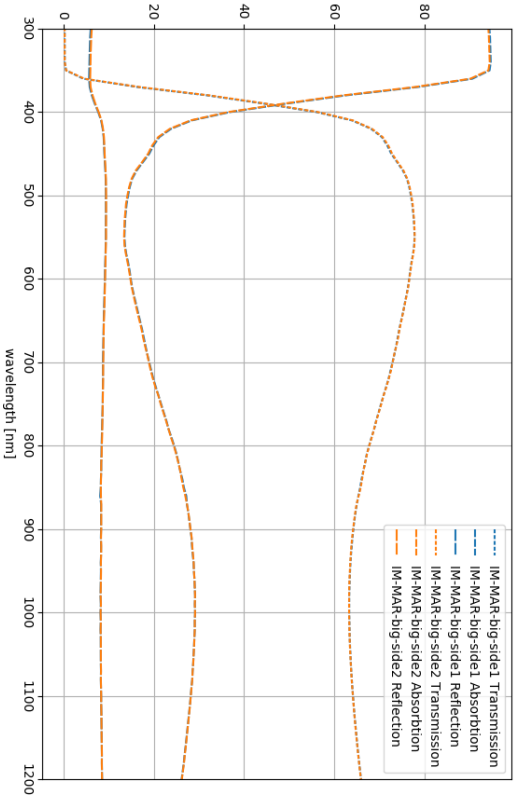

Figure 4.7.7: Measured transmission and reflections spectrum and calculated absorption spectrum of IM-MAR.

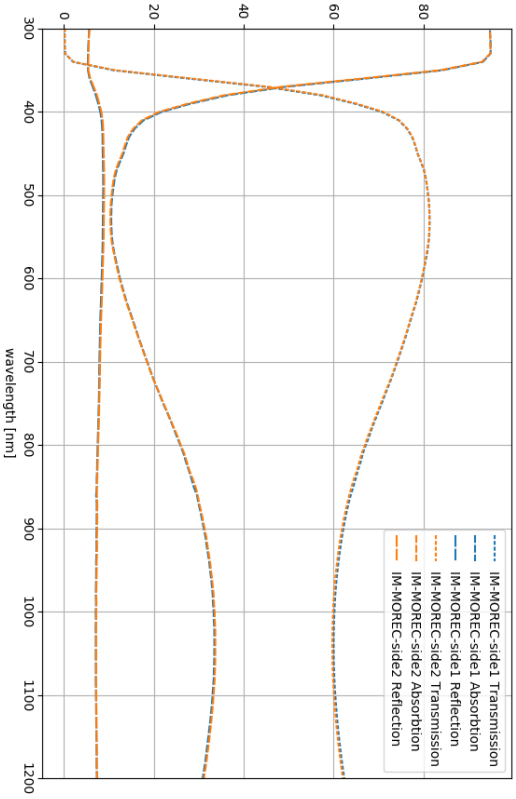

Figure 4.7.8: Measured transmission and reflections spectrum and calculated absorption spectrum of IM-MOREC.

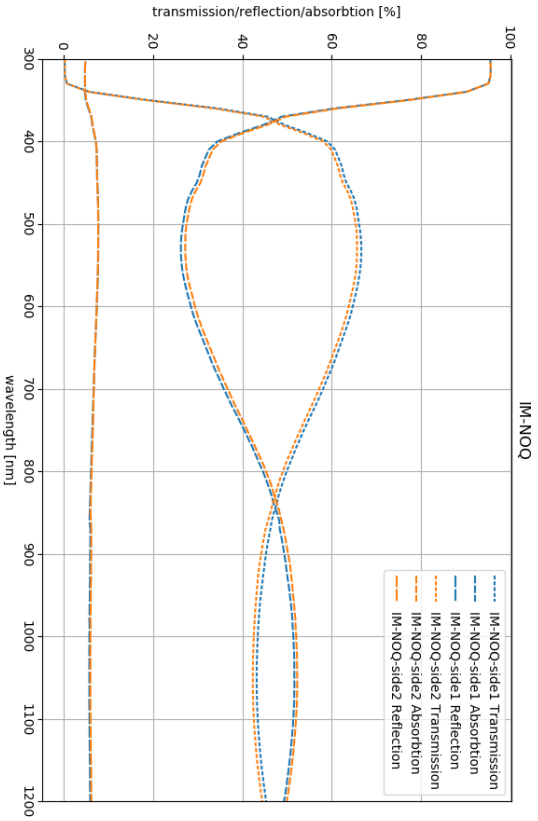

Figure 4.7.9: Measured transmission and reflections spectrum and calculated absorption spectrum of IM-NOQ.

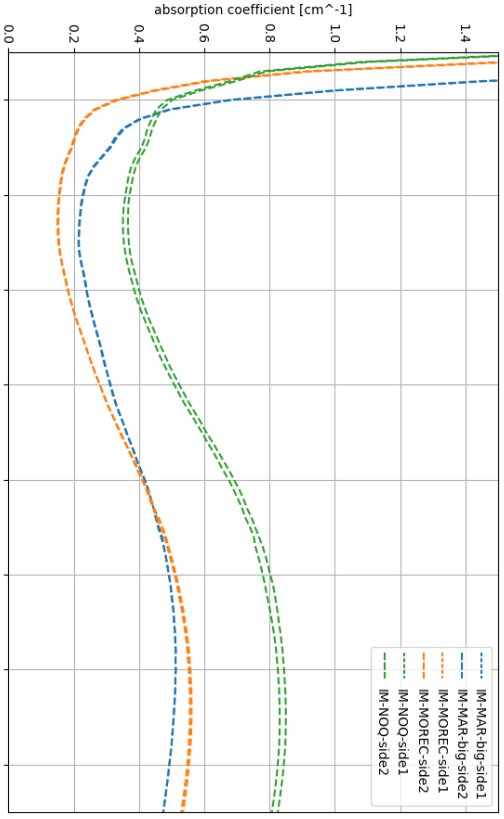

Figure 4.7.10: Calculated absorption coefficient a for all mixtures.

4.7.3. Optical analysis

As the only technique that yielded samples from all mixtures was casting on graphite, it was decided to use these three samples for the optical analysis. Optical measurements were performed before the XRF analysis, as the X-rays cause discolouration of the glass, hence the discrepancies in composition could not be considered before the measurement.

Plots of the raw results of the transmission and reflection measurements, complemented by the calculated absorption, are displayed in figures 4.7.7, 4.7.8 and 4.7.9. Results from measurement in both directions trough the sample are plotted together to show possible differences, in all but the case of IM-NOQ, the graphs completely overlap. The discrepancies between sides for this sample are likely to be caused by the slightly rounded top side.

Using the measured thickness of each sample, the absorption coefficient of the glass was calculated, as presented in figure 4.7.10. These coefficients were then used to calculate the transmission of 3 mm glass following the steps described in section 3.2.9, under the assumption that the reflection would be the same as the measured values. The result is presented in figure 4.7.11. The transmission in this figure not reaching 0 past the (ultraviolet (UV)) cut-off is an artefact of the calculation; as the measured values for transmission contain some noise, 0% transmission leads to a non-infinite absorption coefficient.

All samples display a similar shape of the transmission curve: the UV-cut off close to 350 nm, an inflection between 400 nm and 500 nm, and a maximum around 550 nm, followed by a gradual decrease. The UV cut-off takes place at slightly lower wavelengths for mixtures IM-NOQ and IM-MOREC.

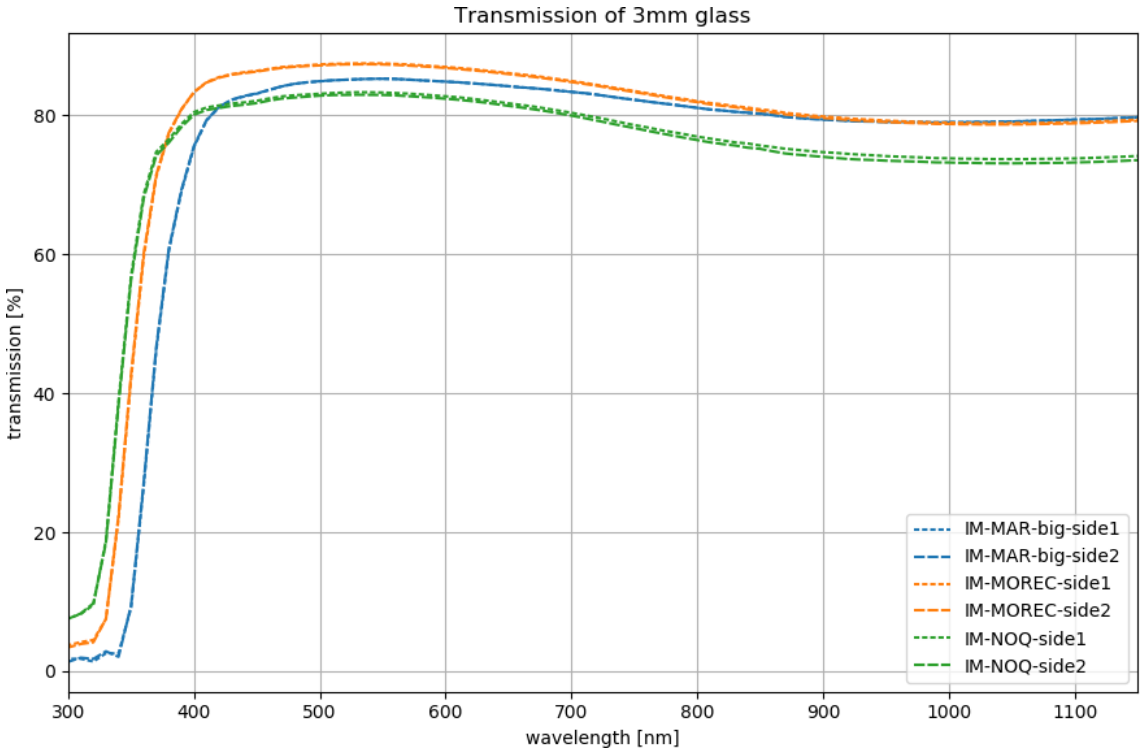

Figure 4.7.11: Calculated transmission spectrum for 3 mm glass of imitation mixtures.

4.7.4. Mechanical analysis

A selection of micrographs of fracture surfaces is presented in figures 4.7.12 to 4.7.15. The orange hue that is seen in some images is caused by reflection of the clamp holding the shard. A photo of the of the sample before breaking is referenced in each caption. Due to the rectangular shape, the sample of IM-MAR cast on steel was suitable to break multiple times, leading to more fracture surfaces to be inspected.

Given the irregular shape and cross-section of the samples, no useful information was gained from load and displacement measurements during the destruction of the samples. The inspection of the fracture surfaces didn't yield quantitative information either, but there are some observations to be made.

In multiple cases, such as figures 4.7.12a&b and sub-image a of the remaining figures in this section, display features reminiscent of mirror, mist, and hackle (figure 2.6.6). While the appearance is similar, the shape is erratic and no clear origin of the fracture, or mirror radius, can be identified.

Figure 4.7.13b displays a large mirror-like area, possibly originated from the thermal crack seen on the right of the sample. Other fractures show a variety of scratches and/or wave like structure, and a complete lack of mirror-like features.

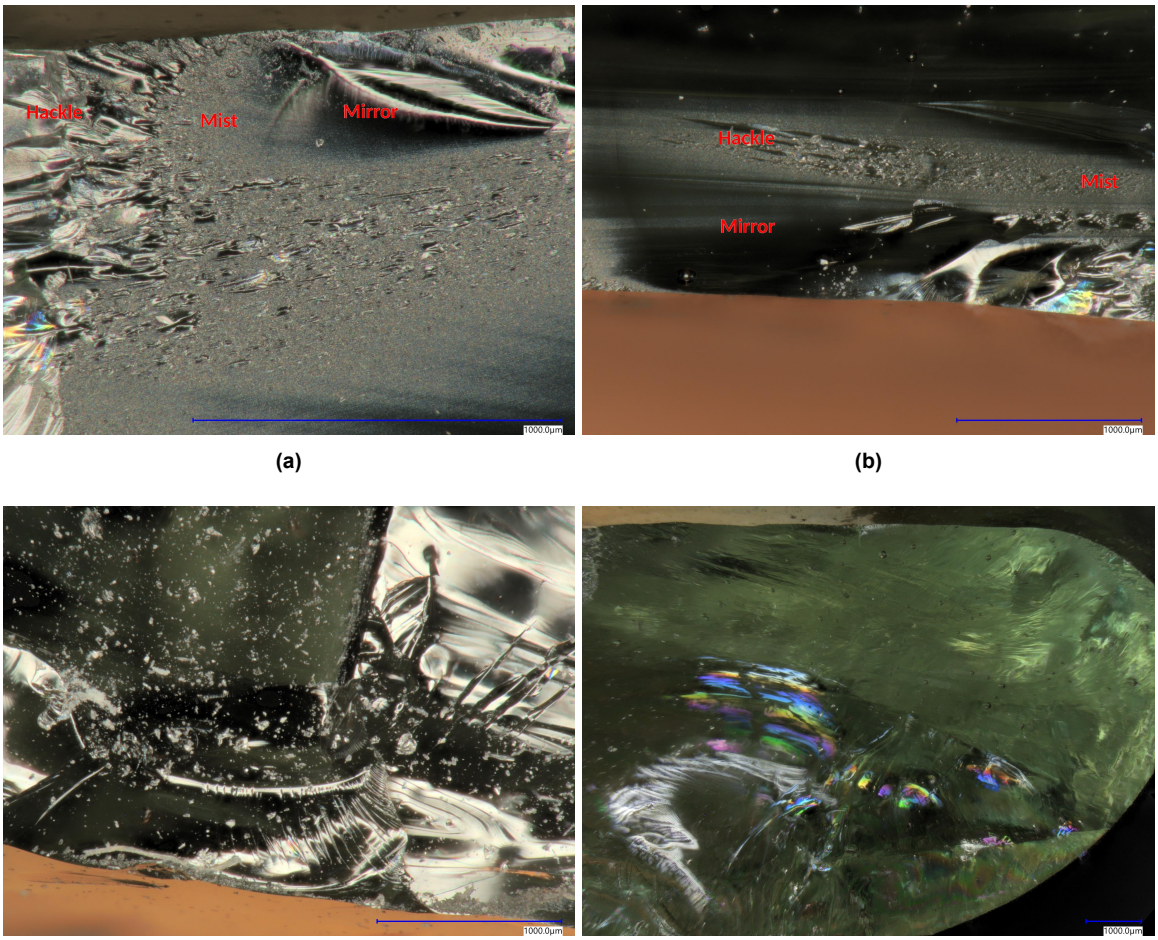

Figure 4.7.12: Micrographs of fracture surfaces of mix IM-MAR cast on steel (figure 4.7.2).

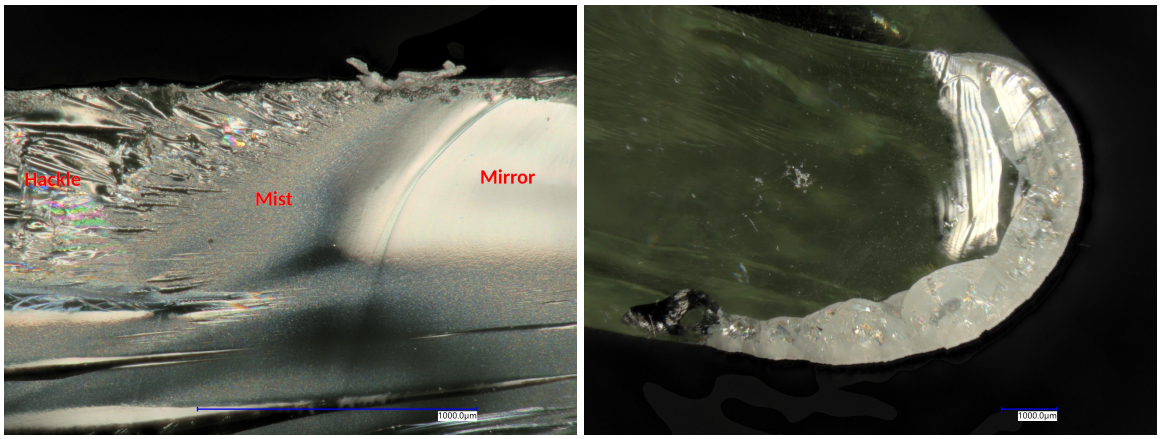

(a) (b)

Figure 4.7.13: Micrographs of fracture surfaces of glass IM-MAR (figure 4.7.1a).

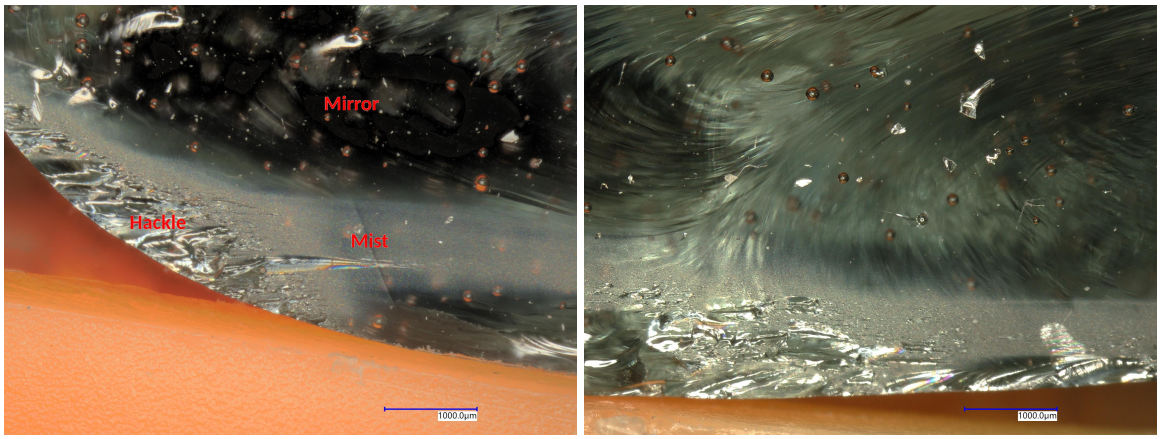

(a) (b)

Figure 4.7.14: Micrographs of fracture surfaces of glass IM-MOREC (figure 4.7.1b).

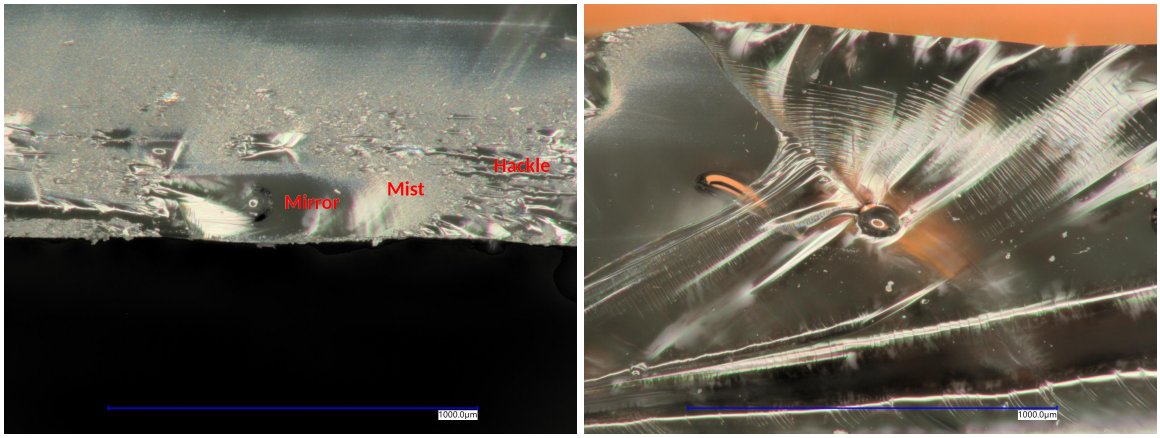

(a) (b)

Figure 4.7.15: Micrographs of fracture surfaces of glass IM-NOQ (figure 4.7.1c).

5

Discussion

In this chapter, the implications from the results presented in chapter 4 are discussed. As such the structure of the main sections is the same, while the subsections vary depending on relevant subjects to be addressed.

Section 5.1 covers the analysis of desert sand, and includes notes on accuracy of X-ray fluorescence (XRF) measurements and the subsequent estimates of mineral content. Furthermore the compositions found are grouped to form a basis for further discussion, and implications for glass making are considered.

The analysis of store bought components is used to verify that their use in synthetic batches is justified in section 5.2.

Modelling of viscosity and melting of unmodified desert sand is discussed in section 5.3. Discussion of the results presented in section 4.3 provides insight on both melt formation and melt behaviour. The reactions between the various minerals in desert sand leading to melt formation are further explored in section 5.4, by discussion of observations made during heating of binary mixtures.

The influence of benificiation on viscosity behaviour and specifically practical melting temperatures is discussed in section 5.5, and used to draw conclusions on composition requirements for creating a meltable desert sand glass.

Assessment of the synthetic mixtures produced based on the hypothetically benificiated desert sands is found in section 5.6. Composition, viscosity, and observed melting behaviour are compared to original desert sand in this section.

The properties of glasses resulting from melting of synthetic batches are discussed in section 5.7. The composition measured by XRF is discussed first, followed by discussion of visual inspection, and optical and mechanical characterisation. It is determined if the properties listed in chapter 1 were attained, and if not, what can be done to attain them in later efforts.

This page is left blank for reading convenience in print.

5.1. Analysis of desert sand

In this section, the analysis of the original desert sand is discussed. First, the precision of XRF-analysis and the mineral estimates will be addressed, followed by a general consideration of both chemical and mineral composition leading to identification of three groups as a basis for further discussion. The section is concluded with a discussion of the implications for the goal of making glass.

5.1.1. Accuracy

XRF & variation of composition in desert sand

First of all, it is of importance to realise that while the XRF results of oxide based mixtures are presented as a list of oxides, XRF does not detect the oxides themselves but rather the electron shell of the (semi-)metal contained within it, after which the oxide composition is calculated using the selected database of oxides.

Furthermore, as XRF is based on exciting electrons from a shell closer to the core of the atom or ion to a higher energy orbital, after which an characteristic X-ray is emitted upon relaxation to the original state, lighter elements such as carbon cannot be detected for lack of additional states to be excited to; this means that carbonates present will not register as such.

Coincidently, the carbonates found in desert sand will release CO_2 and convert to the oxides upon heating (see sections 2.3 and 2.4), so the results presented indicate the expected composition of the glass. For calculations of mineral composition based on XRF data, oxygen and CO_2 need to be factored in based on stoichiometric considerations.

The results of the XRF analysis are delivered by the software used with values up to 3 decimal places and an absolute error in wt% per oxide ranging from 0.1 wt% for the main components, to 0.001 wt% for the trace elements that occur in fractions in the order of 0.01 wt%. While this might be accurate for homogeneous material, desert sand is not.

Tables 4.1.1 and 4.1.2 show that for a repeated measurement of the same milling, these margins hold reasonably for the main components. For the trace elements it stands out that SO_3, NiO and MnO are detected in one measurement of the same milling, but not in the second pellet. When comparing the different millings of the same $\sim$5 g sampling, detected fractions start to deviate outside the margins specified, where the discrepancies in detected trace elements also increase.

Between samplings of the same batch, deviations increase, as the average deviation from the mean value of all measurements can be as high as 21 %, with even larger discrepancies between the highest and lowest recording (table 4.1.2). Variations in the large silica fraction are significantly higher in absolute values, but less severe relative to the measured value.

The consistency in results from repeated measurement of samples prepared from the same milling implies that the significant variations within the same batch are caused by variations in composition. Hence larger variations within deserts, or regions thereof, are to be expected. This is exemplified by some of the references from table 2.3.1, where samples from the same desert appear to vary as much as 15 wt% in silica content, and by a factor two in smaller fractions.

While the large relative variations in small fractions might seem insignificant in absolute values, they can have severe influences on the estimates of mineral content, as will become apparent in the next section.

This means that the XRF results presented, and results based on this data, should be interpreted with appropriate care, as they might not be representative. The small amounts sampled give a rough indication of the elements present, and some of the proportions. The elements detected in amounts $<$0.1 wt% should be taken as an indication that some *might* be present, rather than an absolute quantity. Conversely, an element not being detected by XRF, does not mean that it is not present in small amounts.

Presenting data as received therefore would not be reasonable, and it was decided to round composition data presented in this thesis to one decimal place. While this still might be a representation too precise for the limited certainty, removing all decimals would not show the apparent variations in the smaller fractions.

Estimation of mineralogical composition

When inspecting table 4.1.5, the most obvious indication that the method of estimation, described in section 3.2.2, is an oversimplification are the negative values occurring in the calcite column, and consequently under loss on ignition (LOI), which is directly based on the estimated amount of carbonates.

As the estimate of $CaCO_3$ is based on the amount of Ca left over after distributing it over $CaAl_2Si_2O_8$ and $MgCa(CO_3)_2$ in ratio to the elements that are assumed to be in one mineral only, the assumption that all Al is in feldspars and all Mg is in dolomite both could 'consume' more Ca than is the case in reality, which leads to an underestimation of the Ca left over at the end of the series of calculations, and consequently in the estimate of the $CaCO_3$ fraction.

Considering the feldspars, a possible overestimate caused by the assumption that Al is only found in this type of mineral, will 'pile up' in the anorthite fraction, as this is the last one estimated. The assumption of stoichiometry should not cause severe deviations regarding the total amount of feldspar; while the exact ratio of alkali and plagioclase feldspars remains unclear, the three feldspars used for the estimates occur in solid solution series.

For the carbonates this assumption is more likely to be a source of inaccuracy, as was considered in section 2.3 and figure 2.3.4. Calcite and dolomite form a system with $CaFe(CO_3)_2$ (ankerite), and this set of carbonates will most likely exist in a combination of mixtures of the three in real desert sand. If this is the case, not accounting for iron leads to an additional underestimate of the LOI. Conversely, calcium and magnesium being present in other minerals than the ones considered, might have an opposite effect and lead to overestimation of the amount of CO_2, which appears to be the case for the sands containing large estimated amounts of carbonates.

The estimates of feldspars are based on the determination of concentration of Al_2O_3, Na_2O, and K_2O, which were shown to be subject to quite significant variations between samplings in section 5.1.1. This implies that the amount of feldspars could vary considerably between samples from the same batch.

Table 5.1.1 displays results of an X-ray diffraction (XRD) analysis of a desert sand sample commissioned by Maana Luxembourg, and offers a multitude of possible causes for inaccuracies in the estimates. While in this specific sample potassium appears in feldspars only, sodium occurs as part of the 2:1 layer silicates as well. Aluminium, magnesium and calcium are detected in multiple minerals that are not feldspars, calcite, dolomite or quartz, but the assumption that the bulk of these elements is in these minerals appears to be quite realistic.

The presence of minerals containing H_2O and/or OH groups, not detectable by XRF, but possibly contributing to the LOI by dehydrating upon heating, and of influence on viscosity behaviour, is revealed by table 5.1.1 as well.

For further confirmation, the inductively coupled plasma (ICP) results from the same analysis, found in table 5.1.2, were used to preform the same calculation as was done for the samples investigated during this project, resulting in table 5.1.3. As the method employed here cannot differentiate between alkali and plagioclase feldspars, the totals of the main mineral groups are compared in table 5.1.4.

Interestingly in this case an underestimate of the total amount of feldspars occurs, while an overestimate is most likely according to the reasoning above. This is possibly explained by the fact that $CaAl_2Si_2O_8$ was used in the estimate, compared to $(Na,Ca)AlSi_3O_8$ for the plagioclase series in the XRD results.

The overestimate of carbonates finds an explanation in the presence of epidote and 2:1 layer silicates, both containing calcium assumed to be in calcite and dolomite. Magnesium is found in the layer silicates as well, also contributing to the mismatch.

In conclusion, while there are deviations in the comparison here, and most likely different ones for radically different sands investigated, this method appears to give a reasonable order of magnitude estimate of the main minerals.

If more precise data on (mineral) composition of a specific desert sand is required, additional XRD and/or ICP analysis could be considered. To gauge variation and possibly improve the method of estimation by considering additional minerals, repeated measurements of different samplings from the same region could be employed.

Table 5.1.1: Quantitative bulk mineralogical composition of sample ABU in wt%, from [51].

Mineral	Theoretical formula[3]	Abu 1
Non-layer silicates		
Silicates		
Quartz	SiO_2	49.7
Alkali Feldspar	$(K,Na)AlSi_3O_8$	9.1
Plagioclase	$(Na,Ca)AlSi_3O_8$	7.9
Epidote	$Ca_2(Fe,Al)_3(SiO_4)_3(OH)$	0.4
Garnet*	$(Mg,Fe,Mn)_3Al_2(SiO_4)_3$	<0.1
Zircon*	$ZrSiO_4$	<0.1
Carbonates		
Calcite	$CaCO_3$	27.7
Aragonite	$CaCO_3$	0.3
Dolomite	$CaMg(CO_3)_2$	0.7
Ankerite	$Ca(Mg,Fe,Mn)(CO_3)_2$	0.8
Celestine*	$SrCO_3$	0.1
Oxides		
Rutile	TiO_2	0.1
Anatase	TiO_2	0.1
Hematite	Fe_2O_3	0.1
Magnetite**	Fe_3O_4	0.1
Total non - layer silicates		**96.9**
Layer silicates		
Chlorite	$(Mg,Fe)_5Al(Si_3Al)O_{10}(OH)_8$	0.5
Kaolinite	$Al_2Si_2O_5(OH)_4$	0.2
2:1 layer silicates*	$(Ca,Na)_{0.3}(Mg,Fe)_3(Si,Al)_4O_{10}(OH)_2 \cdot 4(H_2O)$	2.4
Total layer silicates		**3.1**

* The unambiguous identification of these minerals is not possible from this bulk mineralogical analysis. The results could be checked and complemented with additional analysis performed on heavy minerals and clay minerals extracted from the bulk sample.

** Or other spinel minerals such as for example Chromite ($FeCr_2O_4$).

[3] These formulae are general formulae and do not necessarily correspond to the composition of the minerals in these specific samples.

Table 5.1.2: Chemical composition of sample ABU in wt%, determined by ICP, minor elements (PPM) omitted [51].

Element	Unit	Detection limit	Abu 1
SiO2	%	0.01	60.94
Al2O3	%	0.01	3.96
Fe2O3	%	0.01	0.93
MnO	%	0.001	0.027
MgO	%	0.01	1.25
CaO	%	0.01	17.66
Na2O	%	0.01	0.93
K2O	%	0.01	1.14
TiO2	%	0.001	0.185
P2O5	%	0.01	0.03

Table 5.1.3: Estimate of mineralogical composition and LOI of sample ABU using ICP analysis from [51] (table 5.1.2). Measured LOI(m) from same reference.

$KAlSi_3O_8$	$NaAlSi_3O_8$	$CaAl_2Si_2O_8$	$MgCa(CO_3)_2$	$CaCO_3$	SiO_2	LOI(c)	LOI(m)
6.7	7.9	3.3	5.2	27.2	49.7	14.7	12.9

Table 5.1.4: Comparison of total (wt%) of main mineral groups in sample ABU resulting from estimate from the method used here and XRD-analysis by Qmineral Analysis and Consulting [51].

	Feldspars	Carbonates	Quartz
XRD	17.0	31.6	49.7
Estimate	14.6	32.4	49.7

5.1.2. General discussion of composition

When compared to the general trend of desert sand compositions found in the literature (table 2.3.1), the two most remarkable results in table 4.1.3 are samples AE2 and MAR, which stand out by very high CaO content. In the case of AE2, it was assumed that it was a sample from a beach instead of a desert, and therefore not further considered. Sample MAR might be as well, but contains a high enough silica fraction to merit further investigation.

The second important deviation is the large number of samples on the high end of the silica scale: while the maximum in the selection from the literature is about 83.5 wt%, more than half of the samples investigated for this project exceed 90 wt%.

Upon closer inspection, this appears to be connected to the location of the source, marked on a satellite image in figure 5.1.1. The trend seems to be that most of the high silica samples originate from the continent of Africa.

Another trend that appears is that all samples in this set from the Asian continent (IN1, KZ1 and MN2), contain relatively large amounts of Al_2O_3, and consequently a high estimated feldspar content. Furthermore, the samples containing large amounts of CaO and MgO, resulting in high estimates of carbonate content, are collected from (near) coastal regions. Sample JO1 appears to be an exception here, given the high SiO_2 content, while being from a middle eastern region relatively close to the coast.

As the data set considered is small and even in this set counter examples can be found, it would be overzealous to draw any definitive conclusions, but further investigation of similar trends might prove useful in finding appropriate locations.

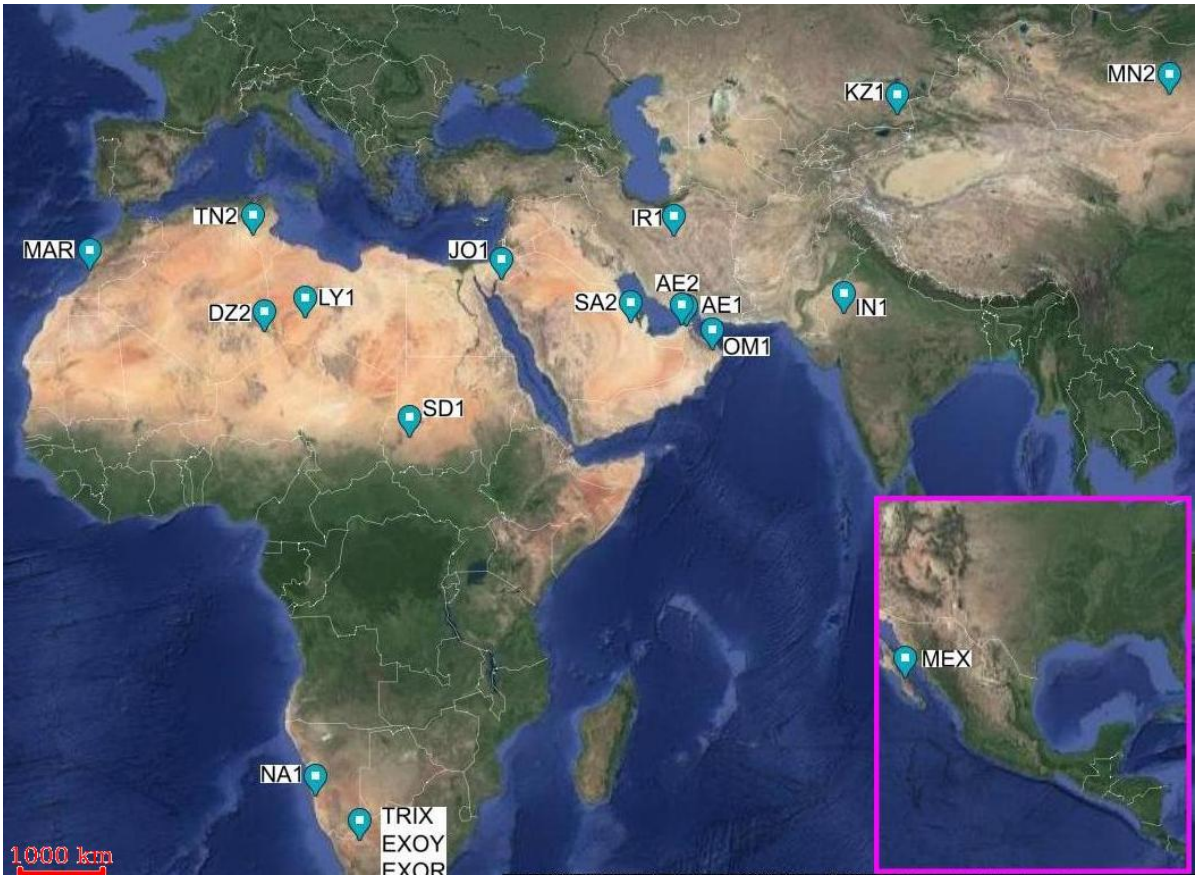

Figure 5.1.1: Approximate locations of origin of desert sand samples, store bought sands are a more rough approximations as 'South Africa' is the most specific designation. Satellite imagery acquired from https://www.google.com/maps/

Regardless of location, the sand investigated here can be roughly categorized to three groups based on tables 4.1.5 and 4.1.3:

1. >90 wt% SiO_2 (including silica contained in feldspars)
2. >25 wt% feldspars
3. >25 wt% carbonates

Note the difference between high silica, and high quartz content. Especially the high feldspar samples, such as NA1, MN2, IN1, KZ1 and MEX, contain more than 70 wt% silica, while the estimated quartz content can be as low as 36 wt%.

Some of the 'high carbonate' samples contain significant feldspar fractions (e.g. samples MAR and IR1). This considered, the boundaries selected are quite arbitrary, but still provide a useful framework for further discussion.

5.1.3. Implications for glass making

With reference to figure 2.2.5, all samples with the exception of MAR fall in the glass forming region, and should be able to form a glass, under the condition that the practical melting point can be reached. Given the high amount of alkaline earth oxides, the alumina in sample MAR will be included as a network former, possibly stabilizing the melt enough to still form a glass.

By inspecting table 4.1.4, it can be seen all sands outside of the high quartz group contain a molar percentage of modifiers higher than the amount of Al_2O_3: glasses formed will be of peralkaline (figure 2.2.8) composition, causing alumina to act as a network former.

In high silica sand, the amount of Al by mole typically seems to be close to the available charge compensation in the form of modifying oxides, creating a glass with equal amounts of Al and charge compensation. Figure 2.2.7 implies that this would mean Al would still become part of the network if melted to a glass.

Within the margins of uncertainty sketched in section 5.1.1, this is both in line with the assumption that the bulk of the alumina is contained in feldspars, as stoichiometric feldspar of any kind carries the exact amount of modifiers for charge compensation of the alumina. Any additional modifiers in the form of alkaline earth oxides will take the mixture into peralkaline territory, meaning any glass from desert sand components will include most alumina present in the network.

Melting wise, the high quartz sands could turn out problematic for their lack of low melting temperature components and high viscosity, this will be further discussed in section 5.5.

From table 5.1.1 and the literature, it appears that part of the iron present is contained in complex carbonates and silicates, often accompanied by modifiers. In the silicates the bulk of the modifiers is found in feldspars containing no Fe, but in the carbonate case, removal of iron might lead to an increase of viscosity as modifiers are removed as well.

Continuing on the subject of iron, in most sands there are quite significant fractions of Fe_2O_3 present, far beyond the ~0.1 wt% found in section 2.7. Achieving the transmission requirement for the unmodified molten desert glass will therefore be unlikely.

Other absorbing species are detected in trace amounts only. Most prevalent is Cr_2O_3, which is found in nearly all desert sands. Further possible causes for lack of transmission are detected less often, but NiO and CuO occur in trace amounts in multiple sands. In all cases, the absorption caused by these elements is most likely insignificant compared to the amounts of Fe.

5.2. Analysis of components

From the XRF-analysis of the store bought components it becomes clear that SO_3 is detected in gypsum. This leads to the conclusion that the available selection of desert sands does not contain significant fractions of the mineral, as SO_3 occurs only in trace amounts. For this reason it was excluded from further analysis and the estimation of mineral content.

Comparing each remaining component to the stoichiometric version, as shown in tables 4.2.1 and 4.2.2 respectively, reveals some deviations from the stoichiometric composition implied by the supplier. The variations in composition of the sodium feldspar (NaSP) and quartz (Q) are minor, and can be explained by uncertainty of the XRF, reasonable deviations from stoichiometry and contamination to be expected in affordable chemicals. The potassium feldspar (KSP), calcite (CAL) and dolomite (DOL) stray further from the stoichiometric composition, which implies that additions were made to ease the life of the home ceramic maker.

The most obvious deliberate addition is the amount of Na_2O in sample KSP. As there also is some CaO present and there is no way to tell from these measurements if this is also contained in feldspars, hence no exact determination of the melting temperature is possible from this data. An estimate based on the ratio between the two oxides can be made; there should be about 40 wt% albite present. Disregarding other contamination, this would lead to a melting temperature of approximately 1200 °C according to figure 2.3.3a.

While less clear, the deviation from stoichiometry in dolomite (DOL) to the side of magnesia puts the composition out of range of the diagram in figure 2.3.4. This could imply that either the diagram is incomplete, or that magnesium carbonate or oxide was added. Whichever is the case, the higher magnesium content can lead to a slight increase in viscosity when the mixture is added to a silicate melt, compared to stoichiometric dolomite, due to the higher ionic field strength (IFS) of the smaller ion with similar valence, as discussed in section 2.5.4. Conversely the lower atomic weight of Mg could mean that there are more modifiers present leading to a decrease in viscosity.

Finally there is quite some silica found in the calcite (CAL). While this will increase the overall viscosity compared to similar amounts of stoichiometric calcite, it might have been added to accelerate the reaction between the calcite and other components in a less than perfectly mixed batch.

All things considered, the store bought components seem acceptable substitutes for the components found in desert sand, as they contain only compounds that were found in sand samples as well.

5.3. Melting of desert sand

The results of modelling the viscosity behaviour of the sands, presented in figure 4.3.1 and table 4.3.1, are consistent with the literature as discussed in section 2.5. High silica sands, while possibly inaccurate because of the range of the model, appear to have excessive melting points and overall high viscosity.

The general shape of the curves predicted for the high feldspar sands is similar, but moved to lower temperatures. The slope of the curve at the annealing point of melts from this group containing large amounts of Ca, is slightly higher, which is explainable by the lower relative silica fraction (see table 4.2.2) in anorthite compared to the alkali feldspars. This is illustrated by figure 5.3.1, containing the predicted viscosity curves of stoichiometric feldspar end members, found on the corners of the diagram in figure 2.3.2, and quartz.

Sands containing larger fractions of carbonates are shown to have significantly lower practical melting temperatures. This is also in line with theory discussed in sections 2.2.2 and 2.5.4, as carbonates only add modifiers to the melt.

The heating rate and power curves recorded, displayed in sections 4.3.2 to 4.3.3, corroborate that the melting of feldspars and reactions between quartz and other components, discussed in section 2.4, take place.

The curves resulting from heating high silica sands, found in figures 4.3.2, 4.3.3 and C.2.1 to C.2.10, do not show significant deviation from the curve of nearly pure quartz (figure 3.2.4), when accounting for noise in the system. The resulting samples are clearly recognisable as sand (figure 4.3.5). This is hardly surprising, as the melting temperature of quartz (1713 °C) was not reached.

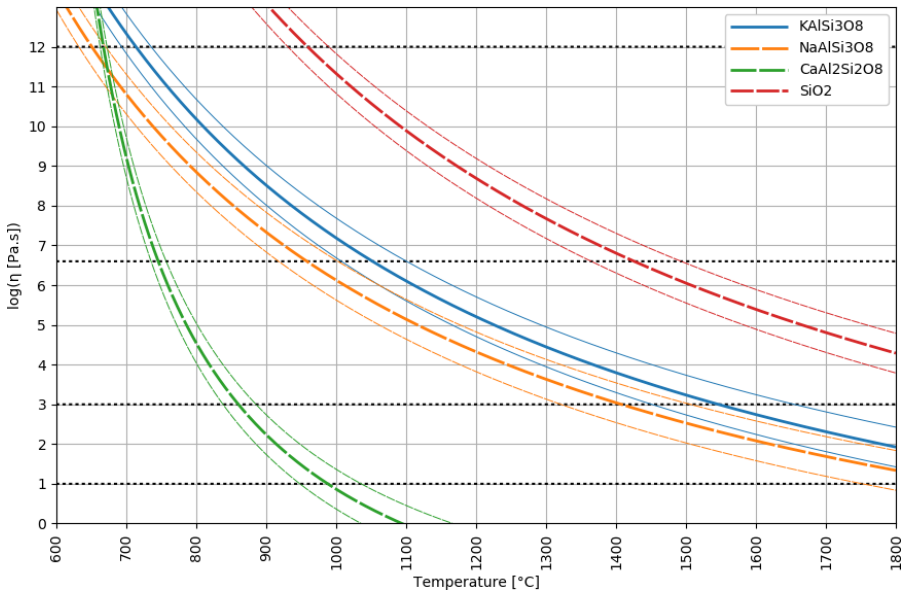

Figure 5.3.1: Calculated viscosity curves including ±0.5 log-unit margin for stoichiometric SiO_2 based components. Silica, while out of range of the model, is added for reference.

The heating rate and power curves for the sands with lower quartz content show some variation between similar samples, which can be explained by any number of causes. Besides the differences in chemical composition and mineral content, the variation grain size and distribution will lead to different heat transport to the surface, at which the pyrometer measures. This will influence the response of the controller and thus the exact output. The exact melting trajectory will also influence the microwave susceptibility of the melt, again influencing the controller response. The interested reader is referred to appendix A for a more detailed discussion.

While the exact shape of the plots for the feldspar containing sands differs (figures 4.3.6, 4.3.7, and C.2.11 to C.2.17), all show the onset of melting effects, between 1200 °C and 1400 °C, which was expected on the basis of figure 2.3.3. It appears samples with relatively high estimated anorthite content (e.g. MEX and IN1) start melting at higher temperatures, but given the uncertainty in emissivity and thus temperature reading, this cannot be confirmed. As the first noticeable effect occurs in sample SA2, it could be said that the detection limit of the system is close to 15 wt% of summed feldspars.

The plots resulting from carbonate containing sands (figures 4.3.12, 4.3.13, C.2.18 to C.2.21) are characterized by a drop in power for a number of cycles just under 1000 °C, possibly explained by the hot CO_2 being released rising to the surface. The sudden changes observed upwards of 1400 °C, in some cases until the maximum temperature is reached, are likely to be caused by eutectic reactions of CaO and SiO_2, expected at 1436 °C and 1455 °C. In addition, the process at high temperature appears to take place in multiple steps in samples AE1, IR1, and MAR (figures C.2.19 to C.2.21), possibly caused by the formation of multiple liquids of different composition at various temperatures.

The resulting samples show a clear distinction. In the high feldspar 'glasses' in figure 4.3.9, the original quartz grains are clearly visible in the mass of glass. The fraction of remaining grains seems inversely proportional to the (estimated) amount of feldspars, as samples NA1 and MN2 display relief in the surface, while the grains in samples IN1 and KZ1 seem completely engulfed.

Figure 4.3.15 shows a different trend for the high carbonate sands. While grain like shapes are still visible in samples OM1 and AE1, they appear to be partially dissolved.

This differences can be explained by the fact that the feldspars melt, but as they contain a high amount of silica, they will be very viscous (see figure 5.3.1), making dissolving of remaining grains less likely. In the carbonate case, a process not unlike soda lime-melting takes place. The CaO left behind after CO_2 release reacts with the quartz, forming a relatively fluid liquid that is able to dissolve more of the quartz.

When the practical melting point of the mixture is reached, the primary melt phases that have formed contain less SiO_2 than the average composition and thus are more fluid than the complete melt would be, accelerating the dissolving process. Based on the resulting glasses, as seen in figure 4.3.15, it appears that the predictions made using Giordano's model [36] are quite accurate; sample IR1 was heated to ∼the calculated practical melting point, and is shown to be in the processes of dissolving the remaining grains. Sample MAR was heated far past the calculated practical melting point and shows no remaining grains. All other samples found their calculated practical melting point out of range, and have not formed a homogeneous melt, as was predicted by the model.

The crystallisation seen in sample MAR is not unexpected, as the silica content is low and CaO is known to cause crystallisation as was discussed in section 2.2.2. Since the cooling was uncontrolled, no conclusions can be drawn on critical cooling rate. If the eventual glass used for production is CaO rich, the tendency to devitrify merits further research. To prevent crystallisation, the critical cooling rate for a specific composition could be determined to ensure it is exceeded, or the maximum CaO content for a certain cooling rate could be found.

Finally, the anomalous effect observed in samples MEX (all figures on page 54) and IN1 (figures C.2.12 and C.2.13), is unlikely to be caused by gas formation, as all dehydration and decarbonisation reactions found in the literature take place under 1000 °C, while in both cases the effect occurs around 1550 °C. As this is close to the melting temperature of anorthite, and these samples have the highest two estimates of content of this mineral (in this data set), one could suspect that the melting of this mineral is involved. It can also not be excluded that the estimates are off, and another mineral is the cause of sudden expansion, hence this will require further research.

In conclusion, the suspicion that melting of desert sand without modification would be difficult is confirmed. While melting reactions occur when minerals other than quartz are present, the process is not completed in most cases due to a too high a practical melting point. The two sands that formed a glass are both rich in carbonates, but contain a significant feldspar fraction as well. Giordano's model, though there are limited examples in this set of data, appears to reasonably predict the temperature needed, at least within the ±∼40 °C uncertainty in the temperature measurements.

5.4. Formation of primary melt phases

The heating rate and power plots recorded for observation of specific melting reactions, shown in figure 4.4.1, show similar characteristics to the ones recorded by heating desert sand, but there appear to be some curiosities.

Most clear is the different appearance of the curve for mixture QCAL in figure 4.4.1a, where the release of CO_2 is expected close to 990 °C, while the first deviation from the quartz curve (figure 3.2.4) is seen between 1000 °C and 1100 °C. The sudden reaction recorded for the high carbonate desert sands appears to be absent until past 1550 °C, where eutectic reactions could take place around 1436 °C and 1455 °C. This ∼100 °C discrepancy is best explained by an error in the emissivity settings of the pyrometer. As seen in figure 3.2.3, the deviation in temperature reading increases with temperature, explaining the larger deviation from expectation for the second artefact at higher temperature.

Furthermore this graph shows a different shape of the plot at the point of CO_2 release, and an unusual amount of scatter. This could be caused by either misalignment of the pyrometer, or the released gasses being trapped in the compacted fine powder.

Conversely, figure 4.4.1b, for mixture QDOL, shows the first effects at relatively low temperature, possibly caused by an emissivity error as well. The more likely explanation is found in one of the three component reactions in table 5.4.1. In the literature review, binary reactions with SiO_2 were considered, while multiple elements are present. Given the uncertainty in temperature measurements, it is impossible to tell which exact reaction takes place, but the first reaction could occur at 1320 °C, followed by a multitude of possibilities before the first SiO_2−CaO eutectic, discussed in section 2.4, is expected. Assuming the estimate of emissivity was correct in this case, this reaction could be the cause of the peak in heating rate and dip in power around 1450 °C.

Table 5.4.1: Invariant points in the ternary SiO_2−CaO−MgO system [29].

Phase reaction	Temperature (°C)	Composition of liquid (percent by weight)		
		MgO	CaO	SiO_2
β-$CaO{\cdot}SiO_2 ss + SiO_2 \rightleftharpoons \alpha$-$CaO{\cdot}SiO_2 + L$	1336	7. 2	31. 3	61. 5
β-$CaO{\cdot}SiO_2 ss + SiO_2 + CaO{\cdot}MgO{\cdot}2SiO_2 \rightleftharpoons L$	1320	8. 0	30. 6	61. 4
$CaO{\cdot}MgO{\cdot}2SiO_2 \rightleftharpoons L$	1391. 5	18. 62	25. 9	55. 48
β-$CaO{\cdot}SiO_2 ss + CaO{\cdot}MgO{\cdot}2SiO_2 \rightleftharpoons L$	1358	11. 5	34. 4	54. 1
β-$CaO{\cdot}SiO_2 ss \rightleftharpoons \alpha$-$CaO{\cdot}SiO_2 + L$	1368	10. 8	35. 3	53. 9
β-$CaO{\cdot}SiO_2 ss + CaO{\cdot}MgO{\cdot}2SiO_2 + 2CaO{\cdot}MgO{\cdot}2SiO_2 \rightleftharpoons L$	1350	12. 6	36	51. 4
α-$CaO{\cdot}SiO_2 + 2CaO{\cdot}MgO{\cdot}2SiO_2 \rightleftharpoons \beta$-$CaO{\cdot}SiO_2 ss + L$	1360	12. 3	36. 7	51
$2CaO{\cdot}MgO{\cdot}2SiO_2 + CaO{\cdot}MgO{\cdot}2SiO_2 + 2MgO{\cdot}SiO_2 \rightleftharpoons L$	1357	20. 2	29. 8	50
$2CaO{\cdot}MgO{\cdot}2SiO_2 + 2MgO{\cdot}SiO_2 \rightleftharpoons CaO{\cdot}MgO{\cdot}SiO_2 + L$	1430	22. 3	33. 3	44. 4
$2CaO{\cdot}MgO{\cdot}2SiO_2 \rightleftharpoons L$	1454	14. 79	41. 14	44. 07
$2CaO{\cdot}MgO{\cdot}2SiO_2 + CaO{\cdot}MgO{\cdot}SiO_2 \rightleftharpoons 3CaO{\cdot}MgO{\cdot}2SiO_2 + L$	1436	18. 3	39	42. 7
$CaO{\cdot}MgO{\cdot}SiO_2 + 2MgO{\cdot}SiO_2 \rightleftharpoons MgO + L$	1502	26. 4	32. 1	41. 5
$3CaO{\cdot}MgO{\cdot}32SiO_2 + CaO{\cdot}MgO{\cdot}SiO_2 \rightleftharpoons MgO + L$	1490	22. 3	37. 3	40. 3
$3CaO{\cdot}MgO{\cdot}2SiO_2 \rightleftharpoons MgO + 2CaO{\cdot}SiO_2 + L$	1575	18. 2	43. 0	38. 8
$2CaO{\cdot}SiO_2 + 2CaO{\cdot}MgO{\cdot}2SiO_2 \rightleftharpoons 3CaO{\cdot}MgO{\cdot}2SiO_2 + L$	1400	6. 8	49. 5	43. 7

The melting of the feldspar rich mixtures, shown in figures 4.4.1c and 4.4.1d, poses a similar problem. The increase occurring in the scatter around 1400 °C in both cases, implies that a reaction between the molten feldspars and the still solid alkaline earth oxides takes place, but it remains unclear which specific reaction is occurring. The options are more plentiful due to the presence of Al_2O_3, K_2O, and Na_2O from the feldspars. The similarities between the two mixtures could imply that MgO does not participate in the reaction, but it could also remain undetected due to the lower concentration in this mixture.

All combinations of components available where shown to form a melt between 1100 °C and 1450 °C, an overview of possible events is given in figure 5.4.1.

While plagioclase feldspars where unavailable, it is likely that a combination with any of the other components will lead to a melt as well. The process in this case would require further research, as the molten state could be reached via eutectic reactions at lower temperature, dissolution by lower melting components, or dissolving of the remaining component(s) by the molten plagioclase when the melting temperature is reached. If there is pure anorthite present, that will be 1550 °C at most, but likely lower, given that feldspars occur in solid solution series in nature. This is corroborated by the significant portions of molten material formed from feldspar rich sand in section 4.3.

Based on this information, it can be concluded that the governing factor in the formation of a melt from desert sand components is the practical melting temperature of the overall mixture.

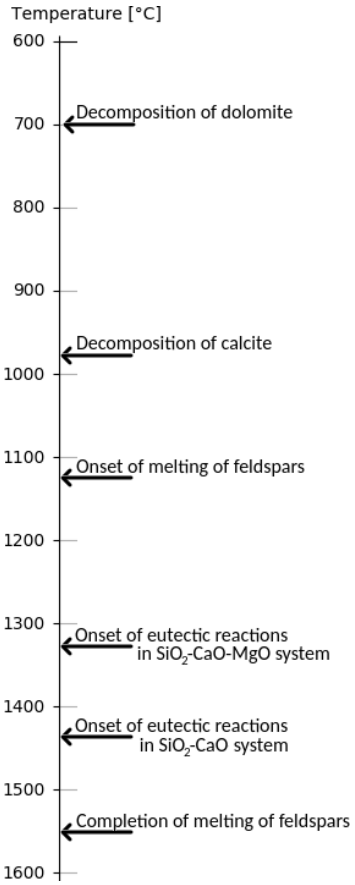

Figure 5.4.1: Overview of possible events leading to melt formation in a desert sand batch.

Ideally, to limit processing times and energy consumption, the composition is tailored to a practical melting point of ∼1550 °C or lower, as then the melt would be fluid enough for further fining at the moment all melting reactions are initiated. Further heating would require additional energy, and probably have a detrimental influence on the equipment used. Eventually a trade-of could be made between the (energy) expense of benification, and the additional temperature requirements for higher melting point mixtures. The practical melting point is addressed in the next section.

5.5. Hypothetical beneficiation

Estimated mineralogical compositions were subjected to the following hypothetical operations. The effect on the practical melting point of the various sands is discussed in order of appearance after the list, where applicable including justification of selections for imitation in a synthetic batch.

- (1) No modification.
- (2) 5 % increase in feldspar content.
- (3) 50 % increase in feldspar content.
- (4) 50 % increase in carbonate content.
- (5) 50 % increase in both feldspar and carbonate content.
- (6) Removal of all quartz.

As was discussed in section 5.1.3, the ordering of unmodified sand samples by calculated practical melting point in column (1) of table 4.5.1, is in line with theory as discussed in section 2.5.4; the viscosity decreases with decreased silica content and higher concentration of modifiers.

Sample MAR has a very attainable practical melting point to begin with, hence it was decided to imitate this sample in its original state, as limiting the processing steps needed to produce glass would increase efficiency of the final system.

Column (2) of the table contains the result of the suggested 5 % increase in feldspar content. As the increase of the 'benificiated' mineral takes place at the expense of the remaining minerals, the influence on the practical melting temperature depends on the overall composition. In the carbonate rich sands, the relative amount of carbonates decreases, causing an increase in melting temperature. When the main component besides feldspars is quartz, the effect will be opposite. This trend is continued in column (3), resulting from a 50 % increase in feldspars, yielding a similar but stronger change in melting temperature.

The operation of increasing the carbonate content by 50 %, as found in column (4), affects the high carbonate sands the most. Under this operation samples IR1, AE1, and OM1 all display attainable melting temperatures. An attempt was made to imitate each composition, but this proved difficult due to the lack of plagioclase feldspars and limited freedom in adapting the CaO to MgO ratio in the available raw materials. As the chemical compositions can be considered relatively similar, it was decided to imitate these samples as a group.

Increasing both feldspar and carbonate content by 50 %, of which the calculated melting temperatures are shown in column (5), did not yield improvements in melting temperature compared to increasing only one of the mineral groups, discussed in previous paragraphs (except for sample MEX, which is included in the last group). It needs to be noted that benificiationg all minerals except quarts could lead to large waste streams, depending on initial composition. Since melting was the goal, and this can be reached by less extreme operations, calculated compositions from this operation were not imitated.

Note that the additional increase in Al_2O_3 content from increasing the feldspar content could have a beneficial effect on glass stability and mechanical properties due to increased connectivity in the glass network, when compared to increasing only the carbonate content. This could be investigated when optimisation is required.

Removing all quartz from the sand yields a glass forming mixture only for the samples that contain large fractions of feldspars. Sample IR1 becomes meltable, but is already included in the selection for the increased carbonates mixtures. The remaining compositions selected for imitation are samples KZ1, IN1, and MEX.

Removal of all quartz also might work for the high silica sands, some of which appear to contain a (small) fraction of feldspars, but this would lead to disposal of most of the input material as most of it is quartz for these sands. This series of calculations would also lead to a set of hypothetical compositions based on a small fraction of a rough estimate, making the accuracy very questionable. Therefore this group was disregarded for this operation.

The selected compositions and calculated imitations are shown in table 4.5.2. The listed compositions all have a silica content around 55 wt%, this puts the practical melting point on the edge of what is attainable (at this time) for the feldspar based compositions, while there is some headroom for increase of silica content in the carbonate case, still leaving a meltable mixture.

Besides SiO_2 and Al_2O_3 there are no significant fractions of (conditional) network formers found in this selection of desert sands, it can therefore be concluded that bringing down the overall silica content of any mixture of desert sand components to $\lesssim$55 wt% will most likely lead to a mixture that will reach the practical melting point under 1650 °C, while this percentage can be slightly higher for carbonate rich sands lacking feldspars.

The selected benificiation operations explored were chosen quite arbitrarily, and in practice a tailored solution for the target desert can be found. Any of the steps undertaken here, in larger or smaller increases than 50 %, could be considered, as could benificiation of specific minerals (if possible), instead of mineral groups. Employing the waste stream of silicon production for the PV-cells could provide additional freedom in adapting the composition of the produced glass, while also increasing efficiency of the system.

While it is difficult to be specific, it can be concluded that desert sands containing significant fractions of carbonates, feldspars, or both, can be benificiated to be meltable. With reference to table 4.1.5, it appears that if the amount of quartz exceeds ~50 wt% in the original sand, heavy benificiation with large waste streams will be necessary to produce a mixture with an attainable practical melting temperature.

Summarizing, from the hypothetical benificiation efforts it can be concluded that:

- Any combination of desert sand components will be meltable if the silica content is ~55 wt%.
  - For feldspar rich sands this can be achieved by removal of all quartz.
  - For carbonate rich sands this can be achieved by increasing the carbonate fraction.
- Sand containing >50 wt% quartz is relatively unsuited as raw material for glass production.

5.6. Assesment of synthetic batches

When comparing the calculated composition of the synthetic mixtures to the target compositions in table 4.5.2, the result of the lack of plagioclase feldspars becomes clear: in all cases the alumina content is lower in the imitations, as adding more alumina using available materials would also increase the Na_2O and/or K_2O content. The lack of alumina is compensated by an increased silica concentration. The CaO concentration was compensated by increasing the fraction of material CAL, hence is closer to the values found in the ‘benificiated’ compositions.

The effect of the less than perfect imitations on the calculated viscosity curves can be observed in figures 4.6.1 to 4.6.3, where the synthetic mixtures are compared to the (‘benificiated’) compostions they were meant to approximate.

Mixture IM-MAR (figure 4.6.1) is predicted to be more viscous in the high temperature range, but as the original has a low practical melting point, the resulting mix is still meltable within current limitations. A similar observation can be made for mixture IM-MOREC (figure 4.6.2), where the viscosity curve for the mixture is calculated to be higher than the ‘benificiated’ curves, but still within the 0.5 log-unit margin and a reachable practical melting point. In both cases the shape of the curve is similar.

The deviation from the target curve is most clear for mixture IM-NOQ (figure 4.6.3), which is to be expected given the mix is mostly feldspar based. The lower alumina content in the imitation leads to a lower annealing temperature, but slightly higher practical melting point. Again the uncertainty margins overlap, and the mixture was deemed an acceptable imitation.

The heating rate and power plots resulting from melting the synthetic batches, displayed in figures 4.6.4 to 4.6.6, show familiar characteristics. As was noted in section 4.6.2, the onset temperatures seem to be on the low side in all cases. This means the intended overestimate of the emissivity was successful, as the actual temperature was higher than the recorded temperature.

Mixture IM-MAR (figure 4.6.4) appears to melt in multiple smaller steps as was seen in multiple previous heating plots in sections 4.3 and 4.4. The initial melting of feldspars seen in the original (figure 4.3.13) was not detected, possibly due to the difference in grain size and heat transport in the crucible.

While mixture IM-MOREC (figure 4.6.5) also shows multiple steps after the first clear reaction, the first one is by far the most clear. This can be explained by the higher dolomite fraction in this sample, as more eutectic liquid can be formed at lower temperature via the reactions discussed in section 5.4.

As the main component of mixture IM-NOQ is feldspars, the shape of the heating rate and power curve in figure 4.6.6 is within expectations, and quite similar to the earlier combinations of feldspars and carbonates displayed in figures 4.4.1c and 4.4.1d.

In conclusion, given the limited raw materials available in this study, the similarities in composition, and calculated and observed melting behaviour, show that all mixtures can be considered fair substitutes for benificiated desert sand for the purpose of proof of concept.

Given this conclusion, and the fact viscosity reference points were not determined experimentally, the calculated viscosity curves (figures 4.6.1 to 4.6.3) can be used to estimate the temperatures of interest. Taking into account all hypothetical mixtures, and the included margin of error, this leads to the estimated temperature ranges in table 5.6.1.

Table 5.6.1: Estimates of minimum and maximum temperatures for viscosity reference points of any desert sand glass.

Reference point	T_{min} [°C]	T_{max} [°C]
Practical melting point ($\eta = 10^1$ Pa s)	1350	1800
Working point ($\eta = 10^3$ Pa s)	1150	1400
Annealing point ($\eta = 10^{12}$ Pa s)	650	750

5.7. Characterization of synthetic glass

The characterisation of the imitation glass produced is discussed in this section. Similar to section 4.7, where the results are presented, the discussion does not represent the chronological order of events.

A comparison of the measured composition to the intended composition and explanation of discrepancies is found in section 5.7.1, followed by discussion of visual results in section 5.7.2. The optical and mechanical characterisation are discussed in sections 5.7.3 and 5.7.4 respectively.

5.7.1. Composition

Most discrepancies between calculated and measured compositions noted in section 4.7.1 are explainable by the accumulation of errors from analysis of the components, weighing, calculation of LOI, variations of composition within the components, and possibly uneven mixing. The consequently lower CaO content implies the LOI of component CAL is higher in reality than in the calculations. The generally lower MgO content could mean the same for component DOL, but the quite accurate approximation of the magnesia content for mixture IM-MAR shows that a weighing error cannot be excluded.

The much higher Al_2O_3 content in resistively heated IM-MOREC and microwaved IM-MAR are likely to be caused by partial dissolving of the crucibles, which are made of this oxide. In some cases the crucibles were visibly thinner where they had been in contact with the melt, confirming this theory.

There seems to be a relationship between the severity of this problem and the temperature reached in comparison to the calculated practical melting point, found in section 4.6.1. As all microwaved samples where heated to >1640 °C, mixture IM-MAR reached a temperature of roughly 350 °C higher than the calculated practical melting temperature, while mixtures IM-MOREC and IM-NOQ exceeded this point by ∼100 °C and ∼0 °C respectively. For the resistively heated samples it is less clear due to limited temperature recordings, but due to practicalities in opening the furnace at high temperature and casting, IM-MOREC was significantly further 'overheated' than the other two samples.

Based on these limited observations, no meaningful conclusions can be drawn, but the corrosion of crucibles warrants further investigation as it could lead to complications during long term operation.

Increased Fe_2O_3 content in the IM-MAR sample cast on steel is also explained by interaction with containers, but is likely to be limited to the surface as the time of contact with steel was only in the order of seconds.

MoO_3 being detected in all resistively heated samples is explained by oxidation of the $MoSi_2$ heating elements during heating. As Mo and W are quite similar in electronic configuration, and both are applied in high temperature applications, the traces of tungsten oxide could stem from either small amounts being present in the heating elements as well, or from mis-detection by XRF.

The detected traces of CuO in sample IM-MOREC from resistive heating does not have an obvious explanation; as only 0.005 wt% is reported in the original data, it could be caused by noise in the analysis. If this is not the case, it could be a result of contamination from the workshop, where copper is used for electrical connections.

The deviations from the calculated composition do not delegitimise the assessment that the mixtures are valid imitations of real (benificiated) desert sand, made in section 5.6, as the measured bulk compositions could theoretically be created from sand. The trace elements introduced during processing would occur in a desert sand batch as well. Furthermore, it is again emphasised that the dissolving of crucibles should be investigated in relation to the practical melting point of the mixture.

5.7.2. Visual inspection

From the photographs presented in section 4.7.2, a series of interesting features can be observed, most of which find an explanation in a combination of composition (table 4.7.1) and processing parameters. These observations are, in order of discussion in this section:

- Thermal cracking in resistively heated IM-MAR.
- Devitrification in microwaved IM-MOREC and IM-MAR cast on graphite.
- Seeds in samples IM-NOQ and resistively heated IM-MOREC.

The resistively heated IM-MAR samples show thermal cracking, while the microwaved version is intact. Other samples that were resistively heated and cast, were handled in a very similar way, but were not damaged in the process. While the lack of cracking in the microwaved sample could also be explained by the smaller volume leading to less extreme thermal gradients while cooling, the higher alumina content in the samples that are intact is curious. Given the network forming properties of alumina, a positive influence on thermal shock resistance would be expected due to improved mechanical properties, and merits further investigation.

A similar observation is made regarding devitrification of the resistively heated IM-MAR sample, and sample IM-MOREC from the microwave furnace. In both cases, the nucleation seems to have taken place heterogeneously. In sample IM-MAR, the crystallisation is localised around thermal cracks, which likely have acted as nucleations sites, while the crystallisation appears strongest along the surface of the IM-MOREC sample. While the uncontrolled cooling trajectory and uncertainty in the calculated annealing temperature could be of influence as well, it stands out that the CaO rich samples that did not crystallize were contaminated with Al_2O_3.

High alumina content was also shown to inhibit crystallisation by one of the unsuccessful casting experiments reported in appendix D. Figure D.0.3 demonstrates that after 12 h of thermal soaking at 1100 °C, mixtures IM-MAR and IM-MOREC are fully crystallized, while mixture IM-NOQ appears to still contain vitreous regions of significant size.

As discussed in section 2.2.2, CaO is known to increase the tendency to crystallise. This finds additional explanation in part in table 5.4.1: the large number of equilibrium reactions, some at high temperature due to the high melting point of the separate oxides, offer possibility of local nucleus formation at relatively low viscosity, while the energy gain of crystal growth would be high at lower temperatures.

Sample IM-MAR, cast on steel provides a counter example, proving that a glass without visible devitrification can be made from a high calcium melt, but it is likely that the critical cooling rate is higher for this type of glass. Exact determination of these critical rates is a subject for further investigation.

Seeds found in resistively heated IM-MOREC and both IM-NOQ samples imply that the practical melting point was not reached, or the melt was soaked for insufficient time. This is in line with the measured compositions, as both samples have higher concentration of network formers and lower overall amounts of modifiers than was calculated.

The viscosity curve for the measured composition of sample IM-NOQ is recalculated and plotted in figure 5.7.1 as an example. It can be seen that the relatively minor variations between intended and actual composition lead to an increase of the expected practical melting point of ∼100 °C. This also explains the microwaved version of this mixture not being castable and the awkward shape of the version produced by resistive heating, as the actual practical melting point was out of range of the microwave furnace, and the overheating for casting was lower than intended.

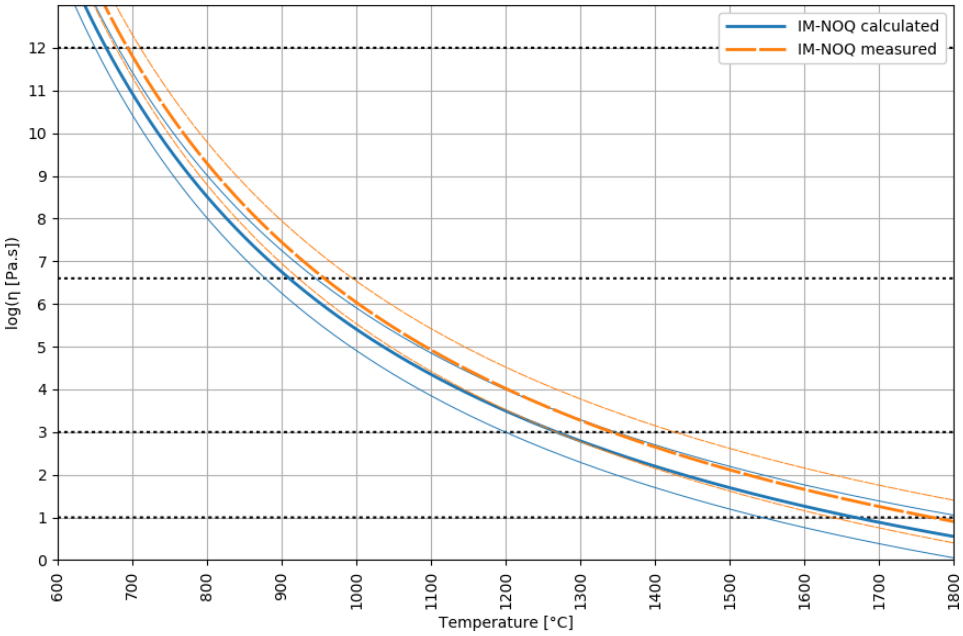

Figure 5.7.1: Calculated viscosity curves for calculated and measured composition of mixture IM-NOQ, including ±0.5 log-unit margin.

While this visual inspection does not yield quantitative information, the importance of careful composition control is emphasised, and it was shown that the predictions made by the model of Giordano et al. [36] were accurate within the margins of error of temperature measurements (±∼40 °C for microwave measurements, unknown for resistive heating). Furthermore the following subjects for further research have surfaced;

- The influence of Al_2O_3 and CaO on:
  - crystallisation and critical cooling rate.
  - thermal shock resistance.
- Exact determination of practical melting point and batch free time.

5.7.3. Optical properties

The general shape of the raw data, shown in figures 4.7.7, 4.7.8 and 4.7.9, is similar for all samples. The notable differences are found in:

- Lower transmission in sample IM-NOQ.
- Crossing absorption coefficients in figure 4.7.10.
- Varying height of the peak around 550 nm.
- Different location of the UV cut-off.

While the significantly lower transmission of sample IM-NOQ could stem from both the large seeds, or composition, the rounded shape of one side of the sample is a more likely cause. This is corroborated by discrepancies between measurements from each surface of the sample. In addition, the use of a single thickness could be questioned, as it is inconsistent over the measuring area of this sample.

Similarities between the shape of the curve(s) in figure 4.7.10 and figure 2.7.3 are striking, implying that the main part of absorption is caused by iron. The fact that the absorption coefficients for samples IM-MAR and IM-MOREC cross each other around 830 nm, could imply that the ratio Fe^{2+}/Fe^{3+} is different, but as the differences are relatively small and the quality of the samples could play a role as well, this would be a premature conclusion.

A comparison of the iron content before rounding, in table 5.7.1, shows that the difference is more likely to be a result of the slightly higher overall iron content of sample IM-MAR. This table also confirms that the lower transmission of sample IM-NOQ is unlikely to be caused by compositional factors.

Table 5.7.1: Fe_2O_3 content as originally reported of samples used for optical measurements, ± 0.01 wt%.

IM-MAR	IM-MOREC	IM-NOQ
0.137	0.123	0.118

The UV cut-off, best compared in figures 4.7.10 and 4.7.11, is unlikely to be the inherent cut off of the network or Fe ions, as it is found at substantially higher wavelength than the cut-off caused by iron ions found in the literature ($\sim$200 nm). Given the location, similar to figure 2.7.3, it seems likely that Fe^{2+} does play a significant role, but by means of 'regular' absorption rather than ultraviolet (UV). The lack of other absorbing species discussed in section 2.7 contributes to this conclusion.

The varying location of the cut-off between samples IM-MAR, IM-MOREC and IM-NOQ appears to be accounted for by differences in composition. Samples IM-MOREC and IM-NOQ, were the UV cut-off is found at lower wavelength, have considerable Al_2O_3 content, while all samples are ordered by CaO content from left to right in figure 4.7.11.

Based on this limited set of data, the mechanism and exact effect cannot be determined and requires further research, but it is apparent that the lower wavelength cut-off can be shifted by varying the composition. As the cut-off for these samples crosses the effective range of the solar cells as well as the edge of the solar spectrum (figure 2.7.1), efficiency could be increased by moving it to lower wavelengths.

More generally, it can be concluded that 85 % transmission in the peak of the solar spectrum is possible for desert sand glass of 3 mm thickness, if the Fe_2O_3 content can be lowered to less than approximately 0.1 wt%. For thicker glass or a wider transmission band it would have to be lowered further. The trace elements found in the store bought components do not seem to have a significant effect on transmission, but contamination found in desert sand would be a subject for further research. As noted in section 5.1.3, the most problematic oxides detected in the analysed selection of desert sand are Cr_2O_3, NiO and CuO.

Summarizing, while the transmission objective of 85 % transmission in the effective spectrum was not reached for the samples produced, the following observations were made on how it could be:

- The Fe_2O_3 content of the feedstock should reduced to <0.1 wt%.
- The (UV) cut-off should be moved to lower wavelength by adapting CaO and/or Al_2O_3 content.
- The influence of absorbing trace elements on transmission should be investigated.

5.7.4. Mechanical properties

As was stated in section 4.7.4, no quantitative results were acquired by the mirror analysis. Further research is needed to answer the mechanical questions stated in the introduction of this thesis, but close inspection of the fracture surfaces yields some useful information. For readability the observations made from section 4.7.4 are listed below.

- Mirror like features are spread randomly in all samples.
- Hackle is observe along some edges.
- Mirror like features vary in size between samples.

The random spread of multiple mirror like features over the surfaces implies that the stress state at fracture was inhomogeneous. This could be caused by residual stresses from insufficient annealing or uneven loading due to the awkward shapes of the samples, and most likely a combination of the two.

The presence of hackle on the outer edges and smooth mirror like areas in the centre of the samples could mean that the fracture originated in the bulk of the material. This is only possible under a bending load if there are local variations in strength, as the maximum stress would be found at the bottom surface. Another explanation could be the load was not a pure bending one, leading to irregular stress.

While the latter was most likely the case as well, inhomogeneities in (local) strength would not be surprising. Both fractures in IM-NOQ found in figure 4.7.15 appear to have originated from a seed causing a stress concentration, while samples IM-MAR and IM-MOREC in figures 4.7.12d and 4.7.14b show a directional structure in the glass mass. On a side note, these inhomogeneities could make it debatable if these samples fulfil the definition of glass given in section 2.1.1.

When comparing the scale on the images of mirror like features closest to figure 2.6.6, presented in figures 4.7.12a, 4.7.13a and 4.7.15a, one might note that an extrapolated radius would be about a factor two smaller for sample IM-NOQ. This could imply both a different mirror constant for the different compositions, or a significantly higher stress at fracture. Intuitively the latter is plausible due to the higher network connectivity in the high alumina glass, and the values for quantities influencing strength in table 2.6.1 point in a similar direction. Conversely, a similar feature would be expected in sample IM-MOREC, but this is not the case.

Based on the literature it appears likely that the required 70 GPa elastic modulus is attainable, as both CaO and Al_2O_3, the major components of desert sand after silica, have a positive influence in silicate glasses. Strength will be dependant on the production process to a great extent. Sufficient fining is imperative, as is controlled shaping and cooling.

Assuming glass can be produced with an acceptably low amount of critical defects, high alumina glasses produced from desert sand are expected to display properties not unlike typical aluminosilicate glasses, and thus are relatively strong compared to other silica based glasses. There is less information available in the literature on the other potential direction of composition, (very) high calcium glasses. In any case, further research is needed.

Summarizing, the mechanical analysis is inconclusive. While the literature implies the objectives are possible, confirmation via production of a series of samples suitable for flexural tests is required.

6

Conclusions & recommendations

The research questions posed in chapter 1, repeated below, are addressed in section 6.1, while recommendations to continue this research are presented in section 6.2.

1. Is it possible to manufacture a cover glass from benificiated desert sand, complying to the specifications provided by Maana Electric?
   - > 85% transmission of the 350 nm to 1100 nm range of light.
   - Youngs modulus > 70 GPa.
   - Flexural strength > 45 MPa.
2. What are the critical process temperatures for such a glass?

The goal in terms of properties is clear from these objectives, but a starting point in the form of a characterizable sample of glass is needed. Hence sections 6.1 and 6.2 are structured in a corrected order: first the glass forming ability of desert sand is addressed, as are the critical process temperatures of a desert sand based glass. Finally conclusions and recommendations regarding optical and mechanical properties of the glass are presented.

6.1. Conclusions

All sands in the selection of desert sand samples investigated, which include examples from the continents of Africa and Asia, the middle east, and a single sample from Mexico, could theoretically form a glass, provided that they can be melted.

- To obtain a meltable composition, benificiation is required in most cases. It was found that any combination of minerals found in significant quantities in desert sand (quartz, feldspars, calcite & dolomite), and thus any desert sand based glass, will have an attainable practical melting point ($<$1650 °C) if the silica content is reduced to $\sim$55 wt%. In carbonate rich sands there is some room to increase this silica content to improve glass formability, while still remaining meltable.

- This composition requirement can be fulfilled by removing all, or part of, the quartz from feldspar rich sands, while increasing the carbonate content in carbonate rich sand will yield result as well. Sands containing more than 50 wt% quartz would require disposal of a large fraction of the input material, and were therefore deemed unsuitable.

- It was shown that reactions instigating melt formation will occur between 1100 °C and 1550 °C for any mixture of minerals. When the melt is formed, the practical melting point of a desert sand glass will be found between 1350 °C and 1800 °C. When cooled, the glass will reach the working point between 1150 °C and 1400 °C, and cross the annealing point in the range of 650 °C to 750 °C. The critical process temperatures are summarized in figure 6.1.1.

- The requirement of 85 % transmission in the range of 350 nm to 1100 nm, while not fulfilled during this project, appears attainable.

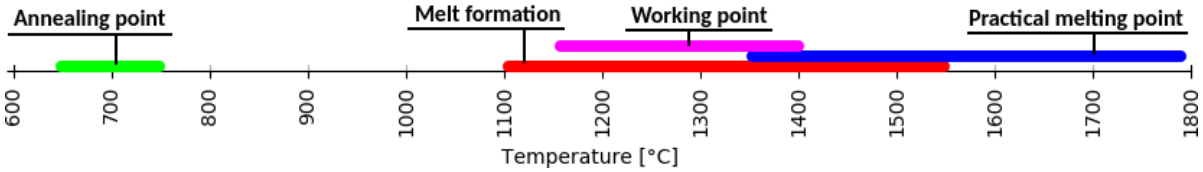

Figure 6.1.1: Overview of (estimated) ranges of critical processing temperatures of desert sand glass.

- It was shown that 85 % transmission of ~550 nm wavelength light, close to the peak in the solar irradiation spectrum, is possible for desert sand glass of 3 mm thickness and Fe_2O_3 content in the order of magnitude of 0.1 wt%. Increase of transmission in the effective spectrum of silicon based solar cells would require lower iron content, and displacement of the (UV) cut-off to shorter wavelengths.
- The shape and number of samples produced was insufficient for mechanical measurements, and mirror analysis of the samples broken in flexure did not yield quantitative data. The results suggested that high alumina content is beneficial for mechanical properties, and the need for fining was emphasized.
- Based on the literature, the mechanical requirements should be attainable, but a definitive assessment requires further research.

6.2. Recommendations for further research

Destruction of alumina crucibles, and resulting contamination of the batch was observed. Refractory corrosion is a known problem in industry, and will be for an autonomous system operating for extended times. The dissolving of the crucible also has to be considered in further research, as results are influenced.

The apparent destructive effect of exceeding the practical melting temperature can be investigated, for example by soaking the same composition in multiple batches for various durations to compare contamination of the glass composition afterwards, or by soaking a range of melts of different practical melting point for the same duration. If the corrosion of alumina can not be limited or prevented, alternative crucible materials can be investigated.

Crystallisation was observed in multiple calcium rich compositions. If a such a composition is selected, investigation of crystallisation behaviour and critical cooling rates would be imperative to prevent loss of transmission and problems during processing. One possible method to achieve this would be to soak a series of identical samples for different durations and/or temperatures, and observe the resulting crystallized fraction. If a specific composition is selected, the critical cooling rate can be determined by repeated cooling experiments at decreasing rate until crystallisation is observed, possibly employing DSC. Temperatures at which crystalline phases are formed, and thus are to be passed quickly when cooling or heating, can be determined by DSC as well.

The viscosity reference points of interest were modelled, not confirmed. While this was sufficient to create glasses for proof of concept for this thesis, more specific information on the processing temperatures would be desirable in further implementation. When a composition (range) is selected based on location and benificiation capabilities, a full viscosity measurement could be executed. Alternatively, two or three points could be determined to provide a more accurate fit for the VFT equation. Examples are determination of the glass transition temperature by DSC, the softening point by beam bending experiments, or the practical melting point by falling sphere viscometry.

Due to a lack of raw materials, reactions involving anorthite, or any plagioclase feldspar, were not confirmed, but could be by acquiring plagioclase feldspars and performing similar experiments to those described in section 3.2.6. In addition, the observed expansion effect in two feldspar rich samples could be related to this type of mineral. This can be confirmed or excluded by the experiment described. Further specification of other reactions occurring could be acquired by high temperature DSC experiments.

To fully answer the research question regarding optical properties, the absorbing qualities of trace elements in desert sand will have to be investigated. This can be done by creating additional synthetic batches with additions of Cr_2O_3, NiO and/or CuO, or by removing the Fe containing minerals from actual desert sand, to be melted to form a glass for transmission measurements.

The transmission spectrum of desert sand glass could be optimised by investigating the influence of the melt oxidation state on the effect of iron, and by identifying the cause of the shifting of the (UV) cut-off, to move the latter out of the effective spectrum. As the shift of the UV cut-off appears to be influenced by the proportions of CaO and Al_2O_3, in addition to additional literature review, a first step can be creation of a range of (synthetic) desert sand glasses were this proportion is varied. Furthermore, prolonged exposure to sunlight could deteriorate the transmission over time, research of solarization is therefore also advised.

The results of the mechanical analysis were inconclusive, hence all mechanical properties specified are left for further research. As achievement of the requirements seems likely based on the literature, on the condition that low defect glass can be produced, it is advisable to focus on melting and shaping first, since a large number of suitable samples is needed for an adequate mechanical analysis. In addition, subcritical crack growth and fatigue behaviour are important properties in the intended application, and should therefore be researched.

References

[1] C. Egenhofer, S. Roth, L. Schrefler, W. Stoefs, and A. Marcu. Final report for a study on composition and drivers of energy prices and costs in energy intensive industries: the case of the flat glass industry, January 2014. URL https://publications.europa.eu/en/publication-detail/-/publication/b43ca37c-ae26-49f3-9341-7558a75d52da.

[2] Keith Burrows and Vasilis Fthenakis. Glass needs for a growing photovoltaics industry. *Solar Energy Materials and Solar Cells*, 132:455–459, 2015. doi: 10.1016/j.solmat.2014.09.028.

[3] W. H. Zachariasen. THE ATOMIC ARRANGEMENT IN GLASS. *Journal of the American Chemical Society*, 54(10):3841–3851, oct 1932. doi: 10.1021/ja01349a006.

[4] Koen H. A. Janssens, editor. *Modern Methods for Analysing Archaeological and Historical Glass*. Wiley-Blackwell, 2013. ISBN 9780470516140.

[5] James E. Shelby. *Introduction to Glass Science and Technology*. Royal Society Of Chemistry, 2005. ISBN 0854046399.

[6] Arun K. Varshneya and John C. Mauro. *Fundamentals of Inorganic Glasses*. ELSEVIER, 2019. ISBN 978-0-12-816225-5.

[7] Bjorn O. Mysen and Pascal Richet. *Silicate glasses and melts*. Elsevier LTD, Oxford, 2018. ISBN 0444637087.

[8] David J. Musgraves, Juejun Hu, and Laurent Calves, editors. *Springer Handbook of Glass*. Springer-Verlag GmbH, 2019. ISBN 331993726X.

[9] V. M. Goldschmidt. *Geochemische Verteilungsgesetze der Elemente VIII*, volume 8. Dybwad, 1926.

[10] A. Dietzel. Die kationenfeldstärken und ihre beziehungen zu entglasungsvorgängen, zur verbindungsbildung und zu den schmelzpunkten von silicaten. *Zeitschrift für Elektrochemie und angewandte physikalische Chemie*, 48(1):9–23, 1942. doi: 10.1002/bbpc.19420480104.

[11] Kuan-Han Sun. FUNDAMENTAL CONDITION OF GLASS FORMATION. *Journal of the American Ceramic Society*, 30(9):277–281, sep 1947. doi: 10.1111/j.1151-2916.1947.tb19654.x.

[12] J. E. Stanworth. The ionic structure of glass. *J. Soc. Glass Technol*, 32(149):372, 1948.

[13] A. Smekal. Über die natur der glasbildenden stoffe. *Glastechn. Ber*, 22:278–289, 1949.

[14] Rawson. The relationship between liquidus temperature, bond strength and glass formation. In *IV. Int. Cong. On Glass, Paris*, 1956.

[15] Paul A. Bingham and Frederick T. Wallenberger, editors. *Fiberglass and Glass Technology*. Springer, 2010. ISBN 1441907351.

[16] Jürn W. P. Schmelzer, Ivan S. Gutzow, Oleg V. Mazurin, Snejana V. Todorova, and Boris B. Petroff. *Glasses and the Glass Transition*. Wiley VCH Verlag GmbH, 2011. ISBN 3527409688.

[17] Arthur Q. Tool. RELATION BETWEEN INELASTIC DEFORMABILITY AND THERMAL EXPANSION OF GLASS IN ITS ANNEALING RANGE□. *Journal of the American Ceramic Society*, 29 (9):240–253, sep 1946. doi: 10.1111/j.1151-2916.1946.tb11592.x.

[18] D. R. Poirier and G. H. Geiger. *Transport phenomena in materials processing*. Springer International Publishing, 2016. ISBN 978-3-319-48090-9. doi: 10.1007/978-3-319-48090-9.

[19] Pinshane Y. Huang, Simon Kurasch, Anchal Srivastava, Viera Skakalova, Jani Kotakoski, Arkady V. Krasheninnikov, Robert Hovden, Qingyun Mao, Jannik C. Meyer, Jurgen Smet, David A. Muller, and Ute Kaiser. Direct imaging of a two-dimensional silica glass on graphene. *Nano Letters*, 12(2):1081–1086, jan 2012. doi: 10.1021/nl204423x.

[20] International Sand Collectors Society. What is sand, 2019. URL https://sandcollectors.org/what-is-sand/. Visited June 18th 2019.

[21] F. J. Pettijohn, Paul E. Potter, and Raymond Siever. *Sand and Sandstone*. Springer, 1987. ISBN 0387963553.

[22] Salih Muhammad Awadh. Geochemistry and mineralogical composition of the airborne particles of sand dunes and dust storms settled in iraq and their environmental impacts. *Environmental Earth Sciences*, 66(8):2247–2256, nov 2011. doi: 10.1007/s12665-011-1445-6.

[23] Narottam P. Bansal and Sung R. Choi. Properties of CMAS glass from desert sand. *Ceramics International*, 41(3):3901–3909, apr 2015. doi: 10.1016/j.ceramint.2014.11.072.

[24] Zhixu Wang, Zhiming Shi, Wenbin Wang, Shigang Wang, and Chao Han. Synthesis of MgSiO3 ceramics using natural desert sand as SiO2 source. *Ceramics International*, 45(11):13865–13873, aug 2019. doi: 10.1016/j.ceramint.2019.04.084.

[25] G. P. Padmakumar, K. Srinivas, K. V. Uday, K. R. Iyer, Pankaj Pathak, S. M. Keshava, and D. N. Singh. Characterization of aeolian sands from indian desert. *Engineering Geology*, 139-140: 38–49, jun 2012. doi: 10.1016/j.enggeo.2012.04.005.

[26] Yuji Hattori, Katsuhiko Suzuki, Masatoshi Honda, and Hiroshi Shimizu. Re-Os isotope systematics of the Taklimakan Desert sands, moraines and river sediments around the taklimakan desert, and of Tibetan soils. *Geochimica et Cosmochimica Acta*, 67(6):1203–1213, mar 2003. doi: 10.1016/s0016-7037(02)01206-1.

[27] H. A. Sanad, N. F. Ismael, and A. J. Nayfeh. Geotechnical properties of dune sands in kuwait. *Engineering Geology*, 34:45–52, 1993. ISSN 0013-7952. doi: 10.1016/0013-7952(93)90042-b.

[28] Qianqian Liu and Xiaoping Yang. Geochemical composition and provenance of aeolian sands in the Ordos Deserts, northern China. *Geomorphology*, 318:354–374, oct 2018. doi: 10.1016/j.geomorph.2018.06.017.

[29] George W. Morey. *Data of Geochemistry*, chapter Chapter L. Phase-equilibrium relations of the common rock-forming oxides except water. United States Government Printing Office, Washington, 6 edition, 1964.

[30] J. F. Schairer. The alkali-feldspar join in the system $NaAlSiO_4$-$KAlSiO_4$-SiO_2. *Geophysical Laboratory, Carnegie Institution of Washington*, 1950.

[31] David R. Lide, editor. *CRC Handbook of Chemistry and Physics 80th Edition*. CRC Press, 1999. ISBN 0849304806.

[32] Narottam P. Bansal and Robert H. Doremus. *Handbook of Glass Properties*. ELSEVIER, 1986. ISBN 0120781409.

[33] D. H. Vogel. Das temperaturabhaengigkeitsgesetz der viskositaet von fluessigkeiten. *Physikalische Zeitschrift*, 22:645, 1921.

[34] Gordon S. Fulcher. ANALYSIS OF RECENT MEASUREMENTS OF THE VISCOSITY OF GLASSES. *Journal of the American Ceramic Society*, 8(6):339–355, jun 1925. doi: 10.1111/j.1151-2916.1925.tb16731.x.

[35] G. Tammann and W. Hesse. Die abhängigkeit der viscosität von der temperatur bie unterkühlten flüssigkeiten. *Zeitschrift für anorganische und allgemeine Chemie*, 156(1):245–257, oct 1926. doi: 10.1002/zaac.19261560121.

[36] Daniele Giordano, James K. Russell, and Donald B. Dingwell. Viscosity of magmatic liquids: a model. *Earth and Planetary Science Letters*, 271(1-4):123–134, jul 2008. doi: 10.1016/j.epsl.2008.03.038. URL https://www.eoas.ubc.ca/~krussell/VISCOSITY/grdViscosity.html.

[37] Eric Le Bourhis. *Glass: Mechanics and Technology*. John Wiley & Sons, Incorporated, 2 edition, 11 2014. ISBN 9783527679423.

[38] M. Janssen, J. Zuidema, and R. J. H. Wanhill. *Fracture mechanics*. VSSD, Delft, 2002. ISBN 9040722218.

[39] David Kinsella and Kent Persson. On the applicability of the weibull distribution to model annealed glass strength and future research needs. *Challenging Glass Conference Proceedings*, 5:593–608, 2016. ISSN 2589-8019. doi: 10.7480/cgc.5.2432. URL https://journals.open.tudelft.nl/cgc/article/view/2432.

[40] F. A. Veer, P. C. Louter, and F. P. Bos. The strength of annealed, heat-strengthened and fully tempered float glass. *Fatigue & Fracture of Engineering Materials & Structures*, 32(1):18–25, jan 2009. doi: 10.1111/j.1460-2695.2008.01308.x.

[41] F. A. Veer. The strength of glass, a nontransparent value. *Heron*, 52(1/2):87–104, January 2007. ISSN 0046-7316.

[42] George Quinn. Guidelines for measuring fracture mirrors. *Ceramic Transactions*, 199:163 – 190, June 2007. doi: 10.1002/9781118144152.ch14.

[43] National Renewable Energy Laboratory (NREL). Reference solar spectral irradiance: Air mass 1.5. URL https://rredc.nrel.gov/solar//spectra/am1.5/. Visited 11-05-2020.

[44] N. E. Powell, David Miller, Jaione Bengoechea, Jayesh Bokria, Michael Köhl, Michael Smith, Michael White, Helen Wilson, and John Wohlgemuth. Examination of an optical transmittance test for photovoltaic encapsulation materials. volume 8825, 08 2013. doi: 10.1117/12.2024372.

[45] C Bamford. *Colour generation and control in glass*. Elsevier Scientific Pub. Co. Distributors for the U.S. and Canada, Elsevier North-Holland, Amsterdam New York, 1977. ISBN 0444416145.

[46] Nadine Sterk and Lonny van Ryswyck. AtelierNL. URL https://aworldofsand.com/. Personal communication.

[47] Ruud Hendrikx, 2019. At the Department of Materials Science and Engineering of the Delft University of Technology is acknowledged for the X-ray analysis.

[48] Gonçalo Meneses Leonel. Conversion of a commercial microwave oven to a sintering furnace controlled by computer. Master's thesis, Técnico Lisboa, 2015.

[49] *Calex PyroUSB Datasheet*. Calex Electronics Ltd, December 2018. URL www.calex.co.uk.

[50] Coosje Pothoven. Extremely high temperature measurements in a microwave environment. Internship report at Maana Electric TU Delft Applied Physics, November 2019.

[51] Qmineral Analysis and Consulting. Analysis report "abu 1". May 2020.

[52] Madhuchhanda Bhattacharya and Tanmay Basak. A review on the susceptor assisted microwave processing of materials. *Energy*, 97:306–338, feb 2016. doi: 10.1016/j.energy.2015.11.034.

[53] Ashis K. Mandal and Ranjan Sen. An overview on microwave processing of material: A special emphasis on glass melting. *Materials and Manufacturing Processes*, 32(1):1–20, feb 2016. doi: 10.1080/10426914.2016.1151046.

Appendix

A

Microwave furnace

This appendix contains additional information regarding the microwave furnace employed in melting experiments. Section A.1 contains a short discussion of the working principles of microwave heating, followed by a description of the insulation package in section A.2 and the control system in section A.3. The appendix is concluded with the baseline measurements conducted on store bought components in section A.4.

A.1. Principles of microwave heating

Microwaves are the part of the electromagnetic spectrum between 300 MHz and 300 GHz. Heating occurs through interaction of the material with the electric and/or the magnetic field resulting from a microwave source. This has the advantage of volumetric heating, circumventing rate limiting heat transfer as in traditional furnaces, as well as the temperature limitations of heating elements [52].

The interaction depends on the on the frequency of the microwave, and on the dielectric constant, magnetic permeability, and magnetic and dielectric loss of the material. Often the latter are combined into an electronic and magnetic loss tangent [52].

The quantity used to quantify the (heating) response of a material is the penetration depth d_p, the distance a microwave can travel in a material before the amplitude is reduced to $1/e = 0.368$ of the initial amplitude, and thus a measure for the fraction of energy from the microwave converted to heat. Materials can be roughly categorised into three groups. Microwave reflectors (d_p in the order of µm), typically are highly conductive materials like metals. Absorbers ($d_p \sim$ cm), and microwave transparent materials ($d_p \sim$ m) can be used in a microwave environment as 'susceptor' and insulation (or container) respectively [52, 53].

The penetration depth is temperature dependent for most materials. Typically it decreases with temperature, increasing absorption in transparent materials, and reducing efficiency in absorbers [52]. This is illustrated by some values for materials similar to those used in this furnace in table A.1.1. Varying of the susceptibility during heating can lead to what is known as thermal runaway, where localised increases in microwave dissipation lead to uneven heating of the material(s), which will lead to a feedback loop causing extreme temperature gradients.

It is important the insulation material in the cavity is as microwave transparent as possible, while also able to resist the high temperatures and provide insulation. In a lot of high temperature microwave applications the material of choice is based on a combination of alumina and silica [48, 52].

In household microwave ovens as used for this project the microwave source is a magnetron, a vacuum tube with resonant structures in a magnetic field. Due to the construction the frequency is locked (typically to 2.45 GHz). The power output can be varied by changing the magnetic field or the cathode current, but in cheaper ovens this is usually done by means of pulse width modulation: simply turning the magnetron on or off [53].

Table A.1.1: Some values for the penetration depth of materials similar to the materials used, at different temperatures. Data from [52].

Material	**T [**°C**]**	d_p **[**m**]**
Alumina	590	4.65
	980	0.84
	1340	0.18
Silicon carbide	25	0.007
	800	0.0047
	1350	0.0025
Alumina Silicate	25	1.39
	800	0.28
	1100	0.12
SLS glass	25	1.03
	700	0.016
	750	0.011

A.2. Insulation package

Insulating materials used are porous, and alumina silicate based. The 30 l cavity of the oven is filled for the most part with ceramic insulation wool rated to 1350 °C, leaving a cavity of approximately 12.5 x 9 x 12.5 cm in the centre, as pictured in figure A.2.1.

The inner box, as seen in figure A.2.2, is machined out of porous insulating brick. The highest operating temperature available at the time was 1540 °C. One might note that temperatures during this project exceded this temperature, leading to cracking of the box. Every time cracking became extensive and structural integrity became compromised, the box was replaced.

The outside dimensions of the box measure 12.5 x 9 x 6.5 cm. The box is set atop and covered with two 2 cm slabs of the same material and footprint. The lid contains a 10 mm hole in the centre to allow for pyrometer measurements from the top.

As the inner cavity is machined by hand, sizes between replacements vary, but approach 8 x 6 x 4.5 cm. The bottom of the cavity is covered with a slab of silicon carbide grinding disc of similar size and about 1.5 cm to 2 cm in thickness.

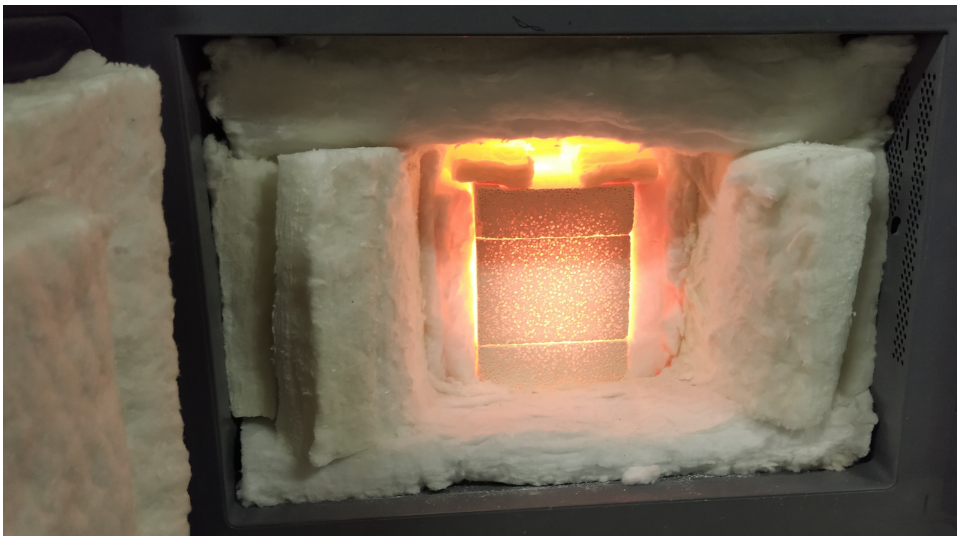

Figure A.2.1: Inside view of the microwave while hot, showing ceramic wool in cavity and attached to the door. During operation an additional piece of wool is placed in the opening, covering the front of the inner insulation box completely.

(a) Inside, empty crucible on top of susceptor.

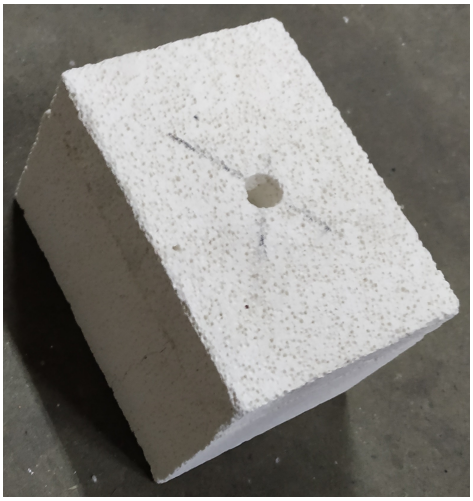

(b) Outside, hole for pyrometer measurements.

Figure A.2.2: Inner insulation box, internal and external view.

A.3. Control and data acquisition system

In the as supplied oven, the pulse width is controlled by a mechanical timer that switches the magnetron on and of at set intervals, leading to an effective power of a set fraction of the maximum 900 W. This system was replaced by a solid state relay controlled by an Arduino Nano (clone), which receives temperature readings from the pyrometer.

The pyrometer is connected to a pc via USB for monitoring and modifying settings, while all readings are taken via the analogue 4 mA to 20 mA output and the Arduino. An overview of the system can be found in figure A.3.1.

A HW-685 current-to-voltage conversion board converts the 4 mA to 20 mA current produced by the pyrometer to a signal readable by the Arduino. The range of temperatures for the output of the pyrometer is set from 450 to 1650 °C, leading to a resolution of $\frac{1650-450}{1024} = 1.17$ °C, given the 10 bit resolution of the input.

As the signal can be noisy, it is read in burst of 50 times every 50 ms, after which the moving average over three readings is taken as the current temperature. This leads to a read temperature well within ± 1 °C of the temperature read using the supplied Calex software. To prevent the Arduino registering 450 °C when the temperature is still out of range, readings under 460 °C are disregarded.

Instead of switching at set intervals, the moving average over 12 s of the temperature measured is recorded, and the magnetron is toggled when this temperature is over a set threshold removed from the reference temperature. The latter can be constant, or follow a linear increase or decrease. The power needed to keep the temperature within specifications is calculated when the magnetron is toggled, by dividing the heating time by the duration of the last complete cycle.

The filament in the magnetron requires some time to heat up when switched on, so to prevent early degradation, the on-part of the cycle needs to be at least 12 s [48], while the off time is set to at least 5 s to prevent to rapidly switching when temperature changes are rapid.

Time index, status of the magnetron, status of the pyrometer, reference temperature, measured temperature, and power information are sent over a serial connection every second, and logged to a comma separated data file using a python script. A second script is used to plot the recorded information. The latter also approximates the slope of heating curve while the magnetron was on, giving an indication of the instantaneous heating rate.

The script written to plot data collected during heating has multiple options for presentation. The reference temperature, measured temperature, power and heating rate can be plotted against time, but as the heating rate is kept constant results were presented in a scatter plot of rate and power versus temperature.

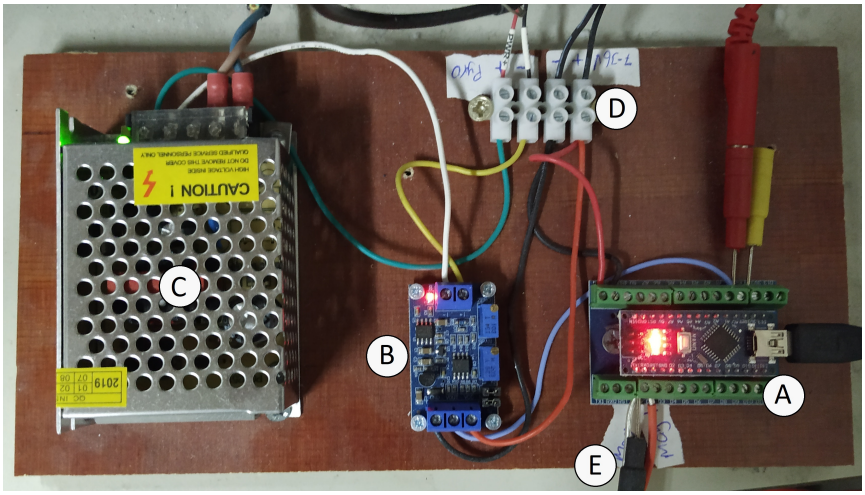

Figure A.3.1: Control and data acquisition system for the microwave furnace: (A) Arduino Nano clone connected to pc, (B) Current to voltage conversion board, (C) 24 V power supply for current loop, (D) Connection to pyrometer and power supply, (E) Connection to relay controlling magnetron.

A.4. Baseline measurements

To confirm the control system leads to repeatable measurements, and provide material for comparison to measurements from actual desert sand, multiple heating curves were recorded. All were heated to the starting temperature of 500 °C at full power, and held at the starting temperature for 30 min before being heated at an (average) rate of 5 °C min^{-1}.

For illustrative purposes, a full heating curve of an empty crucible plotted against time, and a detail of the response of the controller can be found in figures A.4.1 and A.4.2. As the region of interest is the heating range, and the heating rate is kept constant at 5 °C min^{-1}, further graphs will be based on temperature and only cover the range of heating.

The heating curve of a susceptor (A.4.3) was measured by raising it to the same level as the top of the sand would be. An empty alumina crucible was heated from multiple starting situations, including a room temperature start, preheated wool with a room temperature insulation brick, and preheated brick and susceptor with a room temperature crucible, these recordings are presented in figure A.4.5 for comparison.

All available store bought components were measured covered by a thin layer of Q for constant emissivity. These plots are presented in figures A.4.6 to A.4.10. Gypsum was excluded as it was found in section 5.2 that no significant amounts appear to be present in the available desert sand.

Most plots show a decrease in the scatter of the heating rate at high temperature, this can be explained by the method of calculation. As a linear approximation of the temperature is made during the time the magnetron is on, more data points are included in the calculation at the longer cycles at higher temperature, leading to a more consistent average.

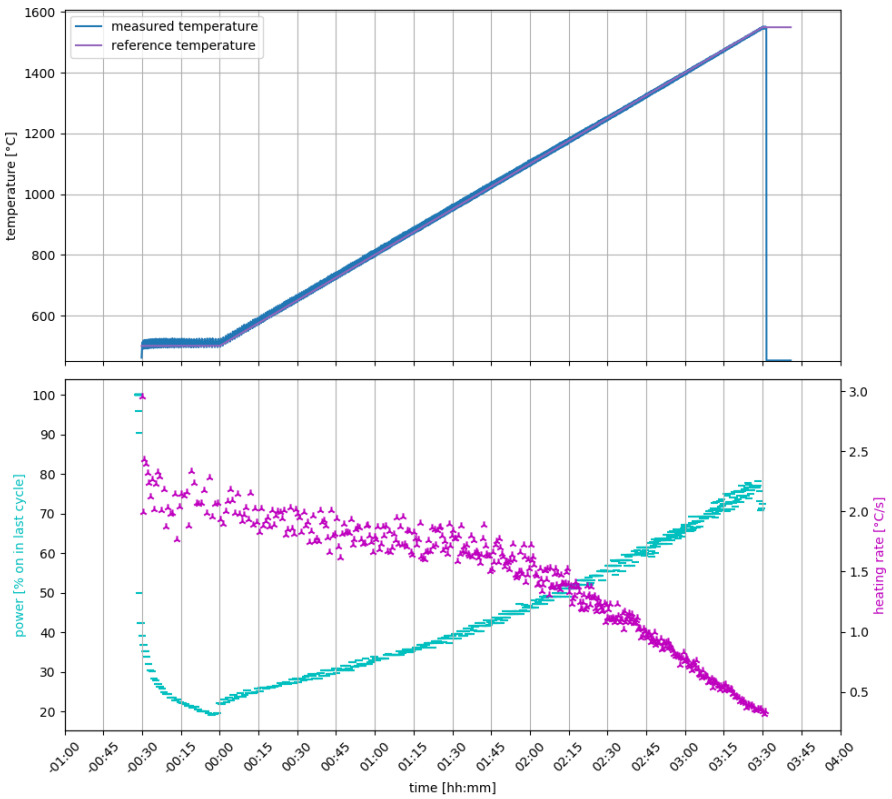

Figure A.4.1: Full heating curve of an empty crucible, $\varepsilon = 0.51$.

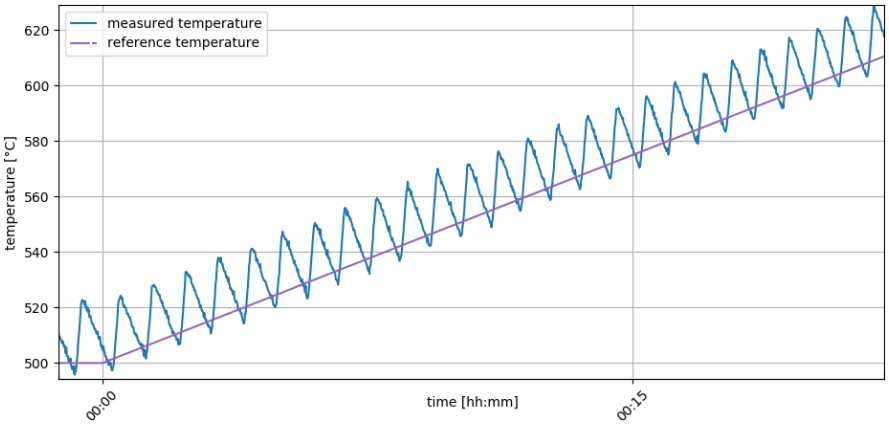

(a) Low temperature detail.

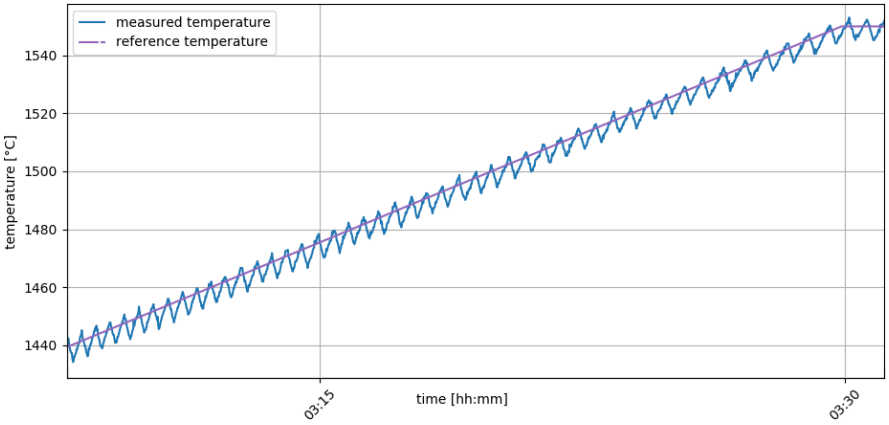

(b) High temperature detail.

Figure A.4.2: Details of the heating curve resulting from the control system heating an empty crucible.

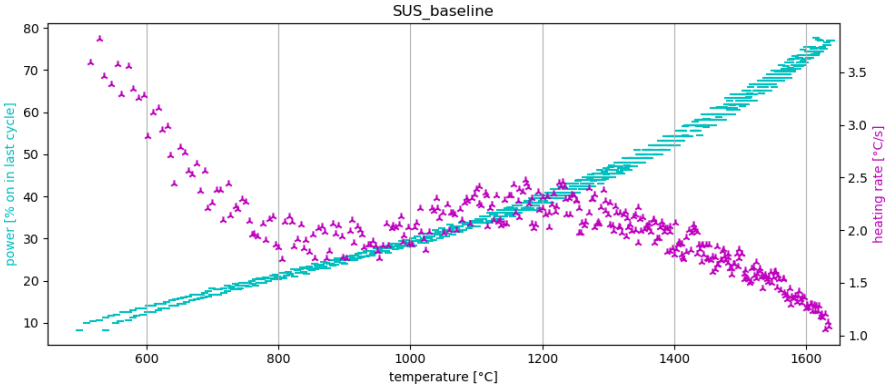

Figure A.4.3: Power and heating rate plot of susceptor, $\varepsilon = 0.55$.

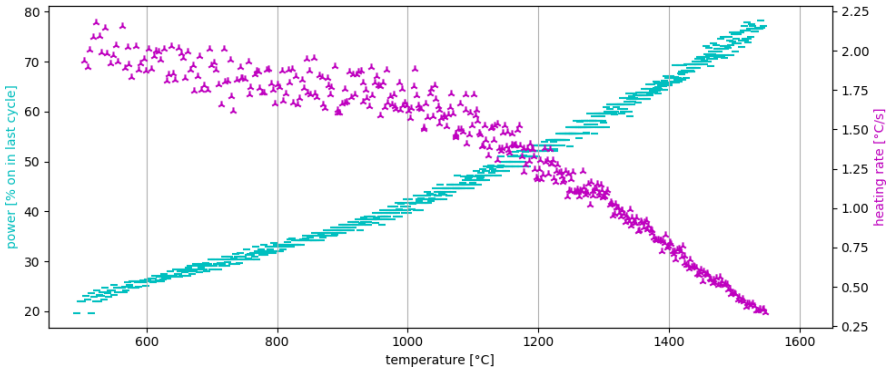

Figure A.4.4: Power and heating rate plot of empty crucible, $\varepsilon = 0.51$.

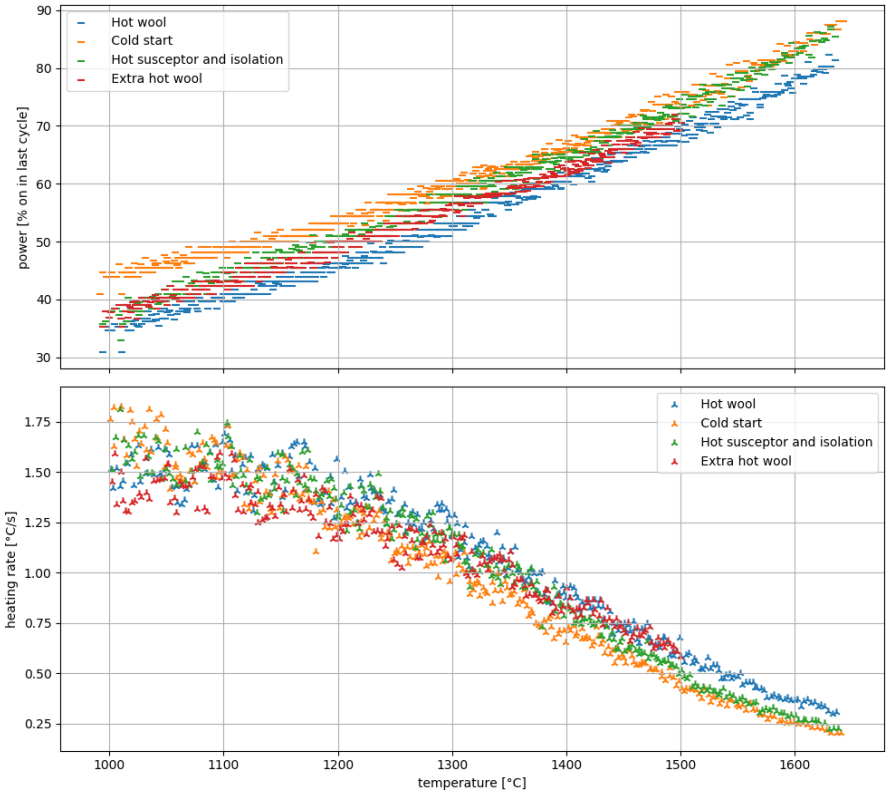

Figure A.4.5: Power and heating rate comparison of empty crucible from different starting situations, $\varepsilon = 0.51$.

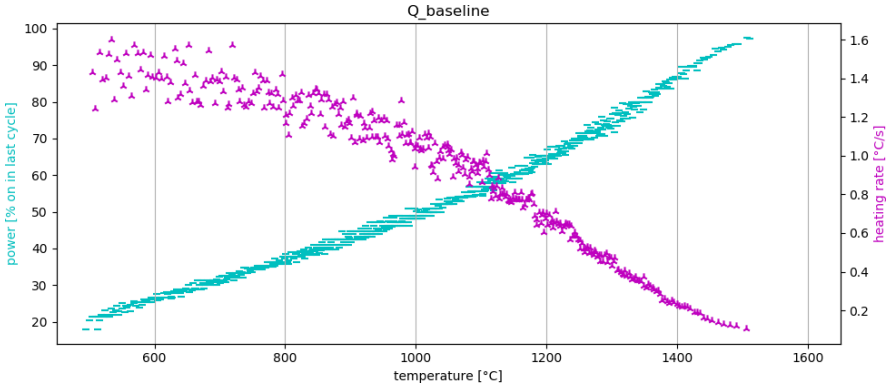

Figure A.4.6: Power and heating rate plot of sample Q, $\varepsilon = 0.64$.

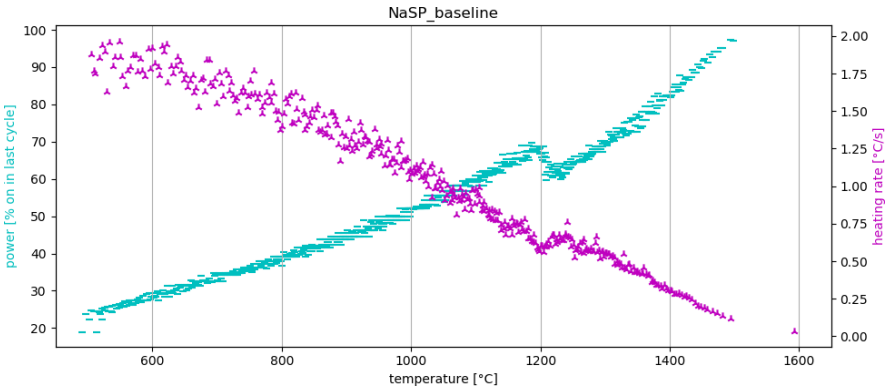

Figure A.4.7: Power and heating rate plot of sample NaSP, thin layer of Q on top, $\varepsilon = 0.64$.

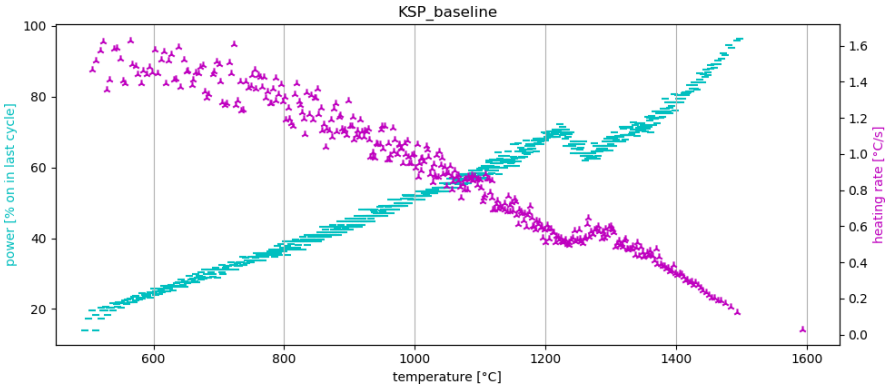

Figure A.4.8: Power and heating rate plot of sample KSP, thin layer of Q on top, $\varepsilon = 0.64$.

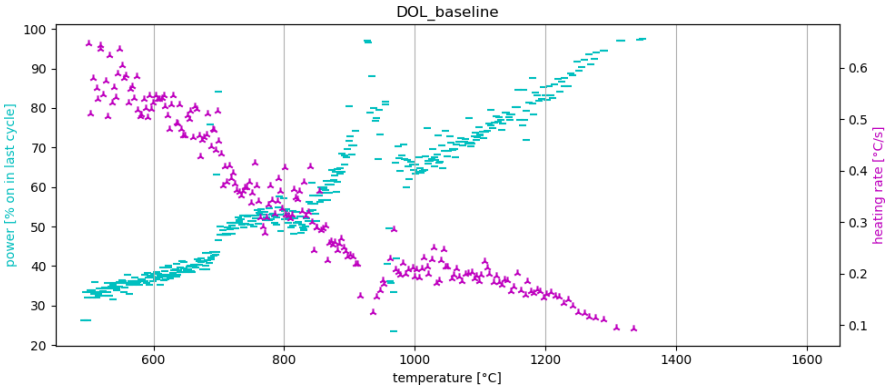

Figure A.4.9: Power and heating rate plot of sample DOL, thin layer of Q on top, $\varepsilon = 0.64$.

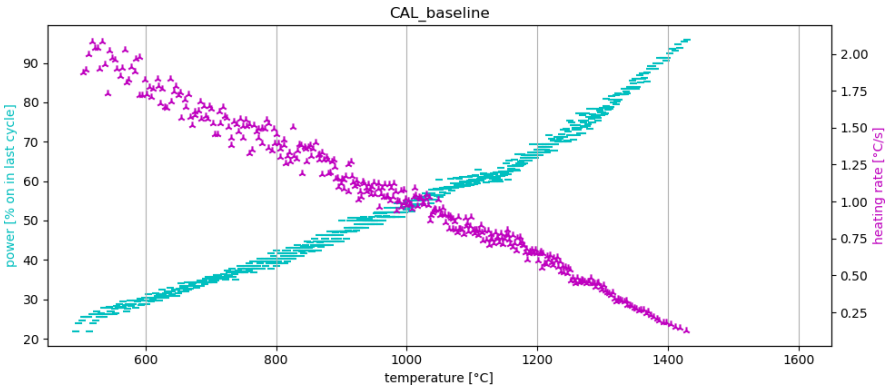

Figure A.4.10: Power and heating rate plot of sample CAL, thin layer of Q on top, $\varepsilon = 0.64$.

B

Emissivity measurements

The emissivity at a given wavelength λ [m], at temperature T [K], is defined as

$$\varepsilon_\lambda = \frac{I(\lambda, T)}{I_{bb}(\lambda, T)}, \tag{B.1}$$

where I_{bb} and I are the infra-red (IR) emission intensity in $\mathrm{W\,m^{-2}}$, of a black body and the object that is measured respectively [49]. For narrow band pyrometer measurements, Wien's approximation of Plank's law is used to calculate the temperature:

$$I_{bb}(\lambda, T) = \frac{2hc^2}{\lambda^5} \exp\left[-\frac{hc}{\lambda k T}\right], \tag{B.2}$$

where c, h, and k are the speed of light, Planck's and Boltzmann's constant respectively [50].

By combining equations B.2 and B.1, the emissivity at a known temperature can be determined, by calculating the intensity measured by the pyrometer given the set emissivity and recorded temperature.

As the microwave system results in observable effects when material in view of the pyrometer melts, it was decided to place a small copper block of known melting point under the surface of the sand to be measured. When melting is observed, the emissivity can be calculated by rearranging the combined equations B.2 and B.1, leading to

$$\varepsilon(T_m, \lambda) = \varepsilon_{set} \exp\left[\frac{hc(T_m - T_o)}{k\lambda T_m T_o}\right], \tag{B.3}$$

where T_o is the melting temperature observed while the emissivity is set to emissivity ε_{set}, and T_m is the known melting point.

As the sand is destroyed in the process, only samples available in sufficient quantity where used. To observe the effect of grain size on emissivity, a measurement of ground SS was also taken. Furthermore the emissivity of a empty alumina crucible was determined by placing the copper block just outside the measuring spot, a similar approach was attempted for the bare SiC susceptor.

All samples were heated at a rate of $5\,^\circ\mathrm{C\,min^{-1}}$ while $\varepsilon_{set} = 0.65$. The measurements using copper where recorded for a measured temperature range of 800 °C to 1300 °C, or until the melting of the copper occurred. Ranges for supporting measurements were slightly different, but also covered a range of temperature around 1085 °C.

The measurement was repeated for some samples, with the block of copper in multiple positions, as well as a repetition with aluminium as the metal of choice ($T_m \approx$660 °C).

Results are summarized in table B.0.1, while the power and heating rate plots used to determine T_o are presented in figures B.0.1 to B.0.19. The temperature chosen for the calculation is marked.

There are multiple possible explanations for the variations seen in table B.0.1, as there are a lot factors of influence. Different heat conduction and resulting temperature distribution in the crucibles, the flow of the melting copper through the different sands, and while the susceptor should be shielded by the crucible, the possibly different reflection effects. This leads to difficulty determining the exact observed melting point as can be observed in the heating rate and power plots.

Table B.0.1: Overview of results of emissivity measurements; employed metal, placement, observed melting temperature for $\varepsilon_{set} = 0.65$ and calculated emissivity (equation B.3).

Sample	Metal	Placement of block	T_O [°C]	ε
Empty crucible	Cu	- Just outside measuring spot	1160	0.51
Susceptor	Cu	- To the side, on top of susceptor	1050	0.74
		- Under small piece of susceptor	1135	0.55
Q	Cu	- Just under measuring spot	1090	0.64
		- Compressed, Cu just under spot	1170	0.49
CAL	Cu	- Just under measuring spot, compressed powder	1040	0.77
SS	Cu	- Just under measuring spot	1180	0.47
		- Slightly deeper under measuring spot	1115	0.59
		- Under surface just outside measuring spot	1175	0.48
		- Stopped before melting	-	-
		- Finely ground sand, Cu just under spot	1140	0.54
	Al	- Just under measuring spot	660	0.65
TRIX	Cu	- Just under measuring spot	1075	0.67
		- Slightly deeper under measuring spot	1100	0.62
MAR	Cu	- Just under measuring spot (2x)	1100	0.62
			1110	0.60
	Al	- Just under measuring spot	665	0.63
EXOY	Cu	- Just under measuring spot	1100	0.62
MEX	Cu	- Just under measuring spot	1100	0.62
EXOR	Cu	- Just under measuring spot	1120	0.58

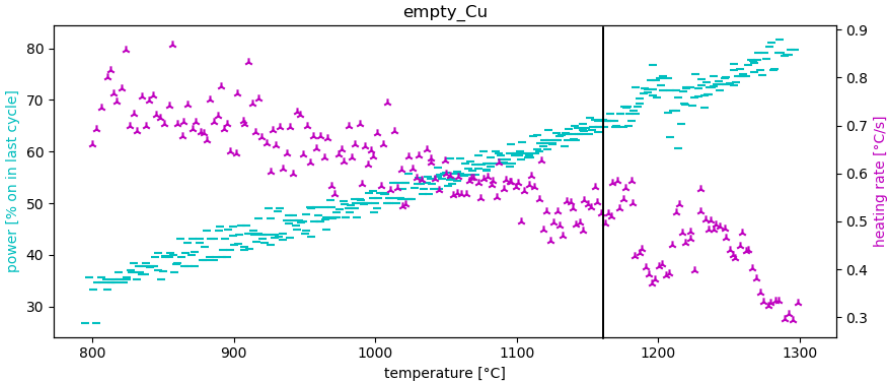

Figure B.0.1: Empty crucible, copper just outside measuring spot.

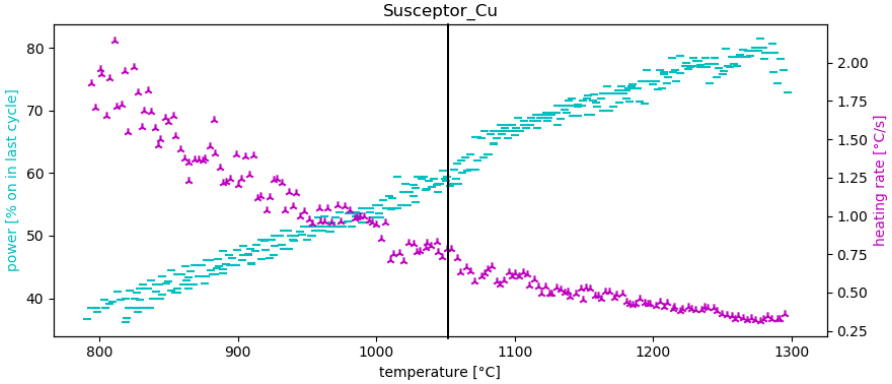

Figure B.0.2: Bare susceptor, copper on top outside of view of pyrometer.

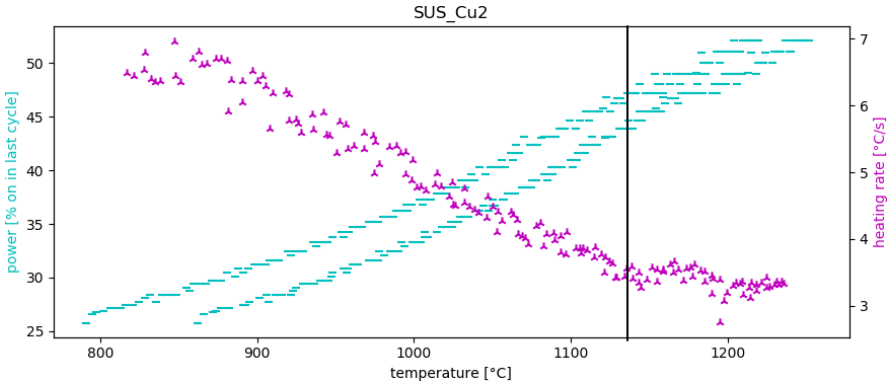

Figure B.0.3: Bare susceptor on top of copper block.

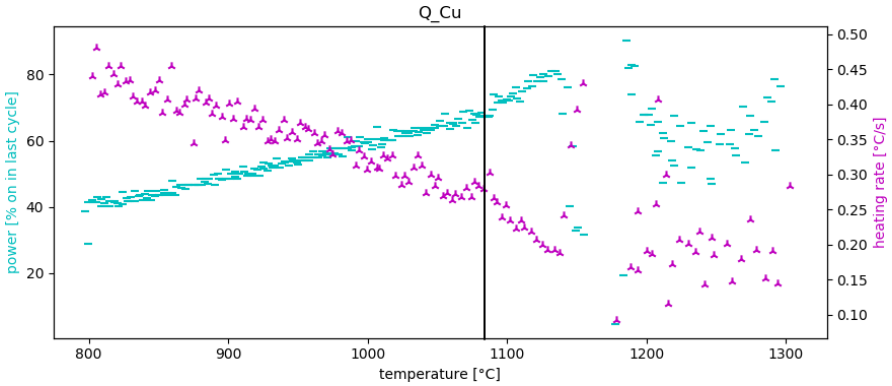

Figure B.0.4: Q, copper just below measuring spot.

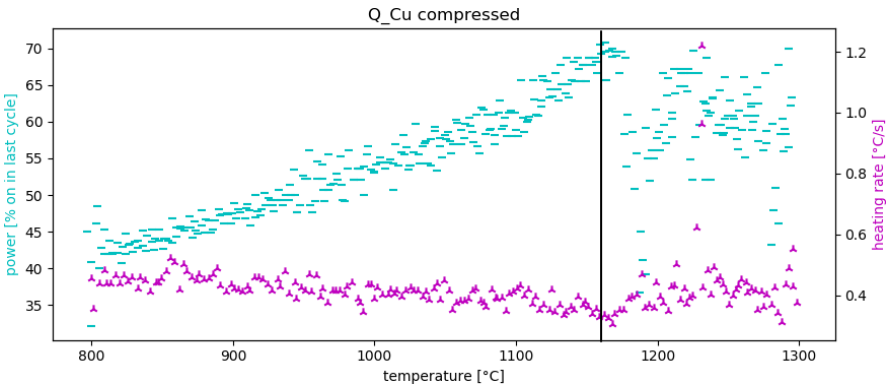

Figure B.0.5: Q compressed, copper just below measuring spot.

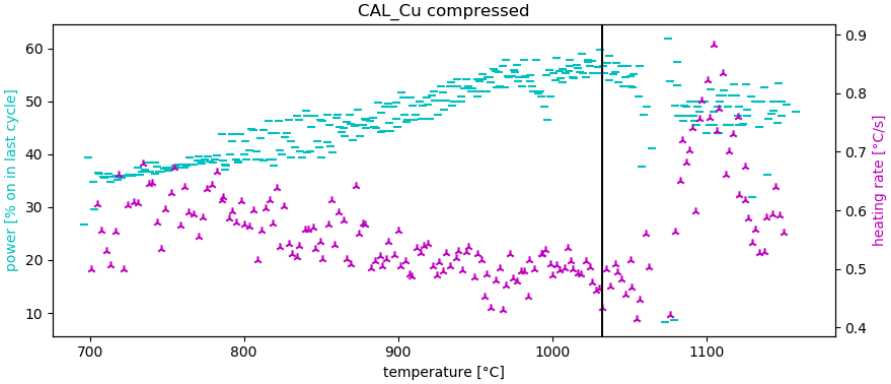

Figure B.0.6: CAL compressed, copper just below measuring spot.

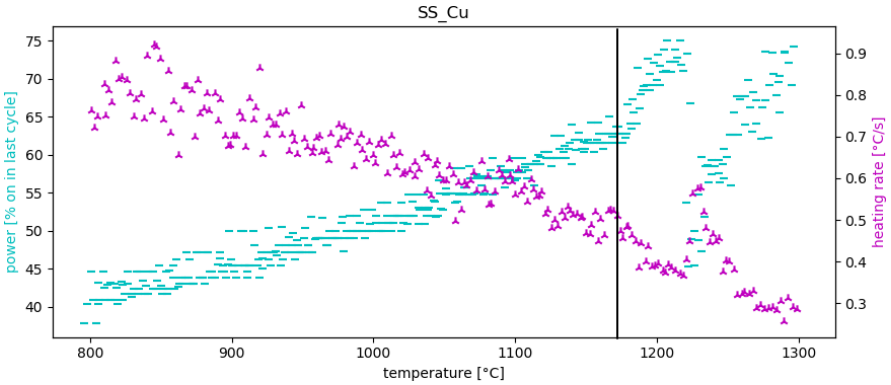

Figure B.0.7: Silver sand, copper just below measuring spot.

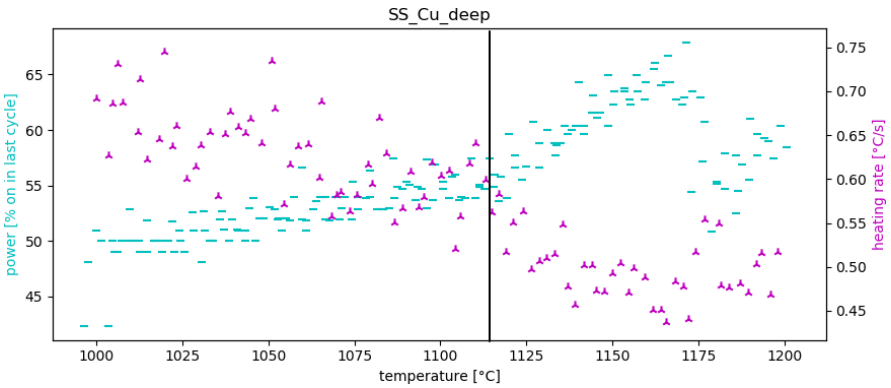

Figure B.0.8: Silver sand, copper slightly deeper under measuring spot.

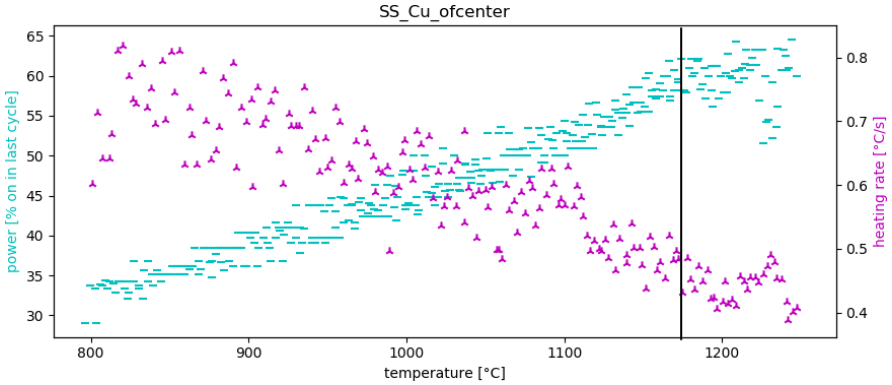

Figure B.0.9: Silver sand, copper just under surface to the side of measuring spot.

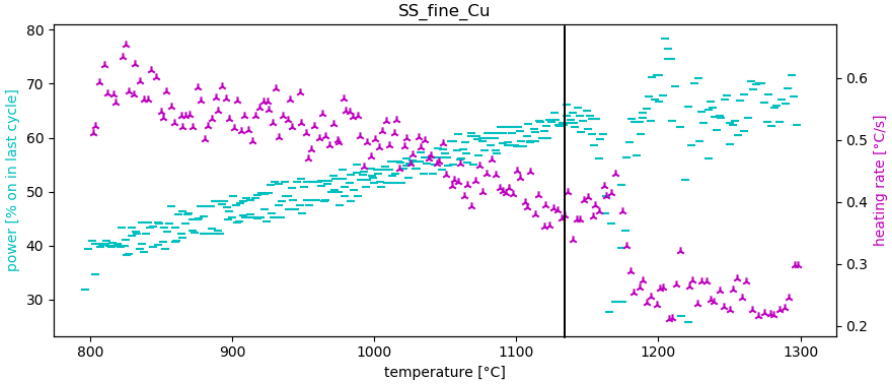

Figure B.0.10: Ground silver sand, copper just below measuring spot.

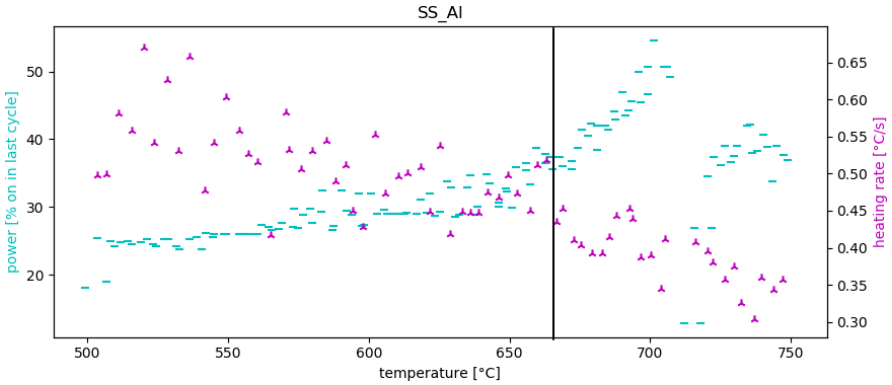

Figure B.0.11: Silver sand, aluminium just below measuring spot.

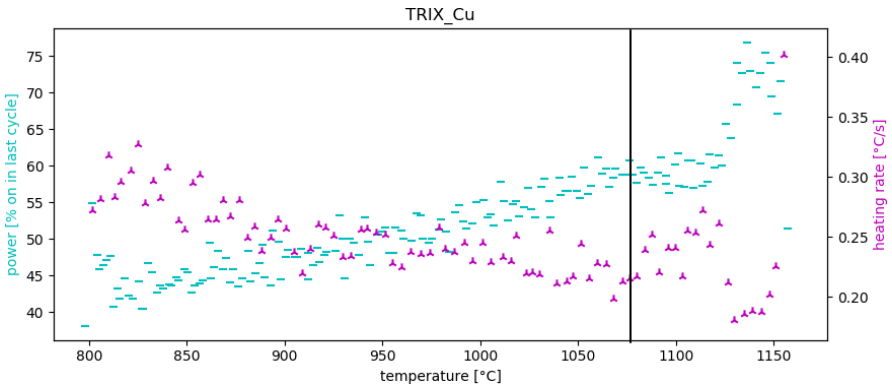

Figure B.0.12: TRIX, copper just below measuring spot.

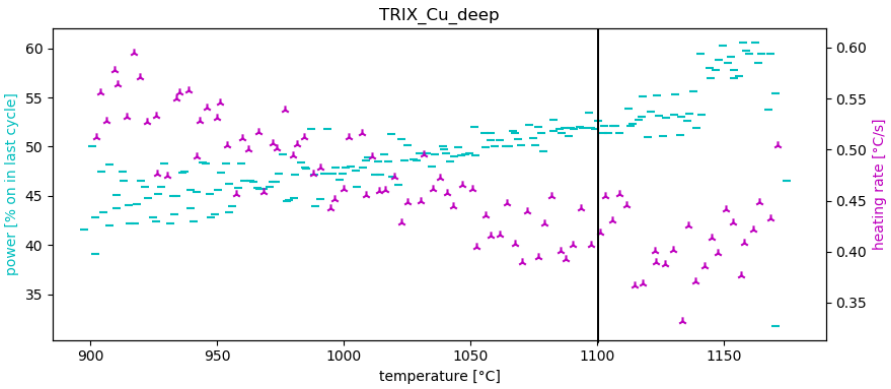

Figure B.0.13: TRIX, copper slightly deeper under measuring spot.

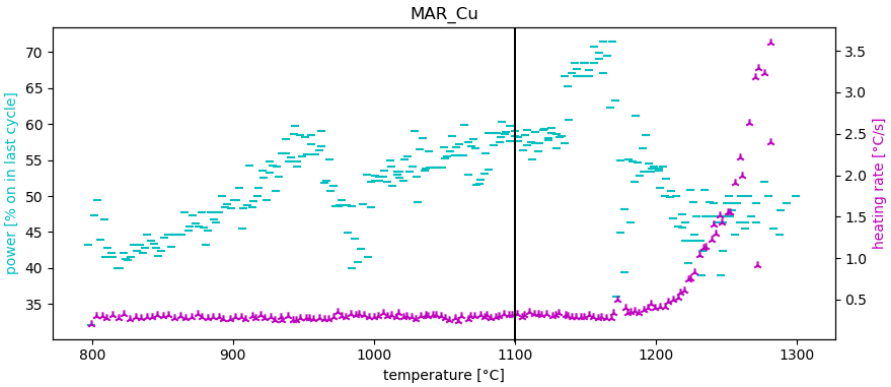

Figure B.0.14: MAR, copper just below measuring spot.

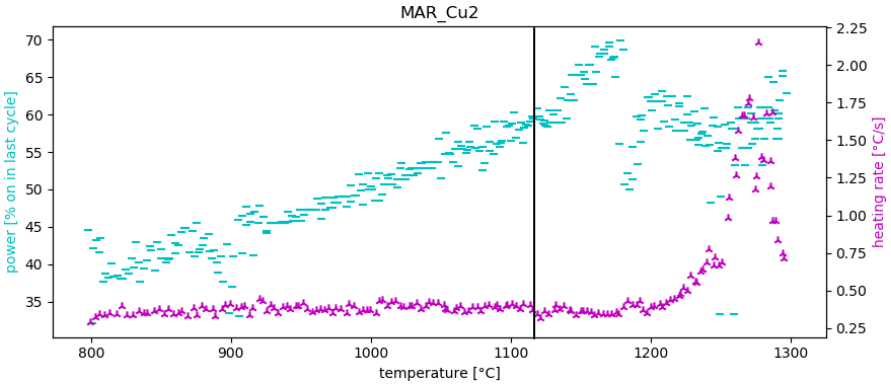

Figure B.0.15: MAR, copper just below measuring spot, second measurement.

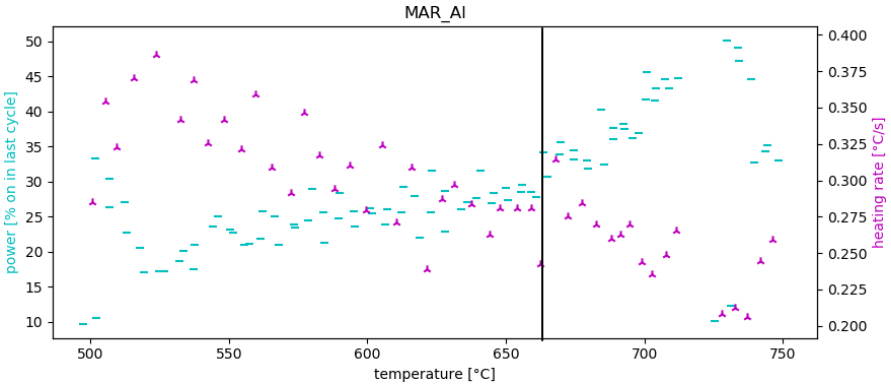

Figure B.0.16: MAR, aluminium just below measuring spot.

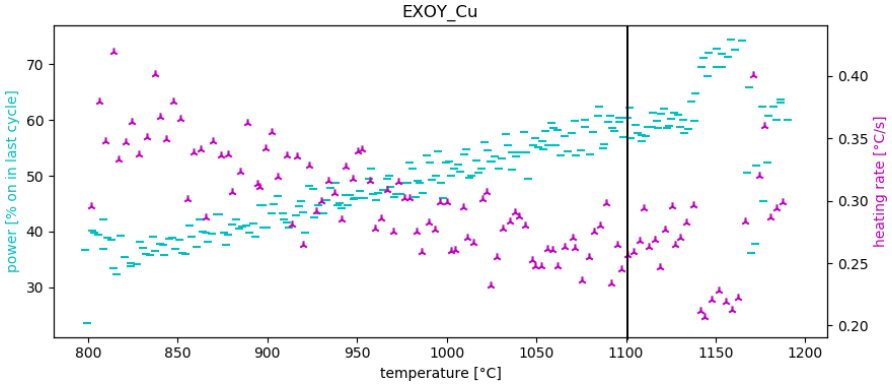

Figure B.0.17: EXOY, copper just below measuring spot.

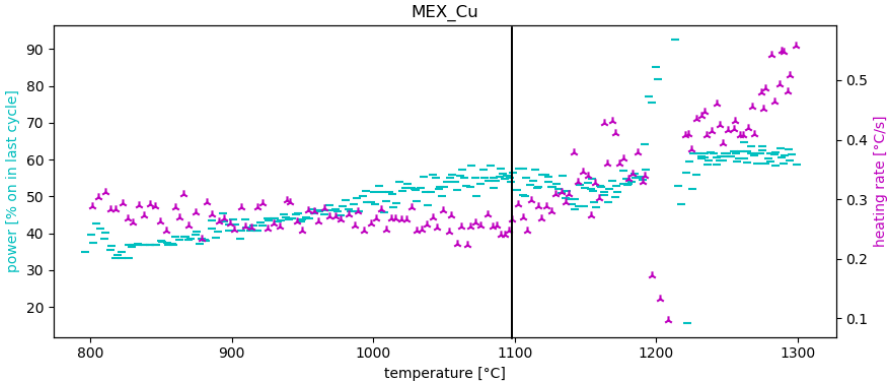

Figure B.0.18: MEX, copper just below measuring spot.

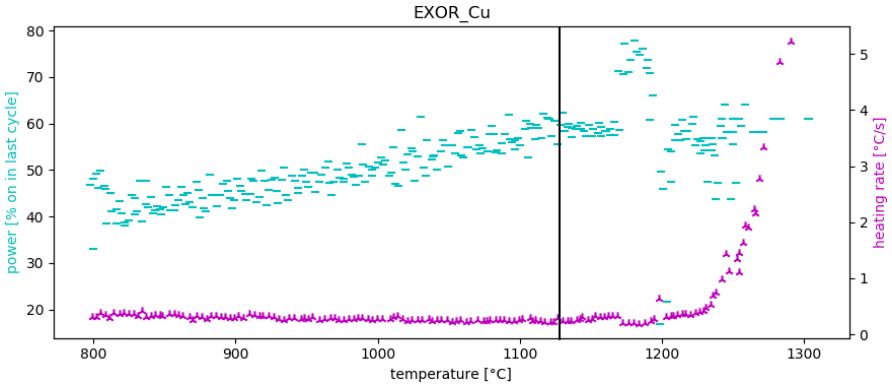

Figure B.0.19: EXOR, copper just below measuring spot.

C

Desert sand

All additional material regarding unmodified desert sand is collected in this appendix. Section C.1 contains micrographs of all sand samples before melting, the heating rate and power plots recorded during melting are found in section C.2, followed by images of the resulting samples in section C.3.

C.1. Micrographs of sand

Before melting, small amounts of the desert sand samples were collected on adhesive labels and laminated for safe keeping. The resulting laminate was inspected under a optical microscope. Lighting was applied in transmission to prevent reflections from the plastic.

The result is presented in figure C.1.1. It seems that with the exception of sample AE1, all samples fit both definitions of sand presented in section 2.3, but as the definitions are broad there is quite some variation to be observed. Grain size reaches from ~0.1 mm for samples TN2 and MEX to ~2 mm for sample SD1, and a variety of colouration is displayed.

Based on this set, there does not seem to be a direct relation between composition and appearance. Samples with higher quartz content do appear more homogeneous, for example sample TN2, JO1, and all store bought samples, are relatively constant in colour and grain size. Samples for which the fraction of feldspars and/or carbonates is higher display more variation, mostly in the form of less translucent grains.

As the quantities of sand available were too small to investigate this possible relationship, this was left for further research.

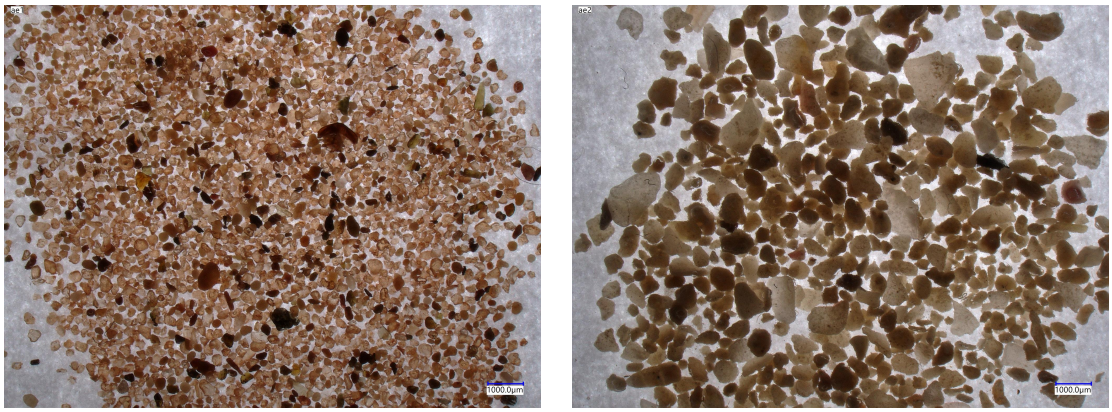

(a) AE1 **(b)** AE2

Figure C.1.1: Sand samples collected on adhesive label, laminated and imaged while illuminated from below. All images are taken at the same magnification, the scale bar in the bottom right corner is 1 mm, each image covers 15 mm in width. (Continued on next page)

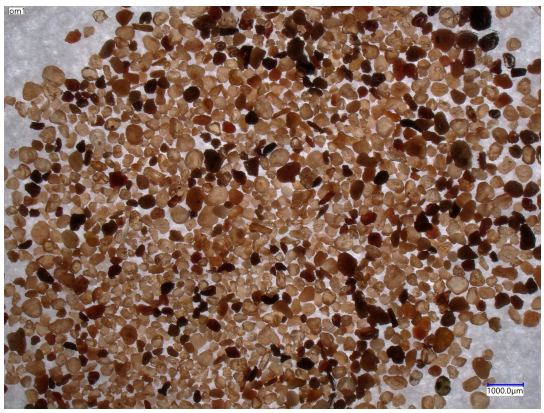

(a) OM1

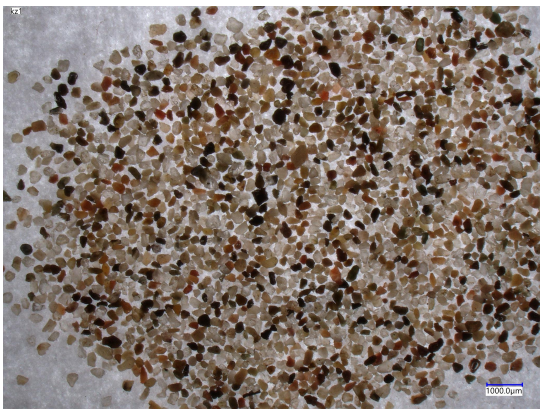

(b) KZ1

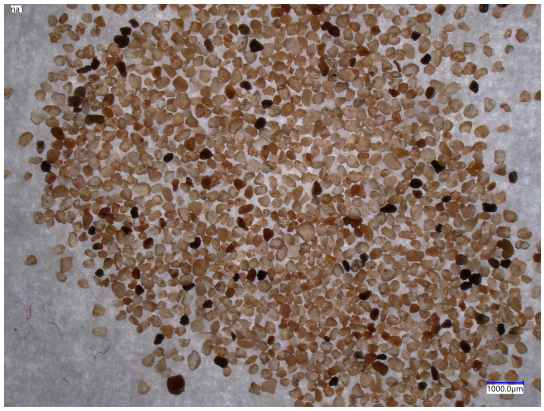

(c) NA1

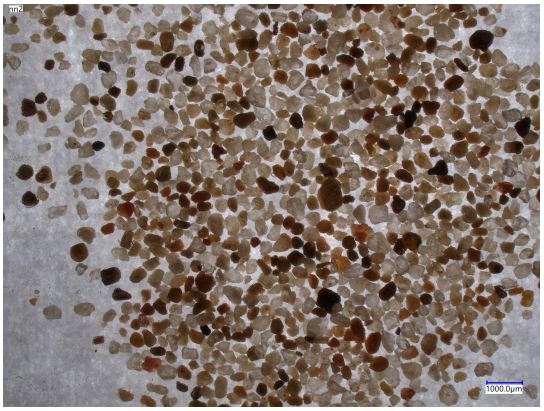

(d) MN2

(e) IR1

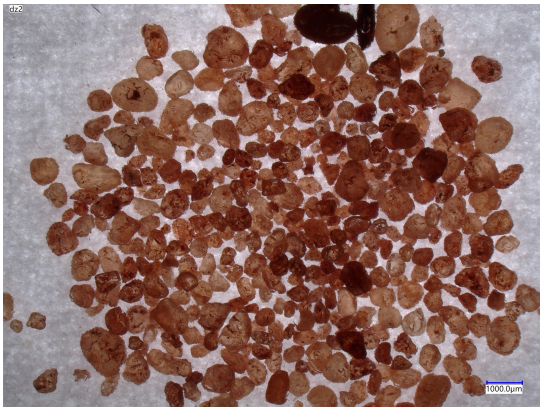

(f) DZ2

Figure C.1.2: Sand samples collected on adhesive label, laminated and imaged while illuminated from below. All images are taken at the same magnification, the scale bar in the bottom right corner is 1 mm, each image covers 15 mm in width. (Continued, continued on next page)

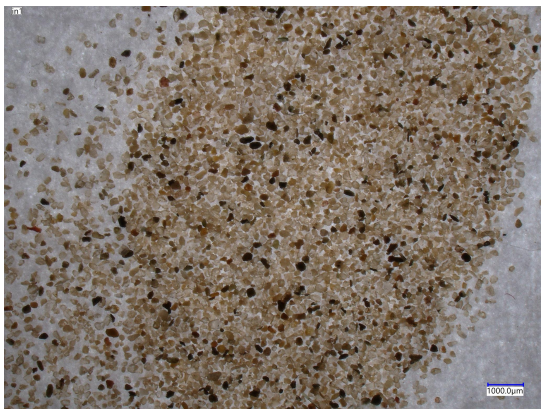

(g) IN1

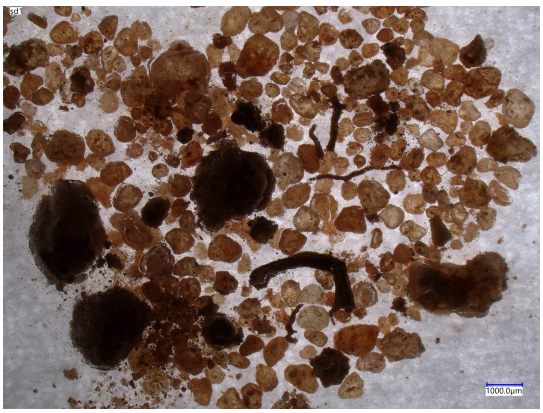

(h) SD1

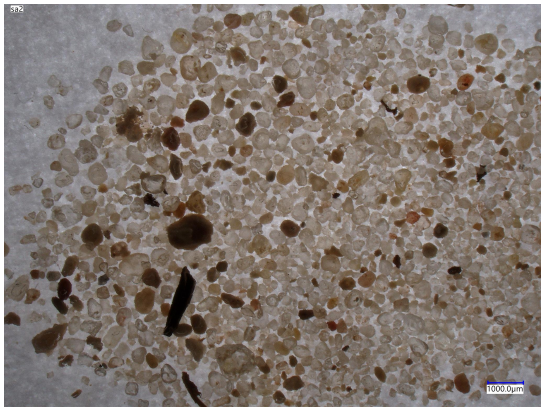

(i) SA2

(j) TN2

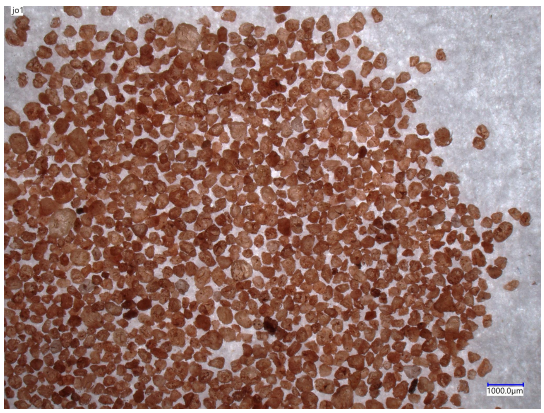

(k) JO1

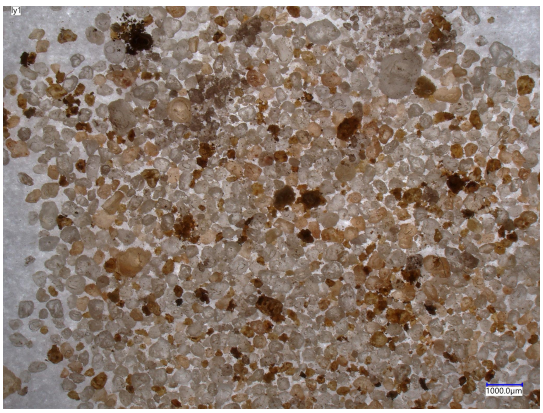

(l) LY1

Figure C.1.2: Sand samples collected on adhesive label, laminated and imaged while illuminated from below. All images are taken at the same magnification, the scale bar in the bottom right corner is 1 mm, each image covers 15 mm in width. (Continued, continued on next page.)

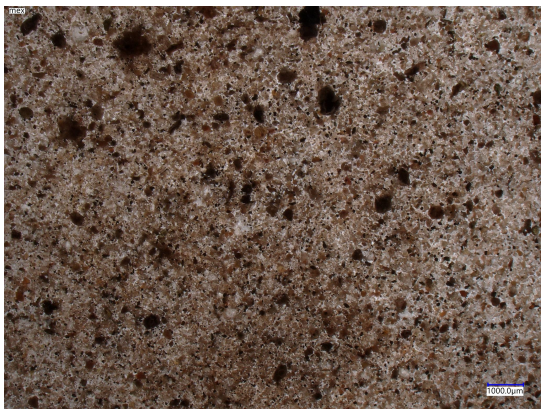

(m) MEX

(n) MAR

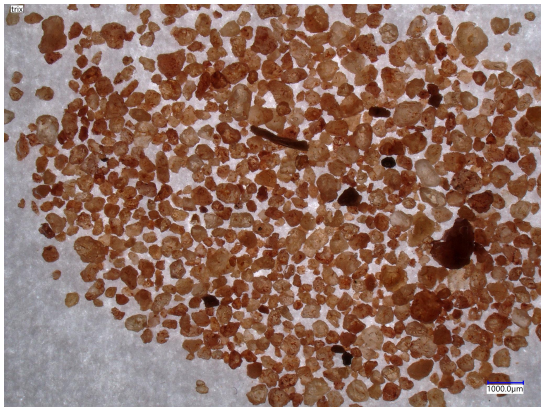

(o) TRIX

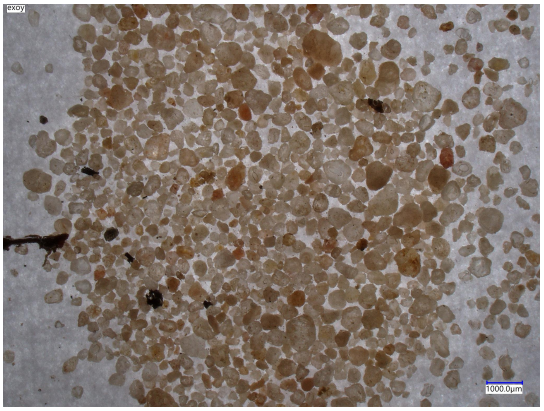

(p) EXOY

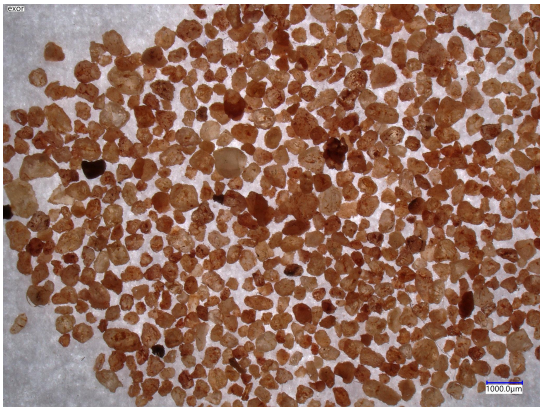

(q) EXOR

Figure C.1.2: Sand samples collected on adhesive label, laminated and imaged while illuminated from below. All images are taken at the same magnification, the scale bar in the bottom right corner is 1 mm, each image covers 15 mm in width. (Continued)

C.2. Heating rate and power plots

Presented in order of decreasing predicted practical melting point. Unless mentioned otherwise, the emissivity was set to 0.62. When applicable, details of the measured temperature curve are presented following the rate and power plot.

The sudden change in rate and/or power when 90 % of full power is reached is caused by the controller halving the heating rate to 2.5 °C min^{-1}.

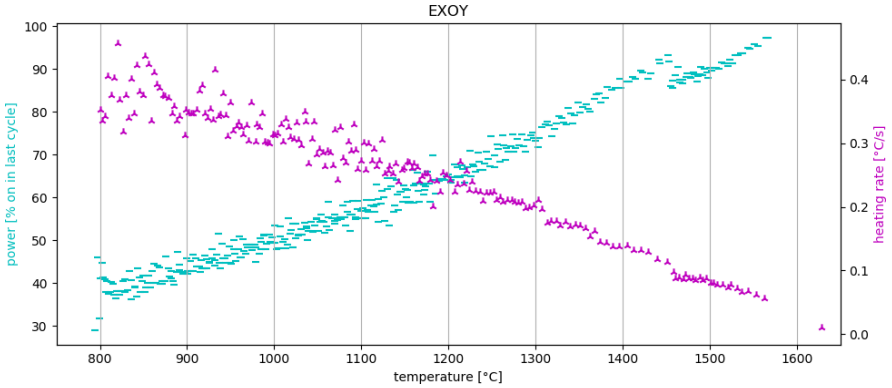

Figure C.2.1: Power and heating rate plot of sample EXOY.

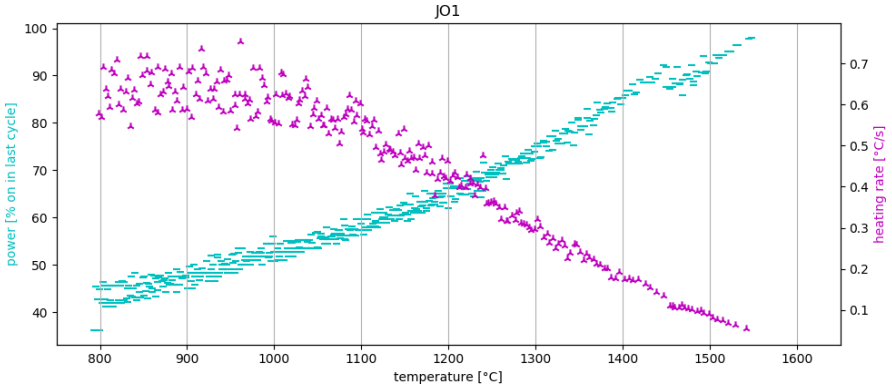

Figure C.2.2: Power and heating rate plot of sample JO1.

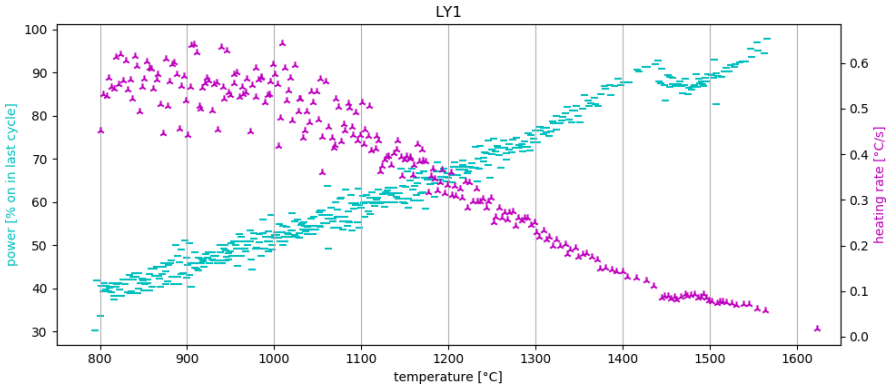

Figure C.2.3: Power and heating rate plot of sample LY1.

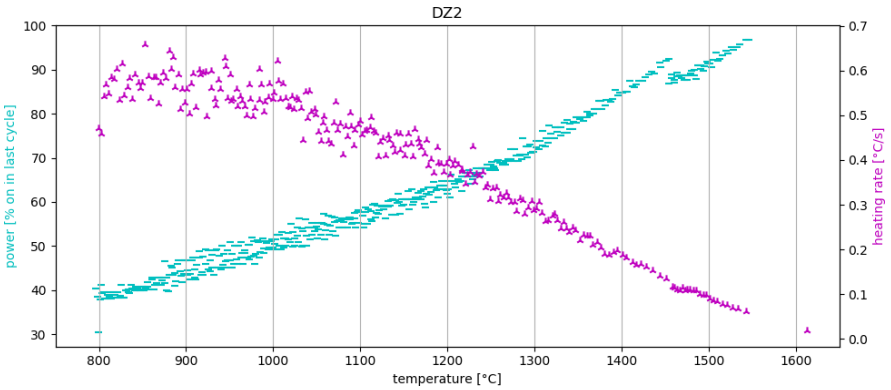

Figure C.2.4: Power and heating rate plot of sample DZ2.

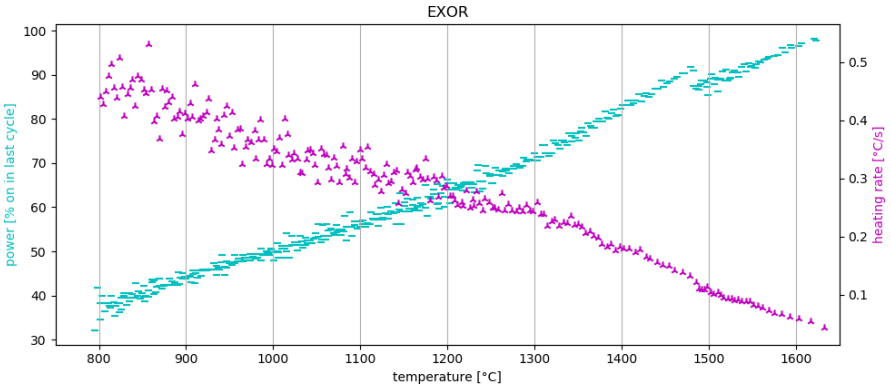

Figure C.2.5: Power and heating rate plot of sample EXOR. $\varepsilon = 0.58$.

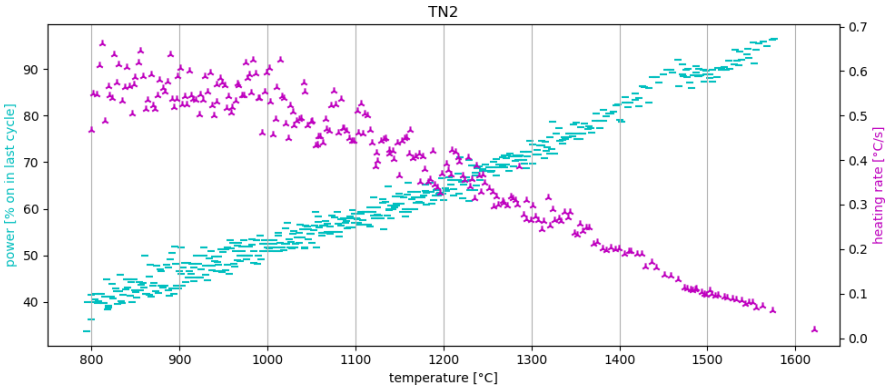

Figure C.2.6: Power and heating rate plot of sample TN2.

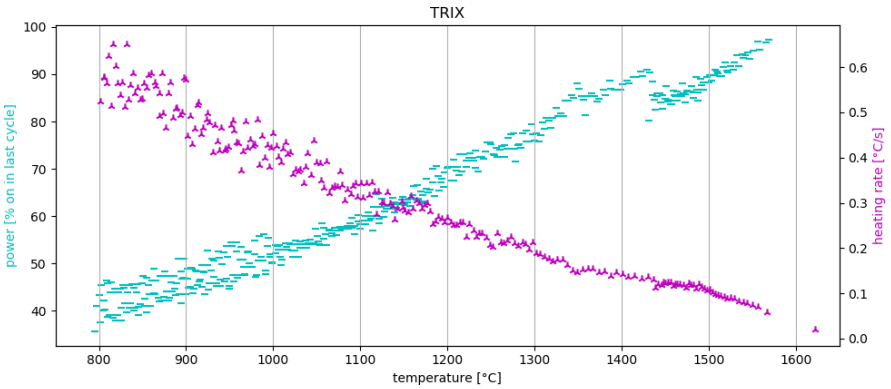

Figure C.2.7: Power and heating rate plot of sample TRIX. $\varepsilon = 0.67$.

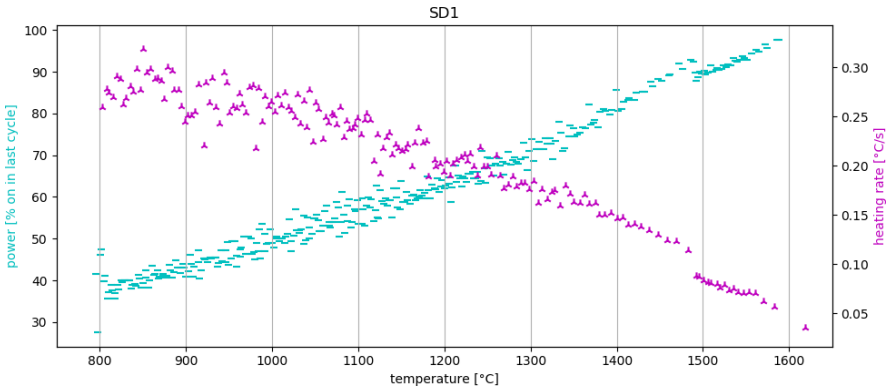

Figure C.2.8: Power and heating rate plot of sample SD1.

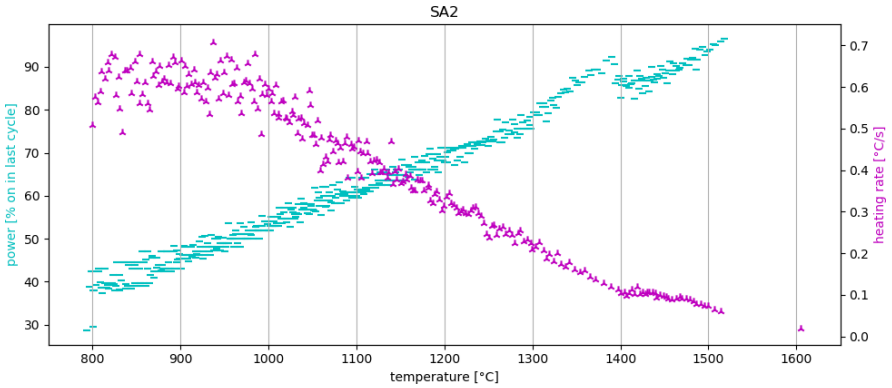

Figure C.2.9: Power and heating rate plot of sample SA2.

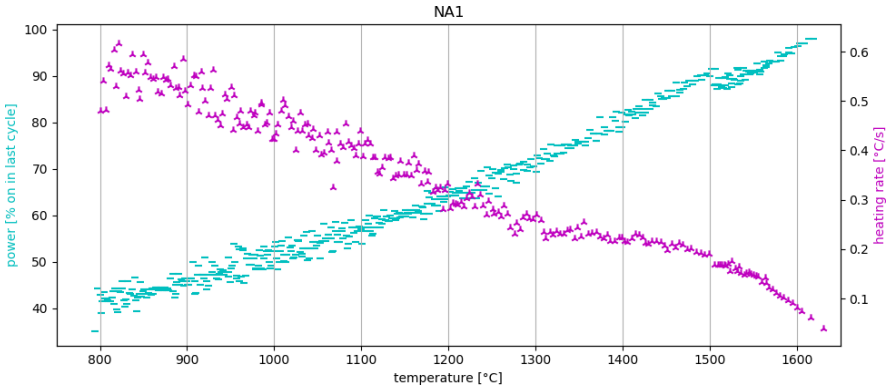

Figure C.2.10: Power and heating rate plot of sample NA1.

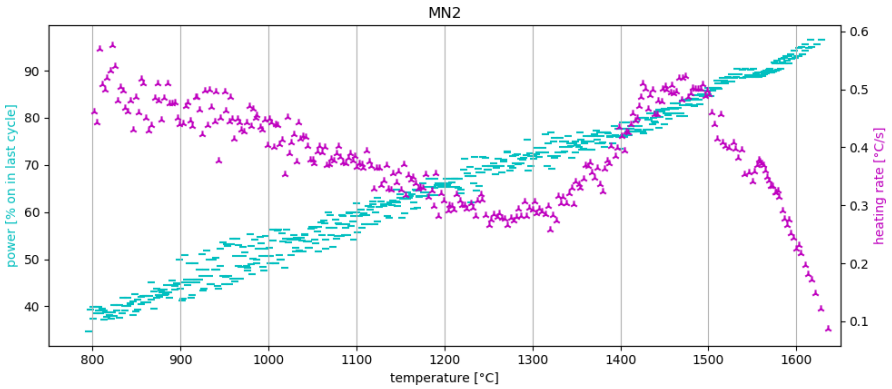

Figure C.2.11: Power and heating rate plot of sample MN2.

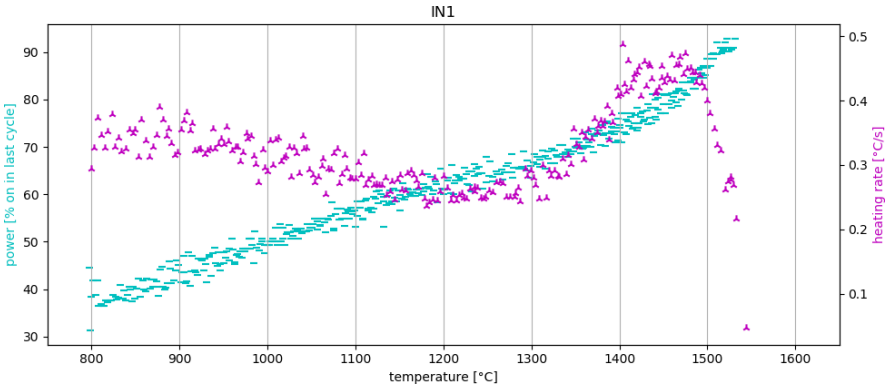

Figure C.2.12: Power and heating rate plot of sample IN1.

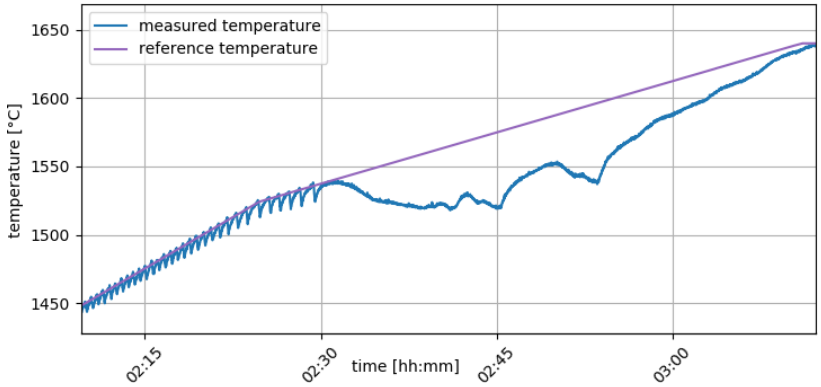

Figure C.2.13: Detail of temperature curve of sample IN1.

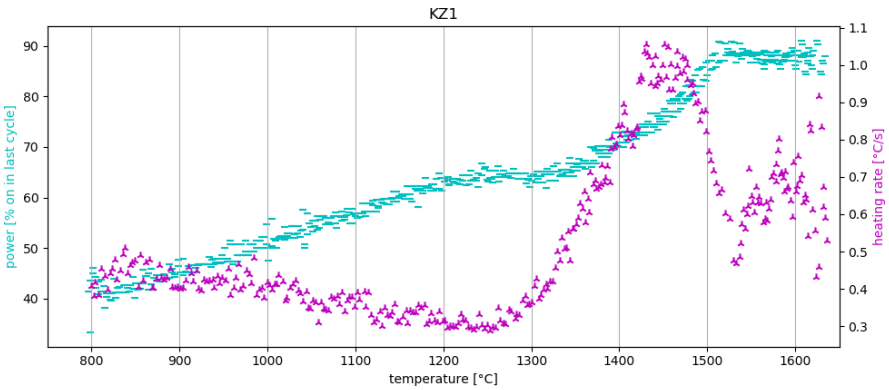

Figure C.2.14: Power and heating rate plot of sample KZ1.

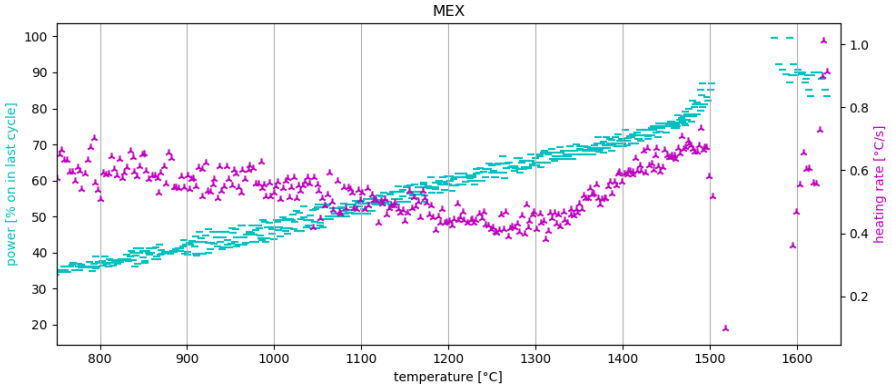

Figure C.2.15: Power and heating rate plot of sample MEX.

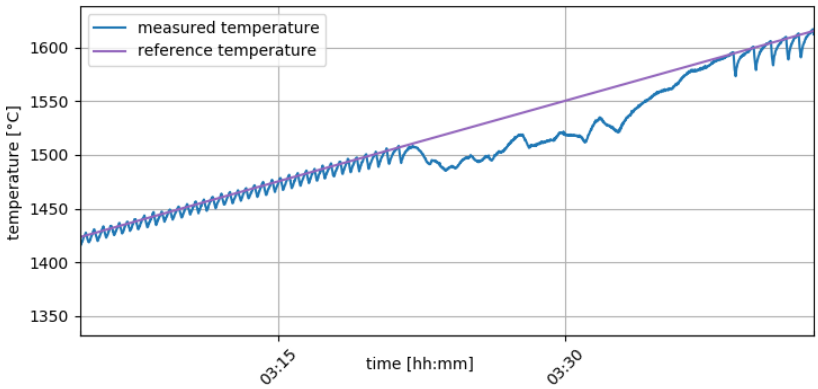

Figure C.2.16: Detail of temperature curve of sample MEX.

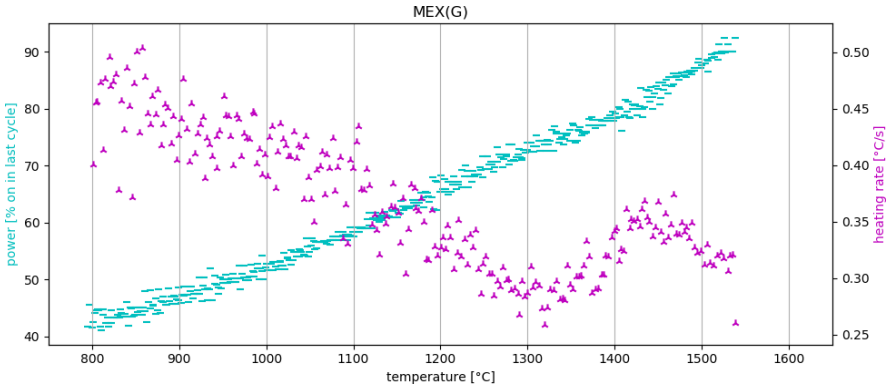

Figure C.2.17: Power and heating rate plot of sample MEX after prior heating to 1100 °C, stopped at sudden expansion at ~1550 °C.

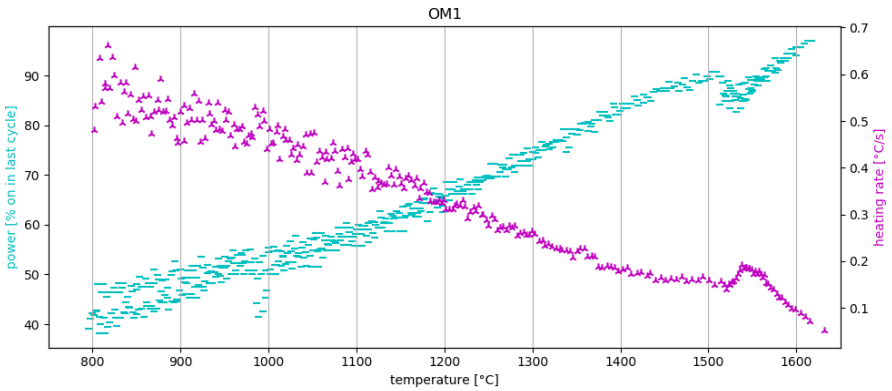

Figure C.2.18: Power and heating rate plot of sample OM1.

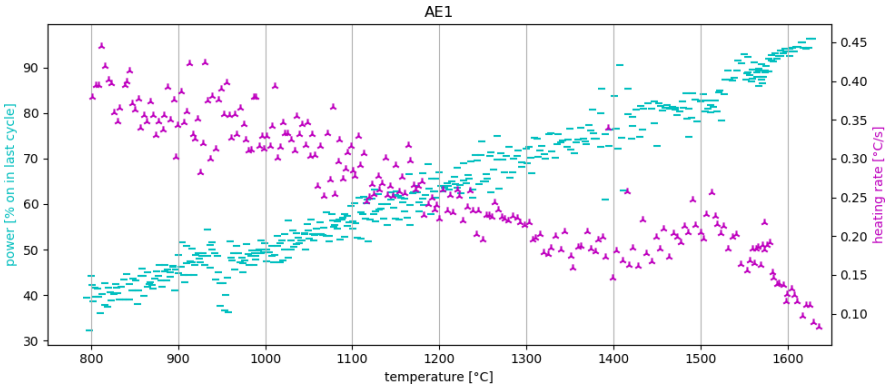

Figure C.2.19: Power and heating rate plot of sample AE1.

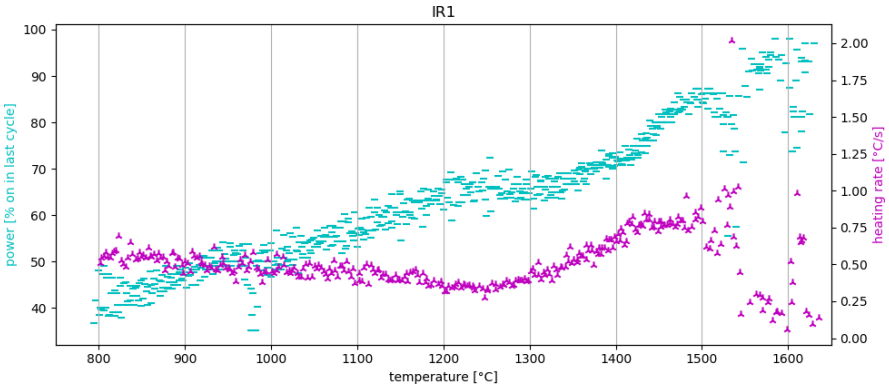

Figure C.2.20: Power and heating rate plot of sample IR1.

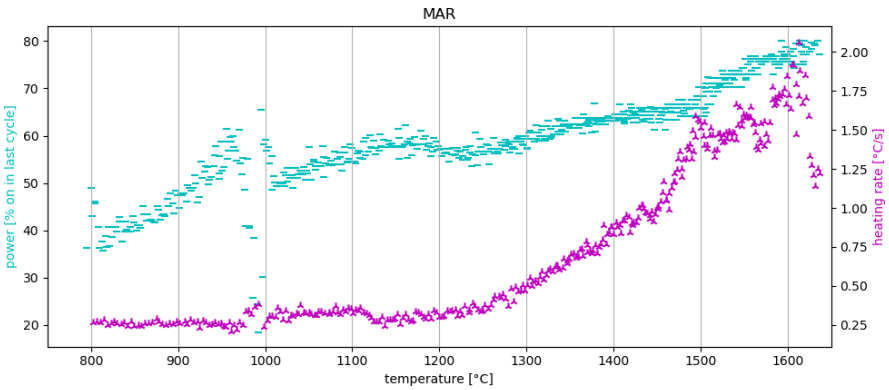

Figure C.2.21: Power and heating rate plot of sample MAR.

C.3. Visual of heated sand

The visual results are presented in order of increasing magnification. First photographs taken immediately after cooling can be found in figure C.3.1, followed by an overview of micrographs at 20x magnification in figure C.3.2.

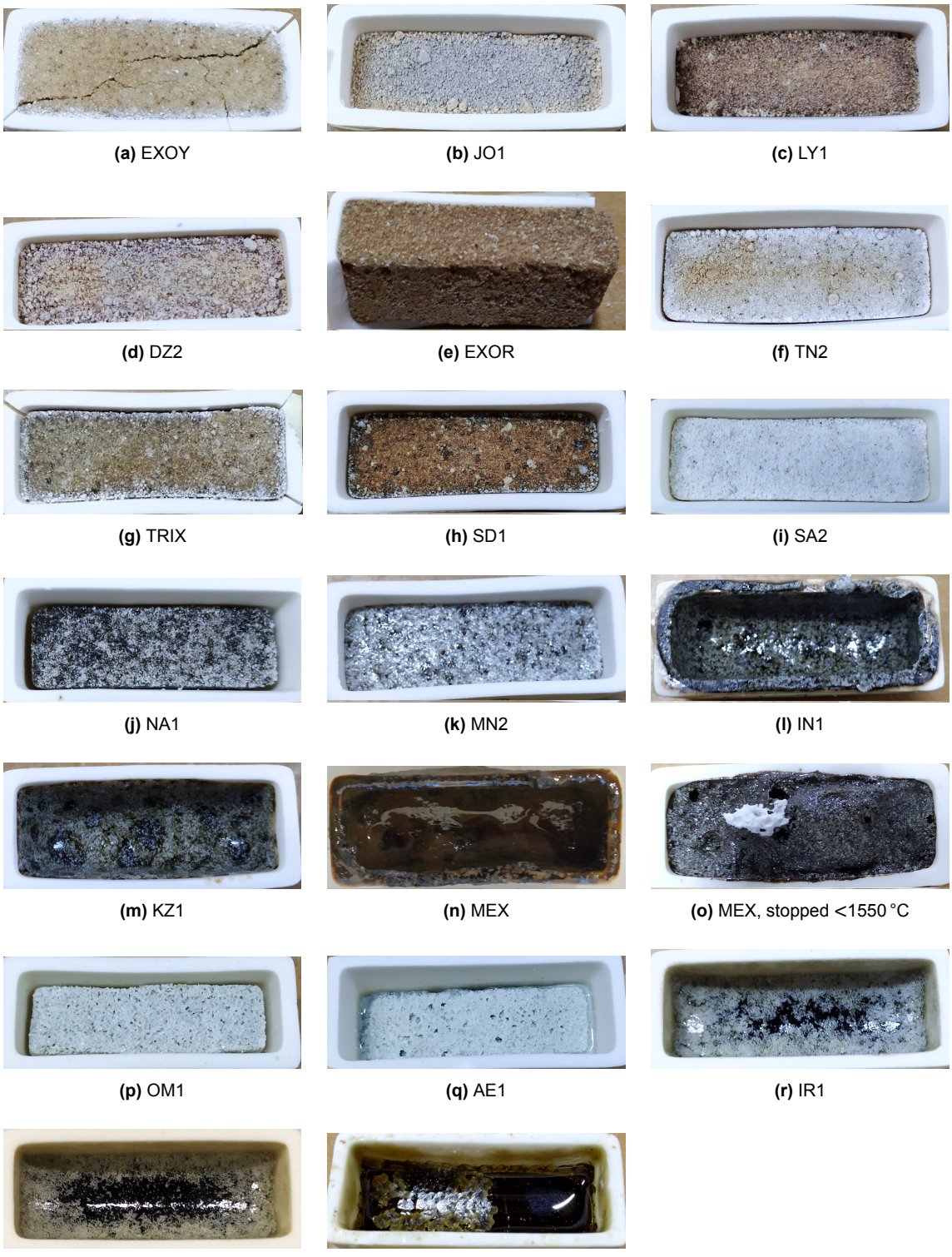

(a) EXOY **(b)** JO1 **(c)** LY1

(d) DZ2 **(e)** EXOR **(f)** TN2

(g) TRIX **(h)** SD1 **(i)** SA2

(j) NA1 **(k)** MN2 **(l)** IN1

(m) KZ1 **(n)** MEX **(o)** MEX, stopped <1550 °C

(p) OM1 **(q)** AE1 **(r)** IR1

(s) IR1, 1+2 h soaking **(t)** MAR

Figure C.3.1: Photographs of samples after being soaked at ~1640 °C for 1 h. Outside dimensions of each crucible are approximately 2 cm × 5 cm.

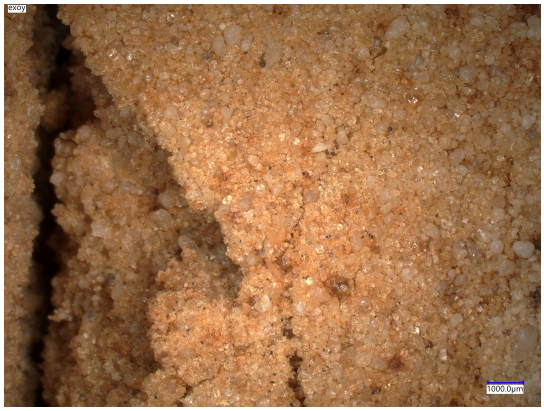

(a) EXOY

(b) JO1

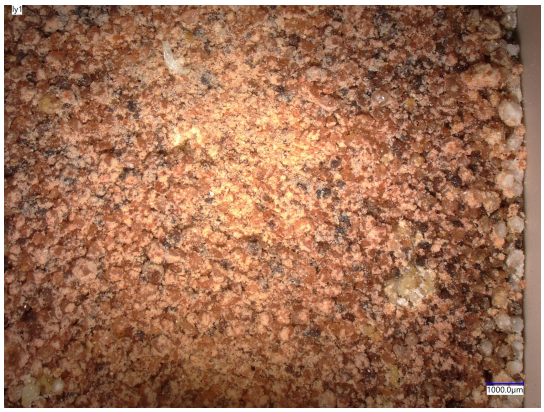

(c) LY1

(d) DZ2

(e) EXOR

(f) TN2

(g) TRIX

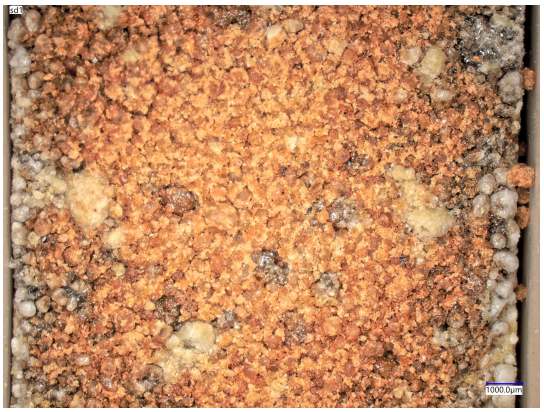

(h) SD1

Figure C.3.2: Micrographs of samples after being soaked at ~1640 °C for 1 h. The scale bar in the bottom right corner is 1 mm in all cases. (Continued on next page)

(i) SA2

(j) NA1

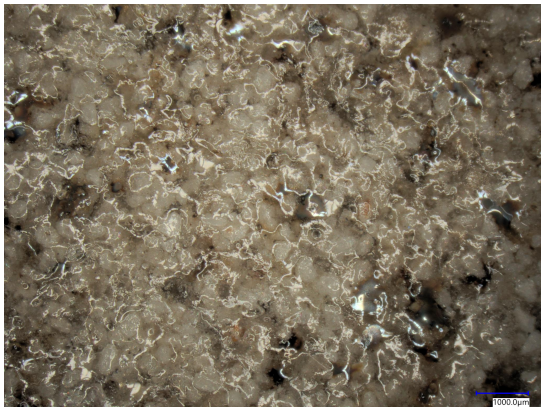

(k) MN2

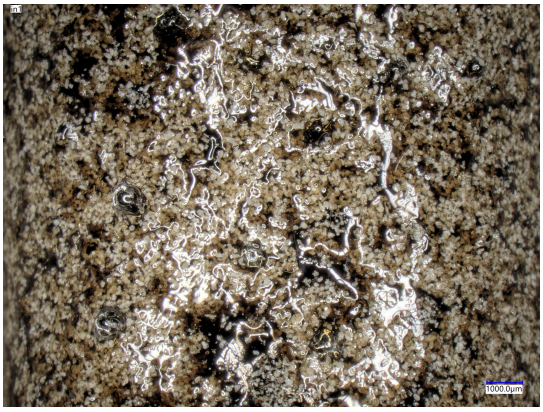

(l) IN1

(m) KZ1

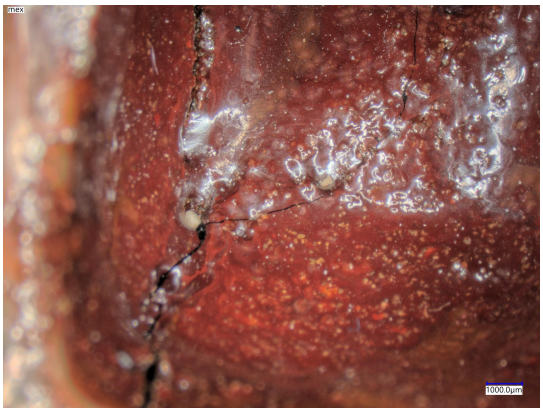

(n) MEX

Figure C.3.2: Micrographs of samples after being soaked at ∼1640 °C for 1 h. The scale bar in the bottom right corner is 1 mm in all cases. (Continued, continued on next page)

(o) MEX <1550 °C

(p) OM1

(q) AE1

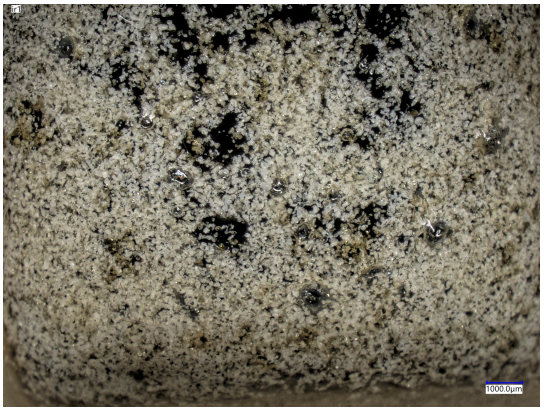

(r) IR1

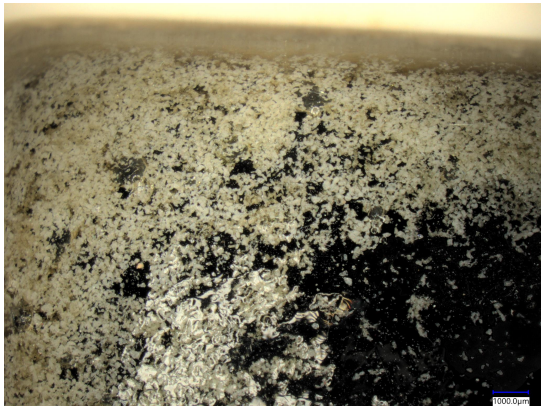

(s) IR1, 1+2 h soaking

(t) MAR

Figure C.3.2: Micrographs of samples after being soaked at ~1640 °C for 1 h. The scale bar in the bottom right corner is 1 mm in all cases. (Continued)

D

Unsuccessful casting experiments

The casts that were successful were presented in section 4.7.2, the less successful ones are collected here. Most involve Crystal Cast, a gypsum and silica based moulding material intended for glass. The maximum temperature of operation is 1100 °C.

Casting on steel did work, but the cracking of a crucible necessitated shutting down the furnace. The remaining crucibles are displayed in figure D.0.1.

As can be observed in figure D.0.2, casting glass at higher temperature onto Crystal Cast preheated to the annealing temperature, resulted in a violent reaction between the melt and the mould material. The release of water from the gypsum based material caused bubble formation. Therefore the other mixtures where not attempted.

Figure D.0.3 displays the result of kiln casting: soaking the glass at high temperature for an extended period of time to let it flow into the mould. It can be seen that most mixtures were too viscous at the maximum operating temperature of the crystal cast, while it was fluid enough to crystallise.

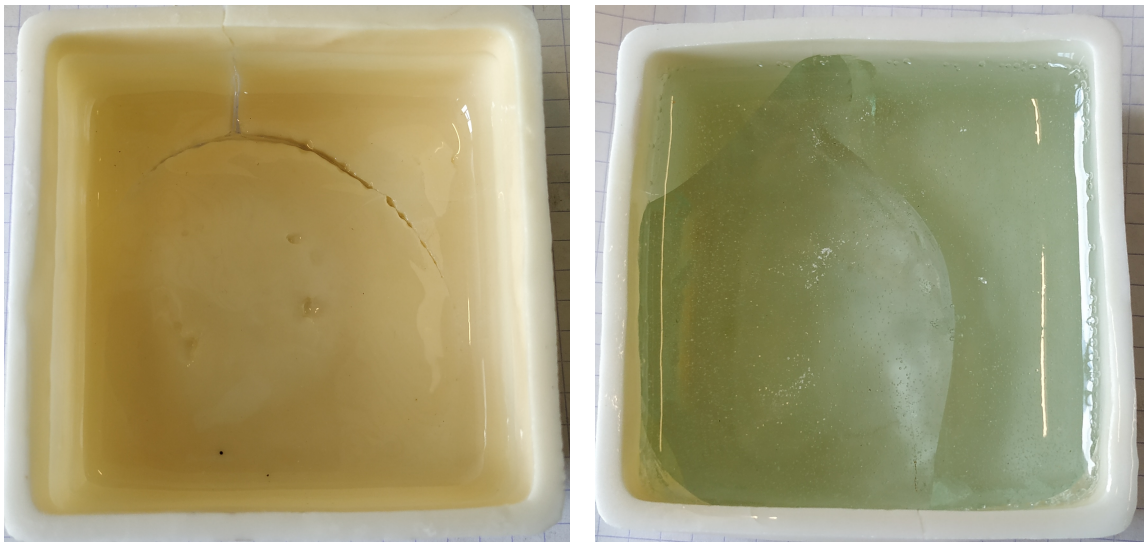

(a) Empty crucible previously containing mixture IM-MOREC, which leaked into the furnace.

(b) Mixture IM-NOQ, in crucible as the experiment was aborted.

Figure D.0.1: Remaining crucibles after resistive heating and shutdown of experiment.

Figure D.0.2: Result of casting mixture IM-MOREC (~1600 °C) onto preheated Crystal Cast (~1100 °C).

(a) Mixture IM-MAR

(b) Mixture IM-MOREC.

(c) Mixture IM-NOQ.

Figure D.0.3: Results of an attempt at kiln casting, 7x7 cm crucibles, soaked for 12 h at 1100 °C.